THE UNIVERSITY of ADELAIDE

Real-time Pipeline Burst Detection and Estimation using the Damping of Fluid Transients

XIAOXUAN DU

SCHOOL OF MECHANICAL ENGINEERING

2022

Real-time Pipeline Burst Detection and Estimation using the Damping of Fluid Transients

Xiaoxuan Du

B.Eng., M.Eng.

Thesis submitted in fulfilment of the requirements for the degree of Doctor of Philosophy

The University of Adelaide

Faculty of Engineering, Computer and Mathematical Sciences

School of Mechanical Engineering

Table of Contents

List of Figures

List of Tables

Statement of Originality

I certify that this work contains no material that has been accepted for the award of any other degree or diploma in my name, in any university or other tertiary institution and, to the best of my knowledge and belief, contains no material previously published or written by another person, except where due reference has been made in the text. In addition, I certify that no part of this work will, in the future, be used in a submission in my name, for any other degree or diploma in any university or other tertiary institution without the prior approval of the University of Adelaide and, where applicable, any partner institution responsible for the joint award of this degree.

The author acknowledges that copyright of published works contained within the thesis resides with the copyright holder(s) of those works.

I give permission for the digital version of my thesis to be made available on the web, via the University's digital research repository, the Library Search and also through web search engines, unless permission has been granted by the University to restrict access for a period of time.

14/01/2022

Candidate's Signature ..... Date

Supervisor Declaration Statement

I have reviewed the content and presentation style of this thesis and declare it is free of plagiarism and of sufficient grammatical clarity to be examined. I confirm that the investigations were conducted in accord with the ethics policies and integrity standards of the University of Adelaide, and that the research data are presented honestly and without prejudice.

18/01/2022

Supervisor's Signature ..... Date

18/1/2022

Supervisor's Signature ..... Date

19/1/2022

Supervisor's Signature ..... Date

Publication List

The following journal papers are included in the thesis.

1. Xiao-xuan Du, Martin F. Lambert, Lei Chen, Eric Jing Hu, and Wang Xi. Pipe burst detection, localization, and quantification using the transient pressure damping method. (2020) *Journal of Hydraulic Engineering*, 146(11): 04020077.

2. Xiao-xuan Du, Wei Zeng, Martin F. Lambert, Lei Chen, and Eric Jing Hu. Approach for near-real-time pipe burst detection, localization, and quantification with low data transmission and sampling rates. (2021) *Journal of Water Resources Planning and Management*, 147(7): 04021032.

3. Xiao-xuan Du, Martin F. Lambert, Lei Chen, and Eric Hu. Approach for Near-Real-time Pipe Burst Detection and Location Estimation Utilizing Any Sequence of Harmonics of the Transient Pressure Signal (submitted for peer review). *Journal of Water Resources Planning and Management*.

4. Xiao-xuan Du, Martin F. Lambert, Lei Chen, and Eric Hu. Linking the Damping of Fluid Transients and Frequency Response Diagram Methods for Pipe Leak and Burst Detection and Localization (submitted for peer review). *Journal of Hydraulic Engineering*.

Abstract

Water is a vital human resource, and the corresponding water distribution pipelines are critical to modern cities' infrastructure. Any burst in the water distribution pipelines can cause significant economic losses, interrupt traffic, and result in negative publicity for water utility companies. As a result, pipeline burst detection technologies have been widely explored; however, the applications of some of the previously-explored techniques, in both the time and the frequency domains, require multiple sensors, which leads to a high cost for the sensing system. Additionally, some of the techniques cannot be applied to real-time data monitoring, indicating that the burst cannot be captured in real-time and, thus, the negative effects from the burst cannot be minimized. Consequently, this thesis aims to investigate an approach for real-time pipe burst detection and estimation (i.e., localization and size quantification) in a pipeline using the measured data in the whole frequency range of the transient pressure signals that are measured by one sensor alone. Earlier research has shown that a pipeline leak can cause additional damping of the transient pressure signals. The additional damping exists in burst problems. Additionally, according to the burst damping equation that is developed in this thesis, the harmonic components of the transient signal are damped differently in all the resonance responses in a newly-developed discrete harmonic spectrogram in the frequency domain, due to the burst. Accordingly, the damped resonance responses can be utilized to detect and estimate the burst. This specific analysis makes pipe burst detection and estimation utilizing transient pressure signals possible in the frequency domain.

The research proposes a novel technique for pipe burst detection, localization, and size quantification using transient pressure signals in the frequency domain. The damping caused by both the friction and the burst exists in the transients of the pressure head. The technique can analyze the resonance responses of the transient pressure signals caused by the burst measured by one sensor alone, during every fundamental period of the signal, to determine the total damping. The steady friction damping can be calculated, and a developed unsteady friction water hammer model for burst initiation enables the unsteady friction damping caused by the burst to be estimated. Therefore, the burst damping can be calculated by subtracting the steady and unsteady friction damping from the total damping, so that the burst can then be identified, localized, and quantified utilizing the burst damping ratios. Only the damping of the first three resonance harmonics is utilized to minimize the number of possible solutions to the burst location.

This technique has been further developed from the perspective of real-time data monitoring. The corresponding algorithm enables the transient pressure signals to be analyzed window by window with a user-defined window length and window gap instead of a fixed value, fundamental period of the signal. The user-defined window gap makes real-time data monitoring possible by letting the window gap equal the reciprocal of the data sampling rate. Additionally, the required data transmission and sampling rates are reduced and only require the Nyquist frequency of the third resonance harmonic of the analyzed signal, since only the damping of the first three resonance harmonics is required.

Further research has been conducted to ease the restriction that only the first three resonance responses of the signal can be utilized. The research has developed an algorithm that enables any sequence of harmonics to be utilized for real-time pipe burst detection and location estimation. The burst location estimation can be fulfilled with acceptable accuracy, and the majority of the incorrect, possible solutions to the burst location can be excluded.

In order to discuss and compare the performance of those techniques that use the damping of fluid transients and those techniques that use the frequency response diagram, the specific relationship between these two techniques has been explored. The detailed and exact relationship between these two techniques has been revealed from both a mathematical perspective and via practical utilization. The two techniques have been discussed and compared from the perspectives of input bandwidth, problem type, low sampling rate capability, robustness, and real-time data monitoring capability, thereby providing an insight into the detailed impact of utilizing different techniques for pipeline inspection.

The overall contribution of this research is the development of novel techniques for pipe burst detection and estimation in real-time, utilizing any sequence of harmonics in the whole frequency range of the transient pressure signals. To date, the developed techniques have been verified both numerically and experimentally. The techniques have the advantages of being applied to real-time data monitoring with low sampling rates and utilizing one sensor alone.

Keywords: Burst detection and localization, hydraulic transients, harmonic analysis, frequency analysis, real-time data.

Acknowledgements

Firstly, I would like to express my gratitude to my supervisors, Dr Lei Chen, Prof. Martin F. Lambert, and Assoc. Prof. Eric Hu for their supervision, mentoring, and help during the period of my Ph.D. candidature. I especially thank Prof. Martin F. Lambert for his significant help during my Ph.D. candidature from the perspectives of academic research, industrial experience, and personal life.

I thank Dr Alison-Jane Hunter at the University of Adelaide for her help regarding editing. I thank Mr Brenton Howie and Mr Simon Golding at the University of Adelaide for their support with some of my laboratory work.

I thank my fellow postgraduate students in the School of Mechanical Engineering and the School of Civil, Environmental and Mining Engineering for their friendship and accompany. I also thank all the staff in both of the Schools for their support and help.

I thank my wife, my parents, and my friends for their support and encouragement. The period of my candidature has been challenging with a number of issues and a pandemic to contend with alongside the usual ups and downs of creating a thesis. Without my family and friends, I would have found the process tougher again. I thank my wife, parents and friends for all their invaluable support and encouragement. I could not have completed this thesis without you all.

I thank the University of Adelaide for providing me with the Adelaide Graduate Research Scholarship to support this research. I thank the Australian Research Council for providing me with the scholarship to support this research. Thank Prof. Martin F. Lambert for helping me to apply for this scholarship.

Acronyms

BER - Broadband electromagnetic radar

CBD - central business district

CCTV - Closed-circuit television

CSD - Cross-spectral density

DFT - Discrete Fourier transform

DHS - Discrete harmonic spectrogram

DMA - district meter areas

DOFT - Damping of fluid transients

FFT - Fast Fourier transform

FOSWH - Free open-source 1D water hammer

FRD - Frequency response diagram

FWDI - First window discontinuity index

IRF - Impulse response function

ITA - Inverse transient analysis

LDI - Leak detection index

MFL - Magnetic flux leakage

MOC - Method of Characteristics

RFEC - Remote field eddy current

RPR - Reservoir-pipe-reservoir

RPV - Reservoir-pipe-valve

SDFT - Sliding discrete Fourier transform

STFT - Short-term Fourier transform

TFR - Transient frequency response

UFWH - Unsteady friction water hammer

WDI - Window discontinuity index

Symbols

A_B	=	burst cross-sectional area (m^3)
A_p	=	inner pipe cross-sectional area (m^3)
A_V	=	valve pipe cross-sectional area (m^3)
A_n, B_n	=	Fourier coefficients
a	=	wave speed (m/s)
b	=	parameter of burst discharge-head relationship
C_d	=	burst orifice discharge coefficient
$C_0^{(m)}, C_n^{(m)}, D_n^{(m)}$	=	Fourier coefficients
D	=	inner diameter of pipe (m)
d	=	window gap (s)
d^*	=	dimensionless interval/time step $= d/(L/a)$
$E_n^{(m)}$	=	amplitude of the nth harmonic of the mth period/window
$E_n^{(1)}$	=	amplitude of the nth harmonic of the first period/window
F	=	a function of dimensionless frequency f^*
$f,\ f_{steady},\ f_{unsteady}$	=	Darcy-Weisbach friction factor
f^*	=	continuous dimensionless frequency
f_0	=	fundamental frequency of the system $= 1/T$ (Hz)
f_0^*	=	dimensionless fundamental frequency of the system $= 1/T^*$
g	=	gravitational acceleration (m/s^2)
H	=	pressure head (m)
H_{B0}	=	piezometric pressure head at the burst before the burst occurs (m)
H_{B0}^*	=	dimensionless piezometric pressure head at the burst before eruption

H_s = Joukowsky head drop (m)

H_1 = reference pressure head (m)

H_0^* = dimensionless steady state pressure head $= H_0/H_1$

$H(\omega)$ = frequency response function

h^* = dimensionless head disturbance from a steady state

$i,\ j$ = index

K, K_B = burst parameter (s^{1-2b}/m^{1-2b})

k = any integer

L = length of pipeline (n)

M = burst parameter (s^{1-2b}/m^{1-2b})

m = period number

n = harmonic component number

n_j = example values of the harmonic component number;

p = pressure (Pa)

Q = flow rate (m^3/s)

Q_0 = steady state flow rate (m^3/s)

Q^* = dimensionless flow rate $= Q/Q_0$

Q_B = flow rate through the burst (m^3/s)

Q_0 = steady state flow rate (m^3/s)

Q_0^* = non-dimensional steady flow

q^* = dimensionless flow disturbance from a steady state

$R, R_s, R_{us}, R_{steady}, R_{unsteady}$ = friction damping

$R_{in\&out}, R_{in\&in}$ = Fourier transform of cross-correlation functions

R_{nB} = burst damping for the nth harmonic

T = fundamental period of pipeline (s)

T^* = dimensionless period $= T/(L/a)$

t = time (s)

t^* = dimensionless time $= t/(L/a)$

t_0 = starting time of analysis (s)

t_0^* = dimensionless starting time of analysis $= t_0/(L/a)$

t_a = length of analyzed time window (s)

t_a^* = dimensionless length of analyzed time window $= t_a/(L/a)$

u = example values;

V_B = flow velocity of the burst (m/s)

x = distance along the pipeline (m)

x^* = dimensionless distance $= x/L$

x_B = location of the burst (m)

x_B^* = dimensionless burst location $= x_B/L$

x_B^{**} = truncated dimensionless burst location

$\hat{x_B^*}$ = dimensionless burst location in the combined pipeline

μ = dynamic viscosity of fluid (Pa·s)

ρ = fluid density (kg/m^3)

τ = orifice opening coefficient

τ_s = steady shear stress (Pa)

τ_{us} = unsteady shear stress (Pa)

$\Delta\tau$ = change of the orifice opening coefficient

ω_0 = fundamental angular frequency of the system $= 2\pi f_0$ (rad/s)

ω_0^* = dimensionless fundamental angular frequency of the system $= 2\pi f_0^*$

$W(\tau)$ = weighting function

$f(x^*),\ g(x^*)$ = piecewise functions in the range of $(0 \leq x^* \leq 1)$

z_B = pipe elevation at the burst (m)

ΔH_B = head acting on the burst location when the burst occurs (m)

ΔH_B^* = dimensionless head acting on the burst location when the burst occurs

δx = distance interval (m^{-1})

Chapter 1

Introduction

1.1 Background

Water is a crucial asset for the survival and efficiency of a society. The complete urban cycle of water requires water treatment plants, pumps, and pipelines. In the working processes of such systems, water transmission and conveyance pipelines are essential, since these components are capable of transporting water to clients. However, in an industrial context, unexpected leaks or bursts of water distribution pipelines are critical, chronic issues, because such accidents can cause serious problems, such as significant environmental damage and economic loss (Anderson and Anderson, 2011; Billmann and Isermann, 1987; Hovey and Farmer, 1993; Khan and Abbasi, 1999). There are a number of triggers that may cause leaks and bursts to pipelines. During the process of construction, incorrect management and poor craftsmanship can damage the structural integrity of the piping system, and thus, damage the corresponding pipelines (Gould et al., 2016). In addition, the pipeline may suffer structural wear for various reasons, such as traffic load, corrosion, and external damage (Rakitin and Xu, 2015; Rezaei et al., 2015; Świetlik et al., 2012). This is a global issue that is faced by almost every developed country. For instance, the median of 25.1 breaks, bursts, and leaks per 100 km in major water utilities, such as Sydney Water, has been reported in Australia in the year from 2019 to 2020 (Bureau

of Meteorology, 2021).

Different techniques have been explored for pipe wall condition assessment, leak detection, and burst detection, so that high-risk pipelines can be identified and repaired. Pipe condition assessment techniques, such as the closed-circuit television (CCTV) method, have been explored widely (Bochud et al., 1994; Duran et al., 2003; Jo et al., 2010). The CCTV technique can be utilized for pipe wall condition assessment using the visual inspection process, which is the process that analyzes the visual signals from the multiple applied cameras. However, the CCTV-based pipe wall condition assessment technique requires multiple cameras to be utilized for its application, which increases the cost of the sensing system. Other pipe wall condition assessment techniques, such as the electromagnetic field-based techniques (Costello et al., 2007; Donazzolo and Yelf, 2010; Hazelden et al., 2003; Liu and Kleiner, 2013; Marlow et al., 2007; Mergelas and Kong, 2001), and conventional leak detection techniques, such as the acoustic-based (Fuchs and Riehle, 1991; Stephens et al., 2018, 2020; Tafuri, 2000) and the ultrasonic-based leak detection techniques (Guenther and Kroll, 2016; Lyu et al., 2021; Tao et al., 2015), can be utilized for leak detection; however, their applications require multiple corresponding sensors to be utilized, which leads to a high cost of the sensing system. Additionally, the electromagnetic field-based and acoustic-based techniques are restricted in their applications to real-time data monitoring due to the requirements of corresponding tools, instruments, and technicians.

The transient-based leak detection techniques, such as the inverse transient analysis (ITA) method, the impulse response function (IRF) method, the time domain reflectometry method, the damping of fluid transients (DOFT) method, and the frequency response diagram (FRD) method, have been explored previously (Brunone, 1999; Gong et al., 2013a; Lee et al., 2005a; Liggett and Chen, 1994; Vítkovskỳ et al., 2003; Wang et al., 2002). Although these techniques have been proved as successful for pipeline leak detection, drawbacks exist in them.

For example, during the application process of DOFT technique by Wang et al. (2002), the damping information contained in the measured leak-affected transient signal was utilized. When there is a leak, the resonance harmonics of the measured leak-affected transient signal are damped to a greater extent than the condition of no-leak. Additionally, the resonance harmonics are damped differently due to the leak. Accordingly, the differently damped resonance harmonics of the measured signal can be utilized for leak detection, and the damping caused by the leak can be used for leak localization and size quantification by using the corresponding equations that are developed by Wang et al. (2002). However, only the first three resonance harmonics were utilized in the work reported by Wang et al. (Wang et al., 2002) to minimize the possible solutions to the leak location, which restricts the application of the technique to utilizing higher harmonics of the signal. Additionally, some of the techniques, such as the DOFT and FRD methods, are both based on the Fourier transform theory, but the exact relationship between them remains unrevealed.

Burst detection technologies have been explored and applied in the past years, such as the ITA method, the time domain reflectometry method, the district meter areas (DMA) method, and the cross-correlation function method, since capturing the eruption of the leak, which is the burst, can minimize the negative effects from the leak (Beck et al., 2005; Lambert, 2003; Liggett and Chen, 1994; Silva et al., 1996; Yazdekhasti et al., 2017). Although these techniques are applicable to the burst detection, they have limitations. For example, the cross-correlation method utilizes the cross-correlation function to determine the arrival time differences of the burst-induced transient signals that are measured by multiple sensors, and thus, to determine the distance between the burst and the sensor (Beck et al., 2005; Gao et al., 2017; Yoon et al., 2012). In the work by Yazdekhasti et al. (2018; 2017), the burst location was determined by measuring the burst-induced transient signals using cross-correlation function, and the severity of the burst was analyzed using the cross-spectral density (CSD) of the signals. Although it has been shown that the cross-correlation function

method is applicable to burst detection, it requires a relatively high sampling rate (i.e., 4000 Hz) for the application, based on the work by Yazdekhasti et al. (2018; 2017). This aspect leads to a high cost of the applied sensors.

1.2 Research Questions

According to the research background mentioned in the previous section, the following research questions drive this research.

1. How can burst detection and estimation (i.e., localization and size quantification) be achieved using one sensor?
2. How can burst detection and estimation be implemented in real-time?
3. How can the requirements of the sensor and sensing system be eased in terms of low sampling rate?
4. How can the applicability of the sensor and sensing system be broadened in terms of the ability to utilize not only the first few resonance harmonics but also any sequence of resonance harmonics?
5. What are the advantages of the developed techniques, which are based on the previous research questions, compared with other techniques using a similar signal processing approach?

1.3 Aim and Detailed Objectives

Based on the research questions, the following aim and detailed objectives are proposed. The overarching and primary aim of the proposed project is to inves-

tigate an approach for real-time pipe burst detection and estimation in a pipeline using the measured data in the whole available frequency range of the transient pressure signals that are measured by one sensor. In order to fulfill the overall aim of this research, detailed objectives have been proposed, as listed below:

1. To investigate an approach for achieving burst detection, localization, and cross-sectional area quantification by using one sensor, and complete the corresponding theoretical model based on the theory of DOFT on two piping systems: reservoir-pipe-reservoir (RPR) and reservoir-pipe-valve (RPV).

2. To investigate the generalization of the approach resulting from Objective 1 in terms of real-time data monitoring. To explore the capability of utilizing the low data transmission and sampling rates for the corresponding signal processing algorithm.

3. To develop an algorithm that extends the approach determined from Objectives 1 and 2, moving from utilizing the first few harmonics to utilizing any sequence of harmonics.

4. To explore and discuss the specific relationship between the DOFT and FRD methods of pressure transients. Discuss and compare them from the perspectives of input bandwidth, problem type, low sampling rate capability, robustness, and real-time data monitoring capability, to emphasize the advantages of the techniques developed from the previous objectives.

1.4 Detailed Organization of the Thesis

This Ph.D. thesis contains seven chapters. Chapter 1 is the overall introduction to this Ph.D. research. Chapter 2 contains the literature review and the corresponding research gaps. Chapters 3-6 are the four journal papers arising from

the research that has been undertaken, of which two have been published, and two have been submitted for publication.

Chapter 1 is the overall introduction to this Ph.D. research, containing the background, research questions, objectives and the organization of the thesis. The contents in this chapter provide the basic ideas and the scope of this research. Additionally, the organization of the thesis in this chapter presents the connections between the four applied journal papers and this thesis.

Chapter 2 is the detailed literature review related to this Ph.D. research. The selected leak and burst detection technologies are reviewed. The research gaps are summarized. It should be noted that the proposed objectives of this Ph.D. research in Chapter 1 fulfill in all the indicated research gaps.

Chapter 3 (**Journal Paper 1**) presents a novel approach for pipe burst detection, localization, and cross-sectional area quantification utilizing the transient pressure signal measured by one sensor, based on the theory of DOFT. The approach is capable of analyzing the burst damping contained in the first three resonance harmonics of the measured pressure signal, and thus determining the burst location and cross-sectional area. In addition to the numerical scenarios of both RPR and RPV systems, two experimental cases have been implemented with different burst and measurement locations. The chapter also presents a developed model, the unsteady friction water hammer (UFWH) model, which is capable of calibrating the unsteady friction of the pipeline prior to the application of the technique in practice. The verification results show that the approach is successful in burst detection and estimation for both RPV and RPR systems. Additionally, the validations of the UFWH model reveal that the unsteady friction damping is dependent on the frequency. The research outcomes have been published in the *Journal of Hydraulic Engineering* (DOI: 10.1061/(ASCE)HY.1943-7900.0001810). The research outcomes address Objective 1.

Chapter 4 (**Journal Paper 2**) shows the work extending the technique in Chapter 3 from the perspective of real-time data monitoring. The corresponding algorithm enables the extended technique, which is based on the theory in Chapter 3 for pipe burst detection and estimation, to be applied to real-time data monitoring with low data transmission and sampling rates. The algorithm enables the window length and gap in each analyzed time window to be predefined. Therefore, real-time data monitoring becomes possible by setting the window gap to be the reciprocal of the data sampling rate. The algorithm only requires the data transmission and sampling rates to be the Nyquist frequency of the third resonance harmonic of the measured signal. Eleven numerical studies are presented, which include slowly developing bursts scenarios. In addition, one experimental test is shown, which verifies the technique. The research findings have been published in the *Journal of Water Resources Planning and Management* (DOI: 10.1061/(ASCE)WR.1943-5452.0001380). The research findings shown in this chapter address Objective 2.

Chapter 5 (**Journal Paper 3 (submitted)**) presents the exploration that eases the limitation of the techniques in Chapters 3 and 4 from the perspective of utilizing any sequence of harmonics of the measured signal instead of the first few harmonics. The proposed technique enables any sequence of harmonics of the signal to be analyzed based on the periodicity of the square of the sinusoidal function. The corresponding algorithm of the technique is capable of excluding the majority of incorrect solutions to the burst location, which are generated by utilizing those harmonics that are higher than the third resonance harmonic. The burst detection can be fulfilled by computing the burst damping and determining the burst location range. Accordingly, the burst location can be estimated using such a range with acceptable accuracy. Additionally, the real-time data analysis can be completed by letting the analyzed window gap equal the reciprocal of the sampling rate. The effects from unsteady friction damping when utilizing the technique in practice have been discussed. The presented numerical and experimental scenarios verify the technique. The research outcomes have

been submitted to the *Journal of Water Resource Planning and Management* for peer review. The work in this chapter addresses Objective 3.

Chapter 6 (**Journal Paper 4 (submitted)**) presents an exploration and discussion of the exact relationship between the DOFT methods and the FRD-based methods mathematically. In addition, they are discussed from the perspectives of input bandwidth, problem type, low sampling rate capability, robustness, and real-time data monitoring capability. The advantages of the techniques developed in Chapters 3, 4, and 5, such as the robustness, have been further explored and emphasized. The results of the research have been submitted to the *Journal of Hydraulic Engineering* for peer review. The research results shown in this chapter address Objective 4.

Chapter 7 presents the conclusions from this Ph.D. research. It summarizes the main research outcomes and contributions of the research, which correspond to each research gap and objective. Additionally, it briefly discusses potential future work deriving from this research.

To date, Research question 1 has been answered in Chapter 3 (**Journal Paper 1**); Research questions 2 and 3 have been answered in Chapter 4 (**Journal Paper 2**); Research question 4 has been answered in Chapter 5 (**Journal Paper 3 (submitted)**); and Research question 5 has been answered in Chapter 6 (**Journal Paper 4 (submitted)**).

Chapter 2

Literature Review and Research Gaps

2.1 Introduction

This section provides an overview of the selected literature related to the research, which is categorized into pipe wall condition assessment, leak detection, and burst detection technologies. A brief explanation of the theories of the reviewed technologies is presented. The research gaps are identified according to the reviewed literature.

2.2 Pipe Wall Condition Assessment

The pipe wall condition assessment methods have been widely explored for pipeline inspection. The laser scanning and CCTV techniques are based on the utilization of laser sensors and CCTV cameras (Bochud et al., 1994; Duran et al., 2003; Jo et al., 2010). These methods use CCTV cameras or laser sensors that are introduced into the pipe through an access point. The pipe inner wall condition can be assessed from the visual signal from the cameras or laser sensors. Accordingly, the leak can be detected by observing and analyzing the visual signal by the corresponding applied visual signal analysis tools or algo-

rithms (Bochud et al., 1994; Duran et al., 2003; Jo et al., 2010). The moving and scanning speeds of the cameras or laser sensors determine the resolution and affect scanning accuracy. However, due to the roughness and color of the pipe surface, the inspection process is difficult to complete. Additionally, these techniques require multiple cameras or laser sensors to implement the inspection process, which leads to the high cost of the corresponding sensing system.

Other pipe wall condition assessment methods, such as the broadband electromagnetic radar (BER) method, remote field eddy current (RFEC) method, and magnetic flux leakage (MFL) method, are based on the electromagnetic field (Hazelden et al., 2003; Liu and Kleiner, 2013; Marlow et al., 2007; Mergelas and Kong, 2001). The BER and RFEC methods are both based on the eddy currents that are generated by the applied packs of transmitting coil to the pipeline. Each pack of transmitting coil generates an electrical current on the surface of the pipe, thereby generating a magnetic field. The lines of force of the magnetic field pass through the metal wall of the pipe and generate a voltage across the pipe, and thus, the eddy currents are produced. Accordingly, a secondary magnetic field is generated in the wall. The wall thickness is estimated indirectly by measuring the signal attenuation and phase delay of the generated secondary magnetic field. Accordingly, the leak can be detected if there is any estimated change of the pipe wall thickness. Packs of strong magnets are utilized in the MFL method during the process of strong magnetic field generation, which happens around a small section of the pipe wall. Flux leakage can be detected if there is a leak in the pipe wall using a magnetic sensor. These methods have been proved capable of detecting pipe wall leaks by observing the singularities of the measured signal. However, each pack of transmitting coil in BER and RFEC methods, and each pack of magnets in MFL method, can only generate a magnetic field covering a few meters of the pipeline. This specific aspect indicates that the sensing system requires multiple sensors to implement the inspection process, which leads to the high cost of the corresponding sensing system (Hazelden et al., 2003; Liu and Kleiner, 2013;

Marlow et al., 2007; Mergelas and Kong, 2001). Additionally, the drawback of these electromagnetic-based methods, which is that the corresponding tools or instruments are required to apply these methods, is reported by Costello et al. (2007) and Donazzolo and Yelf (2010). This specific aspect indicates that the leaks can only be detected whenever the required tools or instruments are utilized. Accordingly, these techniques cannot be applied where the pipe is operational in the area of real-time data monitoring, which therefore cannot be utilized to minimize the negative effects from the leaks.

2.3 Leak Detection

In addition to pipe wall condition assessment methods, conventional leak detection methods have been widely researched. Acoustic-based methods, which are contained in conventional leak detection methods, have been developed over decades, and have been successfully applied in water transmission and distribution pipeline systems (Fuchs and Riehle, 1991; Tafuri, 2000). The acoustic signal with different frequency ranges is emitted by a leaking and pressurized pipeline, and the frequency ranges of such a signal are dependent on the fluid properties, pipeline pressure, and leak characteristics (Juliano et al., 2013). One of the developed acoustic-based methods that utilizes the theory of cross-correlation function, places two acoustic sensors, such as the accelerometers or hydrophones, at two different locations on the pipeline to measure the leak-affected signals. It then uses the computer-based instruments to calculate the cross-correlation function of the measured signals to determine the location of the leak (Fuchs and Riehle, 1991; Gao et al., 2004). In addition, the method has been further improved by adding weighting functions in the leak noise correlators, and the manually carried out analysis process has been proved as successful (Gao et al., 2017). Case studies in Adelaide about the successful application of one of the acoustic-based methods, the acoustic smart water

technology, have been reported in Stephens et al. (2018; 2020). The acoustic data from the acoustic sensor network in the central business district (CBD) of Adelaide was successfully interpreted by the acoustic data analytics team, and thus, approximately 55% of all developing leaks have been successfully detected before the third party economic damage or unplanned interruption of customers (Stephens et al., 2020). Although acoustic methods have been proved as successful in practice, such acoustic-based method by Gao et al. (2017) requires multiple sensors to measure the leak-affected signals, which leads to a high cost of the sensing system. Additionally, both the methods by Gao et al. (2017) and Stephens et al. (2020) require manual processes to be implemented, for example, the method by Gao et al. (2017) requires manual analysis process, and the method by Stephens et al. (2020) requires acoustic data interpretation by the corresponding technical team. This specific aspect indicates that such methods are lack of the ability to achieve real-time data monitoring, because the leak can only be detected whenever the required manual processes are implemented.

In addition to acoustic-based methods, ultrasonic-based methods have been widely explored. The ultrasonic inspection process for a pipeline system is implemented by using the generated sound waves and its corresponding reflections. The ultrasonic waves are generated using a beam with high frequency coherent sound energy, and the corresponding reflections that are reflected by the inner and outer surfaces of the pipe wall are measured (Liu and Kleiner, 2013; Rose et al., 2008). The time lag between the two reflections is utilized to determine the pipe wall thickness, and thus, any change in the density of the pipe wall can be detected. Accordingly, the leak can be detected by confirming the change of the pipe wall thickness. However, the orientation of the leak can affect the accuracy of the detection results, and this type of methods are more suitable for oil, gas, and air pipeline inspection than water pipeline inspection (Guenther and Kroll, 2016; Lyu et al., 2021; Tao et al., 2015). Although the recent work by Liu et al. (2021) showed that ultrasonic-based method can be applied to water pipeline inspection, and to design the water pipeline inspection

software, the drawbacks in this work exist, as shown below. In the work by Liu et al. (2021), a whole pipe has been divided into several sections, and the ultrasonic flowmeters were attached at both ends of each section to measure the flow velocity. One of the utilized ultrasonic flowmeters derives ultrasonic transducers through a circuit to emit ultrasonic wave, and the other one receives the reflection of the ultrasonic wave. The time lag between the emitted and reflected waves can be used to compute the flow velocity, so that any change of the flow velocity can be detected, and thus, the leak that causes the flow velocity change can be detected. Although in the work by Liu et al. (2021), the ultrasonic-based method has been successfully applied to water pipeline inspection, it requires at least two sensors for each section of the pipe, which increases the cost of the sensing system. Additionally, only the section that has the leak can be identified, the accurate leak localization cannot be fulfilled, which limits the method to be applied in practice for leak localization.

In addition to the conventional technologies, there are various techniques based on the hydraulic transient caused by the transient source in the pipeline in the frequency domain that have been researched. The ITA techniques were firstly proposed and explored by Ligget and Chen (1994). The proposed optimization process has been applied, which is the process that matches the generated numerical signal to the measured transient signal that is generated by an external transient source (Covas and Ramos, 2010; Kapelan et al., 2003; Soares et al., 2011; Stephens et al., 2008, 2013). During the optimization process, the least squares regression between the numerical and measured transient signals is utilized for deviation determination between the two signals. The leak is simulated with varying size and at different locations of the modelled pipe, which are usually located at each computational node of the pipe, to generate different numerical signals to match the measured transient signal, and thus, to minimize the deviation between the two signals. Accordingly, the leak location and size that provide the least deviation are the expected solutions to leak location and size. Further explorations have been conducted to improve the efficiency

of the optimization process of ITA method (Zhang et al., 2018a,b). In Zhang et al. (2018a) and Zhang et al. (2018b), the head-based method of characteristics (MOC) model that has a flexible computational grid and a multi-stage parameter-constraining ITA have been developed. However, these methods are time-consuming, since the applications of these methods require numerous numerical tests to implement the previously-mentioned optimization process. Additionally, these methods actually analyze the measured transient signal indirectly with prior knowledge of the pipeline parameters, which is challenging due to pipeline parameter uncertainties.

The IRF techniques that are based on the impulse response of the pressure signal have been explored. The impulse response is the transient pressure response when there is an impulse pressure signal injected to the pipeline, and the reflected transient signal is affected by the friction of the pipe wall and the leak when propagating along the pipeline. This specific aspect results in more damping of the transient signal when, for example, there is a leak, compared to the condition of no-leak (Vítkovskỳ et al., 2003). Therefore, comparing the damping of the measured transient signals under the conditions of leak and no-leak fulfills the leak detection. In the work by Liou (1998), results of the cross-correlation between the pseudo random binary disturbance input and the corresponding system output have been applied to extract the impulse response of the pipeline for leak detection and localization. The real-time leak detection was demonstrated in Liou (1998) by a numerical example. However, the accurate results of the extracted impulse response requires prior knowledge of the leak location and leak flow rate (Liou, 1998). This specific aspect restricts the application of the method. Experimental case studies have been carried out by Nguyen et al. (2018) with pipeline that is operated by the pseudo random binary sequence pattern. However, measurement errors were involved during the measurement process of the dynamic valve opening in the conducted experimental cases, which significantly reduced the accuracy of the extracted IRF (Nguyen et al., 2018).

The time domain reflectometry methods have been widely researched, since they are simple and straightforward for leak detection (Brunone, 1999; Brunone and Ferrante, 2001). The transient wave, which is generated by external transient source and propagates along the pipeline, is partially reflected by the leak. Accordingly, the leak can be detected when the leak-reflected wave is measured, and thus the location of the leak can be calculated simply using the wave speed and the arrival time of the measured leak-reflected signal. The arrival time of the leak-reflected signal is normally estimated by using visual inspection or by using the signal matching between measured and numerical leak-reflected signals, of which the numerical one is generated under the condition of no-leak (Brunone et al., 2008; Lazhar et al., 2013; Lee et al., 2007). Numerical applications of such methods have been conducted by Lazhar et al. (2013), and the experimental applications have been implemented by Ferrante et al. (2014). Although these time domain reflectometry methods have been proved as successful for both numerical and experimental applications, the accuracy of the results of utilizing such methods is dependent on the input signal, which may restrict their application when the input signal is contaminated. In addition, the application of such methods requires visual inspection or signal matching process to be implemented to determine the arrival time of the measured leak-reflected signal. Specifically, the arrival time of the measured leak-reflected signal can only be determined whenever the visual inspection or signal matching process is applied, which restricts its application to real-time data monitoring.

The DOFT techniques have been explored for pipe leak detection, localization, and size quantification by using the signal measured by one sensor (Nixon et al., 2006; Wang et al., 2002). The theory of DOFT-based techniques for pipe leak detection, localization, and size quantification reveals the relationship between the information about the leak and the damping of the resonance harmonics of the transient pressure signal measured by one sensor. The transient signal, which is generated by sharply closing the side discharge valve in pipelines, or other transient generation such as shutting down or starting up the pump,

is damped by the summation of the friction and leak damping. The damping gradient of the transient signal under the condition of leak will be greater than the condition of no-leak. Wang et al. (2002) explored this technique and conducted relevant numerical verifications. Nixon et al. (2006) further explored this technique regarding its validity in terms of materials and so forth.

The process of the modeling in Wang et al. (2002) was based on MOC, which is a widely used theory for pressure wave modeling (Kjerrumgaard Jensen et al., 2018). The formulation that contains the leak information was developed based on the Fourier series and Fourier transform, such as fast Fourier transform (FFT) or discrete Fourier transform (DFT). Based on the conducted numerical studies in Wang et al. (2002), the total damping of each harmonic component of the data can be computed by applying the Fourier analysis, and the total damping consists of the leak damping and the friction damping. Friction damping can be divided into steady and unsteady friction damping. Steady friction damping is consistent, and can be calculated by the corresponding equation shown as Eq. (2.1) (Liou, 1991) in Wang et al. (2002).

$$R = \frac{fLQ_0}{2aDA_p} \tag{2.1}$$

where f is the friction coefficient, L is the total length of the pipe, Q_0 is the steady state flow rate, a is the wave speed, D is the pipe inner diameter, and A_P is the cross-sectional area of the pipe. Unsteady friction damping can be determined by subtracting the steady friction damping from the total friction damping. In Wang et al. (2002), the total friction damping was determined by analyzing the transient signal from a pretest under the no-leak condition. Leak damping is different for each resonance harmonic component, which can be obtained by subtracting the friction damping from the total damping (Wang et al., 2002). Subsequently, the presence of the leak was confirmed by observing the non-zero leak damping, and the location and cross-sectional area of the leak

can be subsequently calculated by using the burst damping ratios for the first three resonance harmonics (Wang et al., 2002).

The DOFT technique can be successfully applied to leak detection, localization, and size quantification. The application of the technique requires the signal measured from one sensor alone. However, the transient event is introduced by a manual operation: closing the valve. This particular operation is interceptive to the normal working cycle of the pipeline, as additional flow must be released from the generator, and then has to be rapidly closed. This specifically required operation is impossible to be applied in real-time, indicating that the leak can only be detected whenever the technique is applied. Additionally, the pretest that is applied to the friction damping determination is time-consuming and increases the cost of the application of the technique. Moreover, this technique is only capable of utilizing the first three resonance responses of the measured signal, otherwise, further incorrect possible leak locations will be determined, and cannot be excluded.

Another transient-based technique that utilizes the Fourier transform has been explored, known as the FRD technique (Gong et al., 2013a,b; Lee et al., 2006, 2005a). Application of the theory of FRD has been researched from the perspective of leak detection and estimation using the signal measured from one sensor (Gong et al., 2013a,b; Lee et al., 2006, 2005a). The general frequency response function (FRF) is defined as the frequency response of the output, which is normally the measured signal in the frequency domain, divided by the input signal in the frequency domain, which is shown as Eq. (2.2).

$$H(\omega) = \frac{S_{xy}(\omega)}{S_{xx}(\omega)} \tag{2.2}$$

where $H(\omega)$ is the frequency response function, $S_{xy}(\omega)$ is the Fourier transform of the cross-correlation function between the input signal, x, and the output sig-

nal, y, and $S_{xx}(\omega)$ is the Fourier transform of the auto-correlation function of the input signal (Covas et al., 2005b, 2003, 2004; Lynn, 2016; Sharma, 2013). Periodic damping of the peak values of the resonance harmonics can be generated if there are leaks in the pipe, and thus, the leaks can be detected (Lee et al., 2006). The damped peak values of the first three resonance responses in FRD results can be utilized to indicate the presence of a leak. The leak localization can be completed utilizing the leak location solution presented in Gong et al. (2013a) by using the amplitudes of the first three resonance harmonics of the measured signal. According to the process of the conducted experimental tests in Lee et al. (2006) and Gong et al. (2016a), the experimental tests verified that leak was detected by observing the differences in the FRD between the conditions of no-leak and leak, and the leak was successfully located by using the corresponding leak location solution.

The FRD-based technique can fulfill the requirements for leak detection and localization. Only the signal measured from one sensor is required. However, application of the technique requires the whole range of the data from the transient to the final steady state, indicating that the leak can only be detected from the transient event until the final steady state, and when the technique is applied. Therefore, the pipeline inspection process cannot be achieved in real-time. Additionally, an accurate input signal is required for application of the technique, which limits its application, when the input signal cannot be obtained.

2.4 Burst Detection

Although the leak detection technologies are widely explored and applied, the negative effects from the leak cannot be minimized if the eruption of the leak, which is the burst, cannot be captured in real-time. Therefore, burst detection

technologies have been researched by a wide range of researchers. There are two basic features in the burst problem, which are commonly utilized by researchers for the study of burst detection techniques, as presented below. A negative pressure wave will be generated and propagates along the pipeline in both directions when there is a burst occurred in the pipeline (Misiunas et al., 2005). In addition, it should be highlighted that burst detection technologies do not require the external transient source to introduce the transient event into the pipeline. Liggett and Chen (1994) introduced the research regarding burst detection using an event detection algorithm. The algorithm is capable of detecting the sudden pressure drop due to the occurrence of the burst, and thus, detecting the burst. The burst localization can be fulfilled by utilizing the ITA techniques that are presented in the previous section, in which the location of the burst is estimated by generating the burst event at different nodes of the pipeline numerically, and then matching the generated signal to the measured signal (Liggett and Chen, 1994). However, similar to the limitation existing in the ITA techniques, this type of method is time-consuming.

The applications of the time domain reflectometry-based burst detection methods have been implemented. A pipeline burst detection and localization method that is based on the time domain reflectometry theory has been presented by Silva et al. (1996). The burst detection was achieved by the visual inspection that focuses on capturing the sudden pressure drop due to the occurrence of the burst. The burst localization was fulfilled by computing the arrival time of the burst-induced pressure waves at different measurement locations using the wave speed (Silva et al., 1996). In the work by Silva et al. (1996), experimental applications were conducted and the corresponding results were reported. During the experimental processes, the burst initiation was simulated by opening a manually controlled solenoid side-discharge valve, and four pressure transducers were utilized for burst detection and localization. Although such technique has been proved as successful for burst detection and localization, the application of it requires at least two sensors, which increases its cost.

Subsequently, Misiunas et al. (2005) explored the burst detection and localization technique based on the time domain reflectometry framework. The applied signal processing algorithm for burst detection is the two-sided cumulative sum algorithm, which can be utilized to detect the sudden pressure drop due to the burst. Additionally, the corresponding offline analysis has been applied to burst localization. Although the technique reported in Misiunas et al. (2005) has been verified as successful for the burst detection problem, the accuracy of the results depends on the bandwidth of the input signal, which is related to the burst opening speed, which may restrict its application when the burst opening speed cannot be identified (Misiunas et al., 2005). In addition, the utilization of the offline analysis limits the application of such a method to real-time data monitoring, since the offline analysis process needs to be implemented for every test after the burst detection (Misiunas et al., 2005).

Similarly, the time domain reflectometry method based on the wavelet transforms has been explored in terms of both burst detection and localization (Srirangarajan et al., 2013). The approach that utilizes the multi-scale wavelet analyses for burst detection and differentiation the burst-induced transient pressure signal from noise-induced transient pressure signal has been researched in depth (Srirangarajan et al., 2013). The burst localization was conducted by using the waves arrival time at different measurement locations and the wave speed. Although the method by Srirangarajan et al. (2013) has been proved as successful for burst detection and localization, the applications of them require multiple sensors to be used to measured the burst-induced transient pressure signals, which increases the cost of the applications of it.

Burst detection methods that are based on the DMA have been explored. The water audit has been utilized commonly for leak detection in a water distribution system, of which the theory is to record the amount of the water flows into and out of the distribution system, or parts of it (Lambert, 2003). Accordingly, the leak can be detected if the recorded water flows into the distribution

system not equal the water flows out of the distributions system. Moreover, the whole water distribution system can be subdivided into DMAs by permanently closing some of the valves. Accordingly, the comparison between water flows into and out of the distributions system can be implemented for every DMA. A method based on DMA theory has been presented by Mounce et al. (2003). The DMA level sensors were utilized to measure the flow rate across a DMA, and thus, the abnormal change of the flow rate due to the burst in the corresponding DMA can be detected (Mounce et al., 2003). Additionally, the corresponding pressure gradient analysis in a DMA was implemented by Mounce et al. (2003), therefore, the pressure drop due to the occurrence of the burst in the corresponding DMA can be captured. Accordingly, the DMA with the burst can be identified. Successful tests were conducted by Mounce et al. (2003) in a real water distribution system, where the bursts were simulated by hydrant flushing. Similarly, Hutton et al. (2015a) developed a real-time pipe burst detection method based on DMA theory. A model that is capable of forecasting the future pipe flows from a DMA level sensor in a DMA was developed and utilized (Hutton and Kapelan, 2015b). Applying this model online enables the comparison between the actually observed and forecast flows to be implemented in real-time. Accordingly, the burst can be detected in real-time if there is a difference between these two flows, and the DMA with the burst can be identified. Although the methods by Mounce et al. (2003) and Hutton et al. (2015a) have been successfully applied, only the DMA that has the burst can be identified, indicating that the accurate burst localization is restricted. Additionally, multiple sensors are required to apply such methods.

Utilization of the cross-correlation function for burst detection based on the transient signal caused by the burst has been explored (Beck et al., 2005; Brennan et al., 2019; Gao et al., 2017; Yazdekhasti et al., 2018, 2017; Yoon et al., 2012). The basic theory of the cross-correlation function for burst detection is to observe the transient signal caused by the burst to detect the burst. The burst localization is completed by utilizing the time lag of the measured sig-

nals from multiple sensors, which are generated by the burst, to determine the distance between the burst and the targeted sensor, and thus, to determine the location of the burst. Yazdekhasti et al. (2018; 2017) attempted to use the transient acceleration signal to confirm the presence of the burst, and then to locate the burst by using the cross-correlation function, based on the work in Rizwan and Paul (2015). This approach is capable of detecting the burst with different cross-sectional areas and eliminating the negative effects of the time delay, since the difference between the conditions of no-burst and burst can be observed from the measured acceleration signal (Yazdekhasti et al., 2018).

By applying the cross-correlation function to the data collected from the accelerometers at multiple locations along the pipeline and the known wave speed, the location of the burst was calculated (Yazdekhasti et al., 2017). Yazdekhasti et al. (2017) attempted to use the CSD of the measured data, which is a transient acceleration signal, to create a novel concept, a leak detection index (LDI), to express the severity of the burst. In addition, the difference in the CSD between the conditions of no-burst and burst can also be helpful to confirm the presence of the burst. The equation for LDI is shown as Eq. (2.3).

$$LDI(x,\ y) = \frac{\int \left| f^{d}_{x-y}(t) - f^{b}_{x-y}(t) \right|}{\int \left| f^{b}_{x-y}(t) \right|} \tag{2.3}$$

where x and y are the two different measurement locations, $f^{d}_{x-y}(t)$ is the CSD of the data from the $x-y$ locations of the no-burst condition, and $f^{b}_{x-y}(t)$ is the CSD of the data from the $x-y$ locations of the burst condition. The LDI is capable of providing information about the severity of the leak, since the magnitude of the LDI is increased with the growth of the cross-sectional area of the leak. Yazdekhasti et al. (2018) conducted experimental tests in a real pipeline system to verify the LDI model. The applied experimental configuration is a pipeline system with two loops, several valves, T-joints, and boundaries with

different elevations. During the process of verification in a real pipeline system, the presence of a burst was detected by observing the sudden changes in the measured acceleration signal caused by the burst in real-time. The outcomes of the conducted experimental verifications indicated that although the diameter of the pipeline can lead to greater attenuation of the transient acceleration signal, the burst can still be detected and estimated by utilizing the transient burst-induced signal and the LDI (Yazdekhasti et al., 2018). In addition, the verified results indicated that multiple bursts can be detected by comparing the transient burst-induced signals of the conditions between single and multiple bursts, since the value of the LDI in a multiple bursts scenario is greater than the same quantity in a single burst scenario.

The cross correlation function-based technique has been explored effectively for burst detection and severity evaluation in real-time. However, based on the work reported by Yazdekhasti et al. (2018), the technique is only capable of processing the measured signal in the high frequency range, which leads to a relatively high sampling rate (i.e., 4000 Hz) of the required sensor. This specific aspect results in the high cost of the required sensing system. Additionally, the utilization of the cross-correlation function requires multiple sensors, which increases the cost of the sensing system itself.

2.5 Research Gaps

The following research gaps are identified from the literature review:

1. Some of the techniques, for example, the cross-correlation function-based techniques, require multiple sensors for the pipeline inspection process, which leads to the high cost of the sensing system.

2. The techniques that utilize one sensor for pipeline inspection, such as the DOFT technique, are limited to the leak rather than the burst detection and estimation, and require an external and manually controlled transient source.

3. Some of the techniques, such as the ITA and FRD techniques, are not practical for application to real-time data monitoring. Additionally, some of the techniques, such as the cross-correlation function-based burst detection techniques, can only process the signal that is sampled by the sensor with high sampling rate.

4. The DOFT technique can only utilize specific information from the signal (i.e., the first three resonance harmonics), which restricts the applicability of the sensor and sensing system to some of the problems, for example, when the first three resonance harmonics are negatively affected by external noise.

5. The signal processing algorithms of the DOFT and FRD techniques are based on the same theory, Fourier transform, but no research has been implemented to reveal the exact relationship between them. Additionally, there is no discussion about the relationships between them in some specific areas that are related to their applications in practice.

To date, Research gaps 1 and 2 have been addressed in Chapter 3 (**Journal Paper 1**); Research gap 3 has been addressed in Chapter 4 (**Journal Paper 2**); Research gap 4 has been addressed in Chapter 5 (**Journal Paper 3 (submitted)**); and Research gap 5 has been addressed in Chapter 6 (**Journal Paper 4 (submitted)**).

Chapter 3

Pipe Burst Detection, Localization, and Quantification Using the Transient Pressure Damping Method

(Journal Paper 1)

Xiao-xuan Du, Martin F. Lambert, Lei Chen, Eric Jing Hu, and Wang Xi

Published in *Journal of Hydraulic Engineering*

10.1061/(ASCE)HY.1943-7900.0001810

Statement of Authorship

Title of Paper	Pipe burst detection, localization, and quantification using the transient pressure damping method
Publication Status	✓ Published ☐ Accepted for Publication ☐ Submitted for Publication ☐ Unpublished and Unsubmitted work written in manuscript style
Publication Details	Du, X.-x., Lambert, M. F., Chen, L., Jing Hu, E., and Xi, W. (2020). Pipe burst detection, localization, and quantification using the transient pressure damping method. Journal of Hydraulic Engineering. 146(11): 0402077

Principal Author

Name of Principal Author (Candidate)	Xiaoxuan Du		
Contribution to the Paper	Conception and design of project Analysis and interpretation of research data Drafting the paper		
Overall percentage (%)	75%		
Certification:	This paper reports on original research I conducted during the period of my Higher Degree by Research candidature and is not subject to any obligations or contractual agreements with a third party that would constrain its inclusion in this thesis. I am the primary author of this paper.		
Signature		Date	14/01/2022

Co-Author Contributions

By signing the Statement of Authorship, each author certifies that:

i. the candidate's stated contribution to the publication is accurate (as detailed above);

ii. permission is granted for the candidate in include the publication in the thesis; and

iii. the sum of all co-author contributions is equal to 100% less the candidate's stated contribution.

Name of Co-Author	Martin F. Lambert		
Contribution to the Paper	Conception and design of project Analysis and interpretation of research data Critically revising the paper		
Signature		Date	19/1/2022

Name of Co-Author	Lei Chen		
Contribution to the Paper	Revising the paper critically Conception and design of project		
Signature		Date	18/01/2022

Please cut and paste additional co-author panels here as required.

Name of Co-Author	Eric Jing Hu		
Contribution to the Paper	Revising the paper critically Conception and design of project		
Signature		Date	18/1/2022

Name of Co-Author	Wang Xi		
Contribution to the Paper	Revising the paper critically Analysis and interpretation of research data		
Signature		Date	18/1/2022

Abstract

The purpose of this paper is to present a technique for burst detection, localization, and cross-sectional area quantification, based on the damping of fluid transients. The Fourier components of the transient signal are damped differently due to the presence of the burst and the unsteady friction it causes. An unsteady friction water hammer (UFWH) model has been developed and validated to determine the unsteady friction damping. The burst damping can then be calculated, and this both indicates the presence of the burst, and contains information about the burst location and the associated cross-sectional area. The corresponding numerical studies and experimental results are presented in this paper. By applying the technique outlined in this paper, the errors of the resultant burst location from the numerical and experimental analyses are $1\% - 1.5\%$ and $1.57\% - 4.05\%$, respectively.

3.1 Introduction

In an industrial context, unexpected bursts or large leaks in pipe systems are critical, chronic issues. The detection of bursts in pipes is necessary for the pipe system, which requires accurate flow rate control and safety flow transformations throughout its working cycle. Pipe bursts are treated as accidents and can cause serious problems, such as significant environmental damage and economic loss (Anderson and Anderson, 2011; Billmann and Isermann, 1987; Hovey and Farmer, 1993; Khan and Abbasi, 1999). There are numerous drawbacks in previously studied pipe leak detection methods. Common non-transient-based leak detection methods are not sufficiently effective to inspect pipelines rapidly (Akylidz et al., 2009; Anguiano et al., 2016; Billmann and Isermann, 1987; Black, 1992; Boon et al., 2012; Bracken and Cain, 2012; Brothers, 2003; Cai et al., 2016; Cheraghi et al., 2005; Dilena et al., 2011; Forrest, 1994; Furness and Reet, 1998; Griebenow and Mears, 1989; Hunaidi, 2012; Hunaidi

et al., 2004; Hyun et al., 2003; Li et al., 2011; Liou and Tian, 1995; Lippitt, 1987; Martini et al., 2015, 2014; McCarthy et al., 2000; Puust et al., 2010; Romano et al., 2012; Smith and Hay, 2000; Sun et al., 2011; Tackett et al., 2011; USEPA, 2010; Van Der Kleij and Stephenson, 2002; Waller, 1969; Wang et al., 2002, 2001; Weil et al., 1994; Yazdekhasti et al., 2018; Yoon et al., 2011). Most of the current transient-based methods are struggling to achieve rapid pipe inspection because they are based on manually introduced transient events, revealing that the leaks can only be detected when the techniques are applied (Covas et al., 2005a,b, 2003, 2004; Evans et al., 2004; Gong et al., 2013a; Lee et al., 2006, 2005a, 2008; Liggett and Chen, 1994; Maloney, 1973; Pudar and Liggett, 1992; Rizwan and Paul, 2015; Stoianov et al., 2007; Vítkovskỳ et al., 2011; Wang et al., 2002; Yazdekhasti et al., 2018, 2017).

Wiggert (1968) investigated the possibility of using the change in the transients caused by the lateral flow to analyze the characteristics of the pipe for pipe leak detection. Wang et al. (2002) studied the transient leak detection method further, based on the damping in the amplitude of Fourier transformation caused by the leak, which occurs in the pressure transients generated by valve closure. The damping caused by the leak can be analyzed to determine the link between the leak location, size and the Fourier series of the measured head disturbance from a steady state (Ziegel, 1987). Additionally, Nixon et al. (2006) and Brunone et al. (2018) explored the damping-based method outlined in Wang et al. (2002) further in terms of the validity range and different materials of the pipe. The application of fast Fourier transform (FFT) for pipe leak detection based on the fluid transients has been studied (Gong et al., 2013a, 2016a, 2018a,b, 2016b, 2013b). The signal processing was completed by applying FFT to the measured signal, which is the signal for the duration from the occurrence of the transient to the steady state. The equations that were used to solve the location of the leak were derived from the transformation matrix method. By applying these equations to the resultant values from the FFT analysis, the location of the leak can be solved, and the severity of the leak can then be

estimated. The results from the implemented numerical and experimental verifications verified the technique. Duan et al. (2011), and Duan (2016; 2018) studied leak detection methods in branched and looped pipeline systems, based on the transient frequency response (TFR) method. The effects of the branch, conjunction, and loop have been researched. Additionally, the sensitivity and accuracy of the TFR method, based on the influence of the leak location and friction effects has been studied.

Leak detection, localization, and leak cross-sectional area quantification (refer to as quantification in the rest of the paper) were fulfilled in the previously mentioned studies. However, based on the assumption that a pipe failure can generate the fluid eruption (burst) when the leak initiates resulting in a mechanism that the burst can generate a measurable pressure wave, there are several aspects can be improved when focusing on detecting bursts instead of existing pipe leaks. Firstly, during the process of verification of these techniques, the transients were generated by manually opening and then closing the valve because they are using the reflected wave caused by the additional transient instead of a transient caused by leak itself. The leak can only be detected, localized, and quantified when a transient wave is generated by the valve, indicating that the inspection of the pipeline cannot be achieved rapidly when, for example, a burst occurs. Secondly, the externally introduced transients require a separate valve closure. This means the application of such a technique requires an operation that interrupts the normal working process of the pipeline, as additional flow must be released from the generator, which then has to be closed rapidly. Thirdly, the steady friction damping can be calculated, however the unsteady damping must be determined by closing the valve of the target pipeline under a no-leak condition when applying these techniques. This particular aspect indicates that whenever applying the technique, a process to determine the friction damping (including steady and unsteady friction damping) has to be implemented prior to leak detection, which is cumbersome. Real-time data-based burst detection methods are capable of inspecting the pipeline when the burst

occurs without using a separate valve closure to generate pressure transients. This is because the burst is the process of first occurrence of the pipe failure, but the existing leak is the fault that has already occurred and is pre-existing. These methods are capable of utilizing the transient caused by the burst itself. Parikh et al. (2008), Ebina et al. (2011), and Hutton et al. (2015a) studied the real-time data-based burst detection methods, but these methods have difficulties in locating and quantifying the burst. Although the real-time data-based technique presented in Kang et al. (2012) has the ability to locate the burst, it requires the additional flow meters for application.

Recent numerical and experimental studies have demonstrated a rapid and non-intrusive burst detection, localization, and burst quantification technique, which is capable of improving all the previously mentioned aspects. The technique is based on the method of damping of fluid transients, but it does not require a manually introduced transient event. An additional developed and validated model is utilized that is capable of determining components of friction damping numerically and accurately. Nixon et al. (2006) support the approach outlined in this paper for burst detection, localization, and quantification using the damping of fluid transients, and they point to ways in which this approach can be applied in more complex systems.

In the following section, transient response modeling, its analytical solution, and the corresponding Fourier analysis of the technique are derived and presented. The theory of burst detection, localization, and quantification is given in the next section, followed by two numerical studies. The validation of the model for obtaining the unsteady friction damping numerically is then presented. Finally, the results of the experimental verification are presented.

3.2 Transient Response Modeling

Based on the application of the Dirac-Delta function to the conservation of mass in Wang et al. (2002), and the water hammer equation, the analysis of the total control volume of burst located between points x_1 and x_2 provides

$$\frac{\partial H}{\partial t}+\frac{Q}{A_p}\frac{\partial H}{\partial x}+\frac{a^2}{gA_p}\frac{\partial Q}{\partial x}+\frac{a^2}{gA_p}Q_B\Delta(x-x_B)=0 \tag{3.1}$$

where H is the head, t is the time, Q is the flow rate, A_P is the cross-sectional area of the pipe, a is the wave speed, g is gravity acceleration, x is the distance along the pipe, Q_B is the flow rate of the burst, $\Delta(x-x_B)$ is the Dirac-Delta function that is defined in Wang et al. (2002).

According to Wang et al. (2002) and Wylie et al. (1993), the equation of the conservation of the momentum along the x direction for single burst scenario gives

$$\frac{\partial}{\partial t}(\rho A_p V)\delta x+\frac{\partial}{\partial x}(\rho A_p V^2)\delta x=\sum F_x \tag{3.2}$$

where F_x is the total force acting on the fluid along the x direction.

The various forces acting on the control volume along the x direction include

1. Pressure forces at the two side areas of each burst: $F_{p1}=pA_p$, $F_{p2}=(p+\frac{\partial p}{\partial x}\delta x)A_p$, where p is the pressure
2. Shear force: $F_s=(\tau_s+\tau_{us})\pi D\delta x$, where τ_s is the steady shear stress, τ_{us} is the unsteady shear stress, and D is the inner diameter of the pipe (Pothof,

2008)

Defining the downstream flow direction as positive, the total force component acting on the control volume is expressed as

$$\begin{aligned}\sum F_x &= pA_p - (p + \frac{\partial p}{\partial x}\delta x)A_p - (\tau_s + \tau_{us})\pi D\delta x \\ &= -A_p\frac{\partial p}{\partial x}\delta x - (\tau_s + \tau_{us})\pi D\delta x\end{aligned} \tag{3.3}$$

where

$$\tau_s + \tau_{us} = \frac{\rho(f_s + f_{us})V^2}{8} \tag{3.4}$$

in which f_s is the Darcy-Weisbach friction factor (Wylie et al., 1993) and f_{us} is the unsteady friction factor (Pothof, 2008; Wang et al., 2002). Substituting Eq. (3.2) into Eq. (3.3), and applying the mathematical process in Wang et al. (2002) provides

$$\frac{\partial H}{\partial x} + \frac{1}{gA_p}\frac{\partial Q}{\partial t} + \frac{Q}{gA_p^2}\frac{\partial Q}{\partial x} + \frac{(f_s + f_{us})Q^2}{2DgA_p^2} - \frac{QQ_B}{gA_p^2} = 0 \tag{3.5}$$

The volume flow rate of the burst Q_B can be expressed based on the orifice equation

$$Q_B = C_d A_B(2g\Delta H_B)^b \tag{3.6}$$

where ΔH_B is the head acting on the burst location when the burst occurs,

C_d is the burst discharge coefficient, and A_B is the cross-sectional area of the burst. Note that $\Delta H_B = H_B - z_B$, where H_B is the piezometric head at the burst location when it occurs, and z_B is the pipe elevation at the burst location. b is the parameter of the burst discharge-head relationship. Its value is typically equal to 0.5.

The following dimensionless quantities are applied to the equations non-dimensionalization as provided in Wang et al. (2002),

$$H^* = \frac{H}{H_1},\ t^* = \frac{t}{L/a},\ x^* = \frac{x}{L},\ Q^* = \frac{Q}{Q_0} \tag{3.7}$$

where H_1 is the reference pressure head, which is usually the pressure head at the tank or the upstream reservoir, L is the length of pipe, and Q_0 is the reference flow rate. According to Wang et al. (2002), substituting Eqs. (3.6) and (3.7) into Eqs. (3.1) and (3.5) gives

$$\frac{\partial H^*}{\partial t^*} + \frac{1}{K}\frac{\partial Q^*}{\partial x^*} + M(\Delta H_B^*)^b \Delta(x^* - x_B^*) = 0 \tag{3.8}$$

$$K\frac{\partial H^*}{\partial x^*} + \frac{\partial Q^*}{\partial t^*} + RQ^{*2} = 0 \tag{3.9}$$

in which

$$R = R_s + R_{us} = \frac{f_s L Q_0}{2aDA_p} + \frac{f_{us} L Q_0}{2aDA_p},\ M = \frac{C_d A_B}{A_p}\frac{2a}{(2gH_1)^{1-b}},\ \textit{and}\ K = \frac{H_1}{H_s} \tag{3.10}$$

Here, R, R_s, and R_{us} are the actual (total), steady, and unsteady friction damping respectively because of the change in the friction factor $f = f_s + f_{us}$ (Bergant et al., 2001; Brunone, 1999; Vardy and Hwang, 1991; Wang et al., 2002; Zielke, 1968). Additionally, $H_s = \frac{aV_B}{g}$ is the Joukwosky pressure head drop, resulting from an instantaneous reduction in the velocity, in which V_B is the flow velocity of the burst. All the previously-mentioned parameters were defined by Wang et al. (2002) and Liou (1991) as two characteristics of the pipe.

Expanding H^* and Q^* as a steady value, minus the transient pressure head loss and transient flow rate due to the burst, provides

$$H^* = H_0^* - h^*, \;\; Q^* = Q_0^* + q^* \tag{3.11}$$

where h^* is the dimensionless head disturbance, and q^* is the dimensionless flow disturbance. By applying the expression of $(\Delta H_B^*)^b$ in Wang et al. (2002), substituting Eq. (3.11) into Eqs. (3.8) and (3.9), and neglecting the terms of q^{*2}, Eqs. (3.8) and (3.9) can be expressed as

$$\frac{1}{K}\frac{\partial q^*}{\partial x^*} - \frac{\partial h^*}{\partial t^*} - M\frac{bh^*}{(\Delta H_{B0}^*)^{1-b}}\Delta(x^* - x_B^*) = 0 \tag{3.12}$$

$$2Rq^* + \frac{\partial q^*}{\partial t^*} - K\frac{\partial h^*}{\partial x^*} = 0 \tag{3.13}$$

where ΔH_B^* is also defined as $\Delta H_B^* = H_B^* - z_B^*$, which is the dimensionless pressure head at the burst, H_B^* is the dimensionless piezometric head at the burst, z_B^* is the dimensionless elevation at the burst, and $\Delta H_{B0}^* = H_{B0}^* - z_B^*$ is the dimensionless steady head at the burst before the occurrence of the burst. According

to Wang et al. (2002), the governing equation is finally expressed as

$$\frac{\partial^2 h^*}{\partial x^{*2}} = \frac{\partial^2 h^*}{\partial t^{*2}} + [2R + K_B \Delta(x^* - x_B^*)] \frac{\partial h^*}{\partial t^*} + 2RK_B \Delta(x^* - x_B^*) h^* \tag{3.14}$$

where

$$K_B = \frac{Mb}{(\Delta H_{B0}^*)^{1-b}} = \frac{\frac{C_d A_B}{A_p} \frac{2ab}{(2gH_1)^{1-b}}}{(\frac{H_{B0}}{H_1})^{1-b}} = \frac{C_d A_B}{A_p} \frac{2ab}{(2gH_{B0})^{1-b}} \tag{3.15}$$

since ΔH_{B0}^* is defined as $\frac{H_{B0}}{H_1}$ if $z_B = 0$.

The analytical solution of Eq. (3.14) is

$$h^*(x^*,\ t^*) = \sum_{n=1}^{\infty} \left\{ e^{-(R+R_{nB})t^*} \left[A_n cos(n\pi t^*) + B_n sin(n\pi t^*) \right] sin(n\pi x^*) \right\} \tag{3.16}$$

where R_{nB} is the damping caused by the burst for the nth harmonic, and can be expressed as

$$R_{nB} = K_B sin^2(n\pi x_B^*) \tag{3.17}$$

where A_n and B_n are the Fourier coefficients expressed in Wang et al. (2002). Although the form of the solution for a burst in Eq. (3.16) is similar to the solution for a leak in Wang et al. (2002) and Wang et al. (2005), due to water hammer theory, the burst itself is the transient source, and the occurrence of a burst causes a sudden pressure drop instead of an additional positive pressure

disturbance when compared with the transients generated by valve closure, as shown in Eq. (3.11). Moreover, when the generator valve closes, it no longer contributes to the damping in the system, unlike the burst. By applying the Fourier series analysis shown in the Appendix, the amplitudes of the first and the nth harmonic in each period are

$$E_n^{(1)} = -\frac{e^{-(R+R_{nB})(t_0^*+T^*)} - e^{-(R+R_{nB})t_0^*}}{(R+R_{nB})T^*} sin(n\pi x^*)\sqrt{A_n^2+B_n^2} \tag{3.18}$$

$$E_n^{(m)} = E_n^{(1)} e^{-(R+R_{nB})(m-1)T^*} \quad (m = 1,\ 2,\ 3, ...) \tag{3.19}$$

where t_0^* is the dimensionless starting time of the Fourier analysis and T^* is the dimensionless period of the signal.

3.3 Approach to Burst Detection, Localization, and Quantification

When considering the steady friction alone, the steps that can be applied for burst detection are shown below, and in Figure 3.1.

1. Set up steady flow in the pipeline and keep measuring the pressure head at one or more points along the pipe.
2. Divide the pressure trace period by period.
3. Decompose the harmonic components from the data of each period by using the discrete Fourier transformation (Ziegel, 1987).

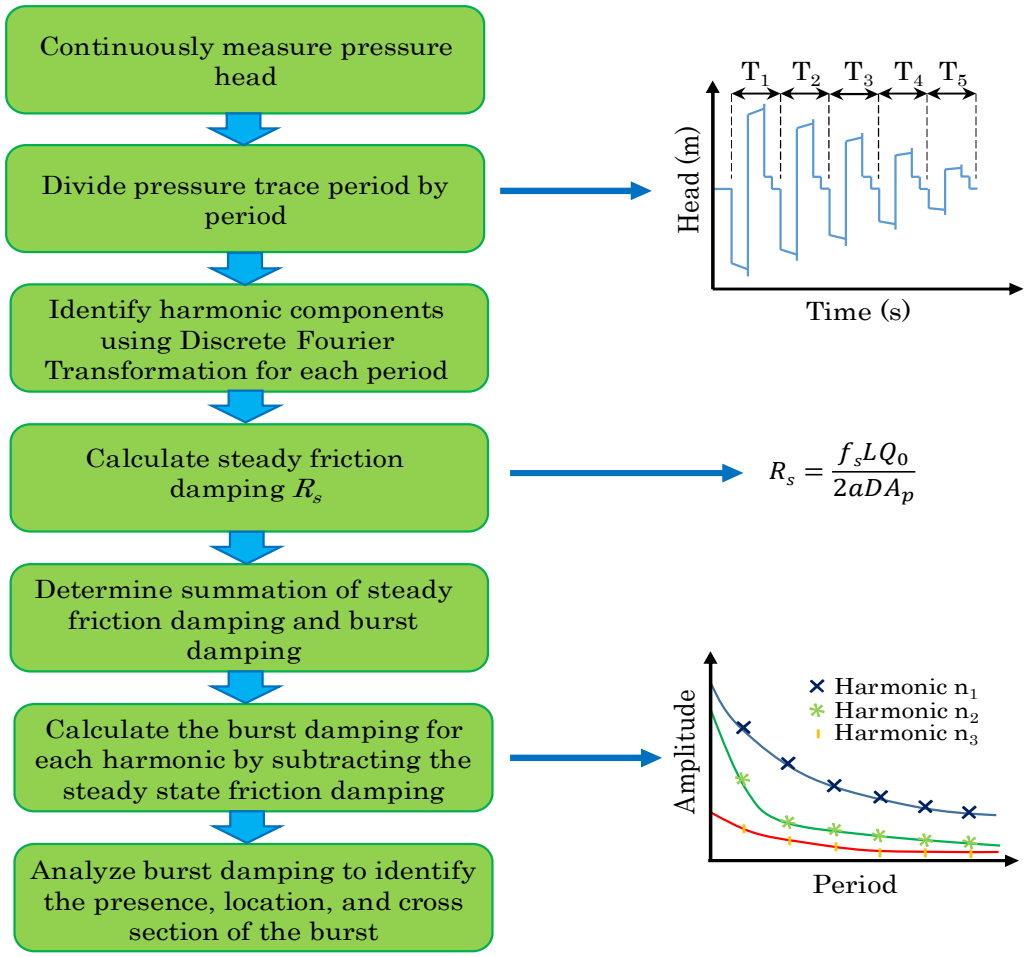

Figure 3.1: Steps of burst detection, localization, and quantification

4. Repeat step three for each period of the measured data.
5. Calculate the summation of the steady friction damping and the burst damping by applying Eq. (3.19).
6. Calculate the burst damping for each harmonic by subtracting the steady friction damping from the results from step five. The steady friction damping can be calculated by using the definition of R_s in Eq. (3.10).
7. Analyze the burst damping to determine the presence of the burst, then localize and quantify the burst.

The details of the process to determine the presence of the burst, then localize and quantify the burst, are presented next.

The presence of the burst can be determined by observing the transient signal of the pressure trace in the time domain, ideally. For the condition of a pipe without a burst, there are no significant pressure fluctuations along the pipeline, and the burst can generate a transient event. However, at a practical level, there will be external noise in the measured pressure trace, thus the analysis of the burst damping should continue. If there is no-burst, the resultant burst damping should be equal or close to zero. Therefore, the presence of the burst can be confirmed by observing the non-zero and differently-valued burst damping.

The dimensionless burst location can be calculated by using the burst damping, which is expressed in Eq. (3.17). The total damping can be calculated by using Eq. (3.19), based on the amplitude of the nth harmonic for each period. The friction damping R_s shown in Eq. (3.10) can be calculated theoretically, using the known parameters of the pipe system.

According to Eq. (3.17), the burst damping of each pair of harmonic compo-

nents $n = n_1$ and $n = n_2$ are

$$\begin{aligned} R_{n_1 B} &= K_B sin^2(n_1 \pi x_B^*) \\ R_{n_2 B} &= K_B sin^2(n_2 \pi x_B^*) \end{aligned} \tag{3.20}$$

The burst location can thus be expressed as a function, which depends on the dimensionless burst location x_B alone. By using the mathematical operation

$$\frac{R_{n_2 B}}{R_{n_1 B}} = \frac{sin^2(n_2 \pi x_B^*)}{sin^2(n_1 \pi x_B^*)} \tag{3.21}$$

the dimensionless location of the burst can be determined by solving Eq. (3.21). The plots of $\frac{R_{2B}}{R_{1B}}$, $\frac{R_{3B}}{R_{2B}}$, and $\frac{R_{3B}}{R_{1B}}$ are shown in Figure 3.2. It can be seen that there is more than one possible solution with one value of the damping ratio, and the number of possible solutions increases with the number of harmonic components, therefore only the first three resonance harmonics are applied.

The relative cross-sectional area of the burst can be calculated by substituting the determined dimensionless burst location x_B into Eq. (3.17), so the relative cross-sectional area can be expressed as

$$C_d A_B = \frac{R_{nB} A_p (2gH_{B0})^{1-b}}{2absin^2(n\pi x_B^*)} \quad (n = 1,\ 2,\ 3,\ ...) \tag{3.22}$$

indicating that the actual cross-sectional area of the burst can be determined by knowing the discharge coefficient of the burst.

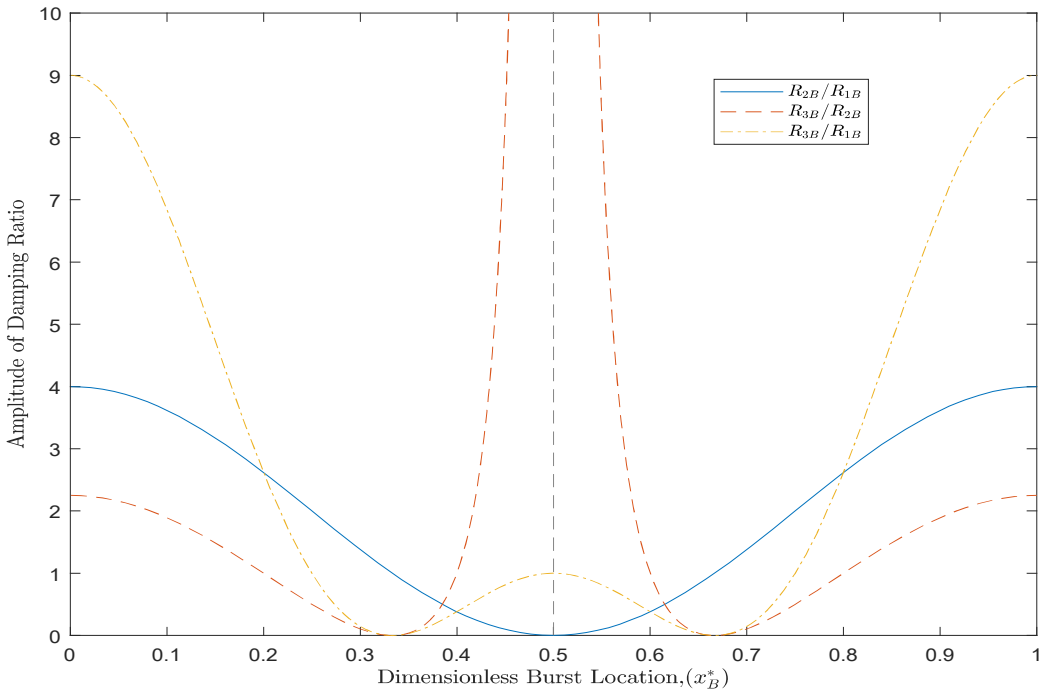

Figure 3.2: Damping ratios

3.4 Computational Verification of the Theoretical Model with Steady Friction

Two scenarios for the computational verifications for single burst problem have been conducted, reservoir-pipe-reservoir (RPR) and reservoir-pipe-valve (RPV) scenarios, referring to as Cases 1 and 2, respectively. Note that the dimensionless periods T^* of Cases 1 and 2 are 2 and 4 respectively. In Test 1 of Case 1, and Case 2, the transient event is initiated by the burst, and the burst is simulated by a suddenly-opened side discharge valve located at $x_B^* = 0.25$, and the measurement location is $x^* = 0.75$ (750 m away from the upstream reservoir). The total testing time is 20 s, and the occurrence time of the burst is 0.3 s. The opening time of the valve can be neglected, since the valve is simulated to open immediately. The wave speed of both cases is $a = 1000$ m/s. The burst in both cases is assumed to be the sharp orifice, thus the value of b is set to be 0.5. The no-burst conditions of both cases are assumed to be at a

steady state.

The artificial setup of Case 1 is shown in Figure 3.3.

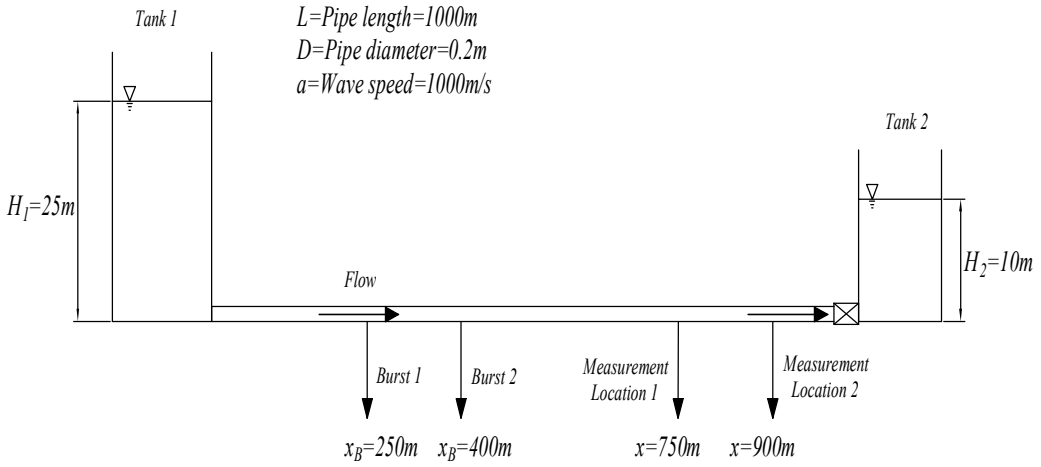

Figure 3.3: RPR setup

There are two tests in Case 1. In both tests in Case 1, the downstream valve is fully opened, so the head loss can be negligible, indicating that the pipe is delivering the water, and the steady flow rate is $Q_0 = 0.0622$ m^3/s. The Darcy-Weisbach friction factor is $f = 0.015$, and the relative cross-sectional area of the burst is $\frac{C_d A_B}{A_p} = 0.002$. The burst and the measurement locations are located at Burst 1 and Measurement Location 1 in Test 1, as shown in Figure 3.3. Figure 3.4 presents the head trace in the time domain under the conditions of no-burst and with a burst of the Test 1.

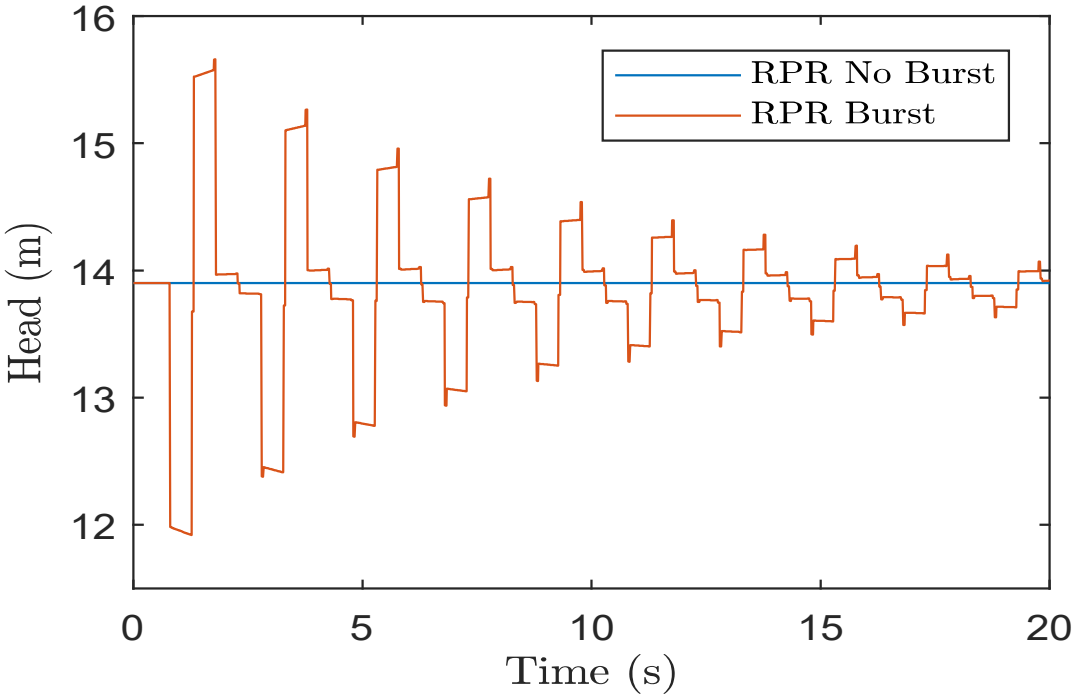

Figure 3.4: RPR time trace

The summation of the steady friction damping and the burst damping is calculated by applying the Fourier analysis, then fitting Eq. (3.19) for the burst condition. The results of the calculated summation of the steady and the burst damping rates are plotted in Figure 3.5. In order to compare the resultant damping rate presented in Figure 3.5 with the steady friction damping rate intuitively, the same process is applied under the condition of no-burst, but the transient is generated by closing the downstream valve under the no-burst condition, and the pressure trace is shown in Figure 3.6. The steady friction damping is calculated by using the definition of the steady friction damping R_s in Eq. (3.10). The Fourier coefficients A_n and B_n are determined by using the measured data. Accordingly, the steady friction damping rate is calculated by substituting the calculated R_s, A_n, and B_n into Eqs. (3.18), and (3.19), which is plotted in Figure 3.7.

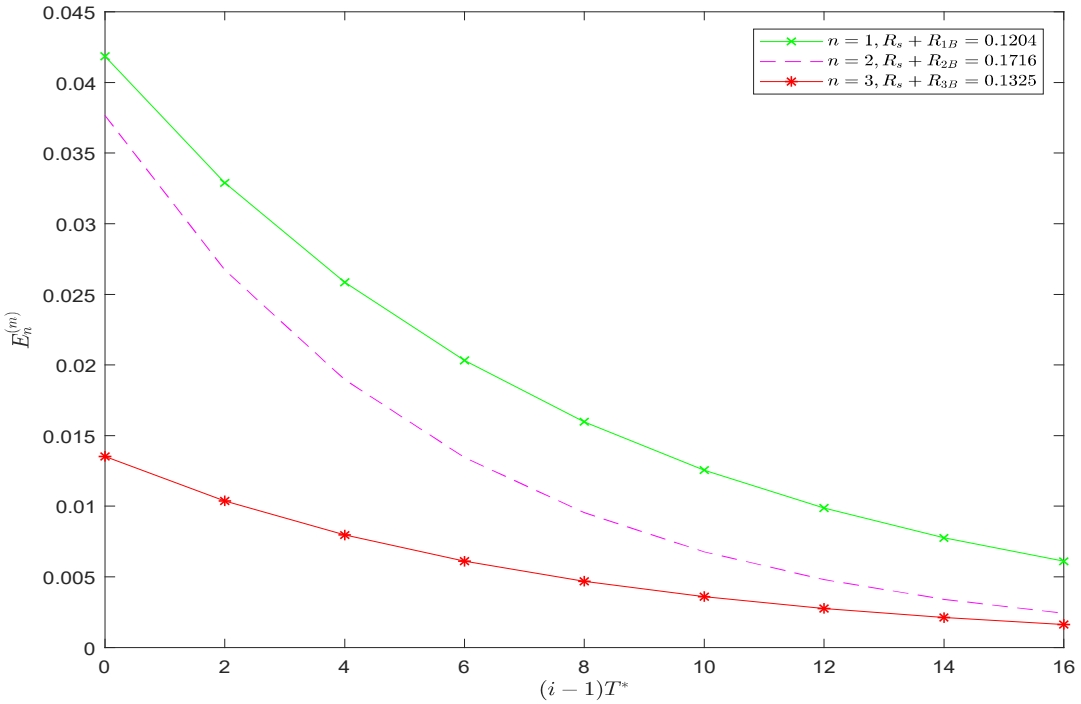

Figure 3.5: Damping rates of RPR burst without external transient

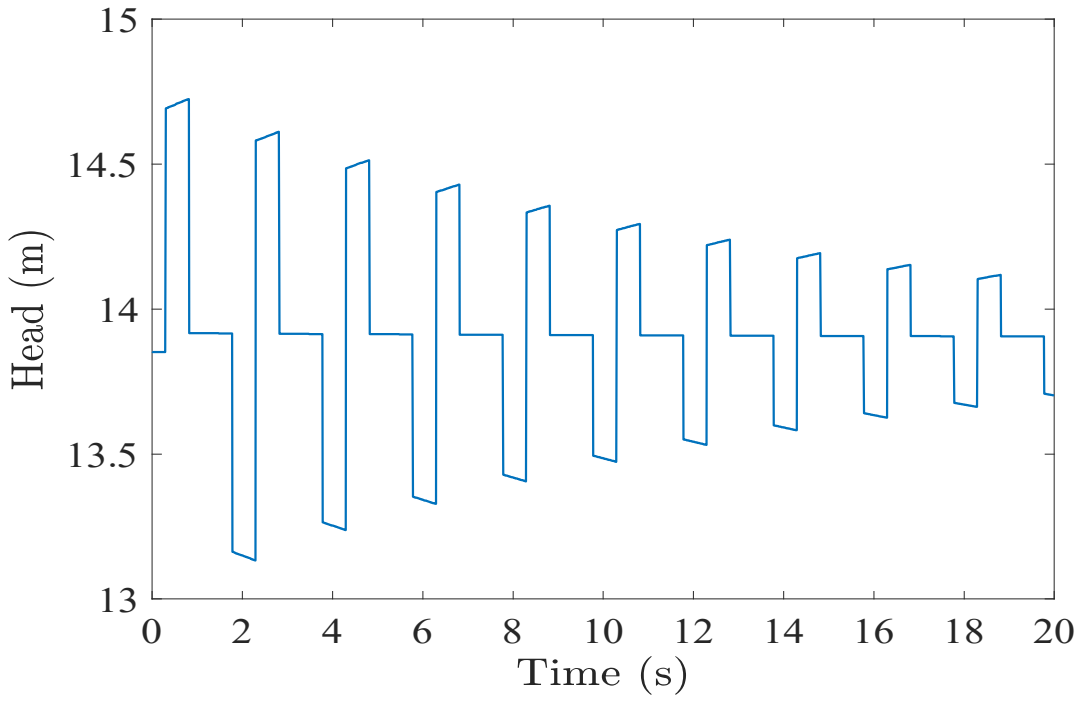

Figure 3.6: RPR with no leak with external transient

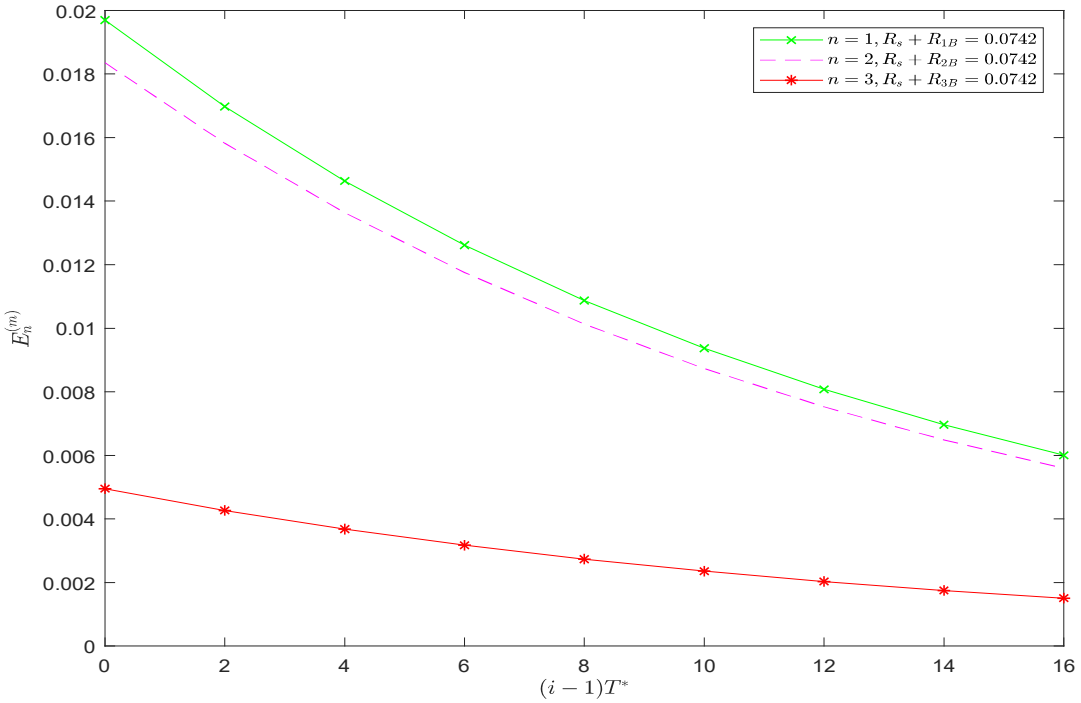

Figure 3.7: Damping rates of RPR with no leak

The steady friction damping is calculated as $R_s = 0.0742$, based on Eq. (3.10). The burst damping of the first three harmonic components can thus be calculated by subtracting R_s from each $R_s + R_{nB}$, as shown in Figure 3.5, and they are $R_{1B} = 0.0462$, $R_{2B} = 0.0974$, and $R_{3B} = 0.0583$. In order to localize the burst, the damping ratio is applied, as shown in Figure 3.2. The calculated dimensionless burst locations are $x_B^* = 0.2412$, $x_B^* = 0.2398$, and $x_B^* = 0.2402$, corresponding to using $\frac{R_{2B}}{R_{1B}}$, $\frac{R_{3B}}{R_{2B}}$, and $\frac{R_{3B}}{R_{1B}}$. The final value of the dimensionless burst location is calculated as $x_B^* = 0.2404$ or $x_B^* = 0.7596$, which corresponds to averaging these three values and subtracting them from 1 respectively. The relative cross-sectional area of the burst can then be determined by applying Eq. (3.22), and the value of the relative cross-sectional area is calculated as $\frac{C_d A_B}{A_p} = 0.002$. The former value of x_B^* and the value of $\frac{C_d A_B}{A_p}$ are close to the actual values of the burst, which are $x_B^* = 0.25$ and $\frac{C_d A_B}{A_p} = 0.002$.

In order to assess the applicability of the technique at different burst and measurement locations, another test has been included in Case 1. In Test 2, the

burst location is changed from 250 m to 400 m from the upstream reservoir, and the measurement location is changed from 750 m to 900 m from the upstream reservoir, which are indicated as Burst 2 and Measurement Location 2 in Figure 3.3. By repeating the previous steps, the determined dimensionless burst location and relative cross-sectional area are $x_B^* = 0.4074$ and $\frac{C_d A_B}{A_p} = 0.002$, which are close to the actual values. A comparison of the results from Case 1 is shown in Table 3.1.

Table 3.1: Comparison of Case 1

Test Number	Dimensionless Burst Location x_B^*	Dimensionless Measurement Location	Resultant x_B^*
1	0.25	0.75	0.2404
2	0.4	0.9	0.4074

Although the mathematical model is derived from an RPR system, the model can still be applied to an RPV system by adding an imaginary mirror part, and the artificial setup of Case 2 is shown in Figure 3.8.

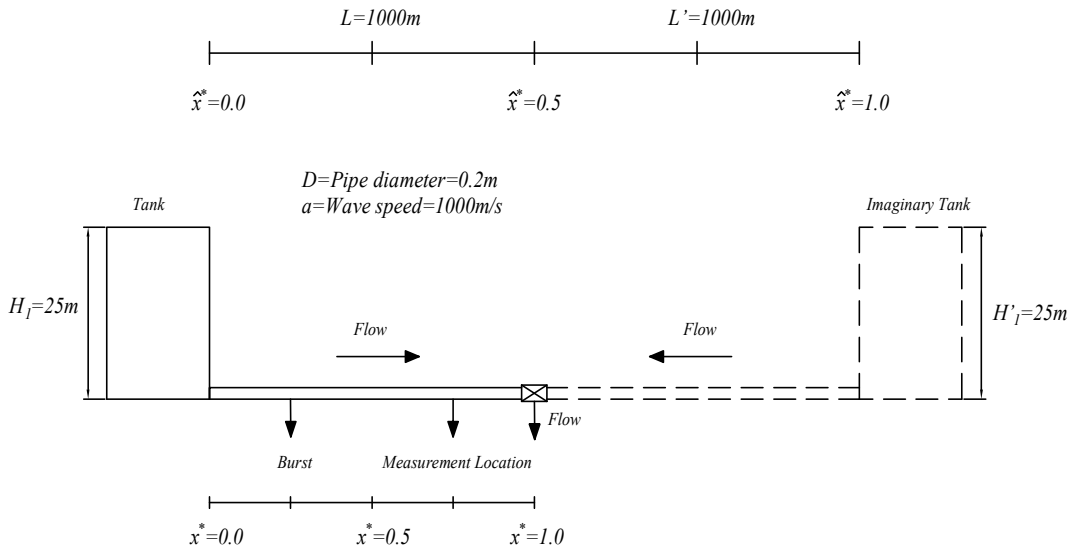

Figure 3.8: RPV setup

In order to reduce the complexity of the flow by reducing the steady friction damping in this scenario, the steady flow rate is set to be $Q_0 = 3.33 \times 10^{-4}$ m^3/s by a partially opened downstream valve. The Darcy-Weisbach friction factor is $f = 0.0302$, and the relative cross-sectional area of the burst is $\frac{C_d A_B}{A_p} =$

0.002, which is the same as Case 1. The pressure traces in the time domain under the conditions of no burst and with a burst are presented in Figure 3.9.

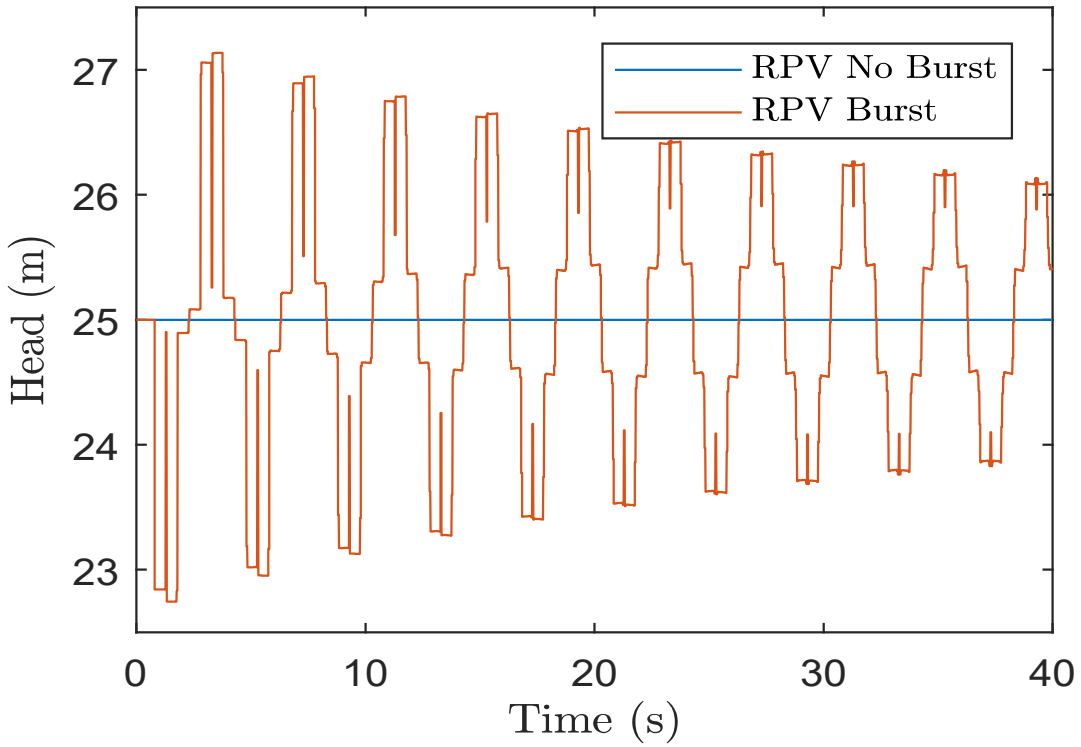

Figure 3.9: RPV time trace

Repeating the procedure applied in Case 1 provides the steady friction damping rate, shown in Figure 3.10. The results of the summation of the steady friction and the burst damping rates are presented in Figure 3.11.

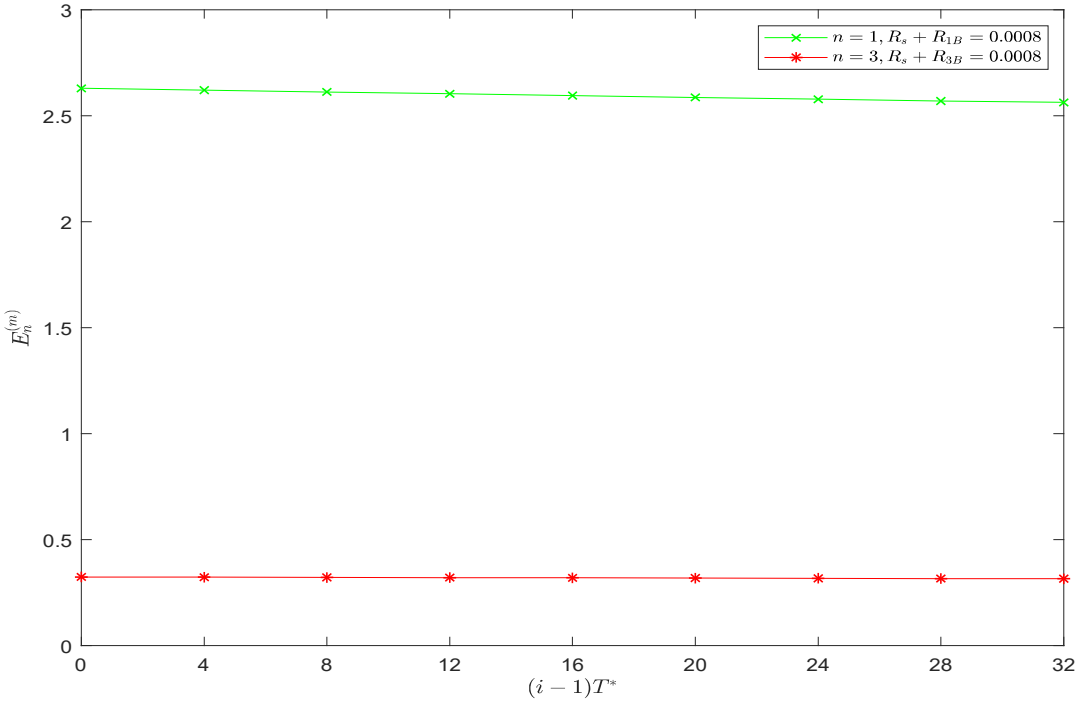

Figure 3.10: Damping rates of RPV with no leak

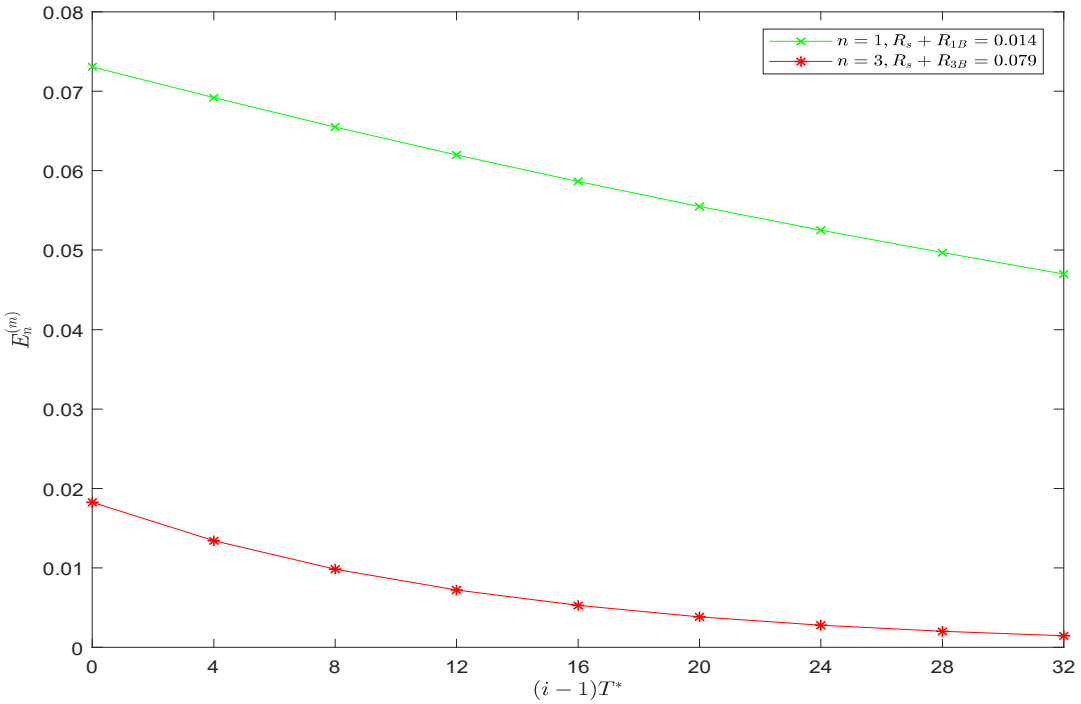

Figure 3.11: Damping rates of RPV burst without external transient

The burst damping of the first and third harmonic components are $R_{1B} = 0.0132$ and $R_{3B} = 0.0782$, achieved by subtracting $R_s = 0.0008$ from each $R_s + R_{nB}$ as shown in Figure 3.11. The calculated dimensionless burst locations are $\hat{x_B}^* = 0.1227$ or $\hat{x_B}^* = 0.8773$, corresponding to $\frac{R_{3B}}{R_{1B}}$, where $\hat{x_B}^*$ is the directly calculated value of the dimensionless burst location. Due to the imaginary mirror part of the RPV system, the direct result of the dimensionless burst location should be doubled, as is shown below

$$\hat{x_B}^* = \frac{x_B}{L+L'} = \frac{x_B}{2L} = \frac{x_B^*}{2} \tag{3.23}$$

Therefore,

$$x_B^* = 2\hat{x_B}^* \tag{3.24}$$

and all the possible solutions located in the mirrored part of the pipeline should be ignored. Thus, the final value of the dimensionless burst location is calculated as $x_B^* = 2\hat{x_B}^* = 0.2454$. The relative cross-sectional area is calculated as $\frac{C_d A_B}{A_p} = 0.002$. The calculated value of the dimensionless location and the relative cross-sectional area of the burst are close to the actual value of the burst, which are $x_B^* = 0.25$ and $\frac{C_d A_B}{A_p} = 0.002$.

The numerical verifications conducted show that the approach presented in this paper can be applied successfully for burst detection, localization, and quantification, when considering steady friction alone (Wang et al., 2002). The approach is capable of being applied at different burst and measurement locations. By applying the sensitivity analysis in Wang et al. (2002), the location errors of all the conducted numerical studies are approximately $1\% - 1.5\%$. However, unsteady friction will also be involved in practice if there is a transient in-

troduced into a pipe, as indicated in the governing equations and the solution. The transient source of the burst scenarios presented in this paper is the burst itself instead of the valve closure in Wang et al. (2002). Based on this particular analysis above, unsteady friction damping cannot be determined by using the method applied in Wang et al. (2002). Therefore, it is crucial to determine the unsteady friction to calculate the burst damping correctly for the burst conditions. The details of the determination of unsteady friction damping are now considered.

3.5 Determination of Unsteady Friction Damping

In order to determine the unsteady friction damping caused by the burst, an unsteady friction water hammer (UFWH) model is built based on the free open-source 1D water hammer (FOSWH) code (Kjerrumgaard Jensen et al., 2018; Vítkovskỳ et al., 2006a,b). The sections of the interior nodes and boundary conditions in the UFWH model have been modified by adding burst discharge points. The UFWH model enables modeling of the bursts along the pipe, and it is validated by reproducing the same results as from the FOSWH model.

To illustrate that the unsteady friction damping caused by the burst can be determined and is different from that caused by the valve closure, a relevant test was conducted. The setup applied in this test is the same as that presented in Figure 3.8. During the process of the test, two scenarios are considered, which are: a) closing the downstream valve under the no-burst condition, and b) initiating the burst at the dimensionless location $x_B^* = 0.005$ with the downstream valve opened normally. These are referred to as Cases 3 and 4, respectively. By initiating the burst close to the upstream boundary, the effect of the burst damping is reduced according to its definition presented in Eq. (3.17). However, the magnitude of the burst damping also depends on the relative cross-sectional

area of the burst, thus the applied relative cross-sectional area is $\frac{C_d A_B}{A_p} = 0.0001$. The resultant burst damping from the first and the third harmonic components are smaller than 5×10^{-5}, which are the harmonic components used in the test, and close to zero. Accordingly, the calculated damping of the burst scenario of each harmonic only contains the summation of the steady and unsteady friction damping. The downstream valve remains open for Case 4 to remove any possible transient caused by the closed downstream valve.

By implementing Cases 3 and 4 with steady friction alone and the summation of steady and unsteady friction, and fitting Eq. (3.19) into the signal after the Fourier series analysis, the steady friction damping and the actual friction damping are determined. Subtracting the steady friction damping from the actual friction damping provides the unsteady friction damping, and the results of the unsteady friction damping for Cases 3 and 4 are shown in Table 3.2.

Table 3.2: Comparison of unsteady friction between Cases 3 and 4

Case Number	$R_{1\ us}$	$R_{3\ us}$
3	0.01	0.018
4	0.014	0.028

It is shown that unsteady friction damping caused by the burst is successfully determined and different from the same quantity caused by the valve closure, based on the results presented in Table 3.2. In addition, the unsteady friction damping for each harmonic component is different from the other. The actual friction damping for the burst localization and quantification can thus be determined by applying the sequences of Case 4 to any burst scenario, indicating that the friction damping can be determined accurately by using the numerical model.

3.6 Experimental Verification

Two experimental tests were conducted in the Robin Hydraulics Laboratory at the University of Adelaide, referring to Cases 5 and 6. The pipeline applied in the experimental tests is a 37.41 m long, straight pipeline, made of copper. The schematic diagram and the relevant parameters are shown in Figure 3.12.

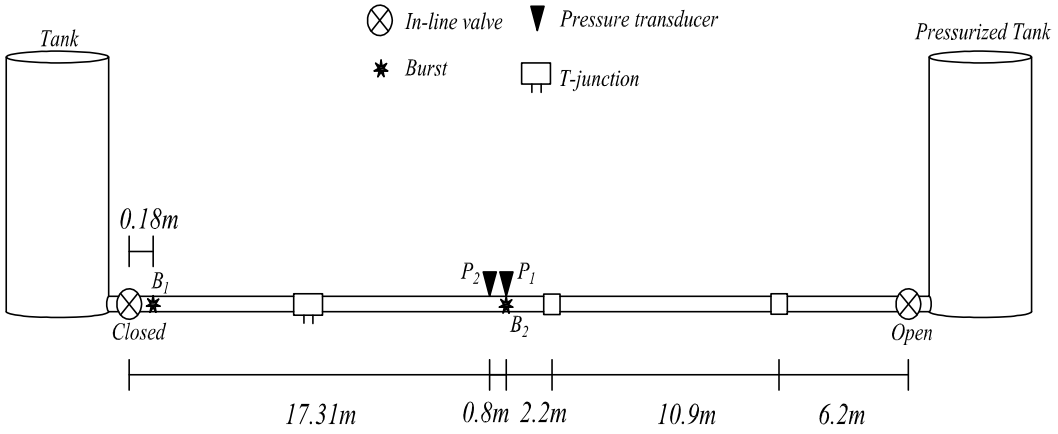

Figure 3.12: Experimental setup

The pressure transducers are located at points P_1 and P_2, and the bursts are located at points B_1 and B_2 for Cases 5 and 6 respectively, shown in Figure 3.12. More details of the experimental rig can be found in Vitkovsky (2007) and Wang et al. (2002). During the process of the tests, the downstream valve of the pipe is set to be closed normally to isolate the west reservoir. In Case 5, the solenoid valve with the relative cross-sectional area $\frac{C_d A_B}{A_p} = 2.12 \times 10^{-3}$ and dimensionless location $x_B^* = 0.9951$ is opened quickly at approximately 3 s to simulate the occurrence of the burst. The total testing time is 6 s. Additionally, the solenoid valve is the sharp orifice, thus $b = 0.5$. The data is measured by the Keller pressure transducer located at P_1. The initial flow rate of the test is $Q_0 = 0$ m^3/s, the wave speed is $a = 1320$ m/s, and the head at the upstream reservoir is $H = 30$ m, which is the east reservoir in Figure 3.12. Note that the system is set to be an RPV system, by using the normally-closed downstream valve, thus all the even harmonic components are inapplicable, and

the dimensionless period is $T^* = 4$. In addition, the burst is actually located near the mid-point of the whole pipeline, by adding the imaginary mirror part of the original pipeline, thus the burst damping of each odd harmonic is not zero. Based on this particular analysis, the UFWH model to determine the actual friction damping is applicable. In order to show that the application of the UFWH model is practical, a comparison between the numerical and the experimental results is shown in Figure 3.13.

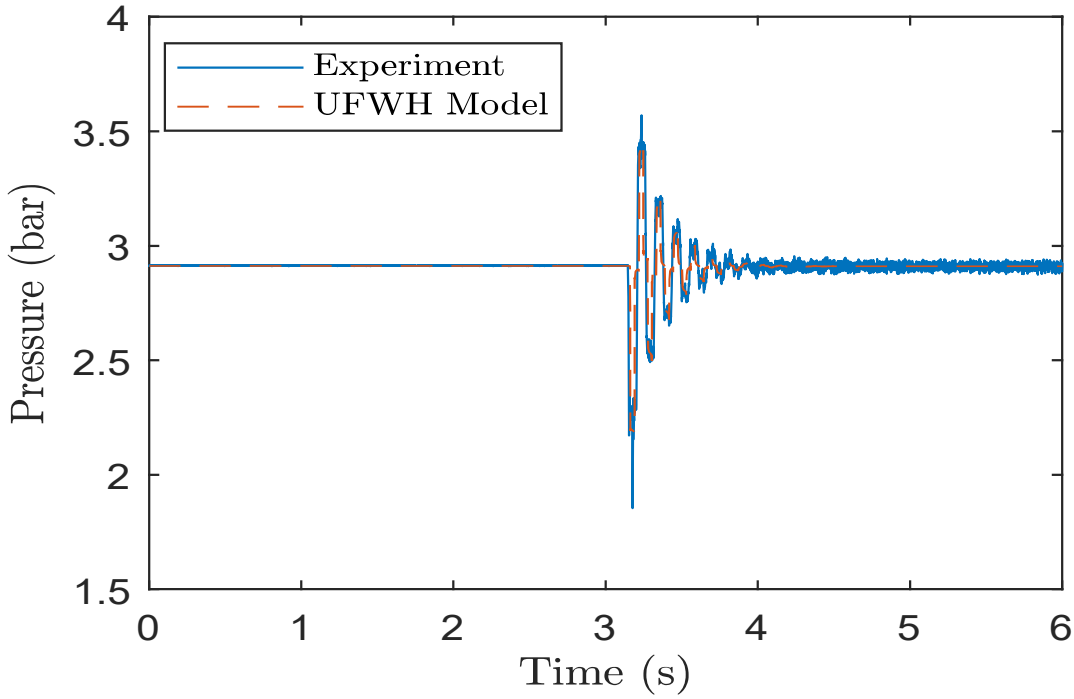

Figure 3.13: Comparison between numerical and experimental results(Case 5)

It can be seen that the results generated by the UFWH model are close to the experimental data, indicating that the UFWH model can be applied to determine the actual friction damping in practice for any single pipeline system. Note that additional transients appear at the first two periods of both the transient signals, numerical and experimental data, are caused by the rapid reflection of the pressure wave due to the closed downstream valve, since the location of the solenoid valve is close to the closed downstream valve. In addition, the differences between them may be caused by external noise and time delay.

The total damping is calculated by applying Fourier analysis to the experimental data, and the actual friction damping is determined by using the UFWH model with the 'Vardy & Brown' unsteady friction model (Kjerrumgaard Jensen et al., 2018; Vardy and Brown, 2003). The burst damping can then be determined by subtracting the actual damping from the total damping. In order to increase the accuracy of the resultant damping ratio, damping of the first, third, and fifth harmonics is used. The calculated damping is presented in Table 3.3. Additionally, the damping rates of the experimental data are shown in Figure 3.14.

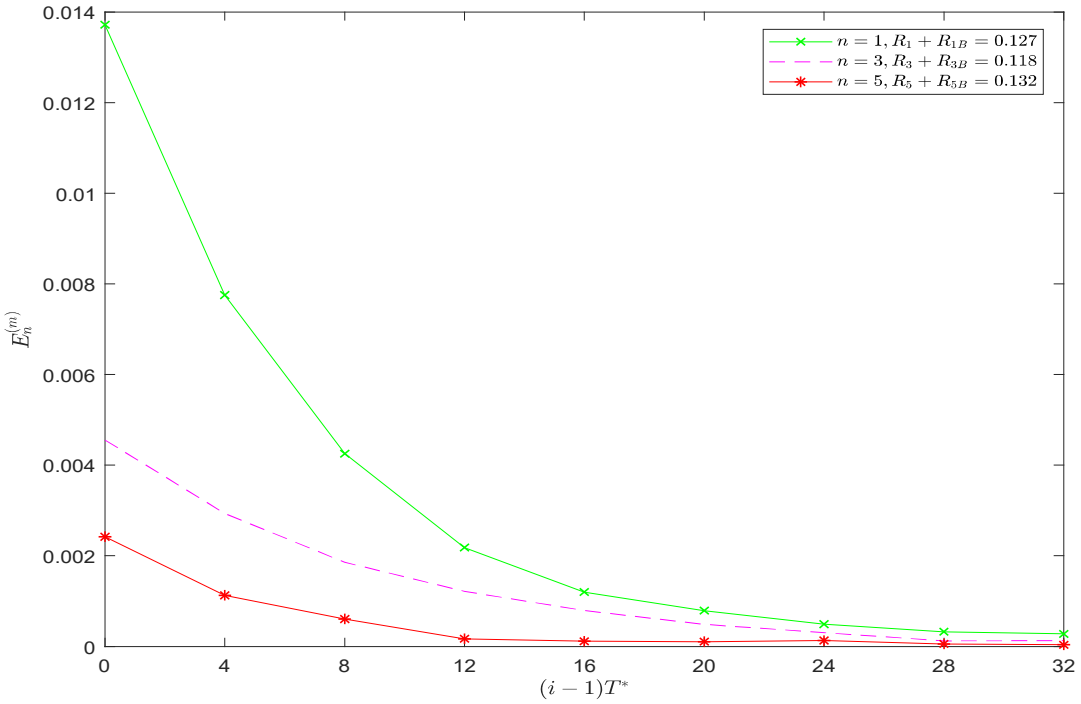

Figure 3.14: Damping rates of experimental data (Case 5)

Table 3.3: Damping of Case 5

Damping Type	$n=1$	$n=3$	$n=5$
Total damping of the data	0.127	0.118	0.132
Actual friction damping	0.012	0.022	0.029
Burst damping	0.115	0.096	0.103

Although the damping of the fifth harmonic is applied for the experimental analysis, the number of possible solutions is not significantly increased. This is because all the bursts located in the range $0.5 < x^* \leq 1$ belong to the imag-

inary mirror part of the RPV system, thus all the possible solutions of x_B^* in this range should be ignored. In addition, only the damping ratio in the range $0<x^* \leq 0.5$ should be applied, and the corresponding damping ratio analysis is shown in Figure 3.15.

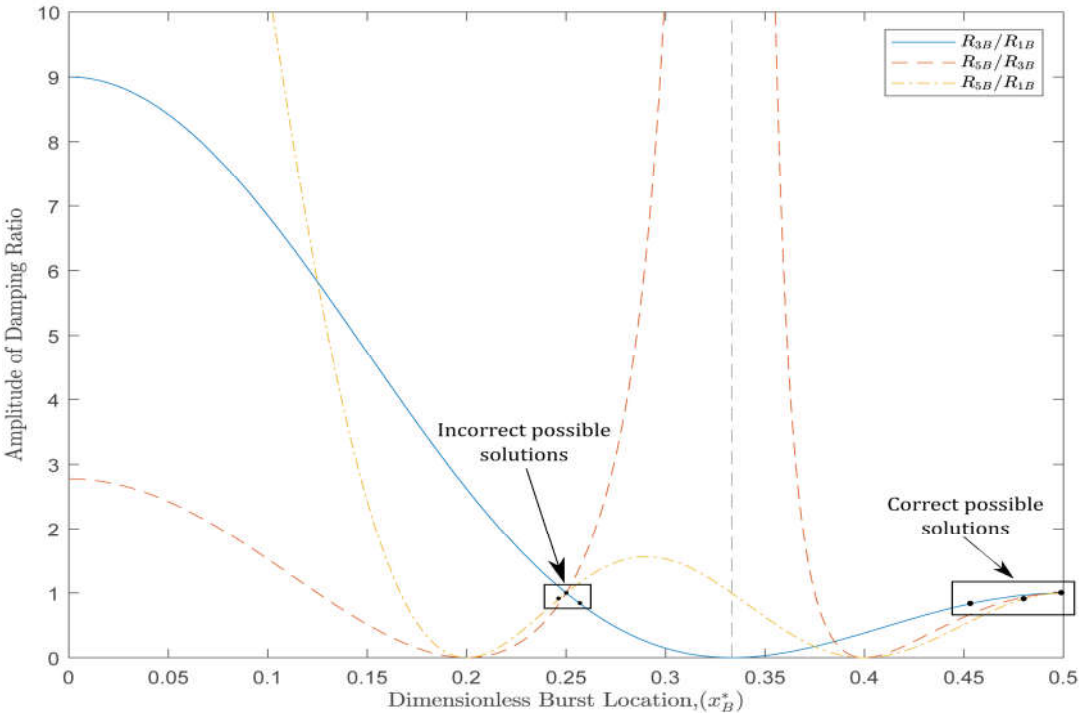

Figure 3.15: Damping ratios for the experimental analysis (Case 5)

The damping ratios are calculated as $\frac{R_{3B}}{R_{1B}} = 0.8343$, $\frac{R_{5B}}{R_{3B}} = 0.9998$, and $\frac{R_{5B}}{R_{1B}} = 0.9081$, corresponding to the dimensionless burst location $\hat{x_B^*} = 0.453$, $\hat{x_B^*} = 0.499$, and $\hat{x_B^*} = 0.48$ respectively by applying these three ratios in Figure 3.15. Averaging them gives the dimensionless burst location $\hat{x_B^*} = 0.4773$. Applied to the real pipeline, the burst location $\hat{x_B^*} = 0.4773$ should be doubled, and so becomes $x_B^* = 0.9546$. Thus the calculated relative cross-sectional area is $\frac{C_d A_B}{A_p} = 2.0055 \times 10^{-3}$. Both the resultant dimensionless burst location and the relative cross-sectional area are close to the actual values of 0.9951 and 2.12×10^{-3}. The corresponding errors are 4.05% and 5.4% respectively based on the sensitivity analysis in Wang et al. (2002). The results of Case 5 verify both the theoretical model for burst detection and the UFWH model. For the damping ratio magnitudes smaller than unity, there will be two possible solutions.

The results of Case 5 also indicate another burst location in the pipeline at $\hat{x}_B^* = 0.25$. Examination of the boundary reflections from the burst allows the correct location to be determined for these low damping ratios, which means only the correct burst location can provide the boundary reflections that fit the experimental data.

In order to verify the applicability of the technique outlined in this paper in terms of different burst and measurement locations experimentally, Case 6 was conducted. In Case 6, the burst location was changed from B_1 to B_2 with the dimensionless location $x_B^* = 0.51$, and the measurement location is changed from P_1 to P_2, while all other parameters and the location of the sensor remain the same as for Case 5. The burst was simulated to happen at approximately 0.1 s, the total testing time was 3 s, and the measured time trace is shown in Figure 3.16. By repeating the data analysis process in Case 5, the total damping rates of the first, third, and fifth harmonic components are plotted in Figure 3.17, and the friction and burst damping are shown in Table 3.4.

Table 3.4: Damping of Case 6

Damping Type	$n=1$	$n=3$	$n=5$
Total damping of the data	0.055	0.117	0.096
Actual friction damping	0.012	0.022	0.029
Burst damping	0.043	0.095	0.067

The calculated damping ratios are $\frac{R_{3B}}{R_{1B}} = 2.2093$, $\frac{R_{5B}}{R_{3B}} = 0.7053$, and $\frac{R_{5B}}{R_{1B}} = 1.5581$, which correspond to $\hat{x}_B^* = 0.211$, $\hat{x}_B^* = 0.2434$, and $\hat{x}_B^* = 0.287$, respectively. Repeating the same location and relative cross-sectional area calculation procedure provides the determined dimensionless burst location $x_B^* = 0.4943$ and relative burst cross-sectional area $\frac{C_d A_B}{A_p} = 2.1587 \times 10^{-3}$. The corresponding errors are 1.57% and 1.82%, according to the sensitivity analysis in Wang et al. (2002). The analysis of the two conducted experimental tests verifies the technique outlined in this paper, and assesses the applicability of the technique at different burst and measurement locations. The resultant location errors are smaller than the burst size errors in the conducted experimental verifications, which supports

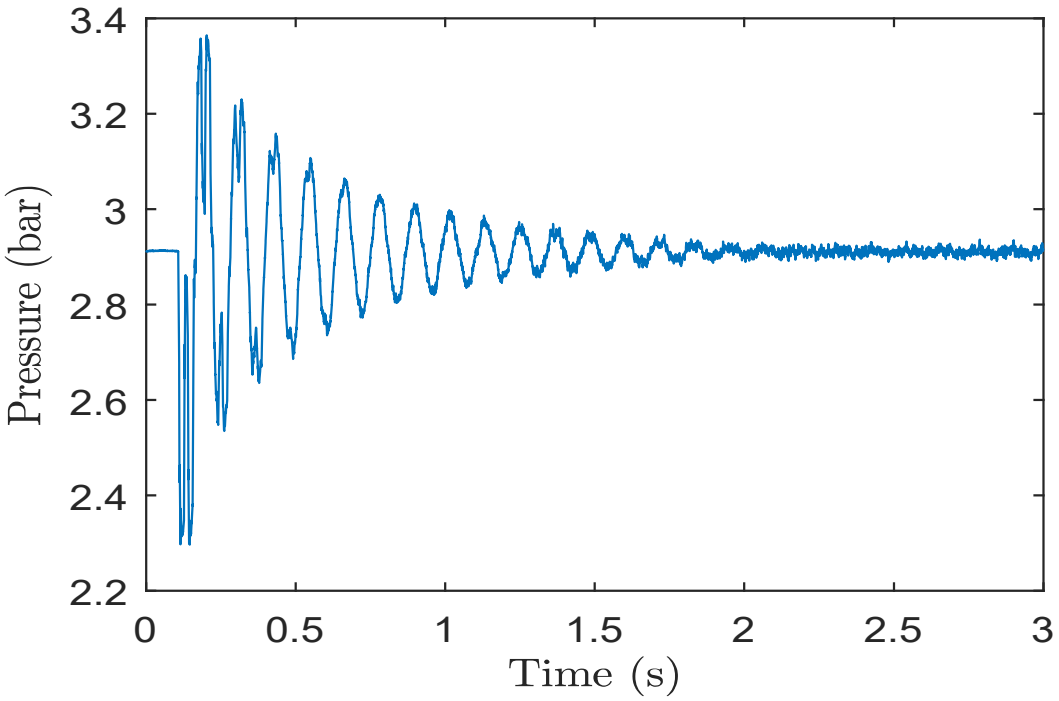

Figure 3.16: Experimental results (Case 6)

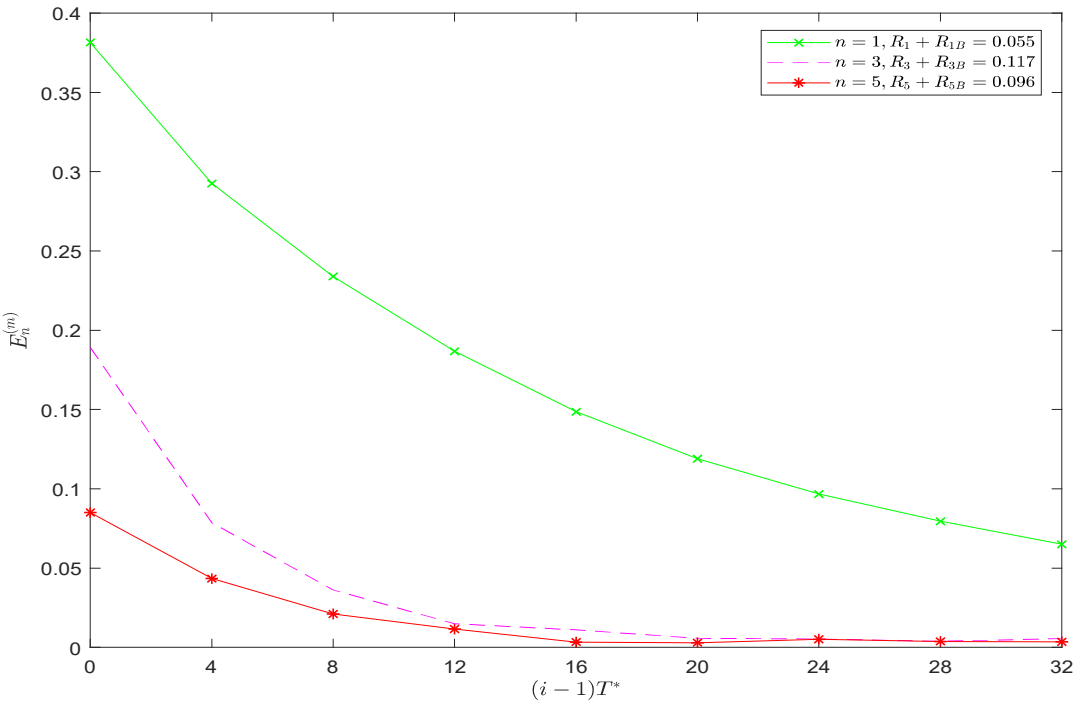

Figure 3.17: Damping rates of experimental data (Case 6)

the concept that the burst localization requires more accuracy than the burst size quantification in practice. Moreover, the resultant errors are in the range of the sensitivity analysis in Wang et al. (2002).

During the process of the experimental tests, the bursts were simulated by opening the electronically-controlled solenoid valves. Since the applied solenoid valves were opened quickly, the generation time of the bursts was neglected. However, in practice, the pipeline bursts are usually generated by the material failure or external damage of the pipeline instead of electronically-controlled solenoid valves. This indicates that the size of the burst may continue to increase after emerging, which means that the transient generation cannot be treated as an instantaneous process. Therefore, the transient generation takes place over a longer time period. Hence, the bandwidth of the injected signal may be decreased, or equivalently, the wavelength of the injected signal may be increased. Consequently, the generated transient waves may not be sharp, creating an excitation of low bandwidth (Keramat et al., 2019; Keramat and Zanganeh, 2019). In the research by Keramat et al. (2019), and Keramat and Zanganeh (Keramat and Zanganeh, 2019), the direct analysis of reflections from the leak when using a separate transient source, shows that the localization error is proportional to the transient generation time. However, the technique outlined in this paper is designed to utilize the damping behavior of the low-frequency components of the signal. Only the first three resonance responses were utilized in the conducted verification scenarios, indicating that the maximum required frequencies that should be present in the signal are $\frac{3a}{2L}$ and $\frac{5a}{4L}$ for RPR and RPV systems respectively. Additionally, the maximum analyzed frequency components of the signal are at 1.5 Hz and 1.25 Hz for RPR and RPV systems respectively in the numerical studies, and at 44.1 Hz in the experimental studies. The transient generation time is less critical to the technique outlined in this paper. The burst can still be located accurately under the conditions of a slow transient generation process.

3.7 Conclusion

The damping caused by both the friction and the bursts exists in the transients of the pressure head. The steady friction damping can be calculated by using its equation and is independent of the transient signal. However, the actual friction damping contains the unsteady friction damping and is dependent on the transient and the type of generation of the transient. The actual and unsteady friction damping are different for different harmonic components of the signal. They can be obtained successfully by using the validated UFWH model. In addition, it is shown in this paper that the unsteady friction damping caused by the burst is larger than the same quantity caused by the valve closure. By subtracting the actual friction damping from the total damping resulting from the Fourier analysis of the signal, the burst damping can be determined successfully. The burst damping is useful for determining the presence of the burst, locating the burst, and quantifying its cross-sectional area. The burst can be detected, located, and quantified with the location errors of $1\% - 1.5\%$ numerically and $1.57\% - 4.05\%$ experimentally. Moreover, the proposed technique is capable of detecting, locating, and quantifying burst at different bursts and measurement locations.

The analytical model indicates that the damping of the fluid transient based on the MOC is applicable for burst detection, localization, and quantification. The steady friction damping and the burst damping are exponential for each harmonic component. The theoretical model has been verified by both the numerical studies and the experimental tests. The technique presented in this paper has the advantage of being compared with the previously-explored MOC-based method, since the technique presented in this paper does not require a manually generated transient. In addition, the experimentally verified UFWH model is capable of determining both the actual and the unsteady friction damping, indicating that the actual friction damping can be obtained numerically in prac-

tice for any burst condition. By continuing to apply the UFWH model and analyzing the measured data, the burst can be possibly detected, localized, and quantified under the condition of continuous real-time monitoring. Although the technique presented in this paper is simple to apply, and has significant advantages, the generality of this technique is limited. This technique can only be applied under burst conditions on a single pipeline, since it requires the occurrence of the burst as the source of the transient, indicating that it will have difficulties in detecting very small leaks that develop slowly without an eruption. The complexity of a pipe system, such as branches, loops, and demands will bring difficulties to the application of this technique, because transients caused by these factors will be difficult to distinguish from the bursts. A transient generated by practical and sudden water use in the pipeline system will be difficult to distinguish from a burst due to it having the same pressure wave generation mechanism. However, the burst will become a leak that exists all the time, which is different from water use that may stop after a certain time. Moreover, the locations of the possible water use will often be known in an established water supply pipeline system, and can therefore be used to distinguish the burst from normal water use, based on the determined transient location by applying the technique outlined in this paper.

Chapter 4

Approach for Near-Real-time Pipe Burst Detection, Localization, and Quantification with Low Data Transmission and Sampling Rates

(Journal Paper 2)

Xiao-xuan Du, Wei Zeng, Martin F. Lambert, Lei Chen, and Eric Jing Hu

Published in *Journal of Water Resources Planning and Management*

10.1061/(ASCE)WR.1943-5452.0001380

Statement of Authorship

Title of Paper	Approach for near-real-time pipe burst detection, localization, and quantification with low data transmission and sampling rates
Publication Status	✓ Published ☐ Accepted for Publication ☐ Submitted for Publication ☐ Unpublished and Unsubmitted work written in manuscript style
Publication Details	Du, X.-x., Zeng, W., Lambert, M. F., Chen, L., and Jing Hu, E. (2021). Approach for near-real-time pipe burst detection, localization, and quantification with low data transmission and sampling rates. Journal of Water Resources Planning and Management, 147(7):04021032.

Principal Author

Name of Principal Author (Candidate)	Xiaoxuan Du		
Contribution to the Paper	Conception and design of project Analysis and interpretation of research data Drafting the paper		
Overall percentage (%)	75%		
Certification:	This paper reports on original research I conducted during the period of my Higher Degree by Research candidature and is not subject to any obligations or contractual agreements with a third party that would constrain its inclusion in this thesis. I am the primary author of this paper.		
Signature		Date	14/01/2022

Co-Author Contributions

By signing the Statement of Authorship, each author certifies that:

i. the candidate's stated contribution to the publication is accurate (as detailed above);
ii. permission is granted for the candidate in include the publication in the thesis; and
iii. the sum of all co-author contributions is equal to 100% less the candidate's stated contribution.

Name of Co-Author	Wei Zeng		
Contribution to the Paper	Conception and design of project Analysis and interpretation of research data Critically revising the paper		
Signature		Date	19/01/2022

Name of Co-Author	Martin F. Lambert		
Contribution to the Paper	Conception and design of project Analysis and interpretation of research data Critically revising the paper		
Signature		Date	19/1/2022

Please cut and paste additional co-author panels here as required.

Name of Co-Author	Lei Chen		
Contribution to the Paper	Revising the paper critically Conception and design of project		
Signature		Date	18/01/2022

Name of Co-Author	Eric Jing Hu		
Contribution to the Paper	Revising the paper critically Conception and design of project		
Signature		Date	18/1/2022

Abstract

The purpose of the paper is to present an approach for pipe burst detection, localization, and cross-sectional area quantification, based on the changes in the discrete harmonic spectrogram and analysis of damping of fluid transients. The amplitude of each resonance response of the burst-induced transient wave in each analyzed time window in the spectrogram is damped differently because of the presence of the burst. A pressure signal processing algorithm for pipe burst detection and estimation has been developed by the authors to explore this specific type of analysis, in conjunction with a predefined gap between each window. Since the window gap can be set to be equal to the data transmission and sampling rates in the analysis to detect and estimate the burst, it can be applied during real-time data monitoring. Unlike other hydraulic transient-based detection methods, the proposed algorithm only requires the Nyquist frequency of the third resonance response as the data transmission and sampling rates, which are significantly lower than the same quantities in commonly used data acquisition systems. The algorithm has been verified both numerically and experimentally.

4.1 Introduction

All pipeline systems require an inspection process of their continuous working cycle (Anderson and Anderson, 2011; Berglund et al., 2020; Billmann and Isermann, 1987; Bohorquez et al., 2020; Hovey and Farmer, 1993; Khan and Abbasi, 1999; Stephens et al., 2020; Wang et al., 2020; Zeng et al., 2020). Different techniques for pipe leak/burst detection have been proposed, such as the transient damping method (Wang et al., 2002), frequency response diagram analysis (Gong et al., 2013a; Lee et al., 2008; Vítkovskỳ et al., 2011), time domain reflectometry methods (Cataldo et al., 2017; Misiunas et al., 2003), and real-time data-based methods (Ebina et al., 2011; Hutton and Kapelan, 2015a;

Parikh and Sundaresan, 2008).

Wang et al. (2002) and Nixon et al. (2006) researched a pipe leak detection technique based on the damping of fluid transients (DOFT) excited by the active operation of a valve. In this system, the amplitudes of the harmonic components (i.e., the resonance peaks) of the pressure wave in the frequency domain are damped differently because of the leaks. The amplitude of each harmonic component can be calculated by fitting the Fourier Series solution period by period: the exponential damping can then be determined. The location and cross-sectional area of the leak can be calculated using the determined damping. The relevant numerical and experimental verifications have been conducted by Wang et al. (2002), where the results verified the model with acceptable errors. Nixon et al. (2006) further explored this approach in terms of the validity range. The DOFT method has been applied for pipe burst detection, localization, and cross-sectional area quantification (referred to simply as quantification in the rest of the paper) in Du et al. (2020). Du et al. (2020) set out the research that extends the method in Wang et al. (2002) from proactive leak detection to passive burst detection.

The application of the direct results of fast Fourier transform (FFT) on the complete signal, based on the fluid transient, has been studied in detail (Gong et al., 2016b; Lee et al., 2008). Lee et al. (2005a; 2008) utilized the FFT-related technique for pipe leak detection through application of the Frequency Response Diagram (FRD). By comparing the resonance peaks on the FRD for a no-leak case with those of a leak case, the leak can be detected. Its location and size can be determined based on both the magnitude and the resonance peaks. Introducing persistent transient signals to extract the FFT with higher reliability was explored by Gong et al. (2018a; 2018b) and Lee et al. (2006). Duan (2018) explored the transient frequency response (TFR) technique for leak detection considering the effects of loop and branch.

Time domain reflectometry methods have been studied by several researchers (Cataldo et al., 2017; Misiunas et al., 2003). Based on the research by Cataldo et al. (2017), leaks can be successfully detected and localized by capturing the arrival time of the leak-induced transient pressure signal. In Misiunas et al. (2003), burst detection and localization were investigated by utilizing the time domain reflectometry technique with relatively high data transmission and sampling rates. The data sampling rate is the reciprocal of the time interval of two data points collected by a sensor. The data transmission rate is the rate that the data is transmitted over the system. It can be either equal to or less than the data sampling rate.

Burst detection techniques based on real-time data monitoring have been researched frequently (Ebina et al., 2011; Hutton and Kapelan, 2015a; Kang and Lansey, 2012; Parikh and Sundaresan, 2008). It has been verified that these techniques are capable of detecting the burst by capturing the transient generated by the burst. Furthermore, the detection process can be achieved once the burst occurs, since the signal is analyzed in real-time. Parikh et al. (2008), Ebina et al. (2011), and Hutton et al. (2015a) studied real-time data-based burst detection methods based on large scale online systems. However, these methods have difficulty in locating and quantifying the burst. The real-time data-based technique presented in Kang et al. (2012) has the ability to locate a burst based on the burst-induced transient signal captured by multiple sensors.

The following gaps exist in the reviewed literature. Firstly, the method in Du et al. (2020), which is an extension of Wang et al. (2002), requires a restricted length and gap in the analyzed time window in the analysis, which impedes its real application. Secondly, conventional transient-based burst detection methods, such as time domain reflectometry methods, normally require relatively high data transmission and sampling rates to obtain an acceptable spatial resolution, which leads to high cost of the pressure monitoring system.

In this paper, the mathematical derivation eases the restriction of the length and the gap of the analyzed time window. This allows the signal to be analyzed in real-time by letting the window gap equal the reciprocal of the data sampling rate. Every new data point that is acquired can then be processed one time step at a time. The proposed approach enables the use of low data transmission and sampling rates of the pressure monitoring system for burst detection, and thus reduces the cost of the pressure monitoring system.

In the following section, the mathematical modeling and its Fourier transform analysis are derived and presented. The procedures for burst detection, localization, and quantification are presented in the next section. Eleven corresponding numerical cases are followed by an experimental verification and, finally, the conclusion.

4.2 Mathematical Modeling

The mathematical model is built based on the general Fourier transform of the head disturbance solution when analyzing the signal window by window. The head disturbance solution was derived in Du et al. (2020). The mathematical modeling contains four major steps as indicated in Figure 4.1. The Fourier coefficients of the head solution are determined by fitting the general Fourier series to the head solution. The resultant Fourier coefficients are applied to the process of the Fourier transform of the head solution. The Fourier transform is completed by substituting the resonance responses. The final mathematical model is derived by generalizing the time range of the Fourier transform from a fundamental period of the signal to an arbitrary number.

In mathematical derivations, the following key assumptions are applied: the pipe wall is elastic; the unsteady friction damping on each harmonic component is

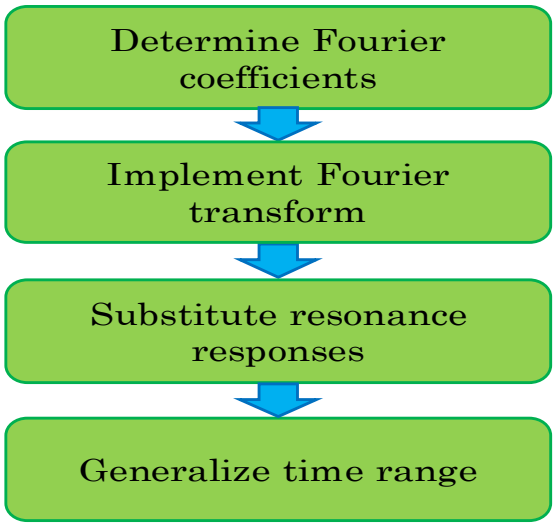

Figure 4.1: Logic of mathematical modeling

exponential; the fluid is slightly compressible; the flow is one-dimensional; the radial velocity is small, and the fluid velocity is much smaller than the wave speed.

The head dimensionless disturbance h^* caused by the burst, which is the measured signal from the pressure transducer divided by the reference head, was derived in Du et al. (2020) based on the work in Wang et al. (2002), and shown as

$$h^*(x^*,\ t^*) = \sum_{n=1}^{\infty} \left\{ e^{-(R+R_{nB})t^*} [A_n cos(n\pi t^*) + B_n sin(n\pi t^*)] sin(n\pi x^*) \right\} \quad (n = 1,\ 2,\ 3, \ldots) \tag{4.1}$$

where x^* and t^* in Eq. (4.1) are the non-dimensionalized distance along the pipe and the non-dimensionalized time respectively, using the following defini-

tions

$$h^* = \frac{h}{H_1},\ t^* = \frac{t}{L/a},\ x^* = \frac{x}{L} \tag{4.2}$$

where h is the head disturbance caused by the burst, H_1 is the reference head, which is the head measured at the boundary reservoir, t is the time, L is the length of the pipe, a is the wave speed, and x is the distance along the pipe.

$$R = R_{steady} + R_{unsteady} = \frac{f_{steady} L Q_0}{2aDA_p} + \frac{16\mu}{\rho D^2 A_p}[\frac{\partial Q}{\partial t} W(\tau)] \tag{4.3}$$

in which R, R_{steady}, and $R_{unsteady}$ are the actual (total), steady, and unsteady friction damping respectively, f_{steady} is the Darcy-Weisbach friction factors for steady friction damping, Q_0 is the initial flow rate, D is the inner diameter of the pipe, A_p is the cross-sectional area of the pipe, μ is the dynamic viscosity of fluid, ρ is the density of fluid, and $W(\tau)$ is the weight function, in which τ, which is time/frequency-dependent, is defined in Kjerrumgaard Jensen et al. (2018). It can be noted that the utilized unsteady friction damping in Eq. (4.3) is based on the Vardy and Brown transient unsteady friction model (Duan et al., 2012; Meniconi et al., 2014; Vardy and Brown, 1995; Zielke, 1968). The unsteady friction damping in this paper is determined by a computational process in Du et al. (2020), and it is frequency-dependent (i.e., different at different resonant frequencies). The term R_{nB} in Eq. (4.1) is the damping caused by the burst in the nth harmonic component, and can be expressed as

$$R_{nB} = K_B sin^2(n\pi x_B^*) \tag{4.4}$$

where x_B^* is the dimensionless location of the burst, and K_B is associated with

the characteristics of the burst and defined as

$$K_B = \frac{C_d A_B}{A_p} \frac{2ab}{(2gH_{B0})^{1-b}} \tag{4.5}$$

in which C_d is the burst discharge coefficient, A_B is the cross-sectional area of the burst, g is the gravity acceleration, and H_{B0} is the steady head at the burst location before the occurrence of the burst. The value of b is typically set to be 0.5 for a sharp orifice.

A_n and B_n are the Fourier coefficients, expressed as

$$A_n = 2\int_0^1 f(x^*)sin(n\pi x^*)dx^* \quad (n = 1,\ 2,\ 3,\ ...) \tag{4.6}$$

$$B_n = \frac{2}{n\pi}\int_0^1 g(x^*)sin(n\pi x^*)dx^* + \frac{(R+R_{nB})A_n}{n\pi} \quad (n = 1,\ 2,\ 3,\ ...) \tag{4.7}$$

where $f(x^*)$ and $g(x^*)$ are the initial conditions that are known piecewise functions, in the range $(0 \leq x^* \leq 1)$, and which are shown as

$$h^*(x^*,\ 0) = f(x^*),\ \ and\ \ \frac{\partial h^*(x^*,\ 0)}{\partial t^*} = g(x^*) \tag{4.8}$$

When analyzing the signal window by window with the window length t_a instead of every fundamental period of the signal, the amplitude of the nth harmonic component in each analyzed time window of the measured pressure sig-

nal is

$$E_n^{(m)} = E_n^{(1)} e^{-(R+R_{nB})(m-1)t_a^*} \tag{4.9}$$

where $E_n^{(m)}$ is the amplitude of the nth harmonic component in the mth window, $E_n^{(1)}$ is the amplitude of the first harmonic component in the mth window, and t_a^* is the dimensionless window length. The details of the derivation of Eq. (4.9) are shown in the Appendix.

4.3 A Discrete Harmonic Spectrogram Algorithm for Burst Detection, Localization, and Quantification

Based on Eq. (4.9), a short-term spectrogram of the measured pressure signal is capable of providing the amplitude of each harmonic component in each time window. When the real-time data acquisition speed and the data transmission rate allow the transmission of the data in the next window to be completed in a very short time, this approach will be able to be applied in real-time. Based on this specific limitation analysis, the window gap, d, which is the interval between the starting points of two contiguous windows, is applied, as shown in Figure 4.2.

Under the previously mentioned condition, when moving the window by a non-period window gap, d, Eq. (4.9) is now expressed as a more general form

$$E_n^{(m)} = E_n^{(1)} e^{-(R+R_{nB})(m-1)\frac{d^*}{t_a^*}t_a^*} = E_n^{(1)} e^{-(R+R_{nB})(m-1)d^*} \tag{4.10}$$

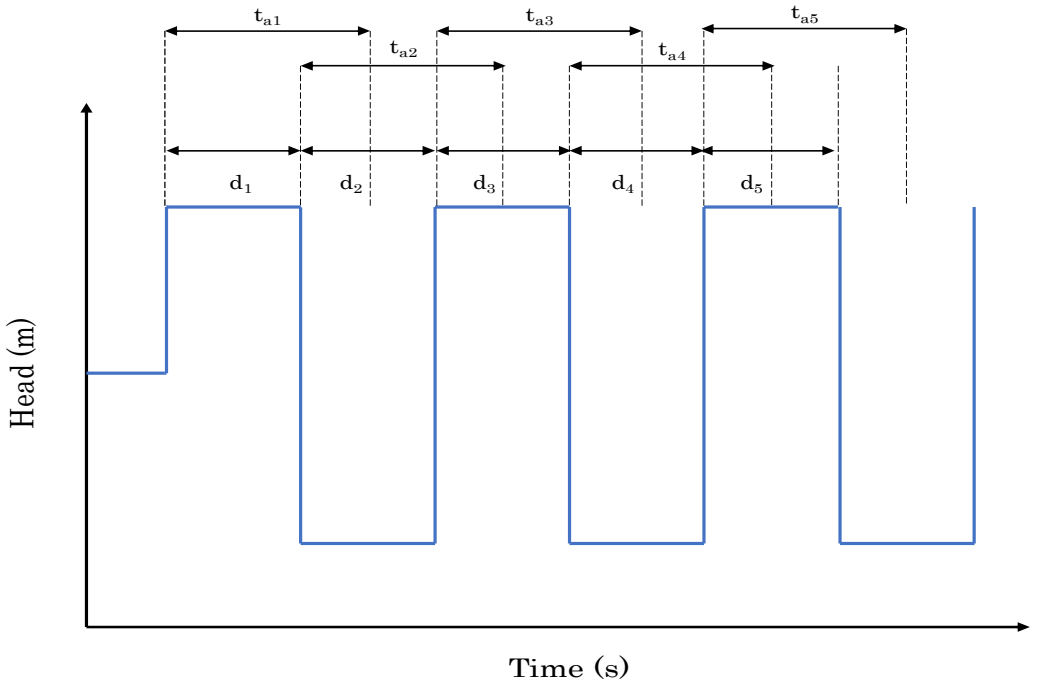

Figure 4.2: Example of analyzing signal window by window with window gap *d*

where d^* is the dimensionless window gap, and Eq. (4.9) is a special case when analyzing the data window by window, when $d = t_a$, thus $d^* = t_a^*$. Eq. (4.10) indicates that as long as the interval between the starting points of two contiguous windows is determined by the user, the summation of the friction and the burst damping can be calculated. In addition, an arbitrary and very small value of d allows the analyzed time window to be moved slightly to adapt to the real-time data acquisition speed. Specifically, when the value of d is equal to the real-time data acquisition speed (i.e., the window gap between two data points), real-time analysis becomes possible.

The presence of the burst can be confirmed by calculating the differently-damped amplitudes of the harmonic components from the generated discrete harmonic spectrogram of the signal according to Eq. (4.10). The dimensionless burst

location can be calculated based on the following equations

$$\begin{aligned} R_{n_1B} &= K_B sin^2(n_1 \pi x_B^*) \\ R_{n_2B} &= K_B sin^2(n_2 \pi x_B^*) \end{aligned} \tag{4.11}$$

where R_{n_1B} and R_{n_2B} are the burst damping of a pair of harmonic components when $n = n_1$ and $n = n_2$. By applying the quotient of R_{n_1B} and R_{n_2B}, the dimensionless cross-sectional area of the burst can be canceled, thus the resultant function depends on the dimensionless burst location alone, and is expressed as

$$\frac{R_{n_2B}}{R_{n_1B}} = \frac{sin^2(n_2 \pi x_B^*)}{sin^2(n_1 \pi x_B^*)} \tag{4.12}$$

The details of Eqs. (4.11) and (4.12) are presented in Du et al. (2020). Therefore, the dimensionless burst location can be calculated by solving Eq. (4.12). The details of the damping ratio $\frac{R_{n_2B}}{R_{n_1B}}$ are presented in Figures 4.3 and 4.4, corresponding to the reservoir-pipe-valve (RPV) and reservoir-pipe-reservoir (RPR) systems respectively. Note that since the application of Eq. (4.1) to an RPV system is achieved by adding an imaginary mirror part to the original RPV system, all the possible dimensionless burst locations on the imaginary mirror part are ignored. The relative cross-sectional area of the burst can then be determined by substituting the resultant dimensionless burst location and burst damping into Eqs. (4.4) and (4.5), thus the relative cross-sectional area of the burst is expressed as

$$C_d A_B = \frac{R_{nB} A_p (2gH_{B0})^{1-b}}{2absin^2(n\pi x_B^*)} \quad (n = 1,\ 2,\ 3,\ ...) \tag{4.13}$$

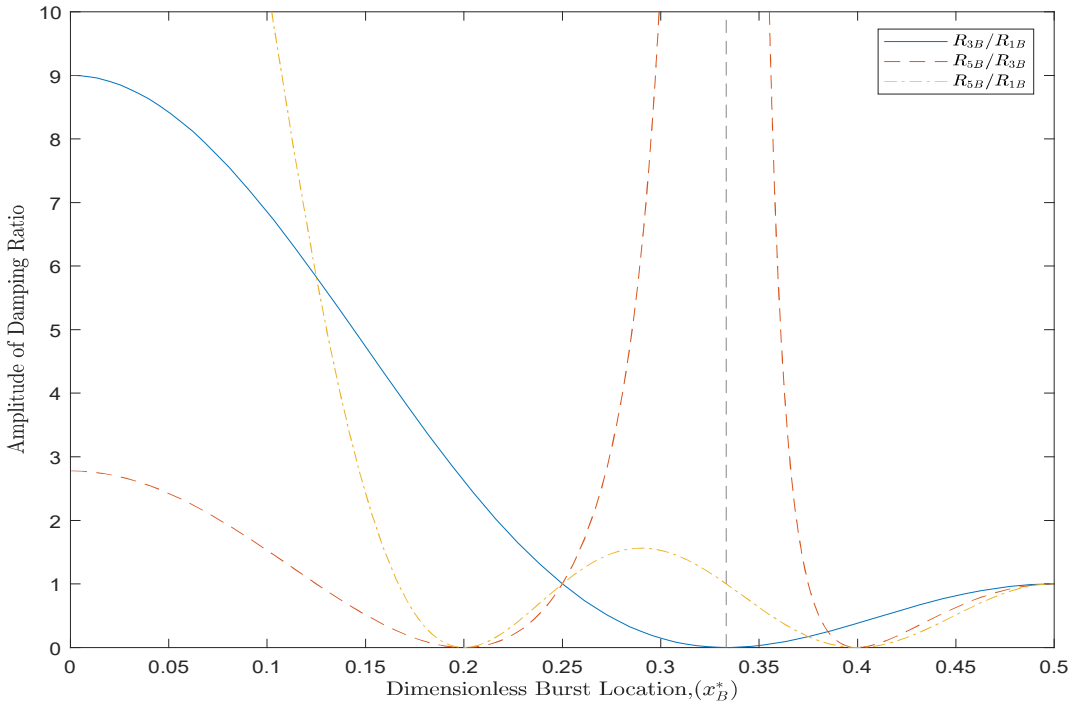

Figure 4.3: Damping ratio for the RPV system

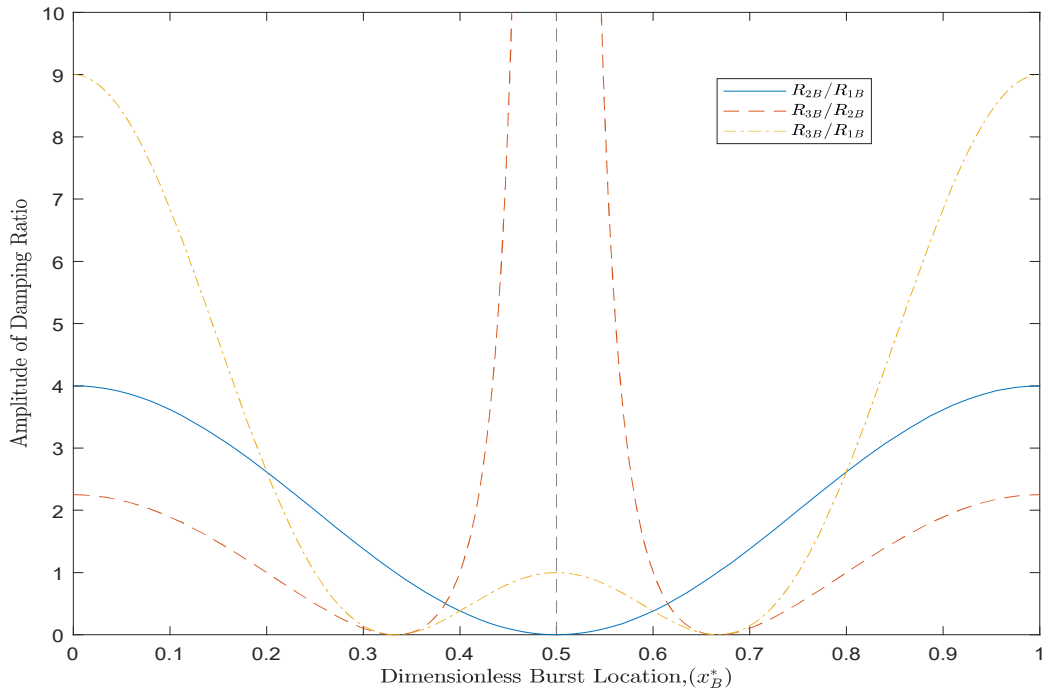

Figure 4.4: Damping ratio for the RPR system

The actual cross-sectional area of the burst can then be determined by knowing the burst discharge coefficient C_d and cross-sectional area of the pipe A_p. It should be noted that the minimum required data transmission and sampling rates of the algorithm need to be equal to the Nyquist frequency of the minimum required harmonic component based on Eq. (4.12). Three damping ratios may be needed for high accuracy to calculate the average value of these three. This fact indicates that the harmonic component that reflects the third resonance response in the discrete harmonic spectrogram of the signal is the minimum required harmonic component. Specifically, the minimum required data transmission and sampling rates of the RPV and RPR systems are $10 \times f_0$ and $6 \times f_0$ respectively, where f_0 is the fundamental frequency of the system, since all the amplitudes of all the even harmonic components are close to zero for RPV systems.

In summary, the algorithm in this paper is capable of detecting, locating, and quantifying the burst by producing the discrete harmonic spectrogram of the signal. The window can be moved with a short window gap according to the actual real-time data acquisition speed, which reveals the applicability of the technique in the area of real-time data monitoring. Additionally, the minimum required data transmission and sampling rates of the algorithm only need to be the Nyquist frequency of the third resonance response in the discrete harmonic spectrogram of the signal. This provides an insight into how to utilize low data transmission and sampling rates.

In this approach, the burst itself is the transient source, and the occurrence of a burst causes a sudden pressure drop. While positive pressure disturbance is generated manually by a fast valve closure in Wang et al. (2002), at a different location from the leak.

The frequency analysis algorithm of the approach presented in this section has some similarities to the short-term Fourier transform (STFT). However, since

only the first three resonance responses in the low-frequency range are desired, the sliding discrete Fourier transform (SDFT) is the preferred approach (Jacobsen and Lyons, 2003). The impact of the spectral leakage caused by the signal discontinuity at the edges within each window is critical because of the periodic nature of discrete Fourier transform (DFT) (Lathi, 1998; Smith, 1997). The DFT views the right boundary of the acquired signal wrapping around and connecting to its left boundary within each window (Smith, 1997). Therefore, the spectral leakage occurs when the signal discontinues at the edges within each window (Schoukens et al., 2006; Wickramarachi, 2003). It may reduce the accuracy of the DFT of the signal within each window. Therefore, the window length t_a should be determined based on the principle of ensuring the continuity at the edges within each window of the signal. Additionally, this specific analysis indicates that the window length t_a can be a random length, but the integer multiples of the fundamental period of the signal are always the most appropriate solutions. In order to quantify the discontinuity at the edges within each window of the signal, a window discontinuity index (WDI) is introduced. The WDI is defined as the difference between the left and the right end points of any window, divided by the reference pressure/head of the system. The WDI of the first window, the first window discontinuity index (FWDI), is selected throughout the paper as an example. FWDI is inversely proportional to the accuracy of the amplitude of the DFT, thus it is inversely proportional to the accuracy of the resultant dimensionless burst location and relative cross-sectional area.

Eight numerical verifications of the algorithm are found by testing the t_a, d, data transmission rate, sampling rate, and different configurations, and are presented in the next section. Furthermore, three additional numerical scenarios regarding the slow transient generation process have been conducted.

4.4 Numerical Verification

A series of numerical verification scenarios have been conducted, where eight numerical verification cases were conducted to verify the algorithm outlined in this paper, and the three additional cases are used to examine the situation where the burst transient generation process is slow. The purpose of the last three cases is to illustrate the validity of the algorithm under the conditions of a slowly developing burst.

The applied pipeline system from the first to the seventh scenarios, referred to as Cases 1-7, respectively, is the RPV system. The corresponding system configuration is shown in Figure 4.5. The applied system of the eighth scenario, referred to as Case 8, is the RPR system, and the system configuration is shown in Figure 4.6. The downstream valve can be controlled manually. Note that the fundamental period of the applied RPV and RPR systems are $\frac{4L}{a} = 4$ s and $\frac{2L}{a} = 2$ s, respectively. Three additional scenarios have been implemented to verify the algorithm under the conditions of slowly developing burst, referred to as Cases 9-11. The applied configuration is the RPV system as is applied in the former cases. Steady friction is considered in all the cases. The data transmission and sampling rates from Cases 1-4, and Cases 9-11 are 100 Hz, while they are reduced to smaller values in Cases 5-8. All the critical parameters of the conditions and results of each case are shown in Tables 4.1 and 4.2.

In Cases 1-7, the transient event is introduced by initiating a burst with the dimensionless location $x_B^* = 0.25$ and the relative cross-sectional area $\frac{C_d A_B}{A_p} = 0.002$. The initiation of the burst is achieved by opening the side discharge valve suddenly in each scenario. The pressure signal is measured at the dimensionless location $x^* = 0.75$. The total test time of each scenario is 60 s, and the burst occurred at 0.3 s. Since the side discharge valve is simulated to be opened instantaneously, the time delay caused by opening the valve can be neglected.

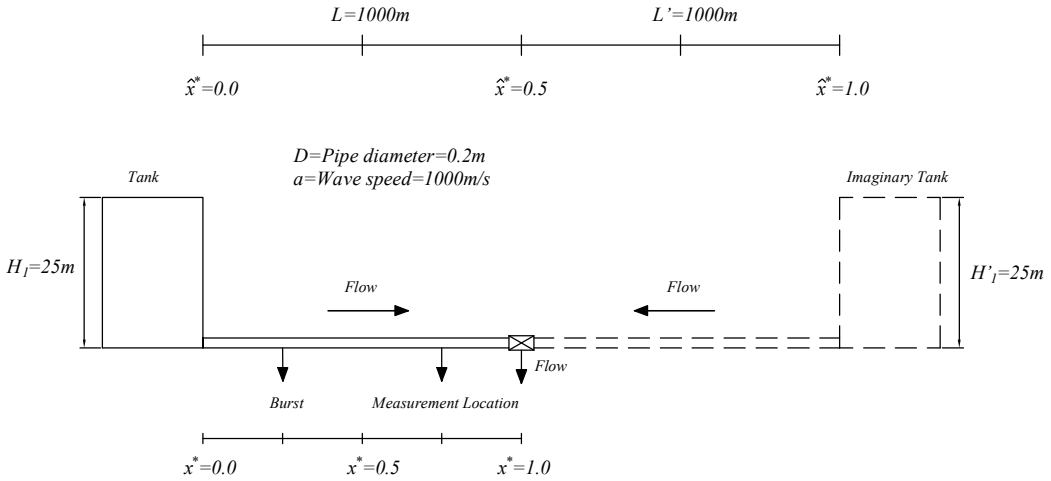

Figure 4.5: RPV system configuration

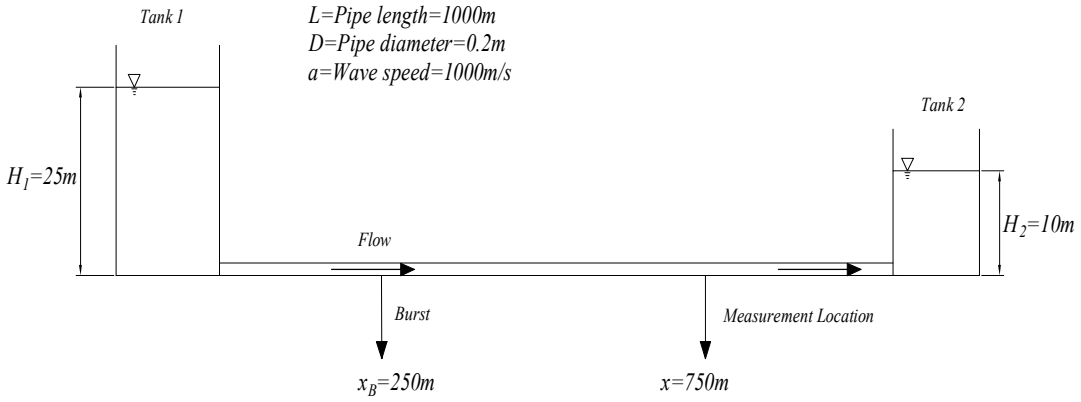

Figure 4.6: RPR system configuration

The simulated bursts in all the scenarios are treated as a sharp orifice, indicating that the value of b in Eqs. (4.5) and (4.13) is 0.5. The wave speed and the inner diameter of all the scenarios are set to be $a = 1000$ m/s and $D = 0.2$ m. The initial flow rate is set to be $Q_0 = 0.001$ m^3/s by letting the downstream valve be partially opened, and the Darcy-Weisbach friction factor is set to be $f = 0.0302$. The measured time trace from Cases 1-4 is shown in Figure 4.7.

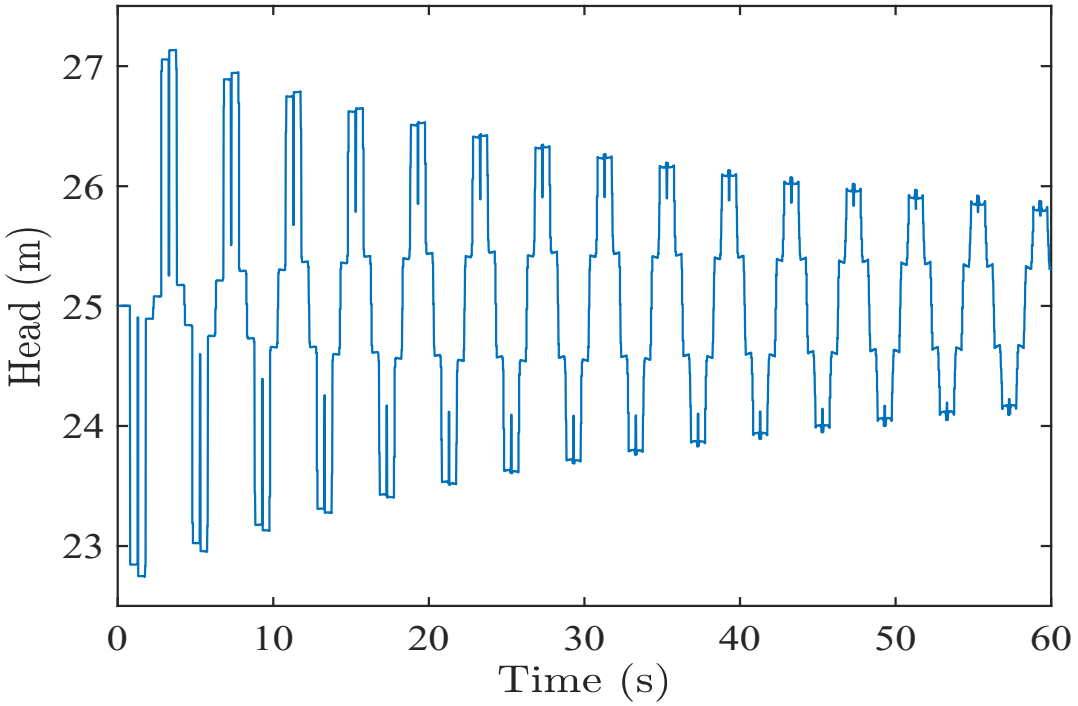

Figure 4.7: Time trace from Cases 1-4

4.4.1 Sensitivity Analysis of the Window Length

Cases 1 and 2 were conducted to verify the fact that the discontinuity of the signal at the edges within each window affects the accuracy of the algorithm negatively, no matter whether the length of the analyzed time window, t_a, is larger or smaller than the fundamental period of the pipeline system. The selected values of t_a and d in Cases 1 and 2 are $t_a = 2.3$ s and $d = 4.8$ s, and $t_a = 4.3$ s and $d = 4.8$ s, respectively.

The corresponding discrete harmonic spectrograms of the first three resonance peaks are plotted in waterfall form focusing on particular frequencies, and are shown in Figures 4.8 and C.1 (Harris, 1992; Redd et al., 2019; Zhang et al., 2017). From Figure 4.8, the changes of the damped amplitudes at the first three resonance frequencies over time are also shown. Additionally, the figure also compares the signal strength across the different resonance frequencies. Applying Eq. (4.10) to the amplitudes at the first three resonance frequencies in the generated discrete harmonic spectrograms provides the total damping as $R_{1B}+R_{steady}=0.0156$, $R_{3B}+R_{steady}=0.0216$, and $R_{5B}+R_{steady}=0.0216$ for Case 1, and $R_{1B}+R_{steady}=0.0156$, $R_{3B}+R_{steady}=0.0346$, and $R_{5B}+R_{steady}=0.0326$ for Case 2. By subtracting the steady friction damping, which is calculated as $R_{steady}=0.0024$ from Eq. (4.3), the burst damping is calculated as $R_{1B}=0.0132$, $R_{3B}=0.0192$, and $R_{5B}=0.0192$, and $R_{1B}=0.0132$, $R_{3B}=0.0322$, and $R_{5B}=0.0302$ for Cases 1 and 2 respectively. By averaging the values of $\frac{R_{3B}}{R_{1B}}$, $\frac{R_{5B}}{R_{3B}}$, and $\frac{R_{5B}}{R_{1B}}$, and applying the damping ratios shown in Figure 4.3, the directly determined dimensionless burst locations for Cases 1 and 2 are $\hat{x_B^*}=0.17295$ and $\hat{x_B^*}=0.16135$ respectively. Due to the imaginary mirror part of the system

$$\hat{x_B}^* = \frac{x_B}{L+L'} = \frac{x_B}{2L} = \frac{x_B^*}{2} \tag{4.14}$$

thus,

$$x_B^* = 2\hat{x_B}^* \tag{4.15}$$

The determined dimensionless burst locations on the real system for Cases 1 and 2 are $x_B^*=0.3459$ and $x_B^*=0.3227$ respectively. Accordingly, the relative cross-sectional areas for Cases 1 and 2 are $\frac{C_d A_B}{A_p}=0.0011$ and $\frac{C_d A_B}{A_p}=9.5006\times 10^{-4}$ respectively, utilizing Eq. (4.13). Based on the error analysis in Wang

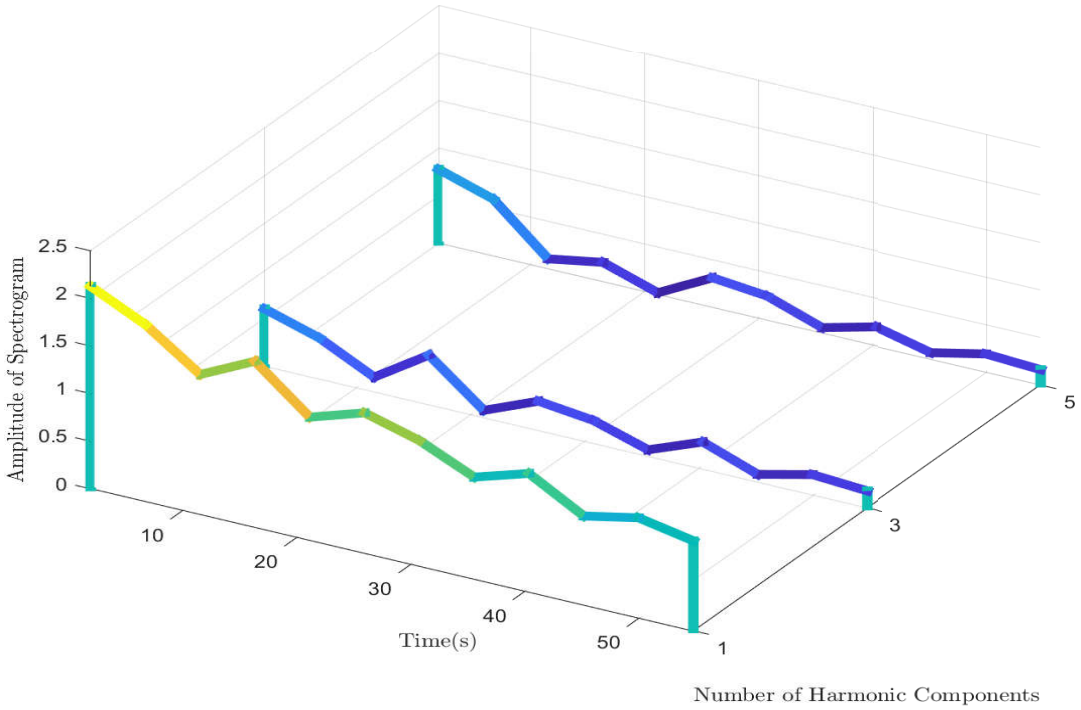

Figure 4.8: Discrete harmonic spectrogram from Case 1

et al. (2002), the burst location errors are 9.59% for Case 1 and 7.27% for Case 2, and the cross-sectional area errors are 45% for Case 1 and 52.5% for Case 2. It can be seen that both the burst location and the cross-sectional area errors are large. This unexpected result can be explained by calculating the FWDI for both cases. They are calculated as 8.2% and 7.92% for Cases 1 and 2 respectively. The FWDI for Cases 1 and 2 are significant, indicating that the accuracy of the resultant discrete harmonic spectrogram has been reduced because of the spectral leakage.

In order to ensure the continuity of the signal at the edges within each window when utilizing the algorithm, any integer multiple of the fundamental period of the pipeline system can be assigned to t_a. As an example, Case 3.1 was conducted with the condition $t_a = 20$ s, which is selected as $5 \times T$, where T is the fundamental period of the pipeline system, and $d = 4.8$ s. The resultant discrete harmonic spectrogram is shown in Figure C.2. Replicating the procedures applied to Cases 1 and 2 provides the determined dimensionless burst location

$x_B^* = 0.2473$, and the relative cross-sectional area $\frac{C_d A_B}{A_p} = 0.002$. The corresponding errors are 0.27% and 0% respectively. The FWDI is calculated as 2%. The result shows that the accuracy of the algorithm is enhanced as the FWDI is decreased by selecting the value of t_a as the integer multiple of the fundamental period of the system. The fundamental period of the pipeline system can be obtained by equations, observing the signal, or the ringdown technique in Baibhav et al. (2018) and Giesler et al. (2019). In the research in Baibhav et al. (2018) and Giesler et al. (2019), the superposition of the fundamental mode plus the first two overtones of the ringdown model provides an accurate representation of the fundamental frequency of the system. Other better solutions than integer multiples of the fundamental period of the system could exist, which provide a small value of FWDI, and these solutions can be determined according to the actual features of the data in practice. Two additional tests, which are indicated as Case 3.2 and 3.3, have been conducted to illustrate the accuracy of the approach in Case 3 when t_a equals T and $2T$, respectively. The corresponding conditions and results are included in Tables 4.1 and 4.2, respectively.

4.4.2 Verification of Real-time Data Monitoring Capability

In terms of applying the algorithm to the area of real-time data monitoring, the window gap between the current and the next windows should be relatively small to adapt to the actual data acquisition speed. Therefore, Case 4 was conducted with a small value of window gap, and the values of t_a and d are $t_a = 20$ s and $d = 0.01$ s. The generated discrete harmonic spectrogram is shown in Figure C.3. Replicating the same sequences in the previous scenarios provides the determined dimensionless burst location $x_B^* = 0.2481$, and the relative cross-sectional area $\frac{C_d A_B}{A_p} = 0.002$. The burst location and relative cross-sectional area errors are 0.19% and 0%. The results from Case 3.1 illustrate the fact that the algorithm can be applied successfully with a small value of d, which is equal to the data acquisition speed, since each data point is ac-

quired every $1/100$ Hz$= 0.01$ s. This specific analysis shows that it is possible to utilize the algorithm in the area of real-time data monitoring, as long as the applied value of d is selected to be equal to the data acquisition speed.

4.4.3 Verification of Low Data Transmission and Sampling Rates

Since only the first three resonance responses are utilized in this algorithm, it is reasonable for the data transmission and sampling rates to be reduced to the Nyquist frequency of the third resonance peak in the discrete harmonic spectrogram. In order to verify this specific analysis, Cases 5 and 6 were implemented. The data transmission rate is reduced to the Nyquist frequency of the third resonance response in Case 5, then the data sampling rate is reduced to the same value in Case 6. In Case 5, the data transmission rate is $2 \times 5 \times f_0 = 2.5$ Hz, given that all the even harmonic components are negligible for an RPV system, while all other parameters remain the same as for Case 4. The fundamental frequency of the pipeline system, f_0, can be determined by the same methods mentioned in the previous section. It should be noted that, although the value of d, 0.01 s, is smaller than the reciprocal of the data transmission rate 0.4 s, signal processing is still achievable, since the data sampling rate is 100 Hz. The time trace transmitted from the sensor at 2.5 Hz is shown in Figure 4.9, and the corresponding discrete harmonic spectrogram is shown in Figure C.4. By replicating the same determination sequences, and ignoring the resultant dimensionless burst locations on the imaginary part of the RPV system, which is shown in Wang et al. (2002) and Du et al. (2020), the resultant dimensionless burst location and the relative cross-sectional area are $x_B^* = 0.2282$ and $\frac{C_d A_B}{A_p} = 2.03 \times 10^{-3}$ respectively, with the errors being 2.18% and 2%. It can be observed that the algorithm can be utilized successfully with acceptable accuracy under the condition of applying the Nyquist frequency of the third resonance peak as the data transmission rate. In addition, the results from Case 5 further verify the potential availability of the algorithm in the area

of real-time data monitoring, since the window gap, 0.01 s, between two contiguous windows, is the same as the data acquisition speed, 0.01 s, which is the reciprocal of the sampling rate.

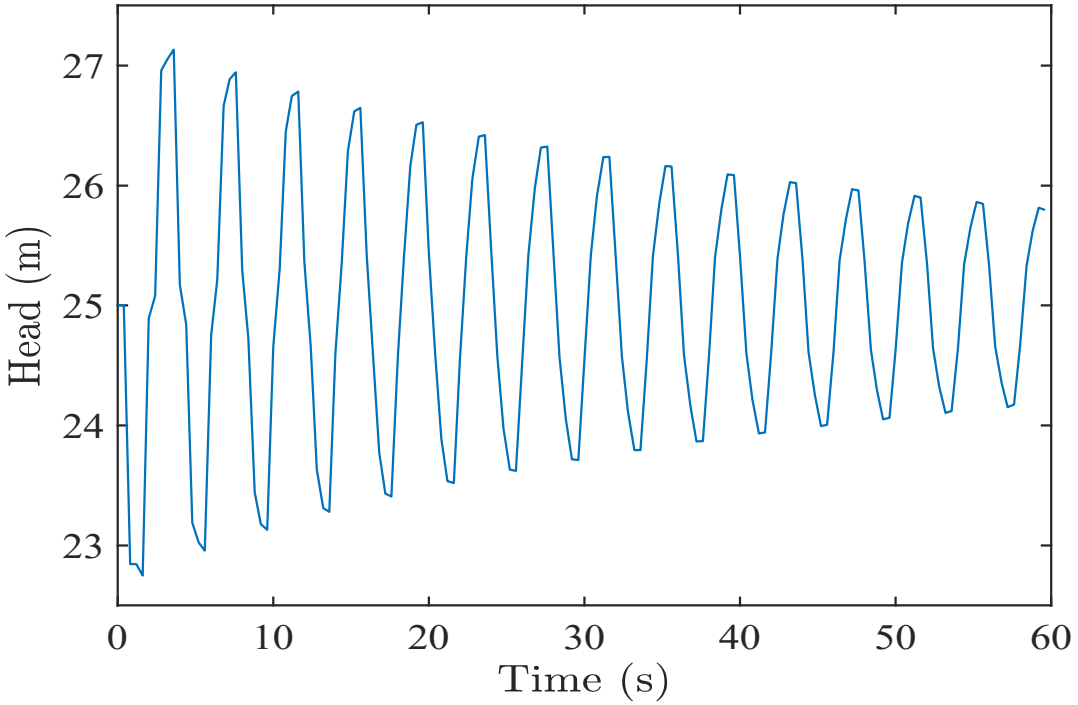

Figure 4.9: Time trace from Cases 5 and 6

Case 6 was conducted to illustrate that not only the data transmission rate but also the sampling rate can be reduced to the Nyquist frequency of the third resonance response in the discrete harmonic spectrogram. In Case 6, the data transmission and sampling rates are both set to be $2 \times 5 \times f_0 = 2.5$ Hz, and the window gap is set to be $d = 0.4$ s, since it is impossible for it to be smaller than the data acquisition speed, while all the other parameters remain unchanged. The re-sampled time trace is exactly the same as that shown in Figure 4.9, and the resultant discrete harmonic spectrogram is shown in Figure C.5. The determined dimensionless burst location and relative cross-sectional area are $x_B^* = 0.2596$ and $\frac{C_d A_B}{A_p} = 0.002$ respectively. The corresponding errors are 0.96% and 0%, which indicate that the algorithm has been utilized successfully with high accuracy. The results from Case 6 illustrate the successful application of the algorithm, both with a low sampling rate and potential application to the

area of real-time data monitoring.

Although Cases 5 and 6 verify the minimum required data transmission and sampling rates of the algorithm outlined in this paper, these two rates are generally set to be both equal to each other, and larger than the Nyquist frequency of the required frequency response in practice. Therefore, Case 7 was implemented with data transmission and sampling rates of $5 \times 5 \times f_0 = 6.25$ Hz, which are $2.5\times$ the Nyquist frequency of the third resonance response in the discrete harmonic spectrograms. The window gap is set to be $d = 0.16$ s, which is the same as the data acquisition speed. All other parameters remain the same as for the previous cases. The re-sampled and transmitted time trace is shown in Figure 4.10, and the corresponding discrete harmonic spectrogram is shown in Figure C.6. The resultant dimensionless burst location and relative cross-sectional area are $x_B^* = 0.2475$ and $\frac{C_d A_B}{A_p} = 0.002$ respectively. Accordingly, the errors are calculated as 0.25% and 0% for the burst location and relative cross-sectional area respectively. By comparing the errors from Cases 6 and 7, it can be seen that the accuracy of the algorithm is enhanced by increasing the sampling rate. This specific analysis indicates that although the minimum required sampling rate of the algorithm could be the Nyquist frequency of the third resonance response in the discrete harmonic spectrogram, higher sampling rates can always be considered as alternatives, depending on the real system in practice.

4.4.4 Verification of the Algorithm on an RPR System

In order to verify the algorithm on an RPR system, Case 8 was implemented based on the configuration shown in Figure 4.6. In Case 8, the downstream valve is fully opened, indicating that the pipe is delivering the water, and the initial flow rate is $Q_0 = 0.0622$ m^3/s. The Darcy-Weisbach friction factor is $f = 0.015$, the testing time is 30 s, and the data transmission and sampling

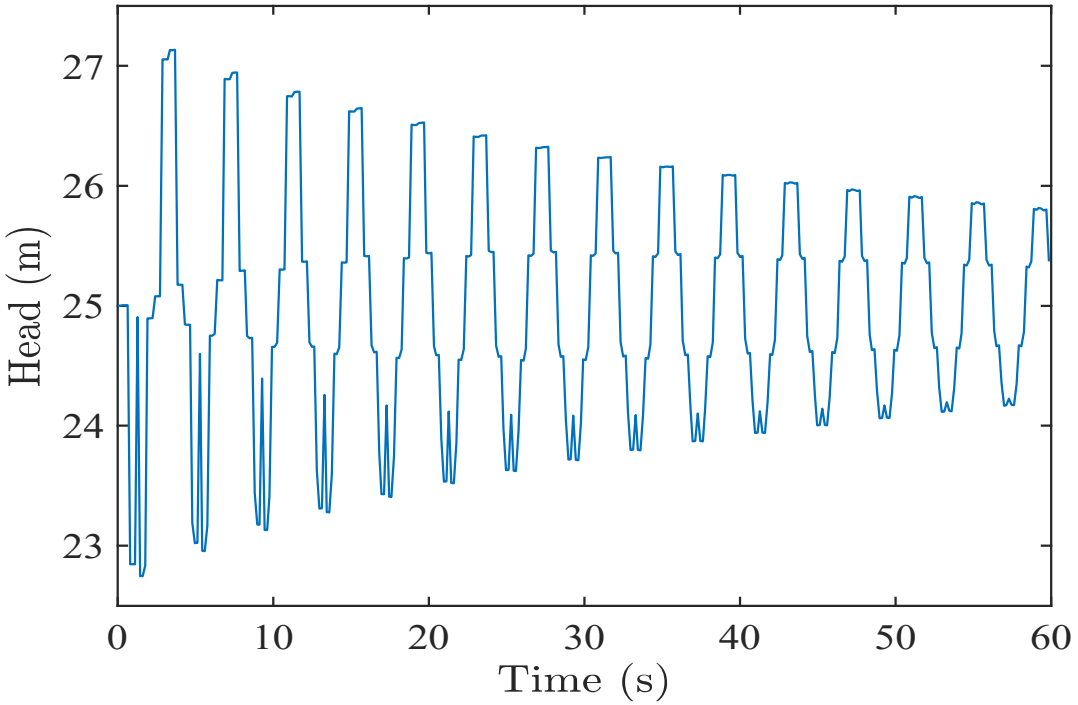

Figure 4.10: Time trace from Case 7

rates are both $2 \times 3 \times f_0 = 3$ Hz. The window gap is $d = 0.34$ s, while all the other parameters remain the same as for Case 5. The measured time trace is shown in Figure 4.11, and the resultant, discrete harmonic spectrogram is shown in Figure C.7. Replicating the same process in Case 5 generates the dimensionless burst location $x_B^* = 0.2415$ and relative cross-sectional area $\frac{C_d A_B}{A_p} = 0.002$. The errors are 0.85% and 0% for the burst location and relative cross-sectional area respectively. This scenario verifies the algorithm on an RPR system with low data transmission and sampling rates, and it also reveals the ability of the algorithm to be applied to the area of real-time data monitoring.

4.4.5 Verification of the Algorithm for the Slow Transient Generation Process

In the research by Keramat et al. (2019), and Keramat and Zanganeh (Keramat and Zanganeh, 2019), direct analysis of reflections from the leak when using

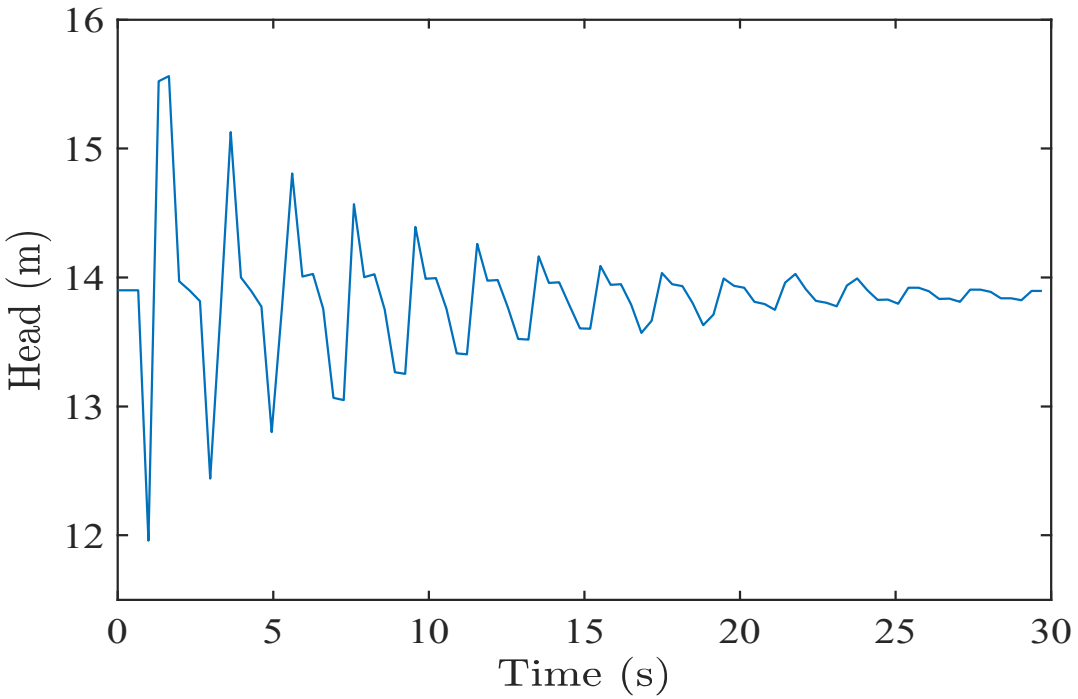

Figure 4.11: Time trace from Case 8

a separate transient source shows that the localization error is proportional to the transient generation time. However, the approach outlined in this paper is designed to utilize the damping behavior of the low-frequency components of the signal. Only the first three resonance responses were utilized in the conducted verification scenarios, indicating that the maximum required frequencies that should be present in the signal are $\frac{3a}{2L}$ and $\frac{5a}{4L}$ for RPR and RPV systems respectively. Therefore, even if the cross-sectional area of the burst is increased gradually after the eruption and the high-frequency components of the signal are not excited, the burst can still be located and the localization error should remain similar as long as the minimum required frequency components of the signal can be reflected in the signal due to the burst.

In order to verify the previously mentioned analysis, Cases 9-11 have been implemented based on the configuration shown in Figure 4.5. The burst is simulated by a side discharge valve. The valve opening time for Cases 9-11 is 4 s, 16 s, and 32 s, respectively, and the valve is set to start opening at 1

s for each of these three cases. The burst is generated at $x^* = 0.75$, which is the same as the measurement location. The applied data transmission and sampling rates are 100 Hz. All other parameters and conditions remain the same as for Cases 1-7. The valve opening processes of three cases are simulated by one-quarter of a sinusoidal wave in a period, as shown in Figure 4.12, where $\gamma = 0$ and $\gamma = 1$ indicate fully closed and fully opened statuses respectively. The steady head has been subtracted from the measured time trace of these three cases, shown in Figure 4.13. Replicating the same data analysis processes provides the results and errors for Cases 9-11. They are summarized in Table 4.2.

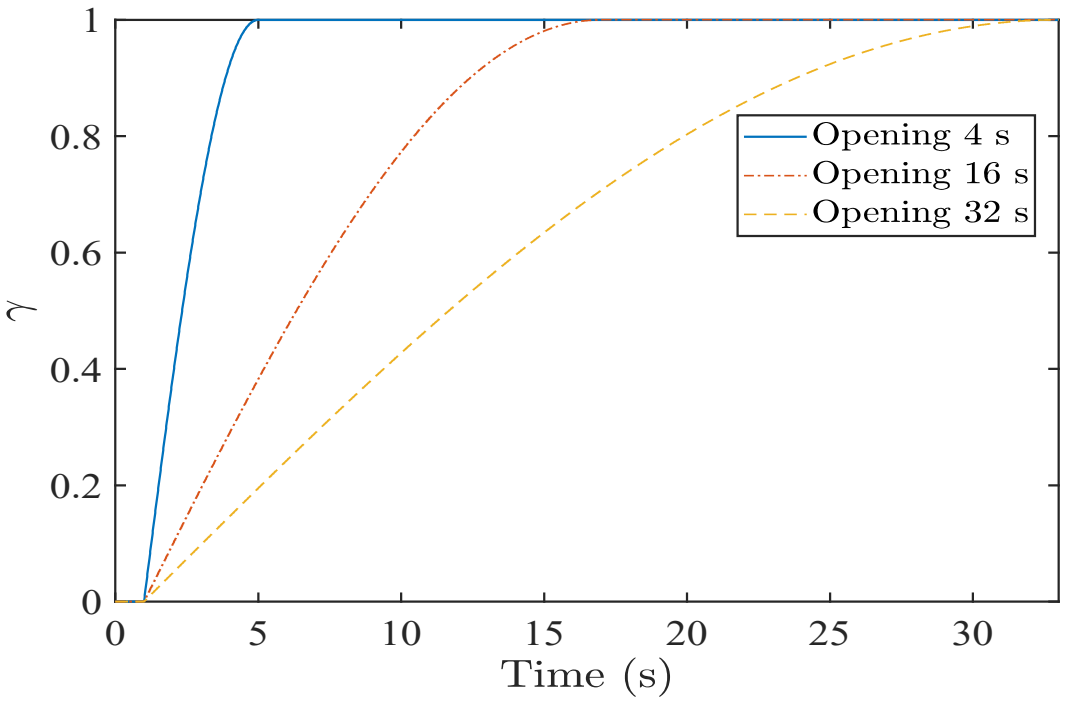

Figure 4.12: Valve opening curves from Cases 9-11

4.4.6 Discussion of Numerical Verification

In summary, all the implemented numerical verifications illustrate that the approach in this paper can be applied successfully for burst detection, localization, and quantification by producing a discrete harmonic spectrogram. The numerical

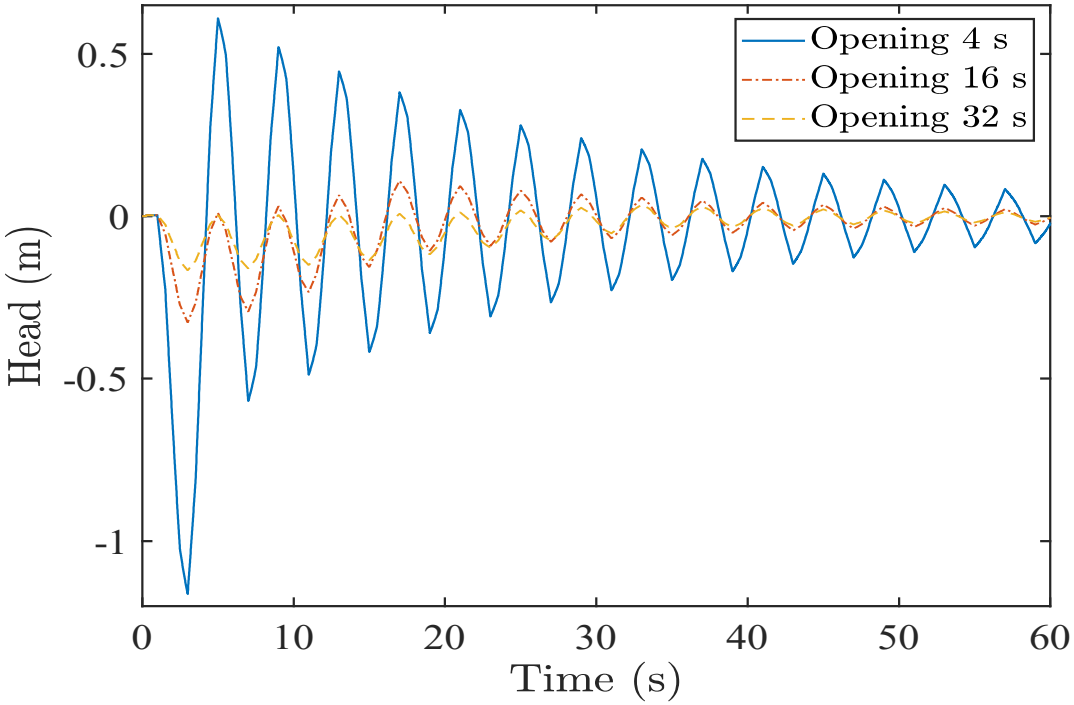

Figure 4.13: Time traces from Cases 9-11

Table 4.1: Conditions of numerical cases

Case Number	System Type	Burst Type	t_a (s)	d (s)	Data Transmission Rate (Hz)	Sampling Rate (Hz)
1	RPV	Rapid	2.3	4.8	100	100
2	RPV	Rapid	4.3	4.8	100	100
3.1	RPV	Rapid	20	4.8	100	100
3.2	RPV	Rapid	4	4.8	100	100
3.3	RPV	Rapid	8	4.8	100	100
4	RPV	Rapid	20	0.01	100	100
5	RPV	Rapid	20	0.01	2.5	100
6	RPV	Rapid	20	0.4	2.5	2.5
7	RPV	Rapid	20	0.16	6.25	6.25
8	RPR	Rapid	20	0.34	3	3
9	RPV	Slowly developing for 4 s	20	4.8	100	100
10	RPV	Slowly developing for 16 s	20	4.8	100	100
11	RPV	Slowly developing for 32 s	20	4.8	100	100

Table 4.2: Results of numerical cases

Case Number	Resultant x_B^*	Resultant $\frac{C_d A_B}{A_p}$	x_B^* Error (%)	$\frac{C_d A_B}{A_p}$ Error (%)	FWDI (%)
1	0.3459	0.0011	9.59	45	8.2
2	0.3227	9.5006×10^{-4}	7.27	52.5	7.92
3.1	0.2473	0.002	0.27	0	2
3.2	0.2519	0.002	0.19	0	2
3.3	0.2496	0.002	0.04	0	2
4	0.2481	0.002	0.19	0	2
5	0.2282	2.03×10^{-3}	2.18	2	1.64
6	0.2596	0.002	0.96	0	1.64
7	0.2475	0.002	0.25	0	1.64
8	0.2415	0.002	0.85	0	0.4
9	0.7571	0.002	0.7133	0	0.006
10	0.7547	0.002	0.4733	0	0.005
11	0.7537	0.002	0.3667	0	0.001

verifications of the method also reveal its potential to be utilized in the area of real-time data monitoring. In addition, the numerical results emphasize that the minimum required data transmission and sampling rates only need to be the Nyquist frequency of the third resonance peak in the discrete harmonic spectrogram, which indicates the ability to utilize low data transmission and sampling rates in the algorithm. The last three numerical cases illustrate that the algorithm in this paper can provide high accuracy under the condition of a slow transient generation process. Generally, any integer multiple of the fundamental period of the pipeline system can be the window length to ensure the signal continuity at the edges within each window. The determination of the fundamental period of the pipeline system can be calculated by equations, observing the signal, or the ringdown approach in Giesler et al. (2019). Experimental verification is presented in the next section.

4.5 Experimental Verification

One experimental scenario was conducted in the Robin Hydraulics Laboratory at the University of Adelaide: the Experimental Case. The pipeline applied in the experimental test is a 37.41 m long, straight pipeline, made of copper. The schematic diagram and the relevant parameters are shown in Figure 4.14. The pressurized tank at the east side is the upstream boundary and the tank at the west side is the downstream boundary.

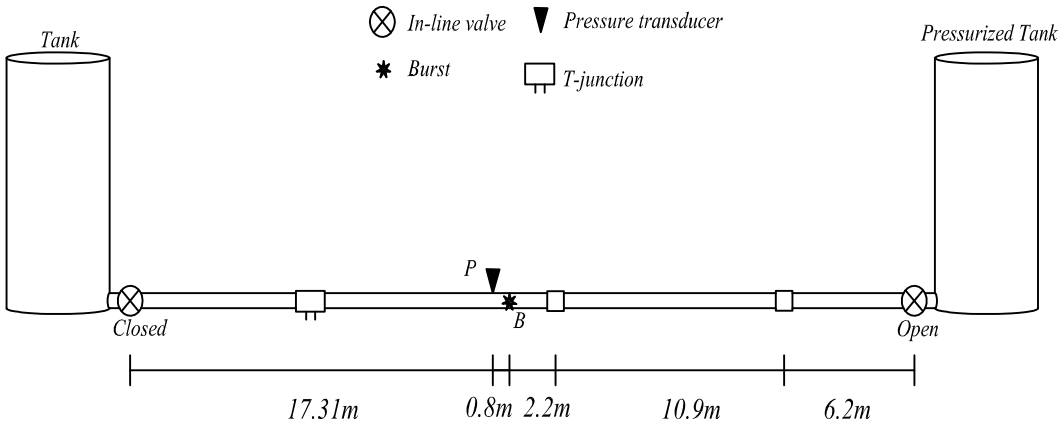

Figure 4.14: Experimental configuration

The pressure transducer is located at point P, and the burst is located at point B for the Experimental Case. More details of the experimental rig can be found in Wang et al. (2002), Vitkovsky (2007), and Du et al. (2020). The downstream valve of the pipe is set to be closed to isolate the west tank from the pipe system. The solenoid valve with a relative cross-sectional area $\frac{C_d A_B}{A_p} = 2.12 \times 10^{-3}$ and dimensionless location $x_B^* = 0.51$ is opened quickly at approximately 0.1 s to simulate the occurrence of the burst. The total test time was 3 s. Additionally, the solenoid valve has a sharp orifice, thus $b = 0.5$. The initial flow rate of the test is $Q_0 = 0$ m^3/s, the wave speed is $a = 1320$ m/s, and the head at the upstream tank is 3.065 bar, which is the east tank in Figure 4.14. Note that the system was set to be an RPV system, using the closed downstream valve, thus all the even harmonic components are inapplicable, and

the fundamental period of the pipeline system is calculated as $T = \frac{4L}{a} = 0.11$ s. The original data acquisition system has the data transmission and sampling rates at 10000 Hz, and the time trace is shown in Figure 4.15. Based on the analyses in the numerical cases, the applied data was re-sampled and re-transmitted with 91 Hz, which is the Nyquist frequency of the third resonance response of the system. The length of the window is set to be equal to the fundamental period of the pipeline system, $t_a = 0.11$ s, and the interval between the starting points of the two contiguous windows is $d = 0.011$ s, which is the same as the actual real-time data acquisition speed of 0.011 s (91 Hz). The applied time trace is shown in Figure 4.16, and the generated discrete harmonic spectrogram is shown in Figure 4.17.

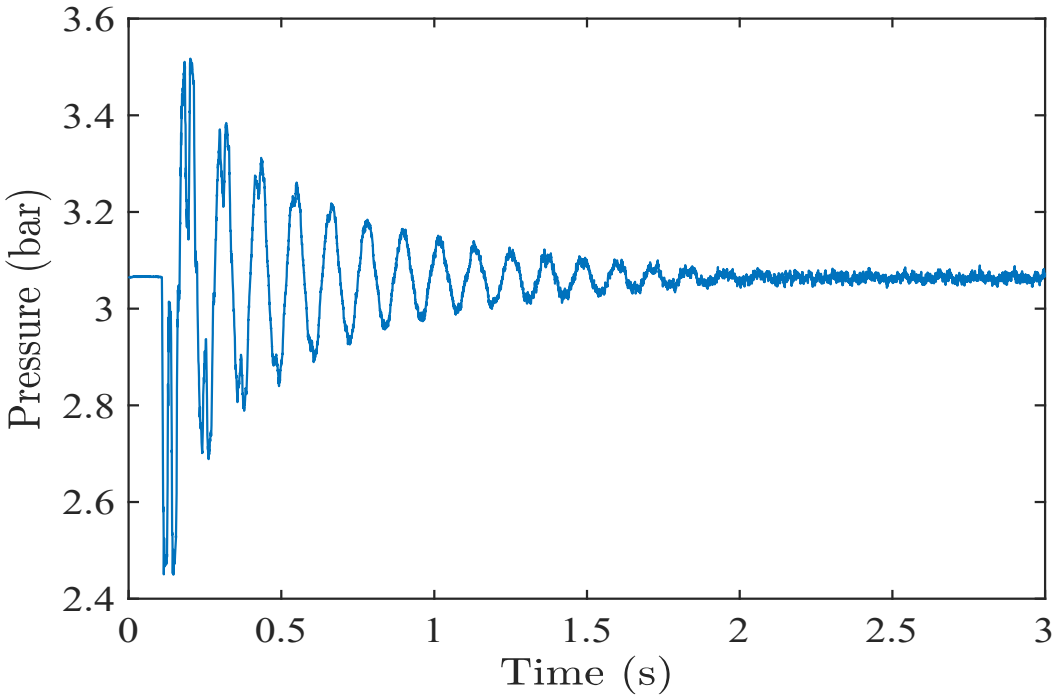

Figure 4.15: Original time trace from the experiment

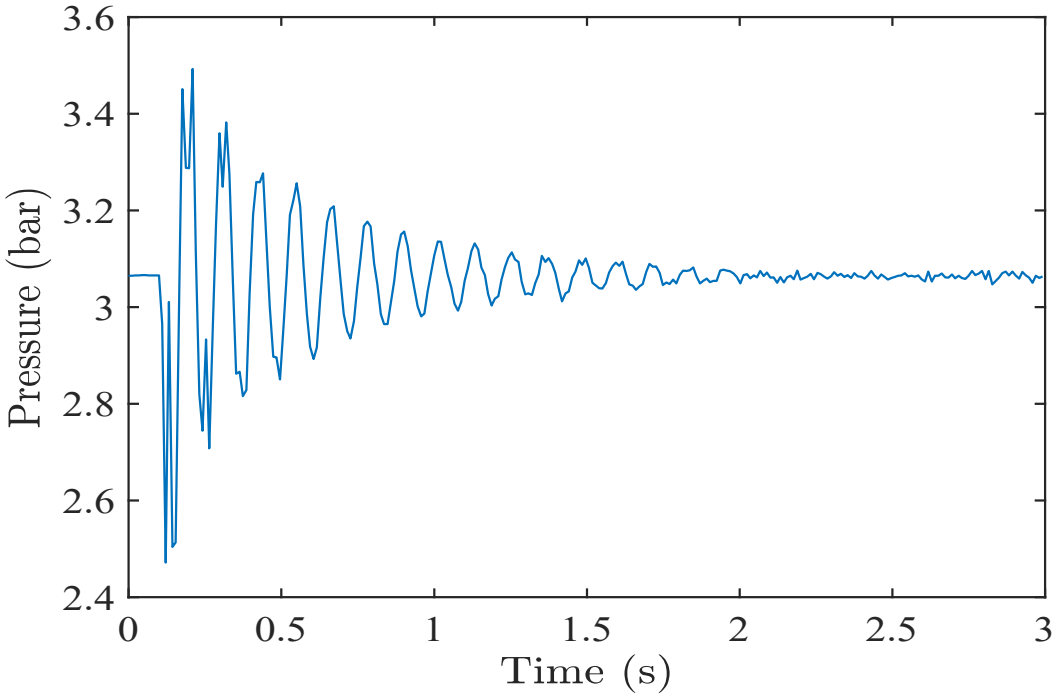

Figure 4.16: Applied time trace from the experiment

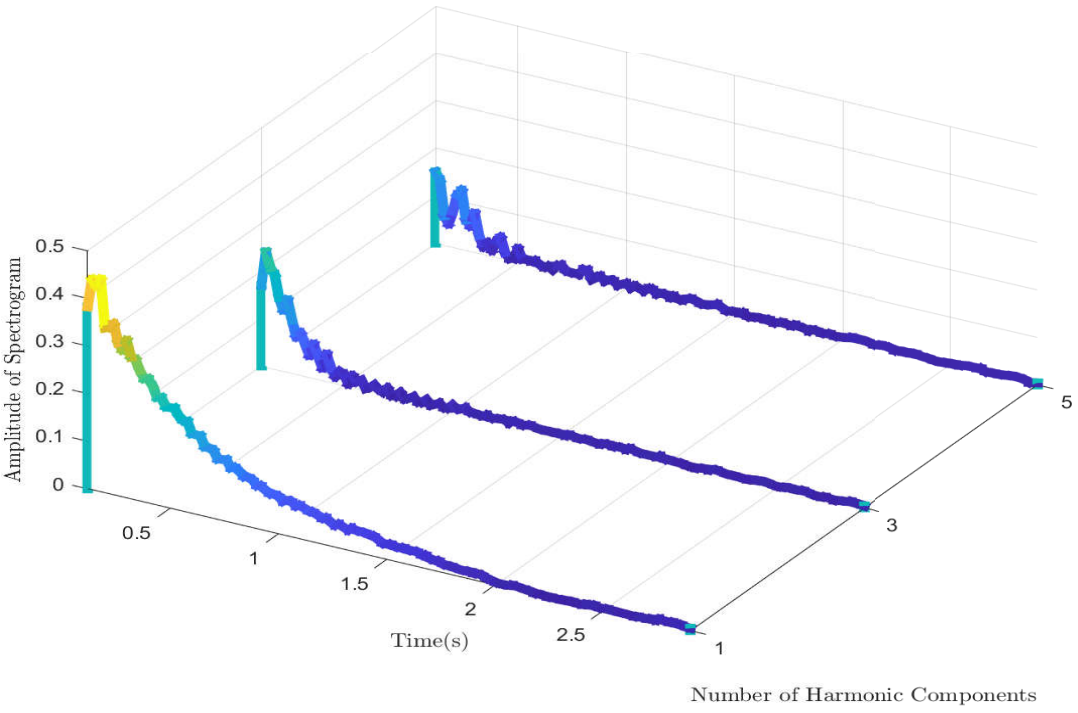

Figure 4.17: Discrete harmonic spectrogram from the experiment

Unsteady friction damping is involved in the analysis when analyzing the real experimental data from the laboratory. The unsteady friction damping was determined by using the Unsteady Friction Water Hammer (UFWH) model developed by Du et al. (2020). The resultant actual friction damping in the Experimental Case is $R_1 = 0.012$, $R_3 = 0.022$, and $R_5 = 0.029$. Replicating the signal analysis process in the numerical verifications provides the determined dimensionless burst location $x_B^* = 0.5016$ and the relative cross-sectional area $\frac{C_d A_B}{A_p} = 2.14 \times 10^{-3}$. Accordingly, the corresponding errors are 0.84%, and 0.94%. Thus, it can be seen that the algorithm can be applied successfully to a real pipeline system with high accuracy, even with significantly reduced data transmission and sampling rates.

The results and corresponding analysis of the implemented experimental test verify that the algorithm outlined in this paper can be utilized for burst detection, localization, and quantification in a real pipeline system with a low sampling rate, and the algorithm could be applied to real-time data monitoring systems.

4.6 Conclusion

The damping caused by the presence of the burst is contained in the transient signal of the pressure head in a pipeline system. Therefore, the harmonic components of the signal damped differently in the first three resonance responses in the discrete harmonic spectrogram. This specific information is useful for burst detection, localization, and quantification by applying the damping ratios.

The approach and its corresponding analytical solution indicate that the damped harmonic components in the discrete harmonic spectrogram can be generated by analyzing the measured signal in each time window, with a very small window

gap. The integer multiples of the fundamental period of the pipeline system are always appropriate solutions for consideration because of the periodic nature of DFT. In addition, the value of the window length can be adjusted according to the features of the data. The window gap can be flexible, with its minimum value associated with the real-time data acquisition speed. Therefore, the algorithm outlined in this paper can be applied to the area of real-time data monitoring with only one sensor.

The minimum required data transmission and sampling rates of the algorithm in this paper only need to be equal to the Nyquist frequency of the third resonance peak in the discrete harmonic spectrogram. This advantage provides an insight into designing a corresponding pressure monitoring system with low data transmission and sampling rates, hence reducing the cost. Specifically, the required data transmission and sampling rates of an RPV system are $10 \times f_0$, and of an RPR system are $6 \times f_0$. Therefore, the algorithm provides an insight into how to utilize low data transmission and sampling rates in practice for a data acquisition system. Additionally, larger values of the transmission and sampling rates can be selected according to the real system in practice, and may provide higher accuracy. Although the minimum required sampling rate is low through application of the algorithm, real-time data monitoring can be achieved by selecting an appropriate value for the window gap.

The approach in this paper has been verified by eleven numerical studies and one experimental study. The window length sensitivity has been explored numerically by introducing WDI. Additionally, the application of the proposed approach to developing burst cases has been verified numerically. The advantages of the algorithm in this paper provide a significant insight into real-time burst detection techniques using a low-frequency data acquisition system.

Although the burst detection approach in this paper is easy to apply, the transients caused by the complicated geometries of the pipe network, such as sud-

denly opened branches and sudden water usage in the network, may bring difficulties for burst identification. The determination of the fundamental period of the pipeline system may be a problem that needs to be solved before utilizing the approach in this paper when integer multiples of the fundamental period of the pipeline system are considered as the window length. This may be solved by applying equations, observing signals, or the ringdown method. Transient damping can be also caused by the pipe wall viscoelasticity in plastic pipes, and it can be calibrated by a preliminary test, similar to the process to obtain the damping caused by friction. This paper focuses on metallic pipes, hence pipe wall viscoelasticity is not discussed in detail.

Chapter 5

Approach for Near-Real-time Pipe Burst Detection and Location Estimation Utilizing Any Sequence of Harmonics of the Transient Pressure Signal

(Journal Paper 3)

Xiao-xuan Du, Martin F. Lambert, Lei Chen, and Eric Hu

Submitted to *Journal of Water Resources Planning and Management*

Statement of Authorship

Title of Paper	Approach for Near-Real-time Pipe Burst Detection and Location Estimation Utilizing Any Sequence of Harmonics of the Transient Pressure Signal
Publication Status	☐ Published ☐ Accepted for Publication ✓ Submitted for Publication ☐ Unpublished and Unsubmitted work written in manuscript style
Publication Details	Du, X.-x., Lambert, M. F., Chen, L., and Jing Hu, E. (Under review). Approach for Near-Real-time Pipe Burst Detection and Location Estimation Utilizing Any Sequence of Harmonics of the Transient Pressure Signal. Journal of Water Resources Planning and Management.

Principal Author

Name of Principal Author (Candidate)	Xiaoxuan Du		
Contribution to the Paper	Conception and design of project Analysis and interpretation of research data Drafting the paper		
Overall percentage (%)	75%		
Certification:	This paper reports on original research I conducted during the period of my Higher Degree by Research candidature and is not subject to any obligations or contractual agreements with a third party that would constrain its inclusion in this thesis. I am the primary author of this paper.		
Signature		Date	14/01/2022

Co-Author Contributions

By signing the Statement of Authorship, each author certifies that:

i. the candidate's stated contribution to the publication is accurate (as detailed above);
ii. permission is granted for the candidate in include the publication in the thesis; and
iii. the sum of all co-author contributions is equal to 100% less the candidate's stated contribution.

Name of Co-Author	Martin F. Lambert		
Contribution to the Paper	Conception and design of project Analysis and interpretation of research data Critically revising the paper		
Signature		Date	19/1/2022

Name of Co-Author	Lei Chen		
Contribution to the Paper	Revising the paper critically Conception and design of project		
Signature		Date	18/01/2022

Please cut and paste additional co-author panels here as required.

Name of Co-Author	Eric Jing Hu		
Contribution to the Paper	Revising the paper critically Conception and design of project		
Signature		Date	18/1/2022

Abstract

The purpose of the paper is to extend an approach for real-time pipe burst detection and location estimation, based on the changes in the harmonics and analysis of the corresponding damping that is caused by the burst. The amplitude of each resonance response of the transient pressure wave caused by the burst is damped differently due to the occurrence of the burst. However, utilizing higher harmonics beyond the first few fundamental frequencies has not previously been possible as it leads to an increasing number of possible solutions to the burst location, which limits the application of the method. An algorithm for damping analysis has been developed, which overcomes this limitation, and is able to exclude most of the incorrect solutions when utilizing the information contained in higher harmonics. Additionally, the gap between data windows can be set so that it enables the real-time data analysis by letting the window gap equal the reciprocal of the sampling rate. Therefore, this algorithm makes utilizing any sequence of harmonics of the signal be possible for real-time burst detection and location estimation. The approach has been verified both numerically and experimentally with acceptable accuracy.

5.1 Introduction

Unexpected bursts or large leaks in pipeline systems are long-lasting issues all around the world (Anderson and Anderson, 2011; Hovey and Farmer, 1993). Different techniques have been proposed and explored in the frequency domain for pipeline faults detection and estimation, such as the damping of fluid transients (DOFT) (Nixon et al., 2006; Wang et al., 2002).

The basic theory and the corresponding analytical technique of the DOFT have been explored (Nixon et al., 2006; Wang et al., 2002). Wang et al. (2002) proposed a foundational technique to analyze the amplitude of the first three

resonance responses in the frequency domain. All the harmonics of the pressure signal are damped differently due to the presence of the leak. Therefore, the damping of each harmonic of the transient signal contains information about the leak. The damping can be calculated by fitting the Fourier solution to the measured data, and thus the leak can be estimated by examining the damping ratio of the first three resonance harmonics of the signal (Wang et al., 2002). Nixon et al. (2006) further researched this technique regarding its validity.

Du et al. (2020) developed a technique based on DOFT theory for pipe burst detection, localization, and cross-sectional area estimation. In this technique, the transient source is the burst itself, instead of the manually controlled, side-discharge valve in Wang et al. (2002). Du et al. (2021) extended this approach from the perspective of real-time data monitoring and low sampling rate using a user-defined number as the analyzed window length and gap instead of the fixed window length and gap-fundamental period of the signal. The approach in Du et al. (2021) enables DOFT theory to be applied for real-time data monitoring and provides an insight into strategies for decreasing the cost of the required sensor and sensing system.

However, the following gaps exist in the techniques for pipe burst detection and estimation based on DOFT. Firstly, the techniques in Du et al. (2020) and Du et al. (2021) can only utilize the first few resonance harmonics, more specifically, the first three resonance harmonics; otherwise, more potential solutions to the dimensionless burst location will be generated. This requires the sensor and sensing system to measure the first few fundamental resonance responses of the signal accurately. This specific aspect brings restrictions to the sensor and sensing system regarding the measuring frequency range. Consequently, it limits the scope of the ability of corresponding sensor and sensing system to deal with the problems from using DOFT. For example, when the signal is negatively affected in the low frequency range by unexpected noise, such as the operation of a pump, the signal in the first few fundamental frequencies will be contam-

inated, and thus, the DOFT analysis cannot be implemented for burst detection and estimation. Secondly, no methods to exclude incorrect solutions that are generated by using higher order harmonics have been discussed and explored in the reviewed literature.

In this paper, an algorithm has been developed to exclude the majority of incorrect solutions to dimensionless burst location that are generated by utilizing any sequence of harmonics for burst detection and location estimation. This specific algorithm eases the restriction that the DOFT-based approach for pipe burst detection and location estimation can only utilize the first three resonance harmonics. Accordingly, this specific aspect broadens the scope of the capabilities of sensor and sensing system of detecting and estimating the burst. For example, the capability of utilizing any sequence of harmonics enables the analysis process to be implemented for burst detection and location estimation when the noise affecting part of the frequency range negatively, or the signal in part of the frequency range is missing.

In the following section, the mathematical theory of the algorithm is presented. The procedure for pipe burst detection and location estimation utilizing any sequence of harmonics is presented in the next section. Four numerical scenarios are followed by an experimental verification, the discussion about unsteady friction damping, and the conclusion.

5.2 Mathematical Modeling

The main applied assumptions are presented as follows:

1. The pipe wall is elastic.

2. The unsteady friction damping on each harmonic component is exponential.
3. The fluid is slightly compressible.
4. The flow is one-dimensional.
5. The radial velocity is small.
6. The fluid velocity is much smaller than the wave speed.

Based on the research in Du et al. (2020) and Du et al. (2021), the head disturbance solution for a burst problem is shown as

$$h^*(x^*,\ t^*) = \sum_{n=1}^{\infty} \left\{ e^{-(R+R_{nB})t^*} [A_n cos(n\pi t^*) + B_n sin(n\pi t^*)] sin(n\pi x^*) \right\} \quad (n = 1,\ 2,\ 3, \ldots) \tag{5.1}$$

where x^* and t^* are the dimensionless distance along the pipe and the dimensionless time respectively, using the following definitions

$$h^* = \frac{h}{H_1},\ t^* = \frac{t}{L/a},\ x^* = \frac{x}{L} \tag{5.2}$$

where h is the head disturbance caused by the burst, H_1 is the reference head, which is the head measured at the boundary reservoir, t is the time, L is the length of the pipe, a is the wave speed, and x is the distance along the pipe. R is the friction damping, which contains the steady and unsteady friction damping. The detailed equation of friction damping is presented in Kjerrumgaard Jensen et al. (2018), and the unsteady friction damping has been proved to be dependent on the frequency (Du et al., 2020). A_n and B_n are the Fourier coefficients that are shown in Wang et al. (2002).

The vital parameter contained in the exponential formulation in Eq. (5.1) is R_{nB}, the burst damping, which contains the burst information. The burst damping of the nth harmonic is defined as

$$R_{nB} = K_B sin^2(n\pi x_B^*) \tag{5.3}$$

where x_B^* is the dimensionless burst location from the upstream of the pipe, and K_B is the burst parameter that associates with the cross-sectional area of the burst, which is defined in Du et al. (2020).

The Fourier solution of Eq. (5.1) is shown as

$$E_n^{(m)} = E_n^{(1)} e^{-(R+R_{nB})(m-1)d^*} \tag{5.4}$$

where $E_n^{(m)}$ is the amplitude of the nth harmonic in the mth window, $E_n^{(1)}$ is the first harmonic in the mth fundamental period, and d^* is the dimensionless window gap between each analyzed window. Equation (5.4) is the key equation for damping determination. Fitting Eq. (5.4) to the damped amplitudes of the harmonics provides the total damping. The friction damping can be calibrated using the unsteady friction water hammer (UFWH) model developed in Du et al. (2020). Therefore, the burst damping can be determined. Utilizing the burst damping ratio can generate a function that only contains the dimensionless burst location. The burst damping ratio is shown as

$$\frac{R_{n_2B}}{R_{n_1B}} = \frac{sin^2(n_2\pi x_B^*)}{sin^2(n_1\pi x_B^*)} \tag{5.5}$$

where n_1 and n_2 are the order number of the applied pair of the harmonics.

The damping ratio of the first three resonance harmonics for a reservoir-pipe-reservoir (RPV) system is shown in Figure 5.1 as an example. Eq. (5.5) allows the location of the burst to be determined if the damping ratio is known. It should be noted that the application of the DOFT technique to an RPV system is achieved by adding an imaginary mirror part to the original system, and thus all the possible solutions to the dimensionless burst location in the imaginary part are neglected (Wang et al., 2002).

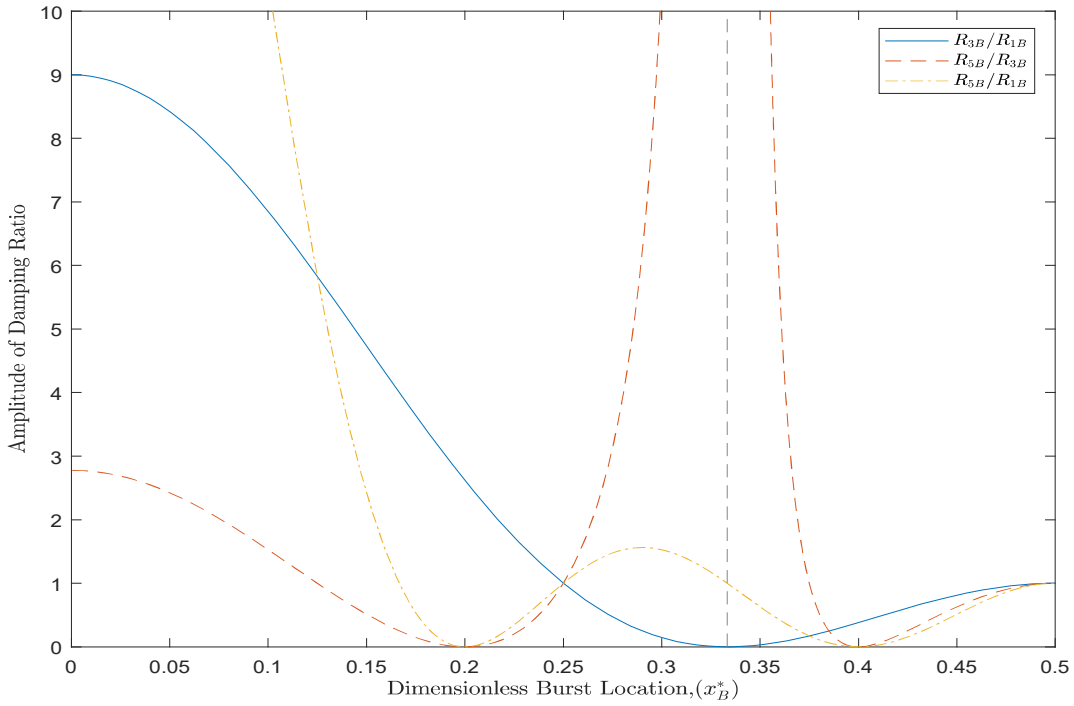

Figure 5.1: RPV damping ratios of harmonics 1, 3, and 5

However, utilizing the damping ratio of higher order harmonics leads to many more possible solutions that correspond to the same damping ratio value. For example, the damping ratio figure for the 51st, 53rd, and 55th harmonics of the RPV system are selected as shown in Figure 5.2. It can be seen that there are too many dimensionless burst locations corresponding to the given damping value of 3. This brings difficulties in determining the correct dimensionless burst location. Utilizing the periodicity of the sinusoidal function and scaling the resolution of the solution provides a method to exclude the majority of

incorrect solutions. Based on the periodicity of the sinusoidal function,

$$|sin(n\pi x_B^* \pm k\pi)| = |sin(n\pi x_B^*)| \tag{5.6}$$

therefore,

$$sin^2(n\pi x_B^* \pm k\pi) = sin^2(n\pi x_B^*) \tag{5.7}$$

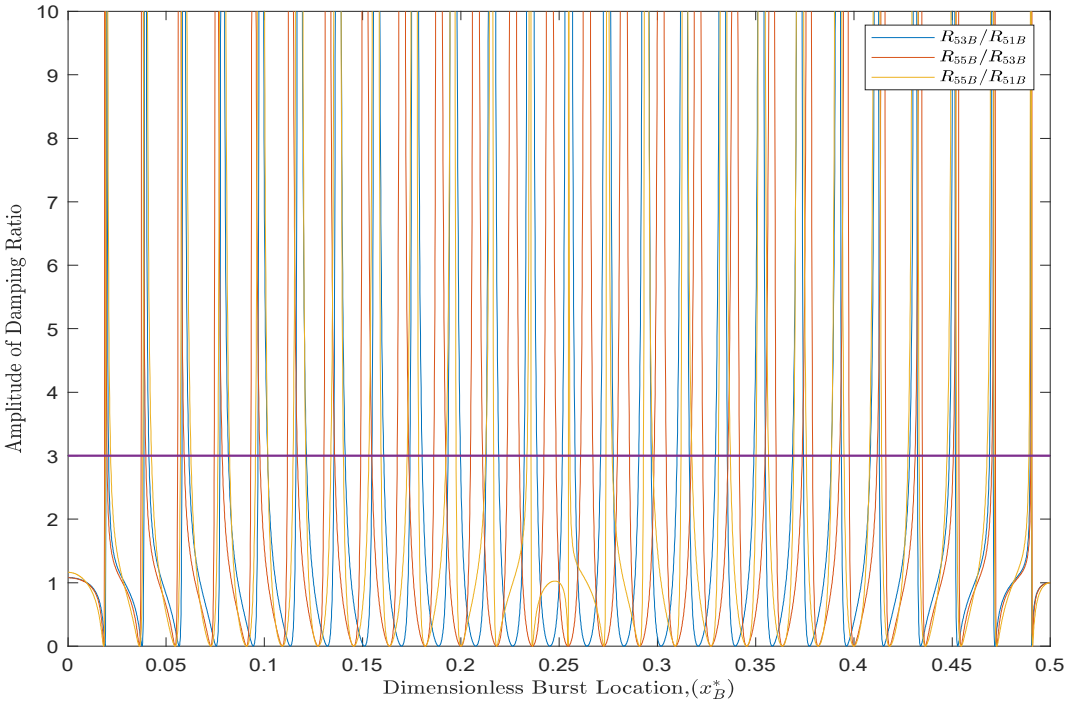

Figure 5.2: RPV damping ratios of harmonics 51, 53, and 55

Based on Eqs. (5.6) and (5.7), the low order harmonic n_3, can be utilized to replace the high order harmonic n_4, for damping analysis. For example, for the low order harmonic n_3, the burst damping is $R_{n_3B} = K_B sin^2(n_3\pi x_B^*)$, and for the high order harmonic n_4, the burst damping is $R_{n_4B} = K_B sin^2(n_4\pi x_B^*)$. Based on Eq. (5.7), if the value of $(n_4 - n_3)x_B^*$ equals integer k, the harmonic of n_3 can be utilized to replace the harmonic of n_4 for damping analysis, which is shown as $R_{n_4B} = K_B sin^2(n_4\pi x_B^*) = K_B sin^2(n_4\pi x_B^* - k\pi) = K_B sin^2[n_4\pi x_B^* - (n_4 - n_3)\pi x_B^*] =$

$K_B sin^2\{[n_4-(n_4-n_3)]\pi x_B^*\} = K_B sin^2(n_3\pi x_B^*) = R_{n_3B}$. Consequently, the incorrect solutions due to the application of high order harmonic n_4, can be excluded, since only the solutions determined by using the low order harmonic n_3, will be generated. The detailed steps of the developed algorithm based on the above mathematical modeling are presented in the next section.

5.3 Algorithm for Burst Detection and Location Estimation using Any Sequence of Harmonics

The developed algorithm, based on the mathematical modeling in the previous section, is an algorithm that determines the target solution to dimensionless burst location, of which the precision has been truncated to the first few decimal places. The algorithm enables any sequence of harmonics to be utilized for pipe burst detection and location estimation, with most of the incorrect solutions excluded. The steps of the algorithm are shown as

1. Determine the target harmonics for the analysis based on the requirements in practice, for example, the harmonics with the order of $11 \leq n \leq 20$.

2. Extract the total damping from any three of the harmonics determined from Step 1, for example, the harmonics with the order of $n = 11$, $n = 12$, and $n = 13$, using the technique in Du et al. (2020).

3. Calibrate the corresponding actual (total) friction damping from the UFWH model, and calculate the burst damping by subtracting the friction damping from the total damping. Generate three damping ratios using Eq. (5.5). Consequently, for the selected example, the applied burst damping is R_{11B}, R_{12B}, and R_{13B}. Accordingly, the applied example damping ratios are $R_{12B}/R_{11B} = u_1$, $R_{13B}/R_{12B} = u_2$, and $R_{13B}/R_{11B} = u_3$.

4. Round down the target solution, x_B^*, with the precision unit of 0.1 (i.e., the value of the solution is an integer multiple of 0.1); therefore, the target solution is truncated, and the truncated solution is defined as x_B^{**}. For example, if $x_B^* = 0.2334$, then $x_B^{**} = 0.2$. Accordingly, the harmonics with the order of $1 \leq n \leq 10$ can be utilized to replace the harmonics with the order of $n > 10$ for damping analysis. For example, for $n = 11$, when determining the truncated solution, x_B^{**}, the burst damping is $R_{11B} = K_B sin^2(11\pi x_B^{**}) = K_B sin^2(\pi x_B^{**} + 10\pi x_B^{**}) = K_B sin^2(\pi x_B^{**}) = R_{1B}$, in which $10\pi x_B^{**} = k\pi$, where $k = 10x_B^{**}$ is an integer due to the truncation.

5. Extract the last digit of the order number of the determined harmonics in Step 2. If the last digit of any order number of the applied harmonics is 0, use 10 as the extracted order number. The extracted order number should be of $1 \leq n \leq 10$. Consequently, the extracted order number of the example harmonics is 1, 2, and 3. Use the harmonics with the extracted order number, $n = 1$, $n = 2$, and $n = 3$, to replace the original harmonics, $n = 11$, $n = 12$, and $n = 13$, from Step 2, but with the same damping ratio values that are generated from Step 3, u_1, u_2, and u_3. Accordingly, the applied harmonic orders from Step 2 are downgraded. Therefore, for example, the damping ratio of the 11th and 12th harmonics, $R_{12B}/R_{11B} = u_1$, becomes $R_{12B}/R_{11B} = sin^2(2\pi x_B^{**} + 10\pi x_B^{**})/sin^2(\pi x_B^{**} + 10\pi x_B^{**}) = sin^2(2\pi x_B^{**})/sin^2(\pi x_B^{**}) = R_{2B}/R_{1B} = u_1$. Consequently, the example damping ratios become $R_{12B}/R_{11B} = R_{2B}/R_{1B} = u_1$, $R_{13B}/R_{12B} = R_{3B}/R_{2B} = u_2$, and $R_{13B}/R_{11B} = R_{3B}/R_{1B} = u_3$.

6. Substitute the damping ratios of the harmonics with downgraded orders, $R_{2B}/R_{1B} = u_1$, $R_{3B}/R_{2B} = u_2$, and $R_{3B}/R_{1B} = u_3$, into Eq. (5.5) to determine the truncated solution, x_B^{**}. Since one damping ratio value may correspond to multiple dimensionless burst locations, multiple potential solutions exist. Because the target solution has been truncated with the precision unit of 0.1, all the resultant solutions in the bracket with the length of 0.1 should be considered. The first decimal places of the resultant so-

lutions in this bracket are the possible values of the first decimal place of the truncated solution, x_B^{**}, and thus, of the target solution, x_B^*. It is worth noting that although the target solution has been truncated with the precision unit of 0.1 in Step 4, the second decimal places of the resultant solutions in this step should be taken into consideration to ensure the accuracy of the first decimal place. For example, if the determined solutions in this step are: $x_B^{**} = 0.12$ using $R_{2B}/R_{1B} = u_1$, $x_B^{**} = 0.15$ using $R_{3B}/R_{2B} = u_2$, $x_B^{**} = 0.17$ using $R_{3B}/R_{1B} = u_3$, and $x_B^{**} = 0.29$ using $R_{3B}/R_{1B} = u_3$, then only the first three determined locations should be considered, since they are in the bracket of $(0.1 \quad 0.2)$, while the fourth determined solution is out of this bracket. Accordingly, the value of the first decimal place of the truncated solution, x_B^{**}, and thus, of the target solution, x_B^*, is 1.

7. Because only the first decimal place of the truncated solution is determined in Step 6, multiple possible truncated solutions exist. Accordingly, a range that contains all the possible truncated solutions with the first decimal places resulted from Step 6 will be generated. Accordingly, the resultant range should contain the target solution. It should be noted that the resultant range that contains the target solution with the minimal length (referred to as correct range in the rest of the paper) should have a dimensionless length of 0.1, since the target solution has been truncated with the precision unit of 0.1. For example, if the actual dimensionless burst location is $x_B^* = 0.15$, and the first decimal places of the resultant solutions from Step 6 are 1, then the first decimal place of the truncated solution, x_B^{**}, and thus, of the target solution, x_B^*, is 1. Accordingly, the truncated solution, x_B^{**}, and thus, the target solution, x_B^*, is in the range of $[0.1 \quad 0.2]$, as shown in Figure 5.3. Based on Figure 5.3, the estimated dimensionless burst location range, which is the correct range, is indicated as $[0.1 \quad 0.2]$. If the correct range is not determined in this step, Step 8 can be applied to determine the correct range. For example, if the determined solutions in Step 6 is in the bracket of $(0.15 \quad 0.25)$, then the

possible values of the first decimal place of the truncated solution, x_B^{**}, and thus, of the target solution, x_B^*, could be 1 or 2. Accordingly, the truncated solution, x_B^{**}, and thus, the target solution, x_B^*, is in the range of [0.1 0.3]. If the resultant correct range is too large to be utilized, Step 9 can be applied to narrow the correct range.

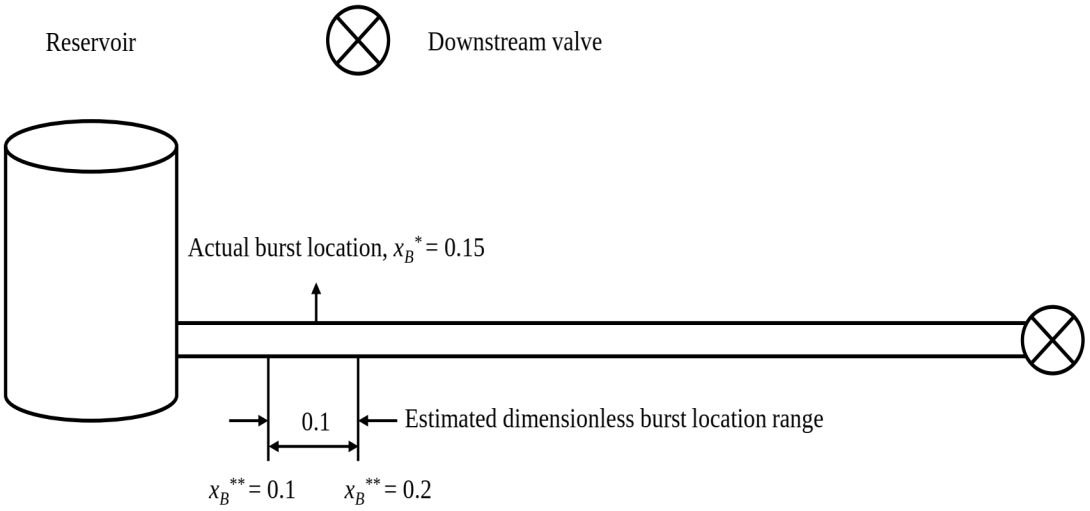

Figure 5.3: Example dimensionless burst location range on an RPV system

8. Apply the algorithm from Steps 1 to 7 to more than three harmonics to generate more ranges in Step 7. Specifically, select more than three harmonics in Step 2, compute the damping ratios as in Step 3, and then apply Steps 4 to 7 to each group of test. Consequently, a range that contains all the possible truncated solutions with the first decimal places that resulted from the original Step 6 will be generated for each group of tests. Because the burst location remains unchanged, and the corresponding burst damping remains the same, the correct range should always be contained in the resulting ranges in Step 7. For example, if two tests are conducted, and the determined ranges are [0.1 0.3] and [0.1 0.2], then the range of [0.1 0.2] has the highest occurrence. Therefore, utilizing more harmonics will provide the highest occurrence in the correct range. Accordingly, the correct range can be determined as the example shown in Figure 5.3, which is the correct range of [0.1 0.2].

9. Steps 1 to 8 can be applied to determine the first two decimal places of the target solution in the range of $[0.1 \quad 0.2]$, using the harmonics with orders that are higher than 100 (if they are available) in Step 2 and round down the target solution with the precision unit of 0.01 (i.e., the value of the truncated solution is an integer multiple of 0.01) in Step 4. For example, for the harmonic of $n = 101$, the burst damping, R_{101B}, becomes $R_{101B} = K_B sin^2(101\pi x_B^{**}) = K_B sin^2(\pi x_B^{**} + 100\pi x_B^{**}) = K_B sin^2(\pi x_B^{**})$, in which $100\pi x_B^{**} = k\pi$, where $k = 100x_B^{**}$ is an integer. Accordingly, a correct range with the minimal length of 0.01 will be generated, and thus the accuracy of the algorithm will be enhanced.

The algorithm presented above allows any sequence of harmonics to be applied to burst detection and location estimation. The determined burst damping and the resultant correct range from Steps 3 and 8, respectively, can be utilized as the indicator for the burst detection, since there is no burst damping and no such ranges can be generated under the condition of no-burst. Additionally, the resultant range from Step 8 can be utilized for enhancing burst location estimation, and excluding any incorrect solutions.

It is worth noting that the target solution x_B^* can be truncated to a certain precision of decimal places to adapt to the selected harmonics. For example, based on Eq. (5.7) and Step 4, if the target solution is truncated to the second decimal place with a certain precision unit of 0.02 (i.e., the value of the truncated solution is an integer multiple of 0.02), then the 1st harmonic can be utilized to replace the 51st harmonic for damping analysis, which is shown as: $R_{51B} = K_B sin^2(51\pi x_B^{**}) = K_B sin^2(\pi x_B^{**} + 50\pi x_B^{**}) = K_B sin^2(\pi x_B^{**}) = R_{1B}$, in which $50\pi x_B^{**} = k\pi$, where $k = 50x_B^{**}$ is an integer due to the truncation. This means that range can be narrowed as the harmonic order rises. Accordingly, this specific aspect can be utilized in Step 9. For example, truncating the target solution with the precision unit of 0.02 and utilizing Steps 5 to 8 in the example correct range $[0.1 \quad 0.2]$ that is shown above, enables the correct range with the

minimal length of 0.02 to be determined. Therefore, for example, the example correct range [0.1 0.2] can be narrowed to [0.24 0.26]. and hence, the accuracy is enhanced. Accordingly, this specific aspect can be applied to the condition that the harmonics with the orders that are higher than 100 cannot be utilized or cannot be captured by the sensor due to, for example, the low sampling rate. The algorithm can be further re-applied to determine the third decimal place of the target solution when the target solution is truncated with the precision unit of 0.001 (i.e., the value of the truncated solution is an integer multiple of 0.001) in Step 4. Consequently, the accuracy can be further enhanced. However, this may require a high sampling rate to allow those harmonics, of which the order number that is higher than 1000, to be utilized. Only the harmonics with the order number that is lower than 120 have been applied and discussed in this paper. Four conducted numerical scenarios are presented in the next section regarding this algorithm for burst detection and location estimation.

5.4 Numerical Verification

Four numerical verification scenarios have been implemented, which are referred to as Cases 1 to 4. The applied system for all the cases is the RPV system. The results of all the conducted numerical scenarios have been summarized in Table 5.5.

5.4.1 Verification of the Algorithm for a Fixed Window Length and Gap

Case 1 is the scenario that verifies the algorithm with a fixed window length and gap, of which the value is the fundamental period of the signal. The corresponding pipeline configuration is shown in Figure 5.4. As shown in Figure 5.4, the transient is initiated by the burst, which is simulated by a suddenly-opened side discharge valve. The location of the burst is at $x_B^* = 0.25$, and the measurement location at $x^* = 0.75$, which are 250 m and 750 m from the upstream reservoir, respectively. The relative cross-sectional area of the burst is $\frac{C_d A_B}{A_p} = 0.002$. The total test recording time is 60 s, and the burst occurrence time is 0.3 s. The utilized side-discharge valve for burst initiation is set to be opened instantaneously, and thus the opening time can be neglected. Additionally, the side-discharge valve is assumed to be the sharp orifice. The no-burst condition is assumed to be at a steady state. The steady flow rate is $Q_0 = 0.001$ m^3/s, given by the partially opened downstream valve of the pipe. The Darcy-Weisbach friction factor is $f = 0.0302$, and only the steady friction is considered. The measured time trace is shown in Figure 5.5. The fundamental period of the signal is $4L/a = 4$ s. The sampling rate is 100 Hz, which is capable of measuring up to 200 harmonics of the signal.

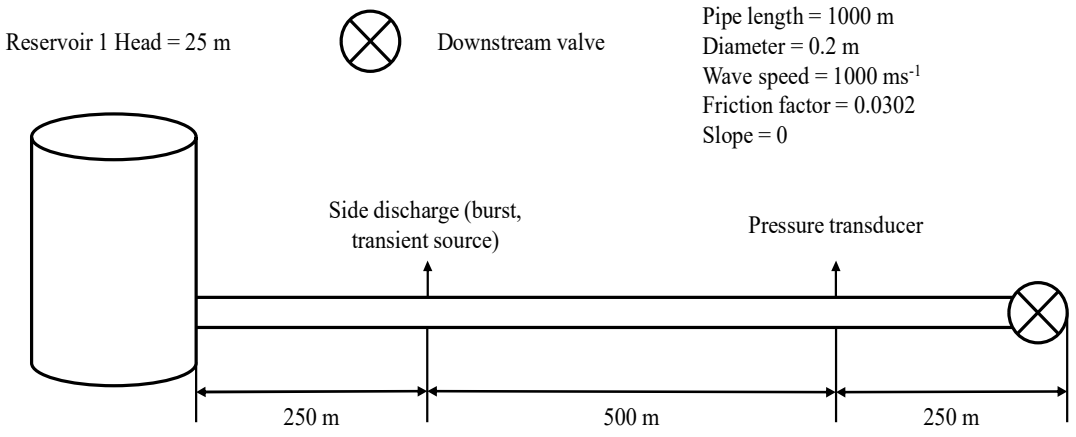

Figure 5.4: RPV system configuration for Cases 1, 3, and 4

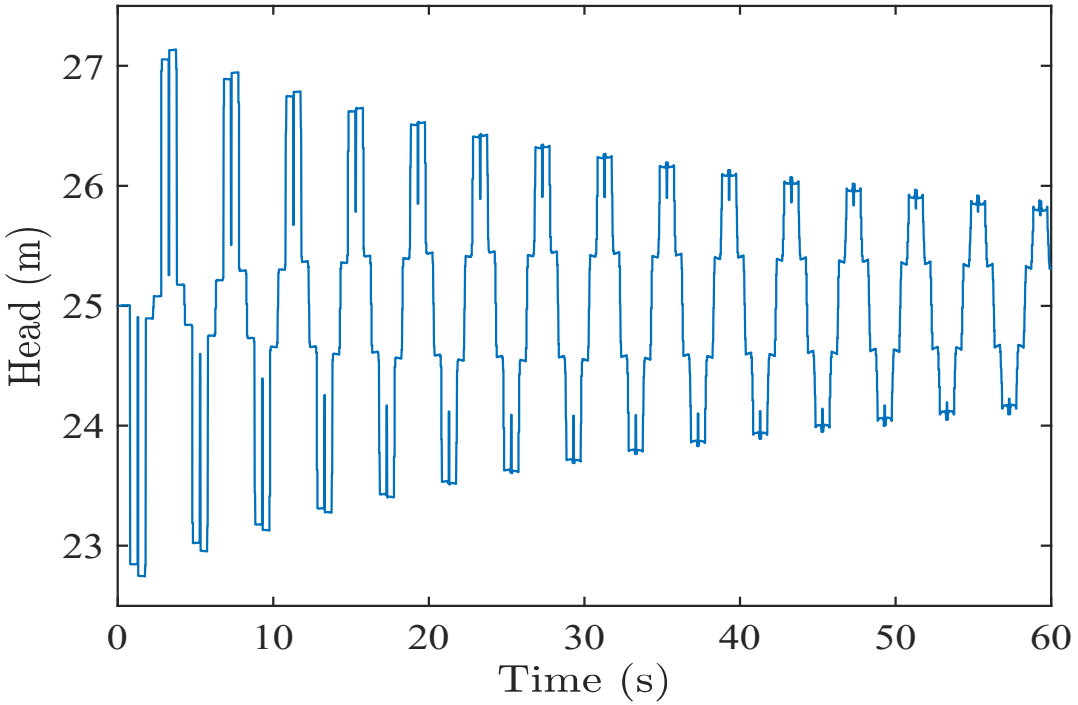

Figure 5.5: Time trace from Cases 1, 3, and 4

The 11th, 13th, and 15th harmonics are selected as the examples for burst detection and location estimation. Utilizing the technique in Du et al. (2021) provides the discrete harmonic spectrogram (DHS) of the corresponding harmonics, which is shown in Figure 5.6. The steady friction damping is calculated as $R = 0.0024$, based on the equation presented in Du et al. (2021). Fitting the Fourier solution for each harmonic shown in Eq. (5.4) provides the corresponding total damping values, which are $R+R_{11B} = 0.0716$, $R+R_{13B} = 0.0866$, and $R+R_{15B} = 0.0356$. Subtracting the steady friction damping from the total damping provides the burst damping values of each harmonic, which are $R_{11B} = 0.0692$, $R_{13B} = 0.0842$, and $R_{15B} = 0.0332$. The corresponding utilized values of the damping ratios are $R_{13}/R_{11} = 1.2168$, $R_{15B}/R_{13B} = 0.3943$, and $R_{15B}/R_{11B} = 0.4798$. Based on Step 4 of the algorithm in the previous section, rounding down the target solution to dimensionless burst location with the precision unit of 0.1 enables the harmonics with downgraded orders to be applied to the same damping ratio values. Specifically, based on Step 5, the applied damping ratios for the determination of the possible truncated solutions

become $R_{3B}/R_{1B} = 1.2168$, $R_{5B}/R_{3B} = 0.3943$, and $R_{5B}/R_{1B} = 0.4798$. Substituting the damping ratios of the harmonics with downgraded orders into Eq. (5.5) provides the resultant solutions. The resultant solutions are: $x_B^{**} = 0.2418$ using $R_{3B}/R_{1B} = 1.2168$; $x_B^{**} = 0.2338$ and $x_B^{**} = 0.1568$ using $R_{15B}/R_{13B} = 0.3943$; $x_B^{**} = 0.2303$ and $x_B^{**} = 0.1763$ using $R_{15B}/R_{11B} = 0.4798$.

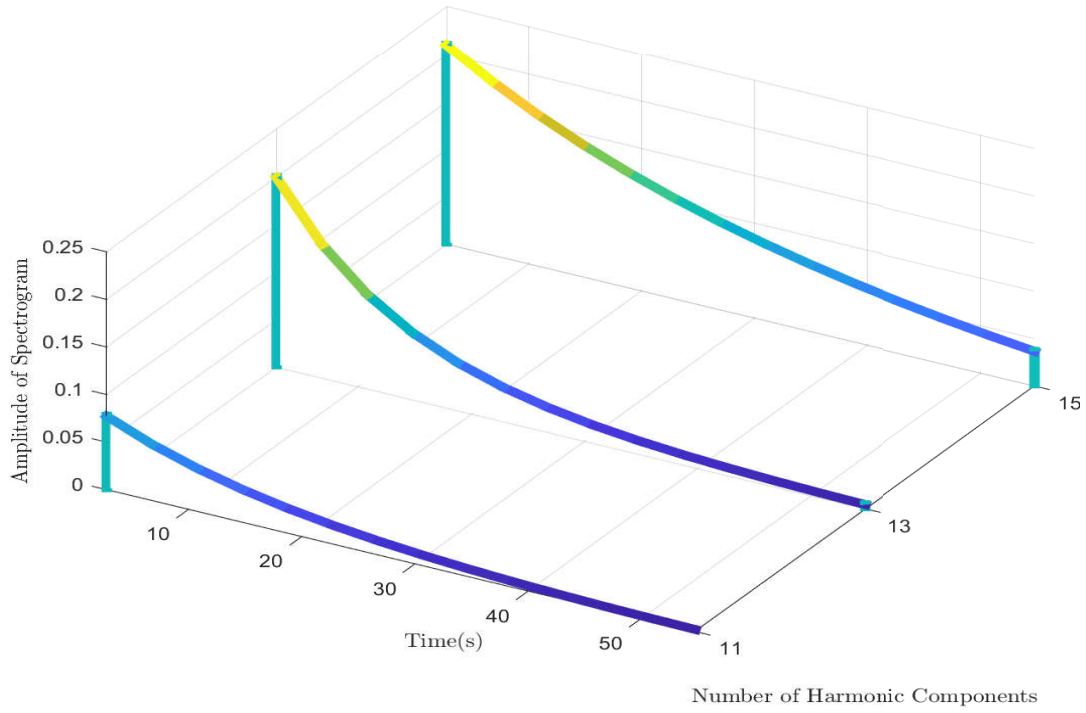

Figure 5.6: Discrete harmonic spectrogram from Case 1

According to Step 6 of the algorithm, although the target solution has been truncated with the precision unit of 0.1, the second decimal places of the resultant solutions is taken into consideration to ensure the accuracy of the first decimal place. Additionally, all the resultant solutions in the bracket with the length of 0.1 should be taken into consideration. Therefore, it can be noticed that the resultant solutions are located in the bracket of (0.15 0.25). Therefore, the values of the first decimal place of the target solution could be 1 or 2, indicating that the range of the target solution is [0.1 0.3], based on Step 7 of the algorithm.

Due to the symmetry of the imaginary mirror part of the RPV system

$$\hat{x_B}^* = \frac{x_B}{L+L'} = \frac{x_B}{2L} = \frac{x_B^*}{2} \tag{5.8}$$

and thus,

$$x_B^* = 2\hat{x_B}^* \tag{5.9}$$

where $\hat{x_B}^*$ is the directly determined dimensionless burst location, the mirror part of the pipeline system has been neglected. Therefore, the final range of the dimensionless burst location is [0.2 0.6], based on Eq. (5.9), which corresponds to a location from 200 m to 600 m from the upstream boundary of the pipeline. The incorrect solutions that correspond to $R_{13}/R_{11} = 1.2168$, $R_{15B}/R_{13B} = 0.3943$, and $R_{15B}/R_{11B} = 0.4798$, such as $x^* = 0.94$, have been excluded. To date, Steps 1 to 7 of the algorithm in the previous section have been successfully applied.

The applied pipeline system for the conducted numerical verifications is the RPV system; therefore, the minimal length of the correct range is 0.2 instead of 0.1, based on Eq. (5.9). However, based on the resultant range of [0.2 0.6] of the pipeline from Case 1, the length of the resultant range is 0.4, which is greater than the length of the correct range. Therefore, the accuracy enhancement strategies in Steps 8 and 9 shown in the previous section have been applied to identify the correct range and narrow the correct range, respectively, which are utilizing more harmonics and truncating the precision of the target solution with the precision unit of 0.01 in the range of [0.2 0.6].

Utilizing different harmonics and damping ratios may provide different dimen-

sionless burst location ranges, as the examples shown in Step 8 in previous section. However, the correct range should always be one/part of the resultant ranges/range, since the burst location remains unchanged, and thus the burst damping for each harmonic remains the same. Accordingly, the correct range should be one/part of the resultant ranges/range when utilizing the three damping ratios of each group of test in Step 8. Therefore, utilizing more harmonics and damping ratios will provide the highest occurrence in the correct range. In order to verify this aspect of the algorithm, Case 1 has been re-conducted utilizing the 11th, 13th, 15th, 17th, and 19th harmonics. Six groups of tests have been conducted, and the applied damping ratios are shown in Table 5.1. As mentioned in Step 6 in previous section, since one damping ratio value may correspond to multiple dimensionless burst locations, and all the resultant solutions in the bracket with the length of 0.1 should be considered, multiple resultant ranges of the dimensionless burst location may be generated for each test. The resultant ranges of the dimensionless burst location of the conducted tests are summarized in Table 5.2.

Table 5.1: Applied damping ratios for re-conducted Case 1 utilizing more harmonics

Test Number	Damping ratio 1	Damping ratio 2	Damping ratio 3
1	13/11	15/13	15/11
2	13/11	17/13	17/11
3	13/11	19/13	19/11
4	15/13	17/15	17/13
5	15/13	19/15	19/13
6	17/15	19/17	19/15

Table 5.2: Resultant dimensionless burst location ranges for re-conducted Case 1 utilizing more harmonics

Test Number	Resultant x_B^* ranges
1	[0.2 0.6]
2	[0.2 0.6], [0.4 0.6]
3	[0.2 0.6], [0.4 0.6]
4	[0.2 0.4], [0.6 1], [0.8 1]
5	[0.2 0.4], [0.2 0.6]
6	[0.2 0.4], [0.6 1], [0.8 1]

The corresponding distribution is generated and shown as a histogram in Figure 5.7. The range that has the highest occurrence is indicated in Figure 5.7, which is the correct range, [0.2 0.4], corresponding to 200 m to 400 m from the upstream boundary of the pipeline. The resultant correct range can be further narrowed with higher accuracy when determining not only the first but also the second decimal place of the truncated solution to the dimensionless burst location. For example, rounding down the target solution with the precision unit of 0.01 in Step 4 enables the 1st, 3rd, and 5th harmonics to be applied to the analysis for the 101st, 103rd, and 105th harmonics, as implemented in Case 1. Applying Steps 3 to 7 of the algorithm in the paper in the range of [0.2 0.4] provides the resultant range of [0.24 0.26], which contains the correct solution, 0.25. The result is summarized in Table 5.5. The maximum burst localization error is 0.01%. The determined burst damping and the location range confirm the presence of the burst, and the burst location is estimated by using the algorithm in the previous section.

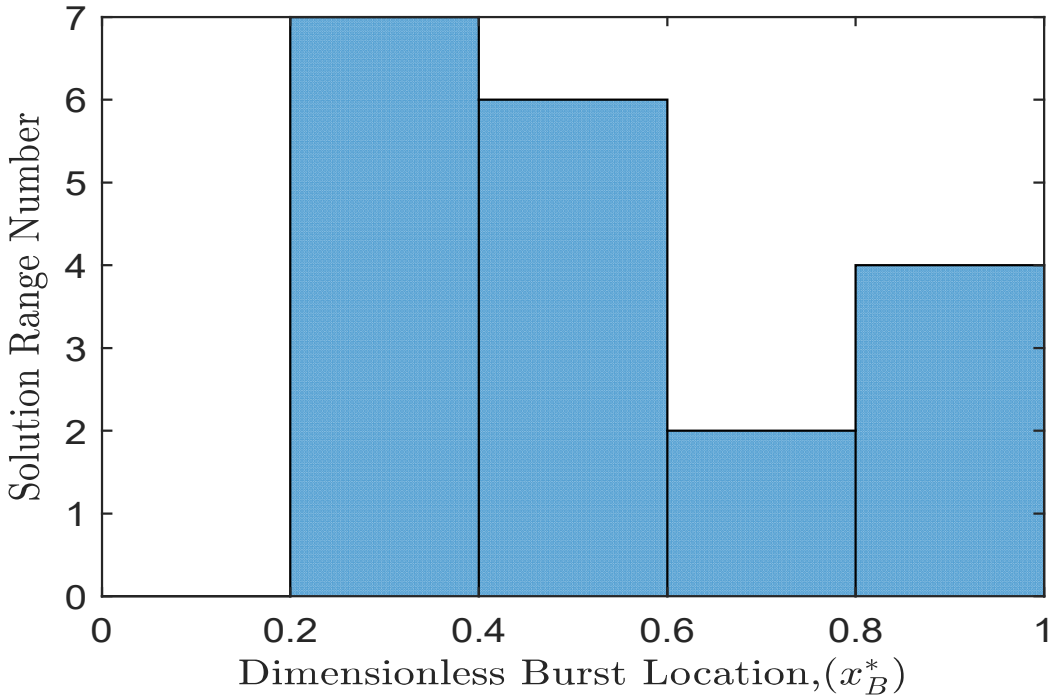

Figure 5.7: Resultant dimensionless burst location range distribution from reconducted Case 1

5.4.2 Verification of a Different Burst Location

In order to verify that the algorithm can be applied to a different burst location scenario, Case 2 has been conducted. In this case, the burst location is moved from $x_B^* = 0.25$ to $x_B^* = 0.68$, as shown in Figure 5.8, while all other parameters remain the same as in Case 1. The time trace and the example DHS are shown in Figures 5.9 and 5.10 respectively. Replicating the same analysis process as in Case 1, the applied burst damping is determined as $R_{11B} = 0.0656$, $R_{13B} = 0.0753$, $R_{15B} = 0.0021$, $R_{17B} = 0.0622$, $R_{19B} = 0.0824$, $R_{101B} = 0.0282$, $R_{103B} = 0.086$, $R_{105B} = 0.0362$. Utilizing the algorithm in this paper, the determined range using from the 11th to 19th harmonics for the first decimal place determination is $[0.6 \quad 1]$, which is indicated in Figure 5.8 as range with one decimal place. The determined range using the 101st, 103rd, and 105th harmonics for the first and the second decimal places determination is $[0.68 \quad 0.72]$, which is indicated in Figure 5.8 as range with two decimal places. The range of $[0.68 \quad 0.72]$ corresponds to from 680 m to 720 m of the pipeline. The corresponding result is shown in Table 5.5, and verifies the algorithm for a different burst location.

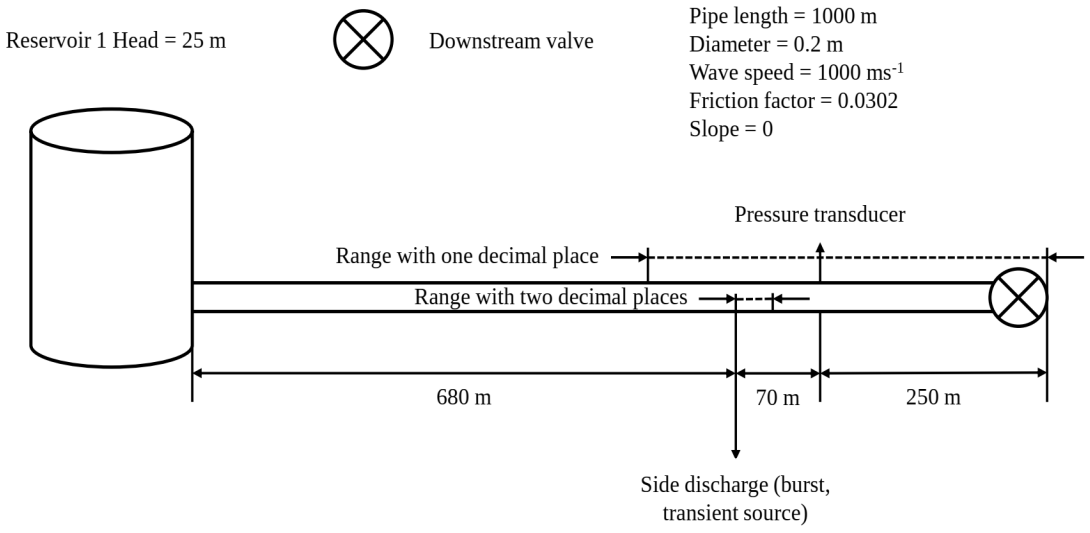

Figure 5.8: RPV system configuration for Case 2

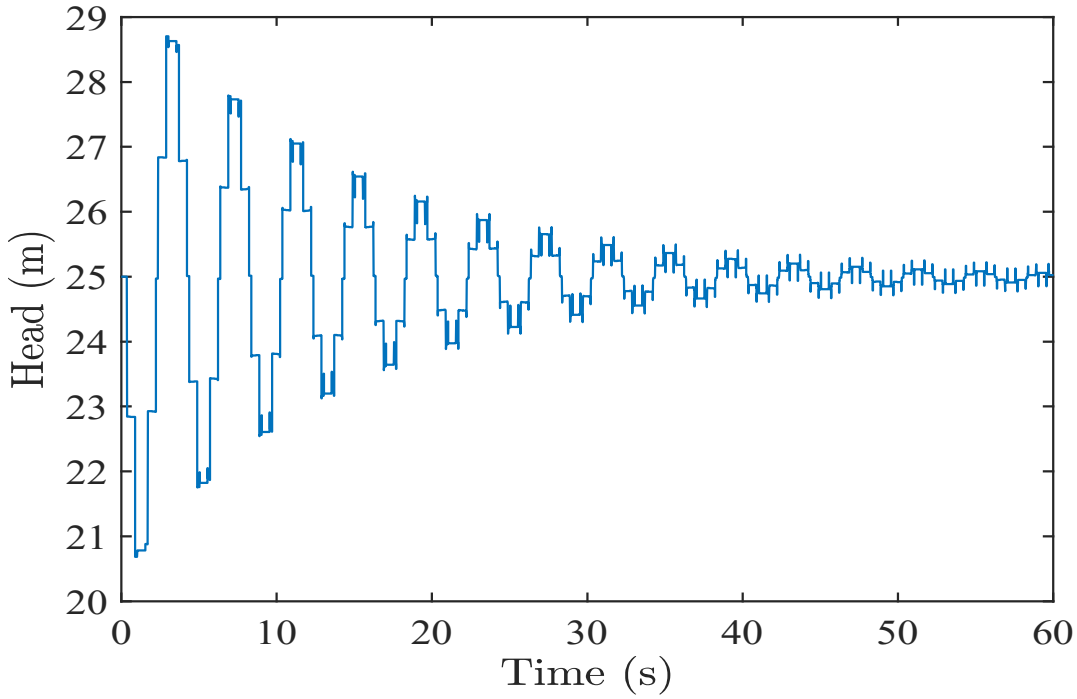

Figure 5.9: Time trace from Case 2

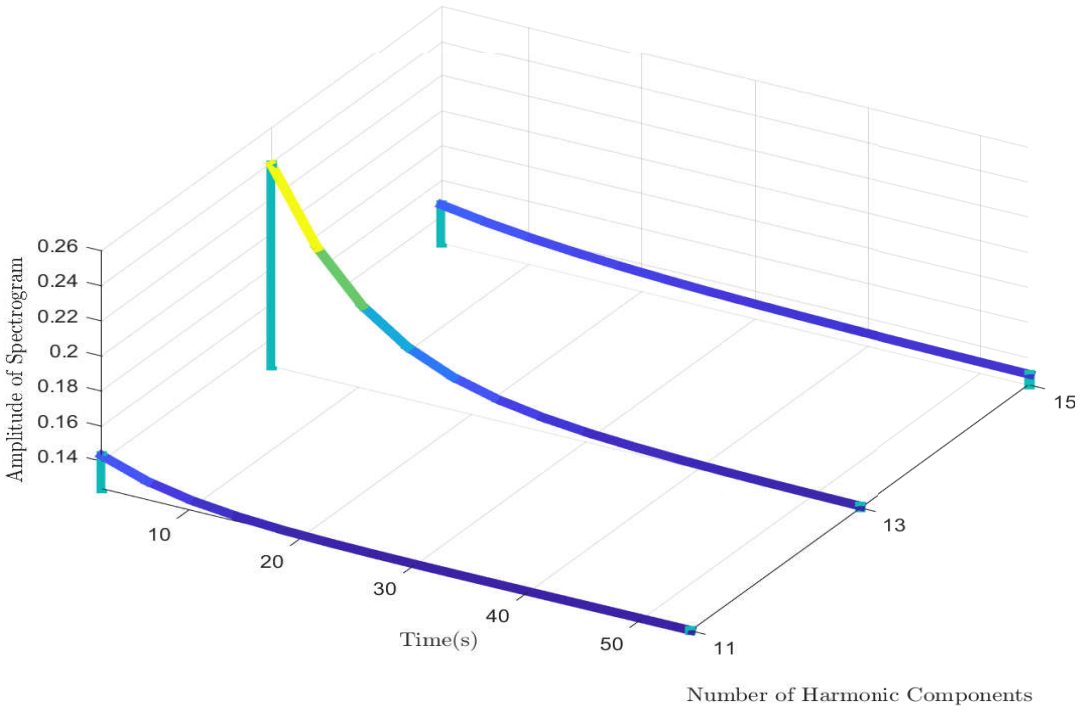

Figure 5.10: Discrete harmonic spectrogram from Case 2

5.4.3 Verification of Real-time Data Analysis Capability

Case 3 has been implemented to demonstrate that the algorithm can be applied to the signal analysis process with a user-defined window length and gap for real-time data analysis, as shown in Du et al. (2021). It is worth noting that the real-time data analysis becomes possible when analyzing the signal window by window, so the window can be moved slightly to adapt to actual data acquisition speed, which is the reciprocal of the sampling rate. This indicates that every new data point that is acquired can be analyzed one time step at a time when the window gap equals the reciprocal of the sampling rate. Accordingly, in Case 3, the analyzed window length and gap are set to be 20 s and 0.01 s, respectively, of which the window gap is the reciprocal of the sampling rate, as an example. All other parameters remain the same as in Case 1, including the burst and measurement locations. The applied time trace is shown in Figure 5.5. The example DHS is shown in Figure 5.11. Applying the same signal analysis process provides the range of the dimensionless location to be from [0.24 0.26], which corresponds to 240 m to 260 m of the pipeline. The result of Case 3 is summarized in Table 5.5, and verifies that the algorithm is applicable to the signal analysis with a user-defined window length and gap for real-time burst detection and location estimation.

5.4.4 Verification of Any Sequence of Harmonics Utilization Capability

Case 4 has been conducted to verify the applicability of applying the algorithm to any sequence of harmonics. In Case 4, the 51st, 53rd, 55th, 57th, 59th, 101st, 103rd, and 105th harmonics are selected as the examples, while all other parameters remain the same as in Case 3. The DHS of the 51st, 53rd, and 55th harmonics is shown in Figure 5.12, as an example. Replicating the signal

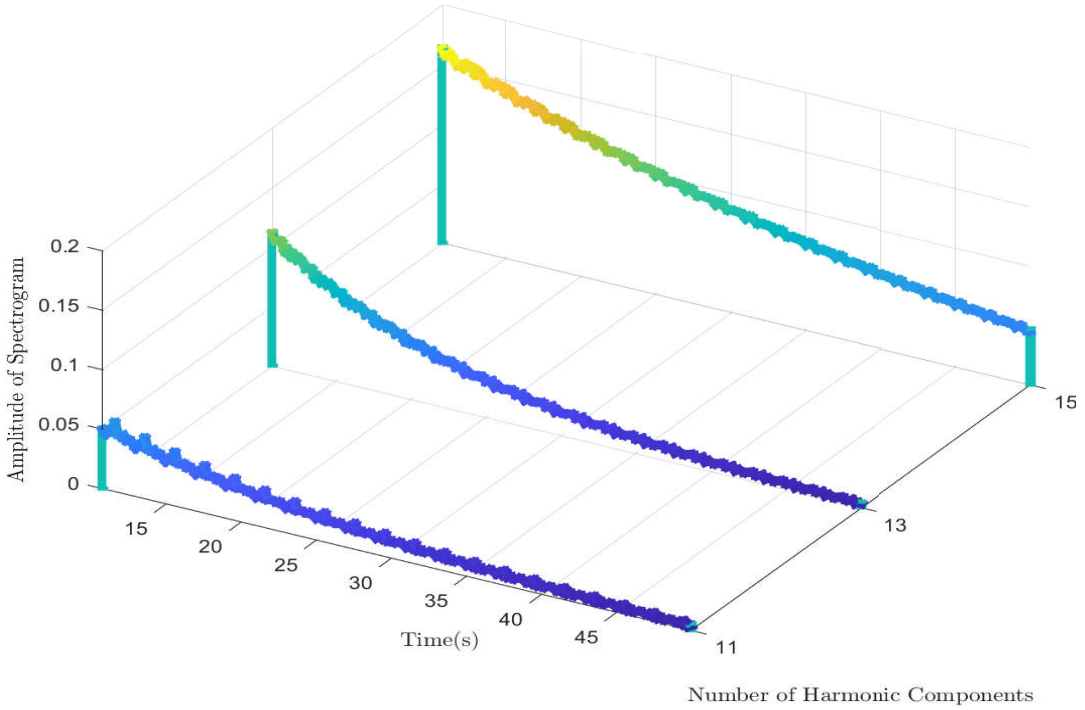

Figure 5.11: Discrete harmonic spectrogram from Case 3

analysis process in Case 3, the determined range of the dimensionless burst location is from [0.24 0.26], which corresponds to 240 m to 260 m of the pipeline. Both burst detection and location estimation are achieved using any sequence of harmonics, based on the result from Case 4, which is shown in Table 5.5.

According to accuracy enhancement aspect of the algorithm in the paper, the target solution to dimensionless burst location, x_B^*, can be truncated with different precision units to adapt to the selected harmonics, and can be utilized in Step 9 for accuracy enhancement. In order to verify this aspect, three additional tests have been conducted. In Test 1, the target solution x_B^* is truncated with the precision unit of 0.1, and the utilized harmonics are the 11th, 13th, 15th, 17th, and 19th harmonics. In Test 2, the target solution x_B^* is truncated with the precision unit of 0.05, and the utilized harmonics are the 21st, 23rd, 25th, 27th, and 29th harmonics. In Test 3, the target solution x_B^* is truncated with the precision unit of 0.02, and the utilized harmonics are the 51st, 53rd, 55th,

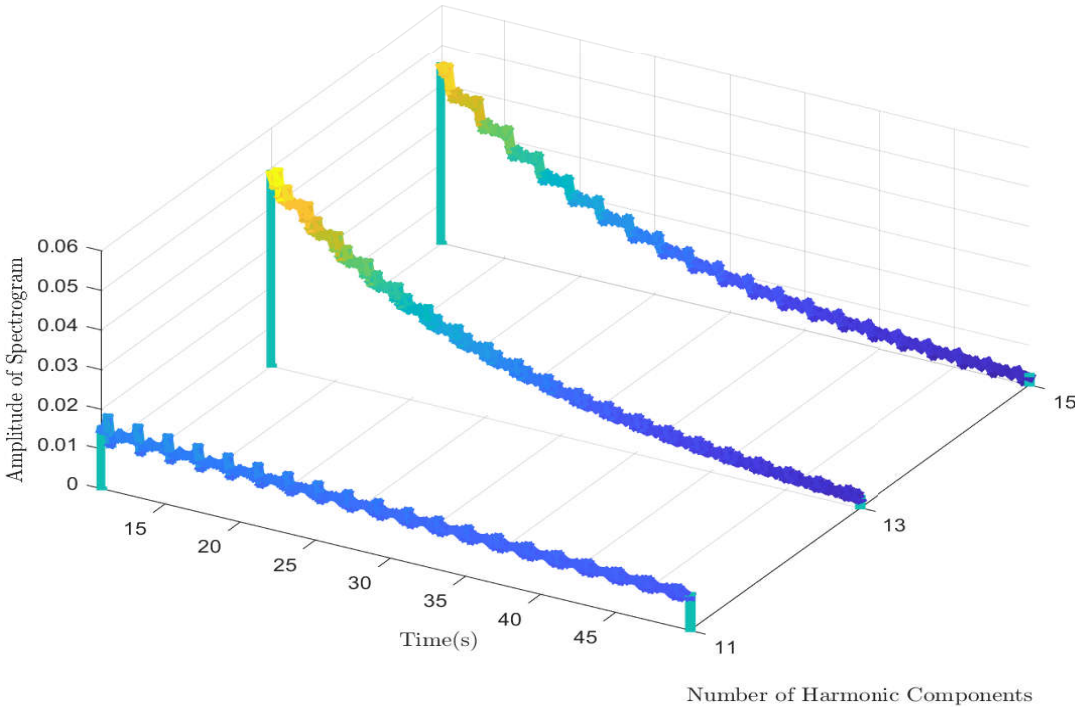

Figure 5.12: Discrete harmonic spectrogram from Case 4

57th, and 59th harmonics. The conditions of the three tests are summarized in Table 5.3. Applying Steps 1 to 8 of the algorithm to Test 1 provides the resultant range of [0.2 0.4]. Based on Step 9 of the algorithm, applying the same steps in the range of [0.2 0.4] to Tests 2 and 3 provides the resultant ranges of [0.2 0.3] for Test 2, and [0.2 0.26] for Test 3. The results of the three tests along with the lengths of the resultant ranges are summarized in Table 5.4 for comparison. Based on the results shown in Table 5.4, it can be seen that as the resolution of the applied precision unit is increased, with the increased order number of the corresponding applied harmonics, the resultant dimensionless burst location range is narrowed from Tests 1 to 3, which verifies the accuracy enhancement aspect of the algorithm in the previous section. Additionally, the additional tests verify the capability of the algorithm of utilizing any sequence of harmonics.

Table 5.3: Conditions of additional tests of Case 4

Test Number	Precision unit	Applied harmonics order number
1	0.1	11, 13, 15, 17, 19
2	0.05	21, 23, 25, 27, 29
3	0.02	51, 53, 55, 57, 59

Table 5.4: Results of additional tests of Case 4

Test Number	Resultant x_B^* range	Length of resultant range
1	[0.2 0.4]	0.2
2	[0.2 0.3]	0.1
3	[0.2 0.26]	0.06

5.4.5 Discussion of Numerical Verification

The results from the conducted numerical cases verify the approach in the paper. The algorithm can be successfully utilized for pipe burst detection and location estimation utilizing the information contained in any sequence of harmonics with a user-defined window length and gap. Accordingly, the successful application with a user-defined window length and gap verifies the approach to be utilized for real-time data monitoring, based on the results from Cases 3 and 4. The utilization of more than three harmonics and the harmonics, of which the orders are higher than 100, can effectively enhance the accuracy of the result. The resultant burst damping and the range of the dimensionless burst location are the indicator of the occurrence of the burst, which can be utilized to achieve burst detection. The resultant range of the dimensionless burst location can be applied to estimate the burst location. Most of the incorrect solutions are excluded, based on the corresponding analysis processes and results. An experimental verification of the algorithm is presented in the next section.

Table 5.5: Final results of numerical cases with enhanced accuracy

Case Number	Real-time	x_B^*	Applied harmonics order number	Resultant x_B^* range
1	No	0.25	11, 13, 15, 17, 19, 101, 103, 105	[0.24 0.26]
2	No	0.68	11, 13, 15, 17, 19, 101, 103, 105	[0.68 0.72]
3	Yes	0.25	11, 13, 15, 17, 19, 101, 103, 105	[0.24 0.26]
4	Yes	0.25	51, 53, 55, 57, 59, 101, 103, 105	[0.24 0.26]

5.5 Experimental Verification

One experimental scenario has been conducted in the Robin Hydraulics Laboratory at the University of Adelaide, which is referred to as Case 5. The applied experimental pipeline is a 37.41 m long, straight pipeline, which is made of copper. A schematic diagram of the pipeline is shown in Figure 5.13.

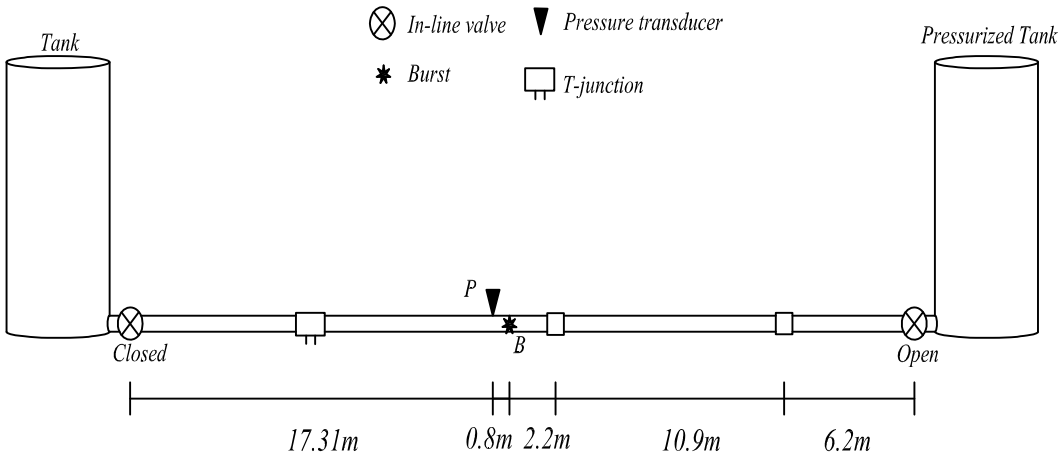

Figure 5.13: Experimental pipeline configuration for Case 5

The system type is RPV, since the downstream inline valve is fully closed to isolate the downstream tank. The burst is initiated at Point B, which corresponds to the dimensionless location $x_B^* = 0.51$, and the pressure transducer is located at Point P. More details of the experimental pipeline can be found in Du et al. (2020) and Du et al. (2021). A solenoid side-discharge valve was applied to initiate the burst, and the valve was opened at approximately 0.1 s, with negligible opening time. The head at the upstream tank is 3.065×10^5 Pa

(3.065 bar). The wave speed is 1320 m/s, and thus the fundamental period of this pipeline system is 0.113 s. The measured time trace is shown in Figure 5.14 with the sampling rate as 1×10^4 Hz. The window length and gap for the analysis have been selected as 0.113 s and 1×10^{-4} s, respectively, of which the window gap was set to be the reciprocal of the sampling rate for real-time data analysis. The utilized harmonics for the analysis are the 11th, 13th, 15th, 17th, 19th, 101st, 103rd, and 105th harmonics. The DHS of the 11th, 13th, and 15th harmonics are shown in Figure 5.15 as the example. Utilizing the algorithm that is applied to the numerical scenarios provides the total damping. The actual (total) friction damping is calibrated as $R_{11} = 0.0463$, $R_{13} = 0.0503$, $R_{15} = 0.0542$, $R_{17} = 0.0577$, $R_{19} = 0.0611$, $R_{101} = 0.1485$, $R_{103} = 0.1555$, and $R_{105} = 0.1608$ utilizing the UFWH model. Replicating the same analysis process and accuracy enhancement strategies as in the numerical verifications determines the range of the dimensionless burst location from $[0.5 \quad 0.53]$, which corresponds to from 18.705 m to 19.8273 m from the upstream of the pipeline. The burst is detected based on the determined burst location range. The correct solution to the dimensionless burst location is contained in the resultant range, with a maximum error of 2%, and thus, the burst location estimation is achieved. The result from Case 5 verifies the approach in the paper on a real pipeline for real-time burst detection and location estimation with acceptable accuracy.

In practice, unsteady friction damping is involved when utilizing the approach in the paper, as implemented in Case 5. Although the actual (total) friction damping, which is the summation of steady and unsteady friction damping, can be calibrated computationally, the unsteady friction damping may lead to the confusion about the burst detection. This is because there may be a difference between the theoretical and actual values of the unsteady friction damping due to various reasons, such as external noise. Additionally, in practice, unsteady friction damping is dependent on the frequency (Kjerrumgaard Jensen et al., 2018). Based on these two specific analyses, when there is a transient event introduced

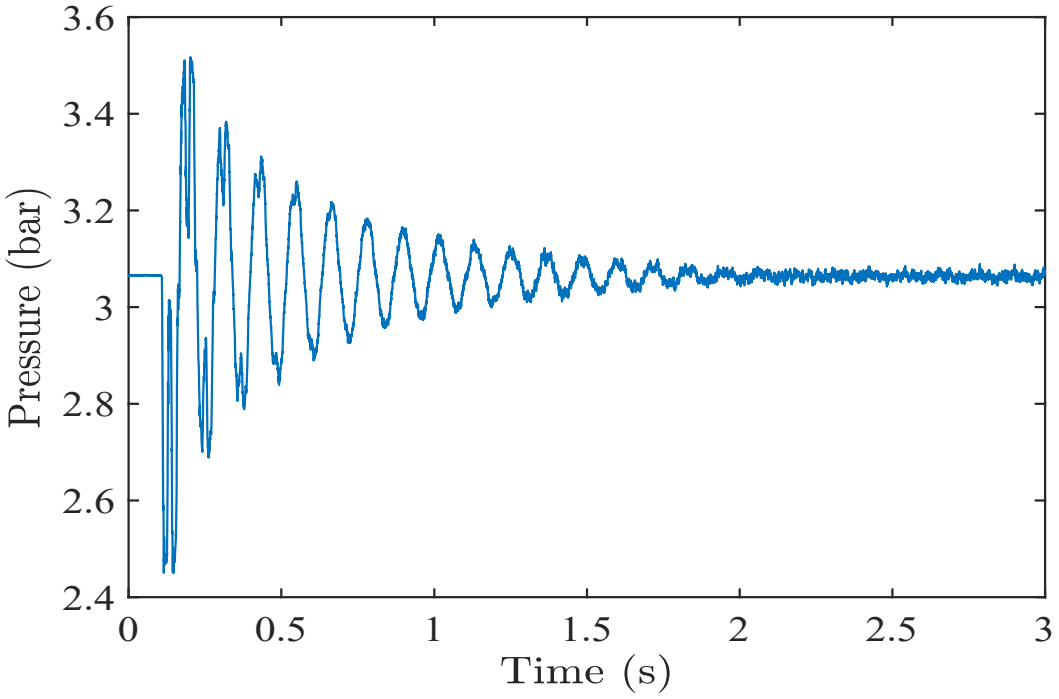

Figure 5.14: Time trace from Case 5

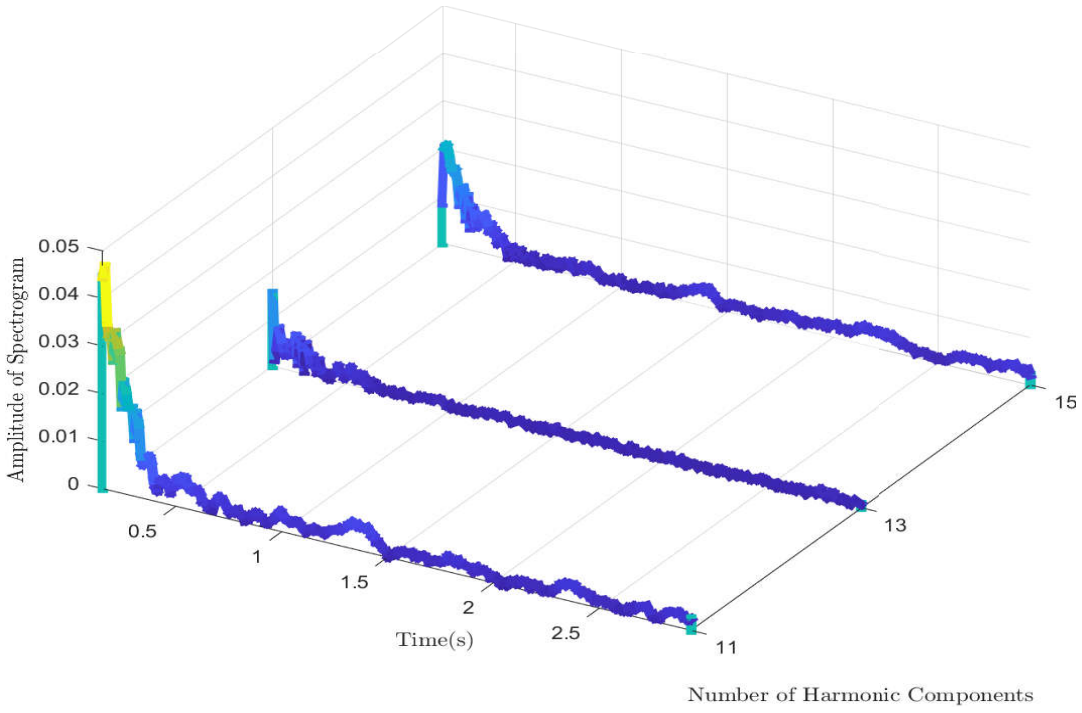

Figure 5.15: Discrete harmonic spectrogram from Case 5

under the burst-free condition due to, for example, sudden valve closure, the resultant damping, after subtracting the calibrated actual (total) friction damping from the total damping, may be non-zero and frequency-dependent. Accordingly, such the non-zero and frequency-dependent damping may be treated as the burst damping, which may result in the fake burst presence. Therefore, the redundant burst detection and location estimation processes may be applied. In order to avoid such a condition that may happen in practice, a method is proposed with an example in the next section.

5.6 Discussion of Unsteady Friction Damping

The previously-mentioned problem that the unsteady friction in practice may cause redundant burst detection and location estimation processes can be solved by following two steps. Firstly, extract the total damping for more harmonics, and then subtract the corresponding calibrated actual (total) friction damping from the total damping. There is no burst damping contained if the resultant damping from the first step is zero. Accordingly, there is no presence of the burst. However, if the resultant damping is non-zero, the second step should be applied. Secondly, compare the trends of the resultant damping and the theoretical unsteady friction damping versus frequency. Accordingly, the resultant damping from the first step can be identified that if it is the burst damping or the unsteady friction damping. This is because the trend versus frequency of unsteady friction damping is rising, but the trend versus frequency of burst damping is oscillating. The details are now presented.

According to the Vardy & Brown unsteady friction equation in Kjerrumgaard Jensen et al. (2018), the weighting function is the only parameter that is dependent on the frequency. The trend versus frequency of the weighting function is rising. According to Eq. (5.3), the trend versus frequency of burst damp-

ing is oscillating when n increases due to the periodicity of the square of the sinusoidal function. An example of a comparison between these two functions is plotted in Figure 5.16 with the fundamental frequency of 10 Hz and dimensionless burst location as 0.25 of the applied pipeline system shown in Figure 5.4. It is worth noting that their amplitudes are normalized by their maximum values.

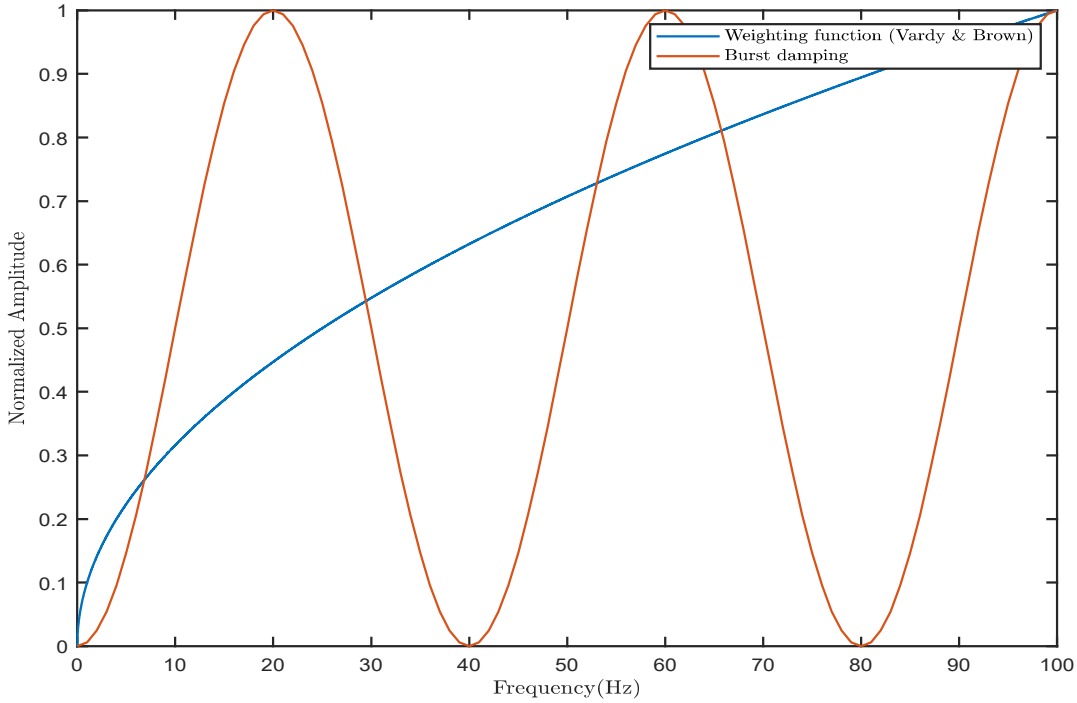

Figure 5.16: Comparison between the weighting function of unsteady friction damping and the burst damping

From Figure 5.16, it can be seen that the trends versus frequency of unsteady friction damping and burst damping are very different. Therefore, computing the damping of more harmonics and comparing the trends versus frequency can be utilized to solve the previously-mentioned problem. For example, for the 11th, 13th, and 15th harmonics in Case 5, the calibrated actual (total) damping increases with increasing harmonic orders, while the burst damping decreases as $R_{11B} = 3.879 \times 10^{-2}$, $R_{13B} = 5.78 \times 10^{-3}$, and $R_{15B} = 3.02 \times 10^{-3}$ with increasing harmonic orders. Hence, oscillating damping can be utilized as an alternative indicator for the confirmation of burst damping, and thus, for burst detection.

5.7 Conclusion

The damping caused by the presence of the burst is contained in the transient pressure signal caused by the sudden burst. Therefore, all the harmonic components of the signal are damped differently due to the burst. The utilization of the burst information contained in the harmonics of the measured signal can be applied to burst detection and location estimation.

The approach in this paper illustrates that any sequence of damped harmonics of the signal can be utilized to calculate the burst damping. The damping ratios of any sequence of damped harmonic can be utilized to determine the range of the dimensionless burst location. Both the calculated burst damping and the resultant dimensionless burst location range can be applied as the indicator for burst detection. The resultant range of the dimensionless burst location can be used to estimate the location of the burst with acceptable accuracy.

The approach in this paper has been verified both numerically and experimentally. The effects from different burst location, analyzed window lengths and gaps, and different sequences of harmonics have been explored. The utilization of user-defined window lengths and gaps makes the real-time signal processing possible by letting the window gap be the reciprocal of the sampling rate. Both the numerical and experimental studies provide sufficient results for verification. The difference between unsteady friction damping and burst damping has been discussed with an example, which provides a solution to the transients generated by a non-burst source and offers an alternative indicator for burst detection.

The approach in this paper extends the application of DOFT techniques for real-time burst detection and location estimation from the low frequency range to the high frequency range. In addition, the exploration of the algorithm in this paper provides an insight into excluding incorrect solutions when utilizing

DOFT techniques to analyze a signal in the high frequency range. The approach broadens the scope of the capability of sensor and sensing system of detecting and estimating burst using DOFT in practice, since no specific harmonic is required. This paper focuses on metallic pipes, hence the pipe wall viscoelasticity is not discussed in detail.

Chapter 6

Linking the Damping of Fluid Transients and Frequency Response Diagram Methods for Pipe Leak and Burst Detection and Localization

(Journal Paper 4)

Xiao-xuan Du, Martin F. Lambert, Lei Chen, and Eric Hu

Submitted to *Journal of Hydraulic Engineering*

Statement of Authorship

Title of Paper	Linking the Damping of Fluid Transients and Frequency Response Diagram Methods for Pipe Leak and Burst Detection and Localization
Publication Status	☐ Published ☐ Accepted for Publication ✓ Submitted for Publication ☐ Unpublished and Unsubmitted work written in manuscript style
Publication Details	Du, X.-x., Lambert, M. F., Chen, L., and Jing Hu, E. (Under review). Linking the Damping of Fluid Transients and Frequency Response Diagram Methods for Pipe Leak and Burst Detection and Localization. Journal of Hydraulic Engineering.

Principal Author

Name of Principal Author (Candidate)	Xiaoxuan Du
Contribution to the Paper	Conception and design of project Analysis and interpretation of research data Drafting the paper
Overall percentage (%)	75%
Certification:	This paper reports on original research I conducted during the period of my Higher Degree by Research candidature and is not subject to any obligations or contractual agreements with a third party that would constrain its inclusion in this thesis. I am the primary author of this paper.
Signature	Date 14/01/2022

Co-Author Contributions

By signing the Statement of Authorship, each author certifies that:

i. the candidate's stated contribution to the publication is accurate (as detailed above);
ii. permission is granted for the candidate in include the publication in the thesis; and
iii. the sum of all co-author contributions is equal to 100% less the candidate's stated contribution.

Name of Co-Author	Martin F. Lambert
Contribution to the Paper	Conception and design of project Analysis and interpretation of research data Critically revising the paper
Signature	Date 19/1/2022

Name of Co-Author	Lei Chen
Contribution to the Paper	Revising the paper critically Conception and design of project
Signature	Date 18/01/2022

Please cut and paste additional co-author panels here as required.

Name of Co-Author	Eric Jing Hu		
Contribution to the Paper	Revising the paper critically Conception and design of project		
Signature		Date	18/1/2022

Abstract

The purpose of the paper is to illustrate the relationship between methods that utilize the damping of fluid transients and the approaches based on the frequency response diagram, and to discuss the two methods for both leak and burst detection. Although both the methods are based on the Fourier transform of the signal, they have different signal processing approaches. This paper reveals the mathematical relationship between the two methods for both the leak and the burst problems. The mathematical relationship between the two methods has been verified both numerically and experimentally. Additionally, the two methods have been compared from the perspectives of input signal bandwidth, problem type, low sampling rate capability, robustness, and real-time data monitoring capability. The applicability of the two methods in these aspects has been discussed.

6.1 Introduction

Transient pressure-based pipeline leak detection methods have been explored by diverse researchers, based on meeting the inspection process requirement during the working cycle of the system (Covas et al., 2005a; Hovey and Farmer, 1993; Lee et al., 2006; Liggett and Chen, 1994; McInnis and Karney, 1995; Pudar and Liggett, 1992; Wang et al., 2002; Ziegel, 1987). Frequency domain-based methods can be applied successfully in practice with high accuracy (Ebina et al., 2011; Gong et al., 2013a; Hutton and Kapelan, 2015a; Kang and Lansey, 2012; Lee et al., 2005a, 2008; Parikh and Sundaresan, 2008; Vítkovskỳ et al., 2011; Wang et al., 2002).

Leak detection methods based on the damping of fluid transients (DOFT) have been researched by Wang et al. (2005; 2002) and Nixon et al. (2006). These methods utilize the damping in the transient signal caused by the leak in the

pipeline. By computing the damped harmonic components in the results of Fourier transform, fast Fourier transform (FFT) or discrete Fourier transform (DFT), and utilizing the different damping of various harmonic components, the leak can be confirmed and located (Wang et al., 2005, 2002). Furthermore, the validity range of the DOFT method has been explored in terms of different materials (Nixon et al., 2006). Du et al. (2020) improved the technique and applied it to the burst problem. Additionally, Du et al. (2021) further improved the technique from the perspective of real-time burst detection, localization, and cross-sectional area quantification with low data sampling and transmission rates.

The application of frequency-based methods to the area of pipeline leak detection has been explored (Gong et al., 2013a, 2016a, 2018a,b, 2016b; Lee et al., 2006, 2005a,b, 2008). The frequency response diagram (FRD) methods in Gong et al. (2013a; 2016a; 2018a; 2018b; 2016b) and Lee et al. (2006; 2005a; 2005b) apply the theory of frequency response function (FRF) on the basis of the energy cross-spectral density of the measured (i.e., output) and input signals, which is the FFT of the cross-correlation function. The leak can be detected by computing the damped FRD, and can then be located, for example, by substituting the peak values of the first three resonance responses from the resultant FRD to the solution of the leak location (Gong et al., 2013a).

The signal processing approaches of the DOFT and FRD methods are based on the theory of the Fourier transform, and have been verified both numerically and experimentally. However, the specific steps of the signal processing approaches in these methods are different. In the DOFT methods, the FFT/DFT of the output signal is utilized. The resultant amplitudes of the FFT/DFT of each harmonic component were compared window by window to determine the damping by fitting the exponential equation form (Wang et al., 2002). In the DOFT method, only the measured signal was utilized, while in the FRD method, both the input and measured signals were applied, and the resultant FRD was computed from the output signal, which is completely damped after the input

signal is applied.

In the FRD methods, the FRD was generated by using the general form of FRF, which utilizes both the input and the output signals. The output signal is the measured signal from the occurrence of the transient until the steady state is achieved. The input signal is the source of the transient. In Lee et al. (2006; 2005a; 2005b), the input signal was modified from a step function into an impulse function by adding a reversed, shifted input signal. During the process of generating FRD, the FFT of the cross-correlation and auto-correlation functions were computed for the whole time period from the transient until the steady state (Gong et al., 2013a, 2016a, 2018a,b, 2016b; Lee et al., 2006, 2005a,b, 2008).

The following gaps exist in the reviewed methods in the literature. Firstly, no exploration has been conducted in terms of the mathematical relationship between these two Fourier transform-based techniques. Secondly, the applicability of the FRD method has not been explored in the areas of burst detection, low sampling rate, robustness, and real-time data monitoring. Thirdly, no research or corresponding discussion have been conducted between the two methods in terms of input signal bandwidth, problem type, low sampling rate capability, robustness, and real-time data monitoring capability. This paper presents the detailed mathematical modeling that reveals the exact relationship between the DOFT and FRD methods from the perspectives of both the leak and the burst problems. This relationship has been verified both numerically and experimentally. In addition, an exploration of the two methods has been undertaken in terms of the previously mentioned aspects.

In the following section, the mathematical relationship between the DOFT and FRD methods is presented, followed by ten numerical verifications. Then, two experimental verifications are presented, followed by the conclusion and discussion.

6.2 Relationship between Transient Damping and Frequency Response Function

The general solution of the dimensionless measured head disturbance, h^*, in Wang et al. (2002) for leak problem is expressed as

$$h^*(x^*,\ t^*) = \sum_{n=1}^{\infty} \left\{ e^{-(R+R_{nL})t^*} [A_n cos(n\pi t^*) + B_n sin(n\pi t^*)] sin(n\pi x^*) \right\} \quad (n = 1,\ 2,\ 3, \ldots) \tag{6.1}$$

where x^* and t^* in Eq. (6.1) are the non-dimensionalized distance along the pipe and the time respectively, using the following definitions

$$h^* = \frac{h}{H_1},\ t^* = \frac{t}{L/a},\ x^* = \frac{x}{L} \tag{6.2}$$

where h is the head disturbance caused by the leak, H_1 is the reference head, which is the head measured at the tank, t is the time, L is the length of the pipe, a is the wave speed, and x is the distance along the pipe. R is the friction damping, R_{nL} is the leak damping, and A_n and B_n are the Fourier coefficients expressed in Wang et al. (2002). By fitting the typical Fourier series form to Eq. (6.1), the amplitudes of the first and the nth harmonic component in each period are

$$E_n^{(1)} = -\frac{e^{-(R+R_{nL})(t_0^*+T^*)} - e^{-(R+R_{nL})t_0^*}}{(R+R_{nL})T^*} sin(n\pi x^*) \sqrt{A_n^2 + B_n^2} \tag{6.3}$$

$$E_n^{(m)} = E_n^{(1)} e^{-(R+R_{nL})(m-1)T^*} \quad (m = 1,\ 2,\ 3, \ldots) \tag{6.4}$$

respectively, where t_0^* is the dimensionless starting time of the analysis, T^* is the dimensionless fundamental period of the pipeline system, and m and n represent the number of the period and the harmonic component respectively.

The utilized FRF in Gong et al. (2013a; 2016a; 2018a; 2018b; 2016b) and Lee et al. (2006; 2005a; 2005b) is expressed as

$$H(\omega) = \frac{R_{in\&out}}{R_{in\&in}} \tag{6.5}$$

where $H(\omega)$ is the FRF, $R_{in\&out}$ is the Fourier transform of the cross-correlation function between input and output signals, and $R_{in\&in}$ is the auto-correlation function of the input signal. In fact, $R_{in\&out}$ is the cross spectral density of the input and output signals, and $R_{in\&in}$ is the auto spectral density of the input signal. However, Lee et al. (2006; 2005a; 2005b) modified the input signal into a finite energy form, and established the output signal as the finite energy signal, thus $R_{in\&out}$ and $R_{in\&in}$ are the cross and auto spectral densities in energy instead of power. According to the relationship between the correlation functions and convolution, and applying the general Fourier transform procedure, Eq. (6.5) becomes (Bracewell, 1965; Papoulis, 1962; Wiener, 1988)

$$H(\omega) = \frac{X(\omega)Y^*(\omega)}{X(\omega)X^*(\omega)} \tag{6.6}$$

where X and Y are the Fourier transform results of the input and output signals respectively, and Y^* is the conjugate of Y.

According to the derivation procedure of the Fourier transform, when $\omega = n\omega_0$, where ω_0 is the fundamental angular frequency of the system, the resonance responses, $X^*(\omega)$ and $Y^*(\omega)$ become

$$\begin{aligned} X^*(n\omega_0) &= X(n\omega_0) \\ Y^*(n\omega_0) &= Y(n\omega_0) \end{aligned} \tag{6.7}$$

since the imaginary number is canceled (Bell, 2012). It can be seen that when considering the resonance responses, Y^* in Eq. (6.6) is actually dimensional Eq. (6.4) when there is only one window of the whole signal, and the length of the window is equal to the time period from the application of input signal to the complete decay of output signal. The details of the derivation of the Fourier transform of Eq (6.4) in each period are presented in the Appendix. Therefore, the FRF in the FRD method is actually the Fourier series solution in the DOFT method scaled by the Fourier transform result of the input signal, with the window length of the time period from the application of input signal to the complete decay of output signal.

According to the time shift and linearity theorems of Fourier transform, adding the time shift formulation to the Fourier transform of the signal period by period is equivalent to the Fourier transform of the whole signal in the time period from the application of input signal to the complete decay of output signal. Therefore, the resonance responses in the Fourier transform of the signal in the dimensionless frequency domain in the time period from the application of input signal to the complete decay of output signal, $Y(n\omega_0^*)$, where ω_0^* is the dimensionless fundamental angular frequency of the system, can be expressed by Eq. (6.4), and shown as

$$Y(n\omega_0^*) = \sum_{m=1}^{N} E_n^{(1)} e^{-(R+R_{nL})(m-1)T^*} e^{-in\omega_0^*(m-1)T^*} \tag{6.8}$$

or

$$Y(nf_0^*) = \sum_{m=1}^{N} E_n^{(1)} e^{-(R+R_{nL})(m-1)T^*} e^{-i2\pi n f_0^*(m-1)T^*} \tag{6.9}$$

where N is the total number of periods contained in the time period from the application of input signal to the complete decay of output signal, and f_0^* is the dimensionless fundamental frequency of the system.

Based on the previous analysis and when considering the resonance responses in the dimensionless frequency domain, the mathematical relationship between the Fourier series solution in the DOFT method and the FRF in the FRD method is shown as

$$\begin{aligned} H(n\omega_0^*) &= \frac{X(n\omega_0^*)\sum_{m=1}^{N} E_n^{(1)} e^{-(R+R_{nL})(m-1)T^*} e^{-in\omega_0^*(m-1)T^*}}{\left[X(n\omega_0^*)\right]^2} \\ &= \frac{X(n\omega_0^*)\sum_{m=1}^{N} E_n^{(1)} e^{-(R+R_{nL}+in\omega_0^*)(m-1)T^*}}{\left[X(n\omega_0^*)\right]^2} \\ &= \frac{\sum_{m=1}^{N} E_n^{(1)} e^{-(R+R_{nL}+in\omega_0^*)(m-1)T^*}}{X(n\omega_0^*)} \end{aligned} \tag{6.10}$$

or

$$H(nf_0^*) = \frac{\sum_{m=1}^{N} E_n^{(1)} e^{-(R+R_{nL}+i2\pi n f_0^*)(m-1)T^*}}{X(nf_0^*)} \tag{6.11}$$

The dimensionless fundamental frequency and the dimensionless fundamental period in the terms $e^{-in\omega_0^*(m-1)T^*}$ and $e^{-i2\pi n f_0^*(m-1)T^*}$ in Eqs. (6.9) and (6.8), respectively, can be canceled, since the signal was analyzed for every fundamental period in Wang et al. (2002), and m and n in Eqs. (6.9) and (6.8) are inte-

gers, thus the terms $e^{-in\omega_0^*(m-1)T^*}$ and $e^{-i2\pi nf_0^*(m-1)T^*}$ are equal to unity in Eqs. (6.9) and (6.8). Therefore, Eqs. (6.10) and (6.11) are simplified as

$$H(n\omega_0^*) = \frac{\sum_{m=1}^{N} E_n^{(1)} e^{-(R+R_{nL})(m-1)T^*}}{X(n\omega_0^*)} \tag{6.12}$$

or

$$H(nf_0^*) = \frac{\sum_{m=1}^{N} E_n^{(1)} e^{-(R+R_{nL})(m-1)T^*}}{X(nf_0^*)} \tag{6.13}$$

Therefore, the mathematical relationship between the DOFT and FRD methods for the leak problem is revealed by Eqs. (6.12) and (6.13). According to the research into burst detection using the DOFT theory presented in Du et al. (2020), Eqs. (6.12) and (6.13) can be simplified into the following forms for the burst conditions

$$H(n\omega_0^*) = \frac{\sum_{m=1}^{N} E_n^{(1)} e^{-(R+R_{nB})(m-1)T^*}}{X(n\omega_0^*)} \tag{6.14}$$

or

$$H(nf_0^*) = \frac{\sum_{m=1}^{N} E_n^{(1)} e^{-(R+R_{nB})(m-1)T^*}}{X(nf_0^*)} \tag{6.15}$$

where $E_n^{(1)}$ has the same form as Eq. (6.3) but with R_{nB} instead of R_{nL}, and

R_{nB} is the burst damping which is defined in Du et al. (2020), and shown as

$$R_{nB} = K_B sin^2(n\pi x_B^*) \tag{6.16}$$

in which K_B is a self-defined burst parameter that contains the cross-sectional area of the burst, which is presented in Du et al. (2020), and x_B^* is the dimensionless burst location along the pipeline. According to the summation of the geometric sequence, Eqs. (6.14) and (6.15) can be simplified as

$$H(n\omega_0^*) = \frac{E_n^{(1)}(1 - e^{-(R+R_{nB})mT^*})}{X(n\omega_0^*)(1 - e^{-(R+R_{nB})T^*})} \tag{6.17}$$

or

$$H(nf_0^*) = \frac{E_n^{(1)}(1 - e^{-(R+R_{nB})mT^*})}{X(nf_0^*)(1 - e^{-(R+R_{nB})T^*})} \tag{6.18}$$

According to the leak localization solution for a reservoir-pipe-valve (RPV) system in Gong et al. (2013a), and substituting Eqs. (6.14) and (6.15), the burst localization solution can be expressed as

$$x_B^* = \frac{1}{\pi} arccos(\frac{\pm\sqrt{1+P_B}}{2}) \tag{6.19}$$

where P_B is a self-defined parameter, and shown as

$$P_B = \left\{ \left[\frac{E_5^{(1)}(1-e^{-(R+R_{5B})mT^*})}{X(5f_0^*)(1-e^{-(R+R_{5B})T^*})} - \frac{E_1^{(1)}(1-e^{-(R+R_{1B})mT^*})}{X(f_0^*)(1-e^{-(R+R_{1B})T^*})} \right] \frac{E_3^{(1)}(1-e^{-(R+R_{3B})mT^*})}{X(3f_0^*)(1-e^{-(R+R_{3B})T^*})} \right\} \Bigg/ \left\{ \left[\frac{E_3^{(1)}(1-e^{-(R+R_{3B})mT^*})}{X(3f_0^*)(1-e^{-(R+R_{3B})T^*})} - \frac{E_1^{(1)}(1-e^{-(R+R_{1B})mT^*})}{X(f_0^*)(1-e^{-(R+R_{1B})T^*})} \right] \frac{E_5^{(1)}(1-e^{-(R+R_{5B})mT^*})}{X(5f_0^*)(1-e^{-(R+R_{5B})T^*})} \right\} \tag{6.20}$$

Thus, the mathematical relationship between the DOFT and FRD methods for the burst problem is revealed by Eqs. (6.14) to (6.20). Ten numerical verifications have been conducted and presented in the next section. They are designed to verify the mathematical relationship, and compare and discuss the methods of the DOFT and FRD from the perspectives of input signal bandwidth, problem type, low sampling rate capability, robustness, and real-time analysis capability.

6.3 Numerical Verification

Ten numerical scenarios have been conducted, which are referred to as Cases 1 to 10, respectively. Case 1 is to verify the mathematical relationship between the DOFT and FRD methods. Cases 2 and 3 are designed to verify the relationship between two methods with different input signal bandwidths. Cases 4 and 5 are implemented to verify the relationship for both leak and burst problem. Cases 6 and 7 are conducted to compare and discuss the two methods in terms of the low sampling rate capability. Case 8, which contains three tests, is designed for robustness comparison between the two methods. Cases 9 and 10 are conducted to compare the two methods regarding the real-time data monitoring capability. Since only the first three resonance responses (i.e., the 1st, 3rd, 5th harmonics for the RPV system) of the measured signal were explored

and discussed in the previous research, only the results of the first three resonance response responses are included in this section (Du et al., 2020; Gong et al., 2013a; Wang et al., 2002).

6.3.1 Verification for the Mathematical Relationship

In order to verify the mathematical relationship between the FRD and DOFT of the signal shown in Eq. (6.13), Cases 1 to 3 have been conducted, of which Case 1 is for numerical verification of the mathematical relationship, and Cases 2 and 3 are for mathematical relationship verification with different input bandwidths. In Case 1, the applied data is from Lee (2005), in which the transient is generated by a manually-controlled valve. The pipeline system for Case 1 is shown in Figure 6.1 along with all the necessary parameters, where C_v is the maximum cross-sectional area of the inline valve, which is located at the downstream boundary of the system. The parameter orifice opening coefficient, τ, is applied to describe the actual cross-sectional area, as defined in Lee (2005). This is expressed as $C_d A_V / (C_d A_p)_{REF}$ for the inline and side discharge valves, where C_v is the orifice coefficient of the valves, A_V and A_p are the cross-sectional areas of the valves and the pipe respectively, and REF indicates the reference quantity.

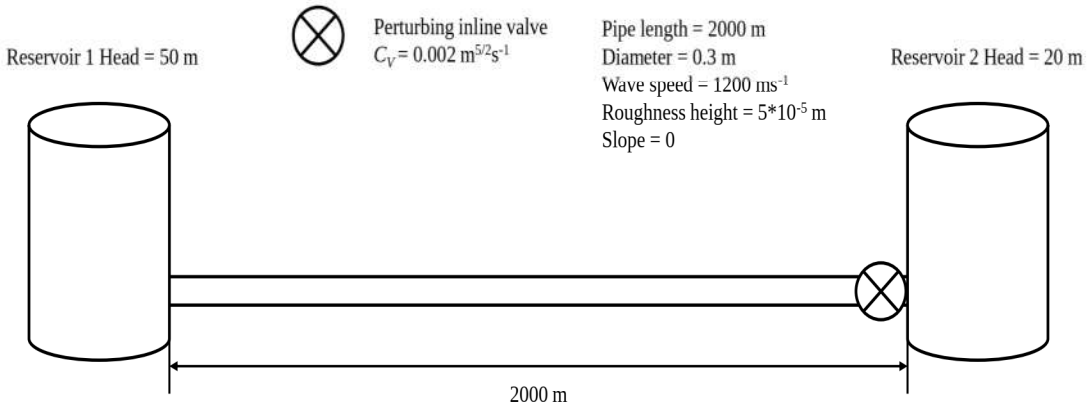

Figure 6.1: Pipeline configuration from Cases 1-3

In Case 1, $\Delta\tau$, the change of the cross-sectional area of the applied inline valve between the status of fully closed and aimed opening, is set to be 0.012. The system is under the condition of no-leak, and the transient is generated by the downstream inline valve. During the process of Case 1, the inline valve was initially fully closed. Then it was opened for a very short time, and fully closed again. In Case 1, the input is the valve perturbation τ, and the output is the head time trace measured at the downstream boundary. The input and the output signals are shown in Figures 6.2 and 6.3.

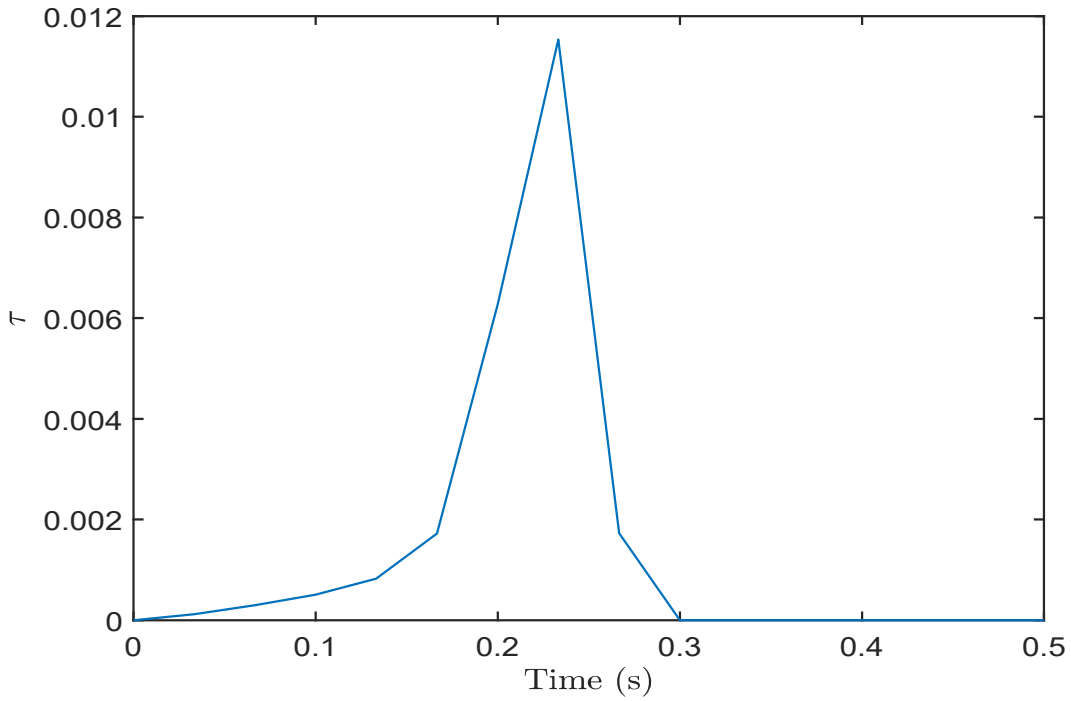

Figure 6.2: Input signal from Case 1

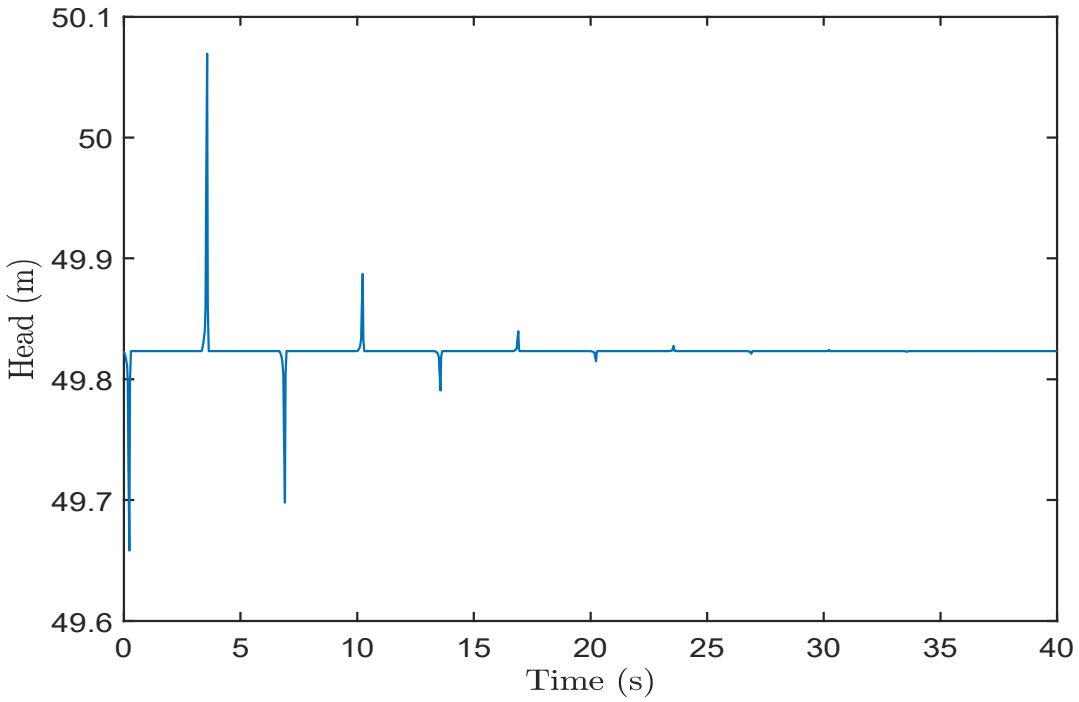

Figure 6.3: Output signal from Case 1

Applying the signal processing algorithm in Wang et al. (2002), Lee et al. (2006), and Du et al. (2020) provides the results shown in Figure 6.4, in which *FRD* is the result of FRF presented as Eq. (6.5), and *DOFT* represents the right side in Eq. (6.13), which is generated by letting the solution in Wang et al. (2002) divided by the frequency responses of the input signal. It is worth noting that the frequency responses of the output signal have been normalized by the frequency responses of the input signal, based on Eqs. (6.5) and (6.13). Based on the results shown in Figure 6.4, it can be shown that the amplitude of the presented quantities is closely matched for the first three resonance response peaks.

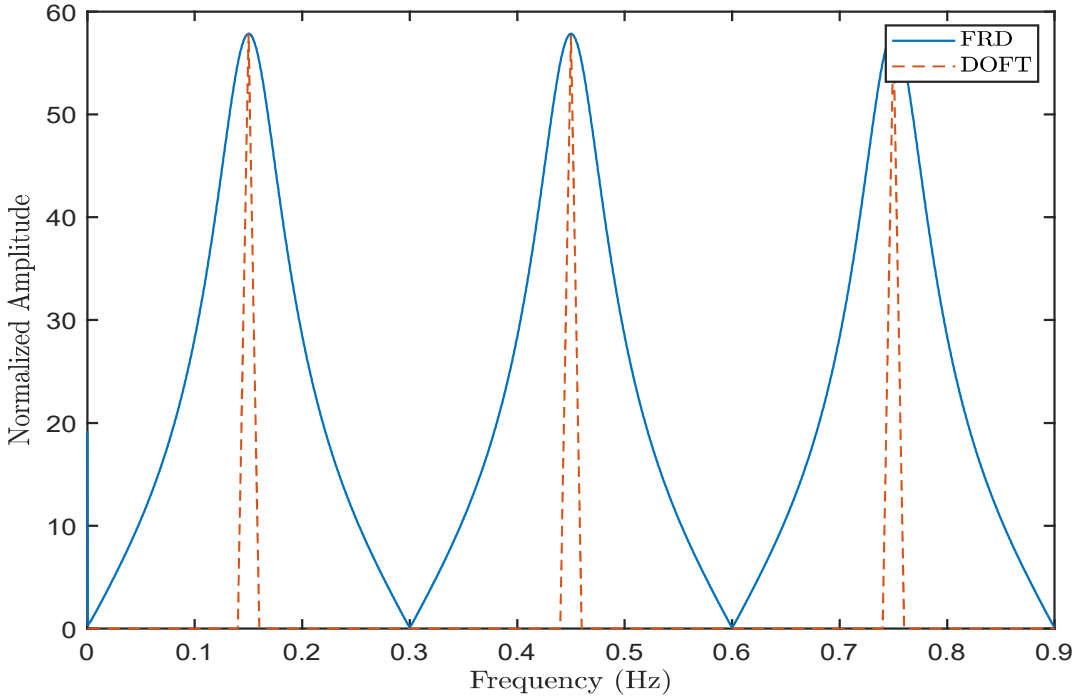

Figure 6.4: DOFT and FRD results from Case 1

6.3.2 Verification for Different Input Signal Bandwidths

Cases 2 and 3 have been implemented to verify the mathematical correlation under the conditions of different input signal bandwidths. The pipeline system for Cases 2 and 3 is the same as the configuration in Cases 1, except that the downstream inline valve is replaced by a side discharge valve. During Cases 2 and 3, the same operation of the inline valve as in Cases 1 was applied to the side discharge valve to generate the transient. The side discharge valve was operated with different opening and closing speeds to generate different input signal bandwidths, and the input signals of these two cases are shown in Figure D.1, in which $InputSignal1$ and $InputSignal2$ represent the input signal of Cases 2 and 3 respectively. The corresponding output signals of these two cases are shown in Figure D.2, in which $OutputSignal1$ and $OutputSignal2$ represent the output signals of Cases 2 and 3 respectively. In the two cases, the applied data are from Lee (2005). The corresponding results are shown in Figures E.5 and D.3. It is worth noting that the magnitude of the input signal is $C_d A_V$

instead of τ.

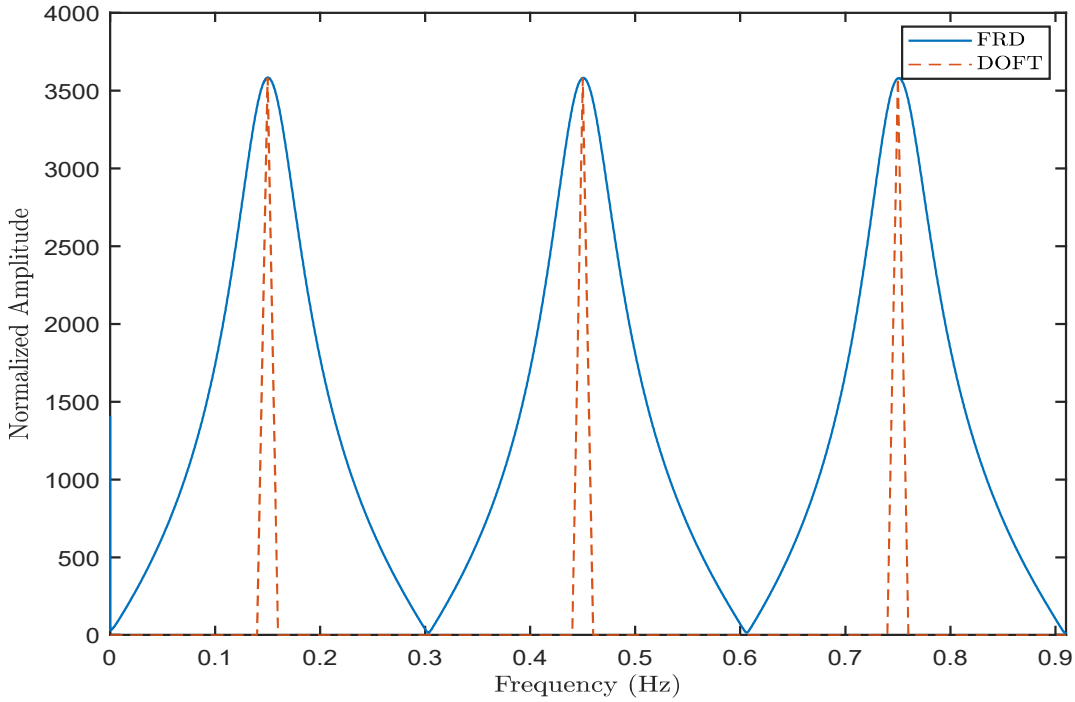

Figure 6.5: DOFT and FRD results from Case 2

Based on the results shown in Figures E.5 and D.3, the mathematical correlation between the DOFT and FRD techniques is verified through different input signal bandwidths.

6.3.3 Verification and Comparison for Leak and Burst Problems

To verify the explored mathematical relationship in the paper, and to compare the DOFT and FRD methods in terms of the problem type, Cases 4 and 5 have been conducted. Case 4 is the leak case and Case 5 is the burst case.

The pipeline system for Case 4 is the RPV system, and is shown in Figure 6.6, along with all the necessary parameters. The leak is simulated by a side discharge valve, which is located at 100 m from the upstream boundary, which has the relative cross-sectional area as $C_d A_L/A_p = 0.02$, where A_L is the cross-

sectional area of the leak. During the process of Case 4, the transient is introduced by opening and then closing the downstream valve rapidly, with relative cross sectional area of $C_d A_V / A_p = 0.001$. In addition, parameter τ is re-defined as the relative cross-sectional area of the downstream valve in Case 4. The operation process of the downstream valve is linear, and the corresponding input signal is shown in Figure 6.7. The measured time trace is shown in Figure 6.8, with the sampling rate of 100 Hz. The corresponding fundamental period is 2 s, which is determined using the ringdown code (Baibhav et al., 2018; Giesler et al., 2019). Replicating the same analysis process as in previous cases, the resultant frequency responses of the first three resonance frequencies using the DOFT and FRD techniques are shown in Figure 6.9. The adequate match verifies the correlation between the two methods. It should be noticed that the resonance responses are significantly damped due to the damping caused by the leak, when compared with the previous cases. By observing the damped amplitude of different harmonics in the frequency domain, the leak can be detected. The estimated leak location is at 99.45 m and 119.8 m utilizing the DOFT and FRD techniques respectively (Du et al., 2020; Gong et al., 2013a; Wang et al., 2002). The corresponding localization errors are 0.11% and 3.96% respectively (Wang et al., 2002).

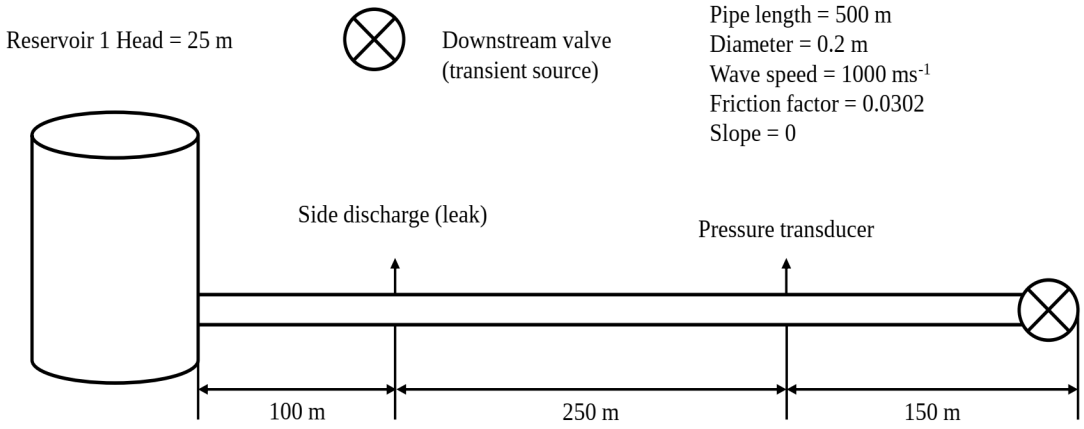

Figure 6.6: Pipeline configuration from Case 4

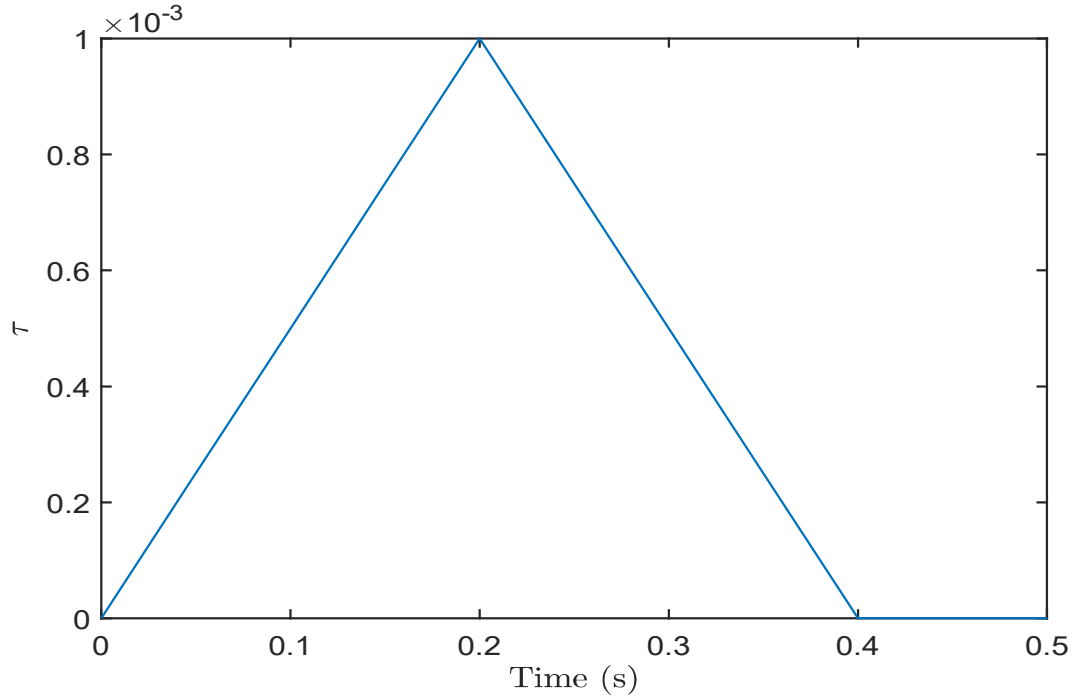

Figure 6.7: Input signal from Case 4

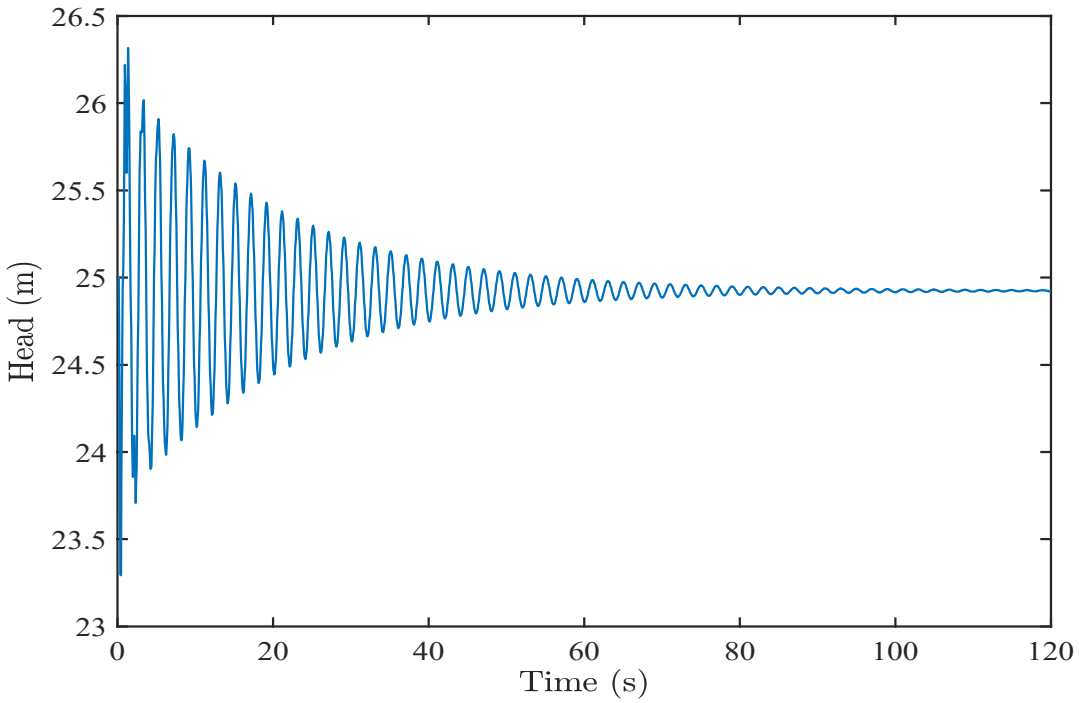

Figure 6.8: Output signal from Case 4

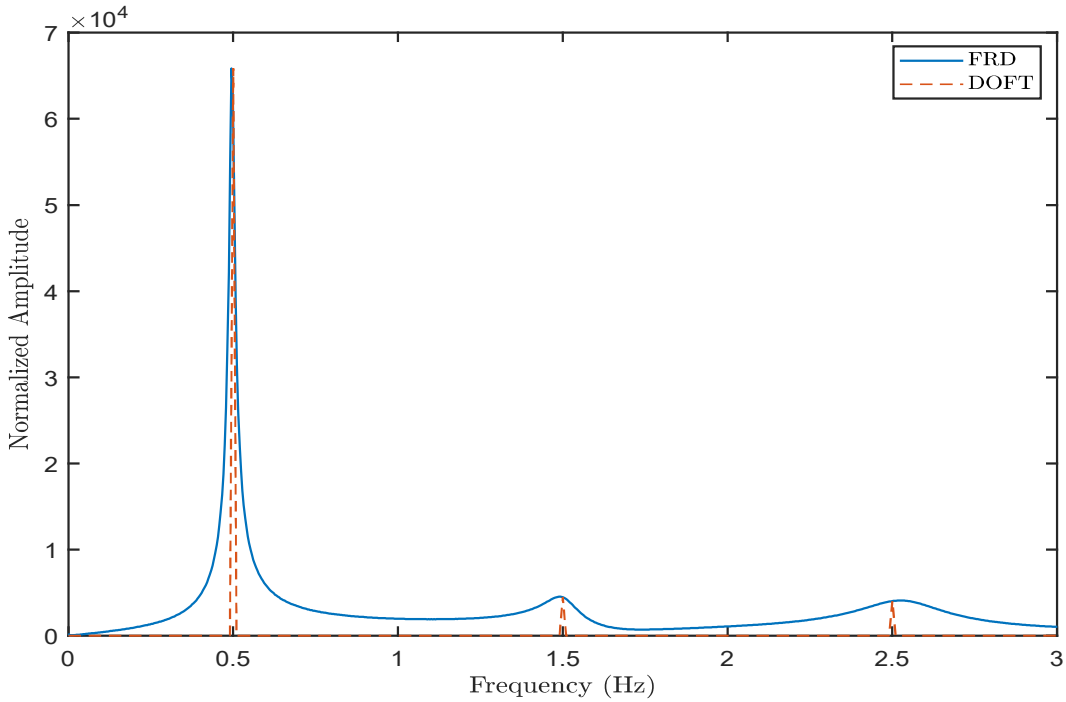

Figure 6.9: DOFT and FRD results from Case 4

The applied pipeline system in Case 5 is an RPV system, which is shown in Figure D.4, in which the burst is simulated by a side discharge at 100 m from the upstream boundary, with the relative cross-sectional area of $C_d A_B/A_p = 0.5$, where A_B is the cross-sectional area of the burst, while all other parameters remain the same as in Case 4. During the process of Case 5, the initial flow rate is set to be $Q_0 = 0.001$ m^3/s by letting the downstream valve be partially opened, and the burst is set to be generated rapidly at around 0.4 s, which is the transient source. Additionally, parameter τ is re-defined as the relative cross-sectional area of the burst in Case 5. The corresponding input and output signals are shown in Figures D.5 and D.6. Since the input signal for a burst case is actually an infinite step function, the signal correction algorithm in Lee (2005) has been utilized to convert the input signal from an infinite step function to a finite impulse function, and the output signal from the infinite step function-based signal to the finite impulse function-based signal. The modified input and output signals are presented in Figures 6.10 and 6.11. The corresponding resultant frequency responses of the signal are shown in Figure

6.12. The results indicate that a mathematical correlation exists in the burst cases. The damped amplitude can be applied to confirm the occurrence of the burst. Utilizing the localization technique in Du et al. (2020) and Gong et al. (2013a) provides the estimated burst location at 108.2 m and 117.4 m, respectively, where the localization error is 1.64% and 3.48%, respectively.

Although the mathematical relationship between the DOFT and FRD techniques has been verified, and the faults localization has been fulfilled by utilizing both the methods, it is impossible to utilize FRD method for burst problems in practice. This is because the application of the FRD technique requires the frequency response of the input signal, but the input signal in the burst problem is generated from the burst itself, which is the unknown element that needs to be detected and estimated.

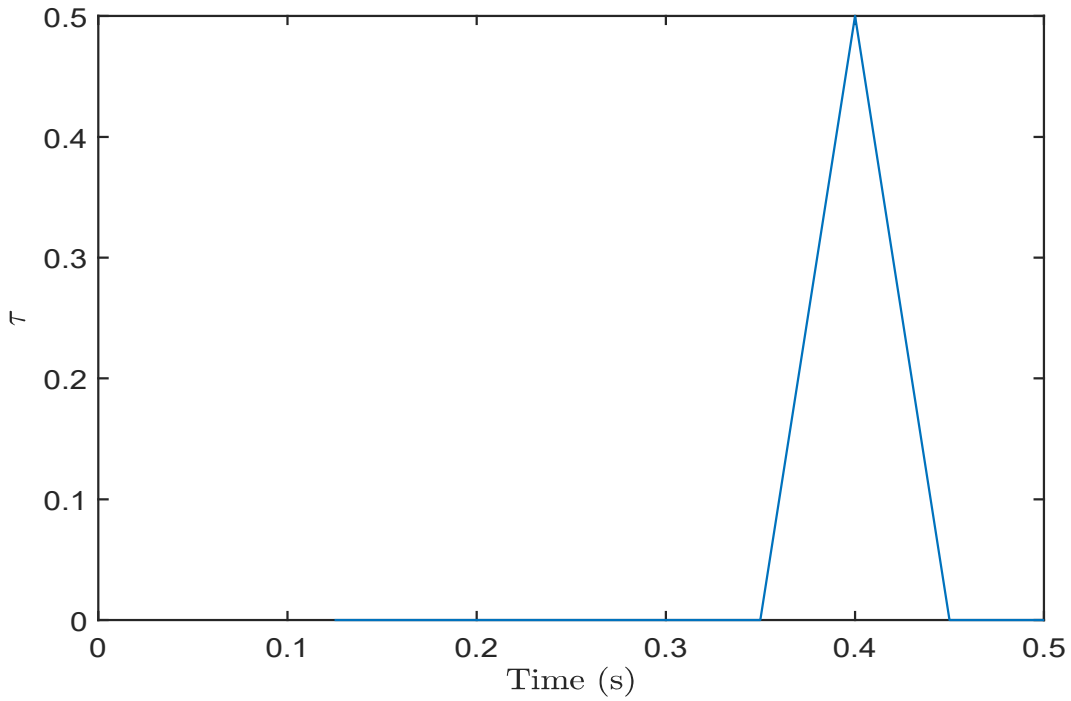

Figure 6.10: Modified input signal from Case 5

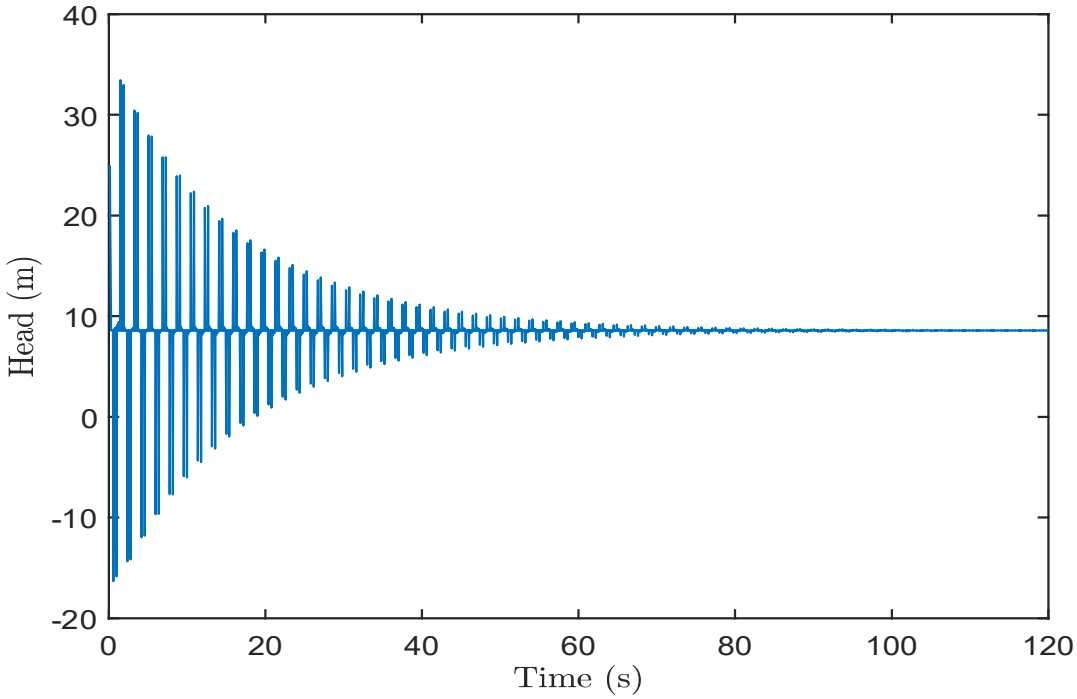

Figure 6.11: Modified output signal from Case 5

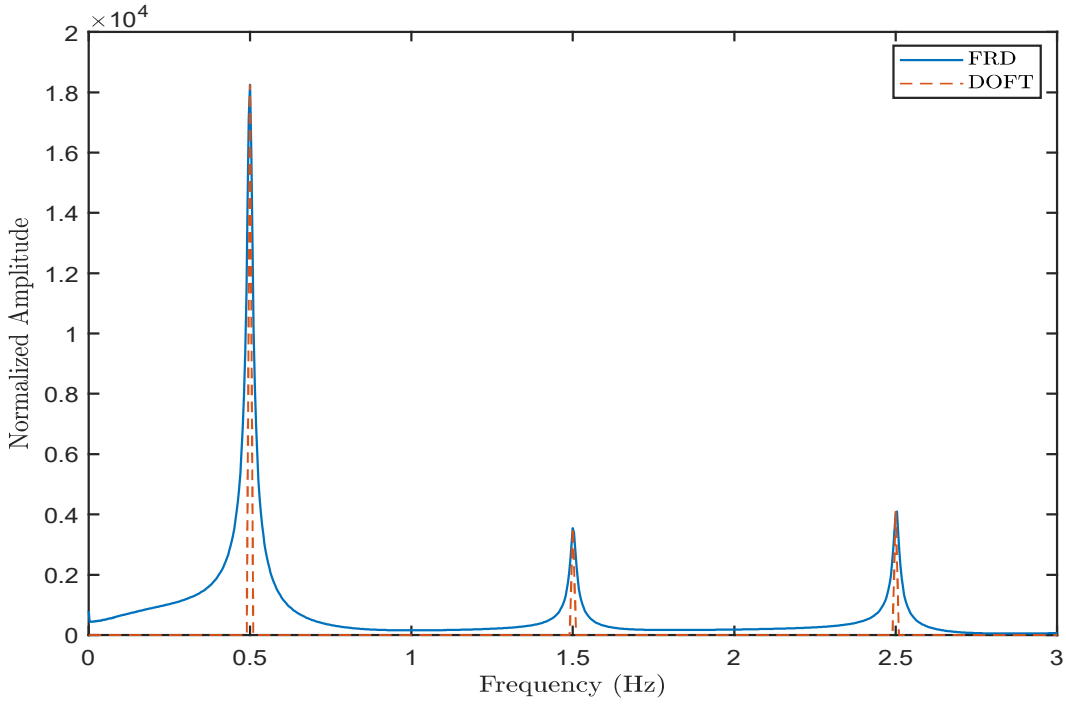

Figure 6.12: DOFT and FRD results from Case 5

6.3.4 Verification and Comparison for Low Sampling Rate Capability

In order to verify and compare the DOFT and FRD techniques from the perspective of low sampling rate capability, Cases 6 and 7 have been implemented. The applied pipeline system and the relevant parameters are the same as in Cases 4 and 5, respectively, except that the sampling rate has been decreased from 100 Hz to 5 Hz, which is the Nyquist frequency of the 5th harmonic of the signal, since only the first three resonance responses are required for both the application of the DOFT and the FRD methods. The re-sampled output signals for Cases 6 and 7 are shown in Figures D.7 and D.8. Replicating the same analysis process in the previous cases provides the frequency responses of the first three resonance responses of the signals from Cases 6 and 7 using the DOFT and FRD methods, as shown in Figures 6.13 and D.9. The leak and burst localization results remain the same.

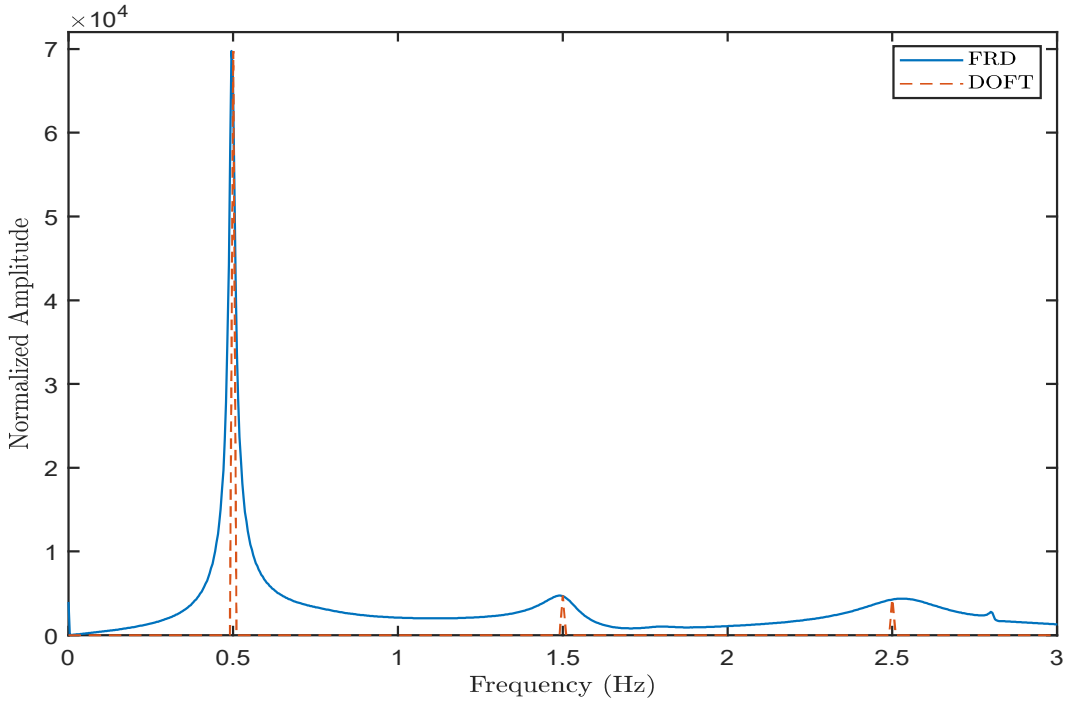

Figure 6.13: DOFT and FRD results from Case 6

Based on the results shown in Figures 6.13 and D.9, the mathematical rela-

tionship between the two methods has been verified. Additionally, the results illustrate that both the methods are capable of utilizing a low sampling rate (i.e., the Nyquist frequency of the 3rd resonance response).

6.3.5 Verification and Comparison for Robustness

The verification of the correlation and the comparison between the two methods in terms of the robustness has been completed by implementing Case 8. In Case 8, the applied pipeline system and the corresponding input and output signals are the same as in Case 4, which are shown in Figures 6.6, 6.7, and 6.8, which are for the leak problem. Case 8 contains three tests, which correspond to three different signal-noise-ratios (SNR). The applied SNRs for Tests 1, 2, and 3 are 30 dB, 20 dB, and 10 dB, respectively, since the general SNR of a measured signal is around 10 dB to 30 dB (Kellman and McVeigh, 2005; Zhang et al., 2008; Zhang, 2011). The time trace for Test 1 is shown in Figure 6.14. By utilizing the technique in Du et al. (2021), which extends the work by Wang et al. (2002), the discrete harmonic spectrogram (DHS) of the signal from Test 1 is presented in Figure 6.15, which contains the information of the leak damping that can be used for leak estimation. Replicating the same analysis processing the FRD method in the previous cases provides the FRD result shown in Figure 6.16. Similarly, the time trace, DHS and FRD results from Test 2, with the SNR of 20 dB, are presented in Figures D.10, D.11 and D.12. Additionally, the time trace, DHS and FRD results from Test 3, with SNR of 10 dB, are shown in Figures D.13, D.14 and D.15. From the results shown in Figures D.12 and D.15, it can be noticed that the resolutions of the second and third resonance responses of the signal decrease significantly when the SNR decreases, which leads to difficulties in the leak estimation. For example, in Tests 2 and 3, the second and third resonance responses of the signal generated by utilizing the FRD method can barely be distinguished from the noise, based on Figures D.12 and D.15. The peak values of the first three resonance responses

in Figures 6.16, D.12, and D.15 are summarized in Table E.1, by reading the values at particular frequencies of the first, third, and fifth harmonics. It should be noted that the peak values of the first three resonance responses from the FRD result in Case 4 have also been added to Table E.1, in order to provide the reference values under the condition of no-noise for comparison. The errors shown in Table E.1 are the relative errors that are generated by comparing the values from Case 8 with the values from Case 4. From Table E.1, it can be noticed that although the values of the first harmonic are similar in the tests, since the main energy is contained in the first resonance response, the values of the third and fifth harmonics are quite different from each other due to the negative effect from the noise.

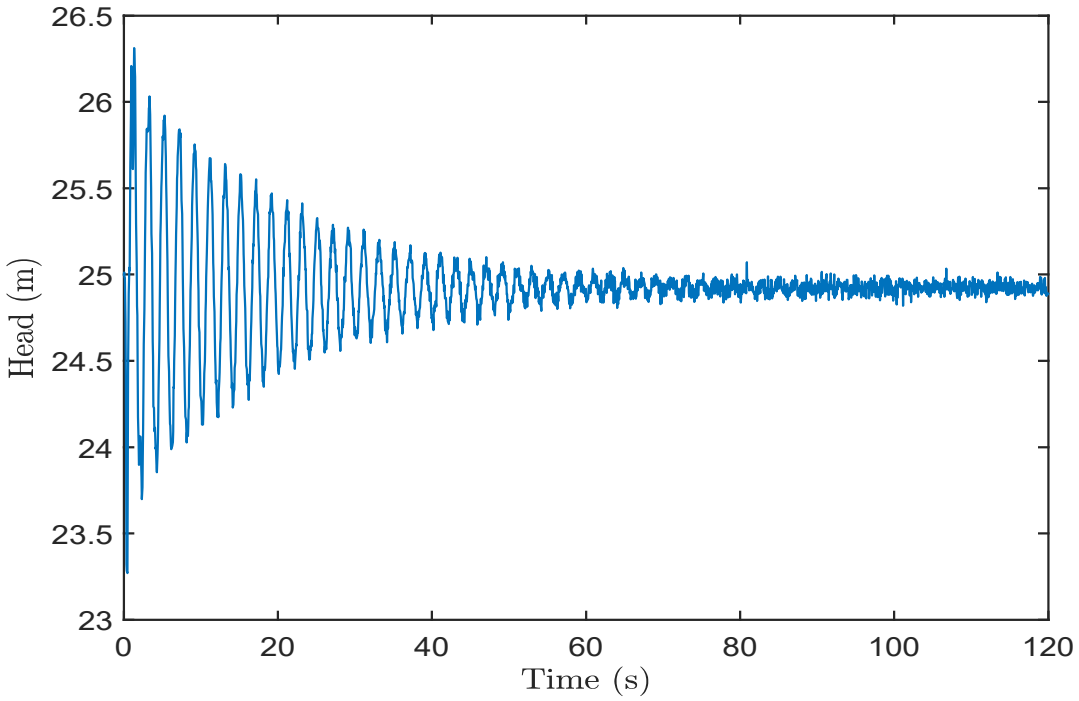

Figure 6.14: Output signal from Test 1 of Case 8

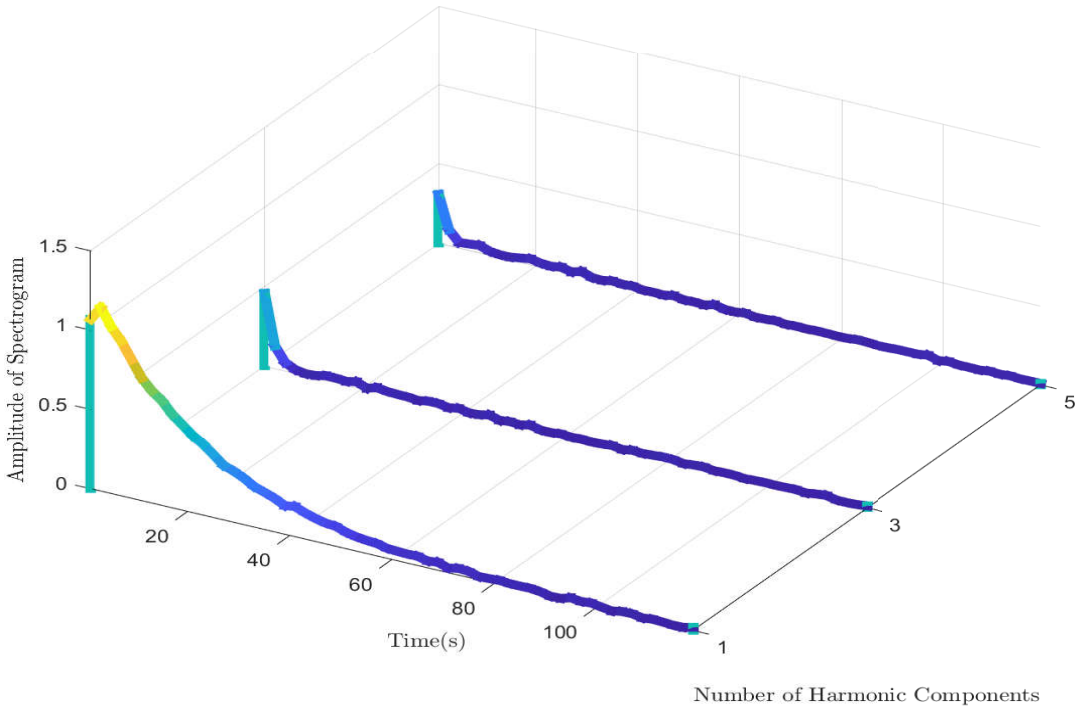

Figure 6.15: Discrete harmonic spectrogram from Test 1 of Case 8

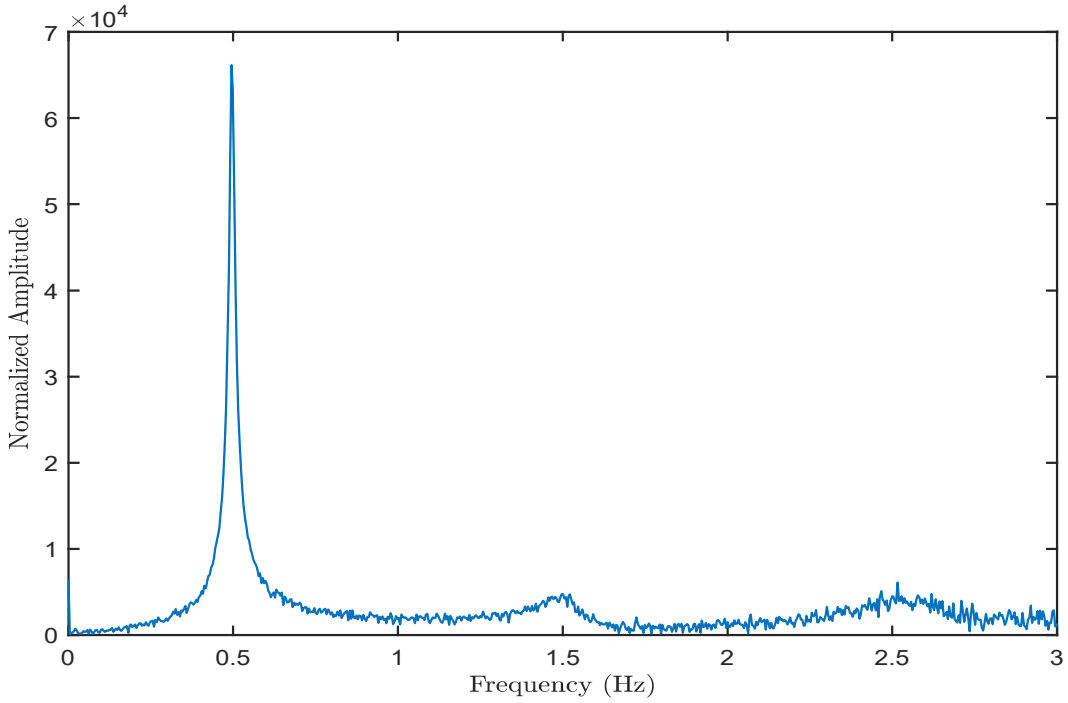

Figure 6.16: FRD result from Test 1 of Case 8

The total damping can be observed from Figures 6.15, D.11, and D.14, although there are some fluctuations in the resultant DHSs. The values of total damping for the first three resonance responses shown in Figures 6.15, D.11, and D.14 are summarized in Table E.2. Similar to Table E.1, the reference values of the damping of the first three resonance responses and the corresponding relative errors for each test in Case 8 have been summarized in Table E.2. Although there is noise, the values of the total damping in Table E.2 are close to each other.

Although the FRD results have been negatively affected by the noise, the leak localization can still be implemented using FRD by reading the values of the FRD results at the frequencies of the first three resonance harmonics, based on the technique in Gong et al. (2013a). Similarly, the leak localization can be conducted using the DOFT techniques in Wang et al. (2002) and Du et al. (2020). The leak localization results of utilizing both the two methods are summarized in Table E.3. Based on the results presented in Table E.3, the accuracy of the leak localization results using the DOFT method is higher than the accuracy using the FRD method. This is because the application of the DOFT method focuses on the attenuation of the frequency responses of the signal at particular frequencies versus time. The damping can still be observed with the noise, since the frequency response of the noise is also damped due the leak on the pipeline. However, the application of the FRD method only focuses the peak values of the first three resonance harmonics at the end of the measurement, and thus the negative effects from noise cannot be eased. Additionally, the DOFT method utilizes more information about the signal with more analysis steps than the FRD method, since the DOFT method analyzes the signal window by window, but the FRD method analyzes the signal at the end of the measurement. Consequently, the DOFT method is more robust for the analysis of noisy signals than the FRD method, based on the results presented in Tables E.1, E.2, and E.3.

Table 6.1: Comparison of peak values of the first three resonance responses in the FRD results from Case 8

Test	SNR	1st harmonic		3rd harmonic		5th harmonic	
Number	(dB)	Value	Error (%)	Value	Error (%)	Value	Error (%)
Reference	no noise	65689.1		4498.41		3929.18	
1	30	66137	0.68	4759.38	5.8	4495.44	14.41
2	20	67041.7	2.06	3127.83	30.47	4150.53	5.63
3	10	62139.1	5.4	3170.02	29.53	8200.01	108.7

Table 6.2: Comparison of values of total damping of the first three resonance responses in the DOFT results from Case 8

Test	SNR	1st harmonic		3rd harmonic		5th harmonic	
Number	(dB)	Value	Error (%)	Value	Error (%)	Value	Error (%)
Reference	no noise	0.0254		0.0957		0.246	
1	30	0.0254	0	0.0944	1.36	0.24	2.44
2	20	0.0261	2.76	0.089	7	0.2186	11.14
3	10	0.0263	3.54	0.1102	15.15	0.2201	10.53

Table 6.3: Leak localization results from Case 8

Test	SNR	Leak location	DOFT result	DOFT error	FRD result	FRD error
Number	(dB)	(m)	(m)	(%)	(m)	(%)
1	30	100	101.35	0.27	122.5	4.5
2	20	100	108.6	1.72	135.3	7.06
3	10	100	112.3	2.46	151.2	10.24

6.3.6 Comparison and Discussion for Real-time Data Monitoring Capability

According to the work in Du et al. (2021), utilizing the Fourier transform-based techniques for real-time data monitoring can be implemented by analyzing the signal window by window with the window gap to be the real-time data acquisition speed, which is the reciprocal of the sampling rate. Accordingly, the analyzed window can be moved slightly to adapt to the real-time data acquisition speed, and thus every new data point that is acquired can then be processed one time step at a time. However, utilizing the FRD method in a window instead of the whole range of data is impossible for application to real-time data monitoring. Firstly, the required signal length for leak localization solution in Gong et al. (2013a) limits its applicability to real-time data monitoring, since the required signal length is from the occurrence of the transient to steady state. Accordingly, the leak cannot be localized when analyzing the signal in a window rather than using the whole range of data via the FRD method, since there is no corresponding solution to the leak location. Secondly, the required input signal limits the potential of the real-time data monitoring capability of the FRD method, based on Eq. (6.5). This is because only when the input signal is non-zero can the result of using the FRD method be generated. Accordingly, for example, if the input signal is the impulse signal, and the lower limit of the selected window is after the impulse, the input signal in the selected window will be all zero values, and thus the FRD result cannot be generated. A numerical scenario, Case 9, has been performed to verify the second point of view of the previously-mentioned analyses, since it is unnecessary to implement a verification scenario for the first one under the condition that there is no solution to the leak location to be applied.

In Case 9, the applied input signal is the same as in Case 4, which is the leak case, as shown in Figure 6.7. The selected window length is the fundamental

period of the signal, which is 2 s. The lower limit of the window is 0.7 s, and the upper limit of the window is 2.7 s. The corresponding FFT result of the input signal in the selected window is shown in Figure 6.17. As shown in Figure 6.17, the FFT result of the input signal in the selected window is inapplicable to the FRD method, since it only contains zero values. Accordingly, the FRD method cannot be utilized. Therefore, analyzing the signal window by window using the FRD method is restricted by the input signal. Based on the fact that there is no solution to the leak location when utilizing the FRD method in a window instead of the whole range of data, and the limitation from the input signal, it is impossible to utilize the FRD method for real-time data monitoring, because real-time data monitoring requires the signal to be analyzed window by window for every sampling time step (Du et al., 2021).

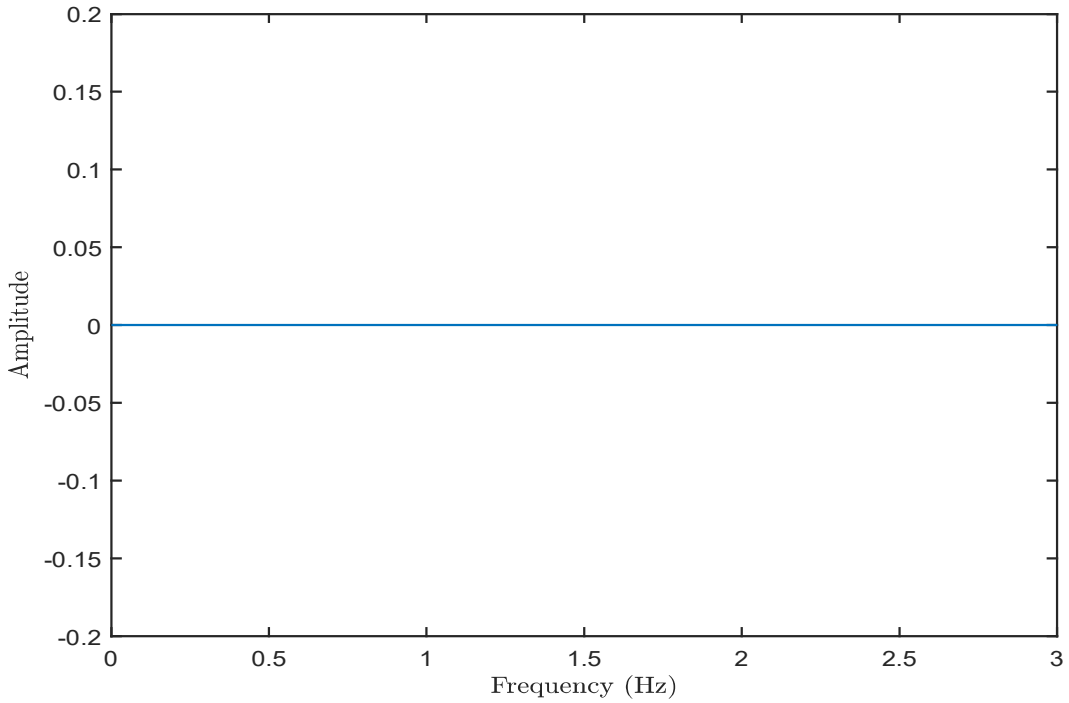

Figure 6.17: FFT result of the input signal from Case 9

Conversely, the DOFT method can be applied to real-time data monitoring based on the previous research, as long as the window gap between the current and the next windows equals the reciprocal of the sampling rate (Du et al., 2021). A numerical scenario, Case 10, has been implemented to verify the DOFT

method for real-time data monitoring of the leak problem. In Case 10, the window length is set to be the fundamental period of the signal, 4 s, and the window gap is set to be the reciprocal of the sampling rate, which is 0.05 s. The applied input and output signals are the same as in Case 4, as shown in Figures 6.7 and 6.8. Utilizing the technique in Du et al. (2021) provides the resultant DHS as presented in Figure 6.18, and the leak localization result of 99.45 m, with the localization error of 0.11%. It is worth noting that the resultant DHS shown in Figure 6.18 is only analyzed in the time period from 0 s to 20 s, since the application of DOFT does not require the signal to be analyzed in the time period from the application of input signal to the complete decay of output signal, which is 120 s in this case. Based on the results from Cases 9 and 10, the DOFT method can be applied to real-time data monitoring, while the FRD method has no capability to be applied to the area of real-time.

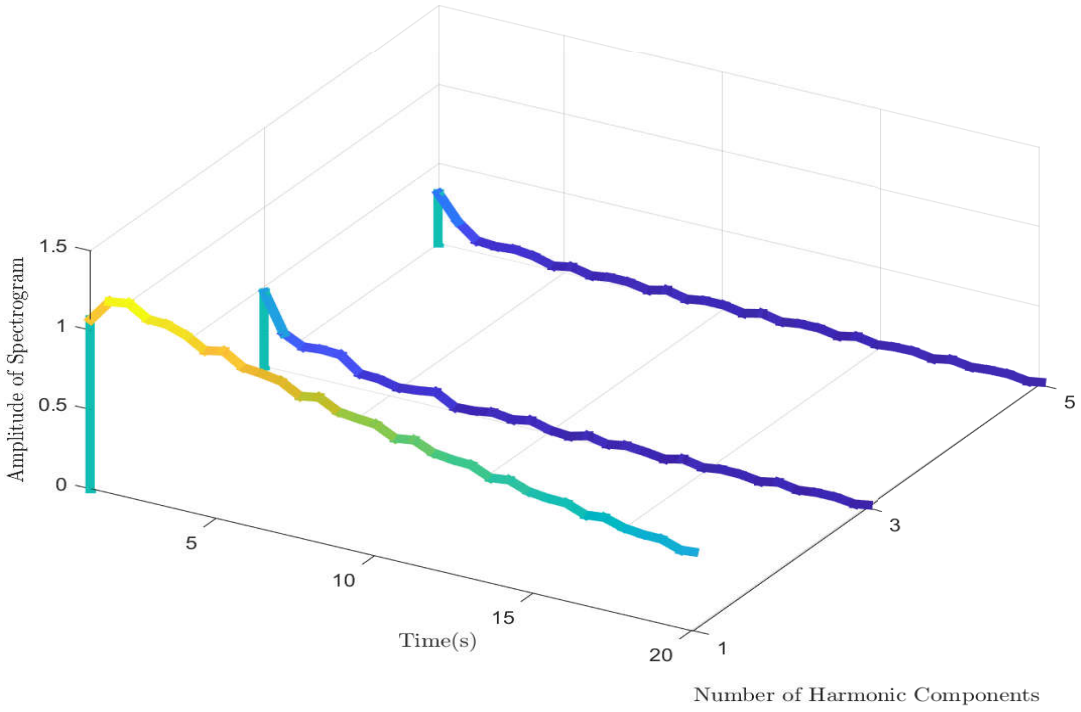

Figure 6.18: Discrete harmonic spectrogram from Case 10

6.4 Experimental Verification for the Mathematical Relationship

Two experimental scenarios have been conducted to verify the mathematical relationship between the DOFT and FRD methods in this paper, which are referred to as Experimental Cases 1 and 2. Both cases were conducted in the Robin Hydraulics Laboratory at the University of Adelaide. In Experimental Case 1, the applied data is from Lee (2005), and the corresponding experimental pipeline system is shown in Figure 6.19. As shown in Figure 6.19, the downstream valve is fully closed, and the transient is generated by closing the side discharge located at 0.16 m from the downstream boundary, which is initially fully opened. The output signal is measured at the same location as the transient source. The corresponding measured signal is shown in Figure 6.20. Replicating the same procedures in Case 1 provides the resultant DOFT and FRD results shown in Figure 6.21. It can be seen that the results using the two methods are matched adequately.

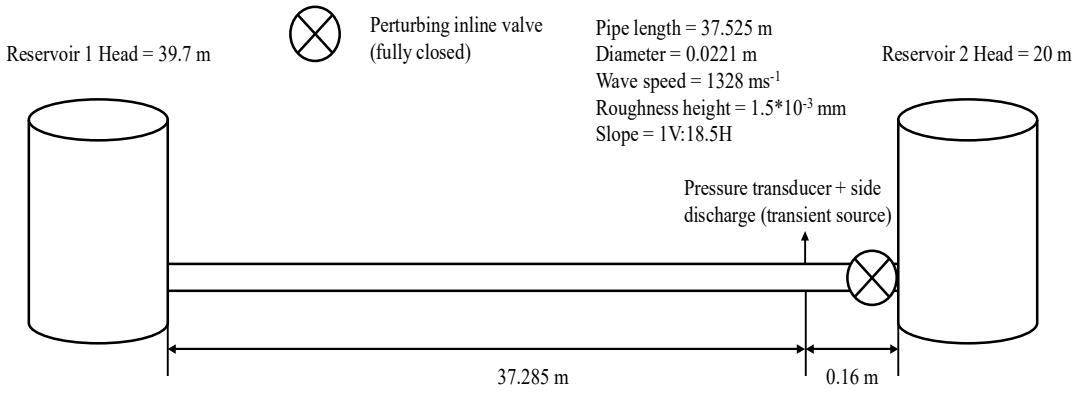

Figure 6.19: Pipeline configuration from Experimental Case 1

Experimental Case 2 was conducted under the condition of a burst. The corresponding experimental pipeline system is shown in Figure D.16. The pressure transducer is located at point P, and the burst is located at point B. More details of the experimental pipeline system can be found in Vitkovsky (2007), Wang et al. (2002), and Du et al. (2020). The downstream valve of the pipe

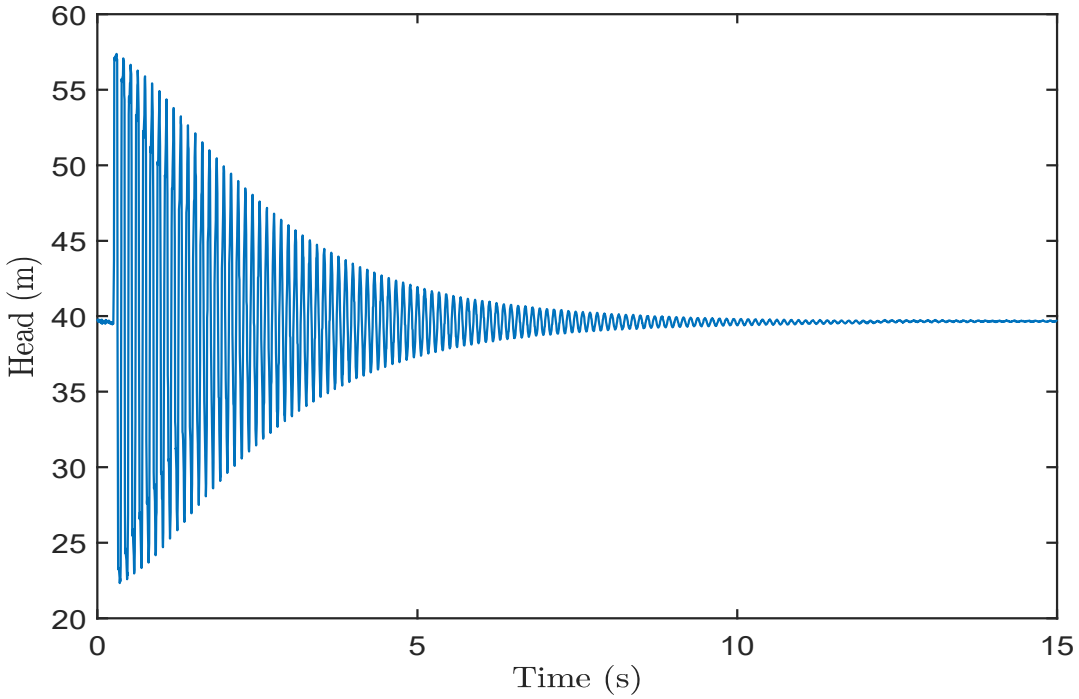

Figure 6.20: Measured time trace from Experimental Case 1

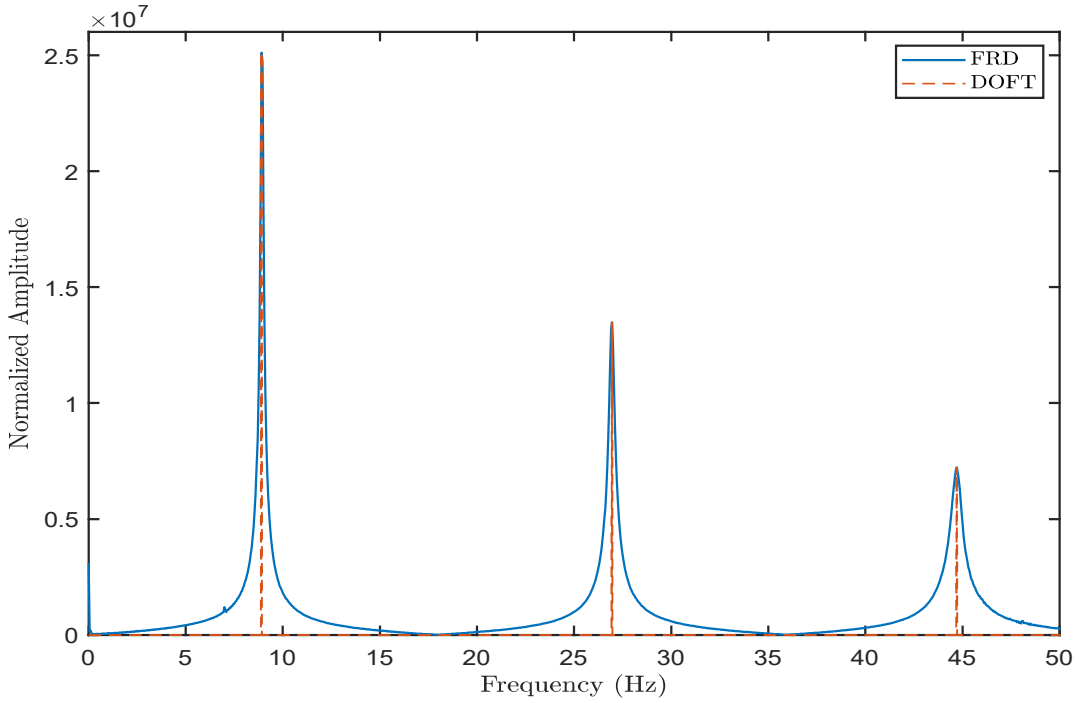

Figure 6.21: DOFT and FRD results from Experimental Case 1

is set to be fully closed to isolate the west tank from the pipe system. The burst is located at 19.3 m from the upstream boundary, and is simulated by a solenoid side discharge valve. The initial flow rate of the test is $Q_0 = 0$ m^3/s, the wave speed is $a = 1320$ m/s, and the head at the upstream tank is 3.065 bar, which is the east tank. The measured time trace is shown in Figure D.17, and the resultant first three resonance responses using the DOFT and FRD methods are shown in Figure D.18. The frequency responses in Figure D.18 are matched with acceptable errors, which verifies the mathematical relationship between the DOFT and FRD methods in the paper. By utilizing the burst localization procedure in Du et al. (2020), the estimated burst location is 18.98 m, where the localization error is 0.84%.

6.5 Conclusion and Discussion

The previously researched leak detection techniques based on the DOFT and FRD methods are both Fourier transform-based techniques. However, they utilize different signal processing algorithms. The mathematical derivation presented in this paper revealed the mathematical relationship between these two techniques from the perspectives of both leak and burst detection. The mathematical solutions of these two techniques are connected by utilizing the Fourier transform theorems and the basic nature of the resonance responses of the signal in frequency domain.

The mathematical relationship between the DOFT and FRD methods has been verified both numerically and experimentally by applying the leak and burst scenarios. Although the DOFT and the FRD techniques utilize different algorithms, the numerical and experimental results both provide an adequate match between them. The discussions between the two methods from the perspectives of input signal bandwidth, problem type, low sampling rate capability, robustness, and

real-time data monitoring capability have been implemented. Although both the techniques match each other with different input signal bandwidths, and are capable of utilizing low sampling rate (i.e., the Nyquist frequency of the 3rd resonance response), the differences between the two methods in other discussed areas exist. It has been shown that the DOFT method can be utilized for both the leak and burst problems. However, the FRD method cannot be applied to the burst problem, since its application requires the Fourier transform of the input signal, which is the unknown element in the burst problem. The DOFT method is more robust than the FRD method with three conducted tests using different SNRs, since the noise is also damped in addition to the signal itself due to the leak, and the DOFT method is able to be utilized to analyze the damping of the signal. The DOFT method can be applied to real-time data monitoring, while this capability of the FRD method is limited by the difficulty in determining the input signal and the lack of the solution to leak location in a time period that is shorter than the time period from occurrence of the transient event to the steady state.

Chapter 7

Conclusions

7.1 Research Outcomes

This Ph.D. research focuses on the development of novel pipe burst detection and estimation techniques and their associated signal processing algorithms. The main outcomes of the research are summarized as follows:

1. A novel technique for pipe burst detection, localization, and cross-sectional area quantification utilizing transient pressure signal measured by one sensor has been developed. The technique enables the transient pressure signal caused by the presence of the burst to be analyzed in the low frequency range during every fundamental period. The total damping can be determined by processing the damped harmonics of the transient pressure signal. Subtracting the friction damping, which is calibrated computationally by the developed unsteady friction water hammer (UFWH) model, from the total damping provides the burst damping. Therefore, the burst location and relative cross-sectional area can be calculated by applying the burst damping ratios.

2. A further developed technique for real-time pipe burst detection, localization, and cross-sectional area quantification using the transient pressure

signal has been proposed based on the previous research outcomes. The technique is capable of analyzing the signal window by window with the predefined window lengths and gaps, which makes real-time data monitoring possible when letting the window gap be the reciprocal of the data sampling rate. The required data transmission and sampling rates for the application of the technique are low (i.e., Nyquist frequency of the third resonance harmonic of the measured signal).

3. Extended research for real-time pipe burst detection and location estimation utilizing any sequence of harmonics of the transient pressure signal has been conducted based on the previous research outcomes. The corresponding approach can analyze any sequence of harmonics within the whole available frequency range. The majority of incorrect possible solutions to the burst location can be excluded by using the approach. The burst can be successfully detected by the computed burst damping, and the burst location can be successfully estimated by the determined burst location range in real-time. The effects from the unsteady friction damping on the burst detection and location estimation resulting from the approach have been explored.

4. The relationship between the damping of fluid transients (DOFT) and frequency response diagram (FRD) techniques has been revealed mathematically. The comparison and discussion between the two methods from the perspectives of input bandwidth, problem type, low sampling rate capability, robustness, and real-time data monitoring capability have been implemented. The advantages of the developed techniques in this Ph.D. research have been emphasized.

7.2 Research Contributions

The overall contribution of the research is the developed novel techniques for pipe burst detection and estimation in real-time. The advantages of the techniques provide alternatives to the sensor and sensing system design depending on the task requirement in practice. The detailed contributions are shown as follows:

1. The pipe burst detection and estimation technique utilizes the presence of the burst as the transient source instead a manually controlled valve. This indicates that the application of this technique does not require an additional valve closure process to generate a transient, which interrupts the normal working process of the pipeline system. The technique extends the application area of the DOFT theory from the leak problem to the burst problem. In addition, the application of the technique only requires one sensor, which reduces the cost of the sensing system. The developed UFWH model is capable of calibrating the unsteady friction damping for the burst problem, which can be implemented numerically. This specific aspect indicates that no unsteady friction damping determination process that interrupts to the pipeline working process is required.

2. The real-time pipe burst detection and estimation approach makes real-time data monitoring possible for the burst problem, which provides an insight into minimizing the negative effects from the burst for pipeline inspection process. The low required data transmission and sampling rates of the application of the technique provide a significant insight into reducing the cost of the sensing system. The technique enables the DOFT theory to be applied in the area of real-time data monitoring.

3. The real-time pipe burst detection and location estimation technique using any sequence of harmonics of the transient pressure signal enables all the

available harmonics of the signal to be analyzed. The technique eases the requirements of the corresponding sensor and sensing system, indicating that the applied sensor and sensing system can be designed depending on the exact requirements in terms of the aimed frequency range in practice. The technique eases the restriction of the DOFT theory, where only the first three resonance harmonics can be utilized for the damping analysis.

4. The revealed mathematical relationship between the methods of DOFT and FRD provides access to the research on the connection between DOFT and FRD theories. Additionally, the exploration and discussion between the two methods in the discussed areas provide an insight into utilizing different techniques for pipeline leak and burst detection problems in practice. Moreover, the advantages of the developed techniques in this Ph.D. research have been further explored and emphasized.

7.3 Future Work

The future work from this Ph.D. research includes the following aspects:

1. Only the single burst problem has been researched in this Ph.D. research. Accordingly, the multiple bursts problem should be included in future work.

2. This Ph.D. research only explored the pipe burst detection and estimation techniques on a single pipeline. Therefore, future work should focus on increasing the complexity of the pipeline system.

3. Since the burst has been treated as a transient source during the process of this Ph.D. research, identification of a burst from other transient generations, such as sudden water use and/or a suddenly opened branch, should be researched in the future.

4. Only a metal pipeline has been discussed in this Ph.D. research. Therefore, the validity of other materials, such as plastic pipes, should be explored in the future.

References

[1] Abramowitz, M., Stegun, I. A., and Romer, R. H. (1988). *Handbook of mathematical functions with formulas, graphs, and mathematical tables*. American Association of Physics Teachers.

[2] Akylidz, I., Lee, W., and Chowdhury, K. (2009). Crans: Cognitive radio ad hoc networks, ad hoc networks. *vol*, 7:810–836.

[3] Anderson, D. A. and Anderson, C. J. (2011). Weather coverage in dailies. *Journalism Quarterly*, 63(2):382–385.

[4] Anguiano, G., Strum, S., Medina, V., Waisner, S., Condit, W., Matthews, J., and Stowe, R. (2016). Innovative acoustic sensor technologies for leak detection in challenging pipe types. Technical report, Naval Facilities Engineering Command Port Hueneme United States.

[5] Baibhav, V., Berti, E., Cardoso, V., and Khanna, G. (2018). Black hole spectroscopy: Systematic errors and ringdown energy estimates. *Physical Review D*, 97(4):044048.

[6] Beck, S., Curren, M., Sims, N., and Stanway, R. (2005). Pipeline network features and leak detection by cross-correlation analysis of reflected waves. *Journal of hydraulic engineering*, 131(8):715–723.

[7] Bell, R. (2012). *Introductory Fourier transform spectroscopy*. Elsevier.

[8] Bergant, A., Simpson, A. R., and Vítkovskỳ, J. (2001). Developments in unsteady pipe flow friction modelling. *Journal of Hydraulic Research*, 39(3):249–257.

[9] Berglund, E. Z., Pesantez, J. E., Rasekh, A., Shafiee, M. E., Sela, L., and Haxton, T. (2020). Review of modeling methodologies for managing water distribution security. *Journal of Water Resources Planning and Management*, 146(8):03120001.

[10] Billmann, L. and Isermann, R. (1987). Leak detection methods for pipelines. *Automatica*, 23(3):381–385.

[11] Black, P. (1992). A review of pipeline leak detection technology. In *Pipeline systems*, pages 287–298. Springer.

[12] Bochud, P.-Y., Eggiman, P., Calandra, T., Van Melle, G., Saghafi, L., and Francioli, P. (1994). Bacteremia due to viridans streptococcus in neutropenic patients with cancer: clinical spectrum and risk factors. *Clinical infectious diseases*, 18(1):25–31.

[13] Bohorquez, J., Alexander, B., Simpson, A. R., and Lambert, M. F. (2020). Leak detection and topology identification in pipelines using fluid transients and artificial neural networks. *Journal of Water Resources Planning and Management*, 146(6):04020040.

[14] Boon, J. et al. (2012). Combined cctv and leak detection technology for in-service water transmission mains. *Water Practice and Technology*, 7(4).

[15] Bracewell, R. (1965). Pentagram notation for cross correlation. the fourier transform and its applications. *New York: McGraw-Hill*, 46:243.

[16] Bracken, M. and Cain, B. (2012). Transmission main and plastic pipe leak detection using advanced correlation technology: Case studies. In *Pipelines 2012: Innovations in Design, Construction, Operations, and Maintenance, Doing More with Less*, pages 147–157.

[17] Brennan, M., Gao, Y., Ayala, P., Almeida, F., Joseph, P., and Paschoalini, A. (2019). Amplitude distortion of measured leak noise signals caused by instrumentation: Effects on leak detection in water pipes using the cross-correlation method. *Journal of Sound and Vibration*, 461:114905.

[18] Brothers, K. (2003). A practical approach to water loss reduction. *Water 21*, pages 54–55.

[19] Brunone, B. (1999). Transient test-based technique for leak detection in outfall pipes. *Journal of water resources planning and management*, 125(5):302–306.

[20] Brunone, B. and Ferrante, M. (2001). Detecting leaks in pressurised pipes by means of transients. *Journal of hydraulic research*, 39(5):539–547.

[21] Brunone, B., Ferrante, M., and Meniconi, S. (2008). Portable pressure wave-maker for leak detection and pipe system characterization. *Journal-American Water Works Association*, 100(4):108–116.

[22] Brunone, B., Meniconi, S., and Capponi, C. (2018). Numerical analysis of the transient pressure damping in a single polymeric pipe with a leak. *Urban Water Journal*, 15(8):760–768.

[23] Bureau of Meteorology (2021). National performance report 2019–20: Urban water utilities, part a. *Melbourne*.

[24] Cai, L., Wang, R., Sun, J., Li, S., and Jing, Y. (2016). Urban water supply network monitoring and management platform based on wireless sensor network. In *Wireless Communications, Networking and Applications*, pages 351–361. Springer.

[25] Cataldo, A., De Benedetto, E., Cannazza, G., Leucci, G., De Giorgi, L., and Demitri, C. (2017). Enhancement of leak detection in pipelines through time-domain reflectometry/ground penetrating radar measurements. *IET Science, Measurement & Technology*, 11(6):696–702.

[26] Cheraghi, N., Riley, M., and Taheri, F. (2005). A novel approach for detection of damage in adhesively bonded joints in plastic pipes based on vibration method using piezoelectric sensors. In *Systems, Man and Cybernetics, 2005 IEEE International Conference on*, volume 4, pages 3472–3478. IEEE.

[27] Costello, S., Chapman, D., Rogers, C., and Metje, N. (2007). Underground asset location and condition assessment technologies. *Tunnelling and Underground Space Technology*, 22(5-6):524–542.

[28] Covas, D. and Ramos, H. (2010). Case studies of leak detection and location in water pipe systems by inverse transient analysis. *Journal of Water Resources Planning and Management*, 136(2):248–257.

[29] Covas, D., Ramos, H., and De Almeida, A. B. (2005a). Standing wave difference method for leak detection in pipeline systems. *Journal of Hydraulic Engineering*, 131(12):1106–1116.

[30] Covas, D., Stoianov, I., Mano, J. F., Ramos, H., Graham, N., and Maksimovic, C. (2005b). The dynamic effect of pipe-wall viscoelasticity in hydraulic transients. part ii–model development, calibration and verification. *Journal of Hydraulic Research*, 43(1):56–70.

[31] Covas, D., Stoianov, I., Ramos, H., Graham, N., and Maksimovic, C. (2003). The dissipation of pressure surges in water pipeline systems. *Pumps, electromechanical devices and systems applied to urban management*, 2:711–719.

[32] Covas, D., Stoianov, I., Ramos, H., Graham, N., and Maksimovic, C. (2004). The dynamic effect of pipe-wall viscoelasticity in hydraulic transients. part i–experimental analysis and creep characterization. *Journal of Hydraulic Research*, 42(5):517–532.

[33] Dilena, M., Dell'Oste, M. F., and Morassi, A. (2011). Detecting cracks in pipes filled with fluid from changes in natural frequencies. *Mechanical Systems and Signal Processing*, 25(8):3186–3197.

[34] Donazzolo, V. and Yelf, R. (2010). Determination of wall thickness and condition of asbestos cement pipes in sewer rising mains using surface penetrating radar. In *Proceedings of the XIII Internarional Conference on Ground Penetrating Radar*, pages 1–5. IEEE.

[35] Du, X.-x., Lambert, M. F., Chen, L., Jing Hu, E., and Xi, W. (2020). Pipe burst detection, localization, and quantification using the transient pressure damping method. *Journal of Hydraulic Engineering*, 146(11):04020077.

[36] Du, X.-x., Zeng, W., Lambert, M. F., Chen, L., and Jing Hu, E. (2021). Approach for near-real-time pipe burst detection, localization, and quantification with low data transmission and sampling rates. *Journal of Water Resources Planning and Management*, 147(7):04021032.

[37] Duan, H.-F. (2016). Transient frequency response based leak detection in water supply pipeline systems with branched and looped junctions. *Journal of Hydroinformatics*, 19(1):17–30.

[38] Duan, H.-F. (2018). Accuracy and sensitivity evaluation of tfr method for leak detection in multiple-pipeline water supply systems. *Water resources management*, 32(6):2147–2164.

[39] Duan, H.-F., Ghidaoui, M. S., Lee, P. J., and Tung, Y.-K. (2012). Relevance of unsteady friction to pipe size and length in pipe fluid transients. *Journal of hydraulic engineering*, 138(2):154–166.

[40] Duan, H.-F., Lee, P. J., Ghidaoui, M. S., and Tung, Y.-K. (2011). Leak detection in complex series pipelines by using the system frequency response method. *Journal of Hydraulic Research*, 49(2):213–221.

[41] Duran, O., Althoefer, K., and Seneviratne, L. D. (2003). Pipe inspection using a laser-based transducer and automated analysis techniques. *IEEE/ASME Transactions on mechatronics*, 8(3):401–409.

[42] Ebina, R., Nakamura, K., and Oyanagi, S. (2011). A real-time burst detection method. In *2011 IEEE 23rd International Conference on Tools with Artificial Intelligence*, pages 1040–1046. IEEE.

[43] Evans, R. P., Blotter, J. D., and Stephens, A. G. (2004). Flow rate measurements using flow-induced pipe vibration. *Journal of fluids engineering*, 126(2):280–285.

[44] Ferrante, M., Brunone, B., Meniconi, S., Karney, B. W., and Massari, C. (2014). Leak size, detectability and test conditions in pressurized pipe systems. *Water resources management*, 28(13):4583–4598.

[45] Forrest, T. (1994). From sender to receiver: propagation and environmental effects on acoustic signals. *American zoologist*, 34(6):644–654.

[46] Fuchs, H. and Riehle, R. (1991). Ten years of experience with leak detection by acoustic signal analysis. *Applied acoustics*, 33(1):1–19.

[47] Furness, R. and Reet, J. (1998). Pipeline leak detection techniques. *Pipe line rules of thumb handbook. Houston: Gulf*.

[48] Gao, Y., Brennan, M. J., Joseph, P. F., Muggleton, J. M., and Hunaidi, O. (2004). A model of the correlation function of leak noise in buried plastic pipes. *Journal of Sound and Vibration*, 277(1-2):133–148.

[49] Gao, Y., Brennan, M. J., Liu, Y., Almeida, F. C., and Joseph, P. F. (2017). Improving the shape of the cross-correlation function for leak detection in a plastic water distribution pipe using acoustic signals. *Applied Acoustics*, 127:24–33.

[50] Gaskill, J. D. (1978). *Linear systems, Fourier transforms, and optics*, volume 576. Wiley New York.

[51] Giesler, M., Isi, M., Scheel, M. A., and Teukolsky, S. A. (2019). Black hole ringdown: the importance of overtones. *Physical Review X*, 9(4):041060.

[52] Gong, J., Lambert, M. F., Simpson, A. R., and Zecchin, A. C. (2013a). Single-event leak detection in pipeline using first three resonant responses. *Journal of Hydraulic Engineering*, 139(6):645–655.

[53] Gong, J., Lambert, M. F., Zecchin, A. C., and Simpson, A. R. (2016a). Experimental verification of pipeline frequency response extraction and leak detection using the inverse repeat signal. *Journal of Hydraulic Research*, 54(2):210–219.

[54] Gong, J., Nguyen, S., Stephens, M., Lambert, M., Marchi, A., Simpson, A., and Zecchin, A. (2018a). Correlation of post-burst hydraulic transient noise for pipe burst/leak localisation in water distributions systems. In *13th International Conference on Pressure Surges*, pages 201–215. BHR Group.

[55] Gong, J., Stephens, M. L., and Lambert, M. F. (2018b). Analysis of the frequency-dependent attenuation of transient pressure waves in plastic pipes. In *WDSA/CCWI Joint Conference Proceedings*, volume 1.

[56] Gong, J., Zecchin, A. C., Lambert, M. F., and Simpson, A. R. (2016b). Determination of the creep function of viscoelastic pipelines using system resonant frequencies with hydraulic transient analysis. *Journal of Hydraulic Engineering*, 142(9):04016023.

[57] Gong, J., Zecchin, A. C., Simpson, A. R., and Lambert, M. F. (2013b). Frequency response diagram for pipeline leak detection: Comparing the odd and even harmonics. *Journal of Water Resources Planning and Management*, 140(1):65–74.

[58] Gould, S. J., Davis, P., and Marlow, D. R. (2016). Importance of installation practices for corrosion protection of ductile iron pipe. *Urban Water Journal*, 13(2):198–211.

[59] Griebenow, G. and Mears, M. (1989). Leak detection implementation: modeling and tuning methods. *Journal of Energy Resources Technology*, 111(2):66–71.

[60] Guenther, T. and Kroll, A. (2016). Automated detection of compressed air leaks using a scanning ultrasonic sensor system. In *2016 IEEE Sensors Applications Symposium (SAS)*, pages 1–6. IEEE.

[61] Harris, F. (1992). Techniques and limitations of spectrum analysis, with the dft. *Time-Frequency Signal Analysis, B. Boashash (Ed.), London, Longman Cheshire*, pages 184–207.

[62] Hazelden, G., Ragula, G., and Roubal, M. (2003). The use of broadband electromagnetic technology for integrity inspection of a 760 mm (30 in.) cast iron and steel line. In *22nd World Gas Conference*, pages 1–6.

[63] Hovey, D. J. and Farmer, E. J. (1993). Pipeline accident, failure probability determined from historical data. *Oil and Gas Journal*, 91(28).

[64] Hunaidi, O. (2012). Acoustic leak detection survey strategies for water distribution pipes. *Construction technology update*, 79:1–5.

[65] Hunaidi, O., Wang, A., Bracken, M., Gambino, T., and Fricke, C. (2004). Acoustic methods for locating leaks in municipal water pipe networks. In *International Conference on Water Demand Management*, pages 1–14. Dead Sea Jordan.

[66] Hutton, C. and Kapelan, Z. (2015a). Real-time burst detection in water distribution systems using a bayesian demand forecasting methodology. *Procedia Engineering*, 119:13–18.

[67] Hutton, C. J. and Kapelan, Z. (2015b). A probabilistic methodology for quantifying, diagnosing and reducing model structural and predictive errors in short term water demand forecasting. *Environmental Modelling & Software*, 66:87–97.

[68] Hyun, S.-Y., Jo, Y.-S., Oh, H.-C., and Kirn, S.-Y. (2003). An experimental study on a ground-penetrating radar for detecting water-leaks in buried water transfer pipes. In *Antennas, Propagation and EM Theory, 2003. Proceedings. 2003 6th International Symposium on*, pages 596–599. IEEE.

[69] Jacobsen, E. and Lyons, R. (2003). The sliding dft. *IEEE Signal Processing Magazine*, 20(2):74–80.

[70] Jo, B. y., Laven, K., and Jacob, B. (2010). Advances in cctv technology for in-service water mains. In *Pipelines 2010: Climbing New Peaks to Infrastructure Reliability: Renew, Rehab, and Reinvest*, pages 538–547.

[71] Juliano, T. M., Meegoda, J. N., and Watts, D. J. (2013). Acoustic emission leak detection on a metal pipeline buried in sandy soil. *Journal of Pipeline Systems Engineering and Practice*, 4(3):149–155.

[72] Kang, D. and Lansey, K. (2012). Novel approach to detecting pipe bursts in water distribution networks. *Journal of Water Resources Planning and Management*, 140(1):121–127.

[73] Kapelan, Z. S., Savic, D. A., and Walters, G. A. (2003). A hybrid inverse transient model for leakage detection and roughness calibration in pipe networks. *Journal of Hydraulic Research*, 41(5):481–492.

[74] Kellman, P. and McVeigh, E. R. (2005). Image reconstruction in snr units: a general method for snr measurement. *Magnetic resonance in medicine*, 54(6):1439–1447.

[75] Keramat, A., Ghidaoui, M. S., Wang, X., and Louati, M. (2019). Cramer-rao lower bound for performance analysis of leak detection. *Journal of Hydraulic Engineering*, 145(6):04019018.

[76] Keramat, A. and Zanganeh, R. (2019). Statistical performance analysis of transient-based extended blockage detection in a water supply pipeline. *Journal of Water Supply: Research and Technology-Aqua*, 68(5):346–357.

[77] Khan, F. I. and Abbasi, S. (1999). Major accidents in process industries and an analysis of causes and consequences. *Journal of Loss Prevention in the process Industries*, 12(5):361–378.

[78] Kjerrumgaard Jensen, R., Kær Larsen, J., Lindgren Lassen, K., Mandø, M., and Andreasen, A. (2018). Implementation and validation of a free open source 1d water hammer code. *Fluids*, 3(3):64.

[79] Lambert, A. (2003). Assessing non-revenue water and its components: a practical approach. *Water*, 21(2):50–51.

[80] Lathi, B. P. (1998). *Signal processing and linear systems*. Oxford University Press New York.

[81] Lazhar, A., Hadj-Taïeb, L., and Hadj-Taïeb, E. (2013). Two leaks detection in viscoelastic pipeline systems by means of transient. *Journal of Loss Prevention in the Process Industries*, 26(6):1341–1351.

[82] Lee, P., Lambert, M., Simpson, A., Vítkovskỳ, J., and Misiunas, D. (2007). Leak location in single pipelines using transient reflections. *Australasian Journal of Water Resources*, 11(1):53–65.

[83] Lee, P. J. (2005). *Using system response functions of liquid pipelines for leak and blockage detection.* PhD thesis.

[84] Lee, P. J., Lambert, M. F., Simpson, A. R., Vítkovskỳ, J. P., and Liggett, J. (2006). Experimental verification of the frequency response method for pipeline leak detection. *Journal of Hydraulic research*, 44(5):693–707.

[85] Lee, P. J., Vítkovskỳ, J. P., Lambert, M. F., Simpson, A. R., and Liggett, J. A. (2005a). Frequency domain analysis for detecting pipeline leaks. *Journal of Hydraulic Engineering*, 131(7):596–604.

[86] Lee, P. J., Vítkovskỳ, J. P., Lambert, M. F., Simpson, A. R., and Liggett, J. A. (2005b). Leak location using the pattern of the frequency response diagram in pipelines: a numerical study. *Journal of Sound and Vibration*, 284(3-5):1051–1073.

[87] Lee, P. J., Vítkovskỳ, J. P., Lambert, M. F., Simpson, A. R., and Liggett, J. A. (2008). Discrete blockage detection in pipelines using the frequency response diagram: numerical study. *Journal of Hydraulic Engineering*, 134(5):658–663.

[88] Li, W., Ling, W., Liu, S., Zhao, J., Liu, R., Chen, Q., Qiang, Z., and Qu, J. (2011). Development of systems for detection, early warning, and control of pipeline leakage in drinking water distribution: A case study. *Journal of Environmental Sciences(China)*, 23(11):1816–1822.

[89] Liggett, J. A. and Chen, L.-C. (1994). Inverse transient analysis in pipe networks. *Journal of Hydraulic Engineering*, 120(8):934–955.

[90] Liou, C. P. (1991). Maximum pressure head due to linear valve closure. *Journal of fluids engineering*, 113(4):643–647.

[91] Liou, C. P. (1998). Pipeline leak detection by impulse response extraction. *Journal of Fluids Engineering*, 120.

[92] Liou, J. C. and Tian, J. (1995). Leak detection—transient flow simulation approaches. *Journal of energy resources technology*, 117(3):243–248.

[93] Lippitt, T. (1987). Williams' system signals advance in leak detection. *Oil Gas J.;(United States)*, 85(29).

[94] Liu, Z. and Kleiner, Y. (2013). State of the art review of inspection technologies for condition assessment of water pipes. *Measurement*, 46(1):1–15.

[95] Lynn, P. A. (2016). *An introduction to the analysis and processing of signals*. Macmillan International Higher Education.

[96] Lyu, Y., Jamil, M., Ma, P., He, N., Gupta, M. K., Khan, A. M., and Pimenov, D. Y. (2021). An ultrasonic-based detection of air-leakage for the unclosed components of aircraft. *Aerospace*, 8(2):55.

[97] Maloney, C. A. (1973). Locating cable faults. *IEEE Transactions on Industry Applications*, (4):380–394.

[98] Marlow, D., Heart, S., Burn, S., Urquhart, A., Gould, S., Anderson, M., Cook, S., Ambrose, M., Madin, B., and Fitzgerald, A. (2007). Condition assessment strategies and protocols for water and wastewater utility assets. CSIRO.

[99] Martini, A., Troncossi, M., and Rivola, A. (2015). Automatic leak detection in buried plastic pipes of water supply networks by means of vibration measurements. *Shock and Vibration*, 2015.

[100] Martini, A., Troncossi, M., Rivola, A., and Nascetti, D. (2014). Preliminary investigations on automatic detection of leaks in water distribution net-

works by means of vibration monitoring. In *Advances in Condition Monitoring of Machinery in Non-Stationary Operations*, pages 535–544. Springer.

[101] McCarthy, J. R., Weber, W. R., and Mancha, R. L. (2000). Coriolis flowmeter casing. US Patent D427,096.

[102] McInnis, D. and Karney, B. W. (1995). Transients in distribution networks: Field tests and demand models. *Journal of Hydraulic Engineering*, 121(3):218–231.

[103] Meniconi, S., Duan, H., Brunone, B., Ghidaoui, M. S., Lee, P., and Ferrante, M. (2014). Further developments in rapidly decelerating turbulent pipe flow modeling. *Journal of hydraulic engineering*, 140(7):04014028.

[104] Mergelas, B. and Kong, X. (2001). *Electromagnetic inspection of prestressed concrete pressure pipe*. American Water Works Association.

[105] Misiunas, D., Vítkovskỳ, J., Olsson, G., Simpson, A., and Lambert, M. (2003). Pipeline burst detection and location using a continuous monitoring technique. In *Advances in Water Supply Management: Int. Conf. on Computing and Control for the Water Industry (CCWI)*, pages 89–96.

[106] Misiunas, D., Vítkovskỳ, J., Olsson, G., Simpson, A., and Lambert, M. (2005). Pipeline break detection using pressure transient monitoring. *Journal of Water Resources Planning and Management*, 131(4):316–325.

[107] Mounce, S. R., Khan, A., Wood, A. S., Day, A. J., Widdop, P. D., and Machell, J. (2003). Sensor-fusion of hydraulic data for burst detection and location in a treated water distribution system. *Information Fusion*, 4(3):217–229.

[108] Nguyen, S. T. N., Gong, J., Lambert, M. F., Zecchin, A. C., and Simpson, A. R. (2018). Least squares deconvolution for leak detection with a pseudo random binary sequence excitation. *Mechanical Systems and Signal Processing*, 99:846–858.

[109] Nixon, W., Ghidaoui, M., and Kolyshkin, A. (2006). Range of validity of the transient damping leakage detection method. *Journal of hydraulic engineering*, 132(9):944–957.

[110] Papoulis, A. (1962). The fourier integral and its applications. *Polytechnic Institute of Brooklyn, McCraw-Hill Book Company Inc., USA, ISBN: 67-048447-3*.

[111] Parikh, N. and Sundaresan, N. (2008). Scalable and near real-time burst detection from ecommerce queries. In *Proceedings of the 14th ACM SIGKDD international conference on Knowledge discovery and data mining*, pages 972–980. ACM.

[112] Pothof, I. (2008). A turbulent approach to unsteady friction. *Journal of Hydraulic Research*, 46(5):679–690.

[113] Pudar, R. S. and Liggett, J. A. (1992). Leaks in pipe networks. *Journal of Hydraulic Engineering*, 118(7):1031–1046.

[114] Puust, R., Kapelan, Z., Savic, D., and Koppel, T. (2010). A review of methods for leakage management in pipe networks. *Urban Water Journal*, 7(1):25–45.

[115] Rakitin, B. and Xu, M. (2015). Centrifuge testing to simulate buried reinforced concrete pipe joints subjected to traffic loading. *Canadian Geotechnical Journal*, 52(11):1762–1774.

[116] Redd, B., Ebert, J., and Twitchell, A. (2019). Dft-based frequency offset estimators for 16-apsk. International Foundation for Telemetering.

[117] Rezaei, H., Ryan, B., and Stoianov, I. (2015). Pipe failure analysis and impact of dynamic hydraulic conditions in water supply networks. *Procedia Engineering*, 119:253–262.

[118] Rizwan, M. and Paul, I. (2015). Leak detection in pipeline system based on flow induced vibration methodology in pipeline. *Int. J. Science and Research (IJSR)*, 4:3326–3330.

[119] Romano, M., Kapelan, Z., and Savić, D. A. (2012). Automated detection of pipe bursts and other events in water distribution systems. *Journal of Water Resources Planning and Management*, 140(4):457–467.

[120] Rose, J. L., Mu, J., and Cho, Y. (2008). Recent advances on guided waves in pipe inspection. In *Proceedings of the 17th World Conference on Non-Destructive Testing, Shanghai, China*, pages 25–28. Citeseer.

[121] Schoukens, J., Rolain, Y., and Pintelon, R. (2006). Analysis of windowing/leakage effects in frequency response function measurements. *Automatica*, 42(1):27–38.

[122] Sharma, V. (2013). *Vibro-acoustic monitoring of pipeline leakage and corrosion*. PhD thesis, University of Calgary.

[123] Silva, R. A., Buiatti, C. M., Cruz, S. L., and Pereira, J. A. (1996). Pressure wave behaviour and leak detection in pipelines. *Computers & chemical engineering*, 20:S491–S496.

[124] Smith, J. W. and Hay, B. R. (2000). Magnetic flux leakage inspection tool for pipelines. US Patent 6,023,986.

[125] Smith, S. W. (1997). Digital signal processing: Scientist and engineers guide. San Diego: California Technical Publishing.

[126] Sneddon, I. N. (1995). *Fourier transforms*. Courier Corporation.

[127] Soares, A. K., Covas, D. I., and Reis, L. F. R. (2011). Leak detection by inverse transient analysis in an experimental pvc pipe system. *Journal of Hydroinformatics*, 13(2):153–166.

[128] Srirangarajan, S., Allen, M., Preis, A., Iqbal, M., Lim, H. B., and Whittle, A. J. (2013). Wavelet-based burst event detection and localization in water distribution systems. *Journal of Signal Processing Systems*, 72(1):1–16.

[129] Stephens, M., Gong, J., Marchi, A., Dix, L., Wilson, A., and Lambert, M. (2018). Leak detection in the adelaide cbd water network using permanent acoustic monitoring. In *Proceedings of the OzWater 18 Conference*.

[130] Stephens, M., Gong, J., Zhang, C., Marchi, A., Dix, L., and Lambert, M. F. (2020). Leak-before-break main failure prevention for water distribution pipes using acoustic smart water technologies: Case study in adelaide. *Journal of Water Resources Planning and Management*, 146(10):05020020.

[131] Stephens, M., Simpson, A., and Lambert, M. (2008). Internal wall condition assessment for water pipelines using inverse transient analysis. In *Water Distribution Systems Analysis 2008*, pages 1–11.

[132] Stephens, M. L., Lambert, M. F., and Simpson, A. R. (2013). Determining the internal wall condition of a water pipeline in the field using an inverse transient. *Journal of Hydraulic Engineering*, 139(3):310–324.

[133] Stoianov, I., Nachman, L., Madden, S., and Tokmouline, T. (2007). Pipeneta wireless sensor network for pipeline monitoring. In *Proceedings of the 6th international conference on Information processing in sensor networks*, pages 264–273. ACM.

[134] Sun, Z., Wang, P., Vuran, M. C., Al-Rodhaan, M. A., Al-Dhelaan, A. M., and Akyildiz, I. F. (2011). Mise-pipe: Magnetic induction-based wireless sensor networks for underground pipeline monitoring. *Ad Hoc Networks*, 9(3):218–227.

[135] Świetlik, J., Raczyk-Stanisławiak, U., Piszora, P., and Nawrocki, J. (2012). Corrosion in drinking water pipes: The importance of green rusts. *Water research*, 46(1):1–10.

[136] Tackett, N., Jovanov, E., and Milenković, A. (2011). An implementation of time synchronization in low-power wireless sensor networks. In *System Theory (SSST), 2011 IEEE 43rd Southeastern Symposium on*, pages 61–66. IEEE.

[137] Tafuri, A. N. (2000). Locating leaks with acoustic technology. *Journal-American Water Works Association*, 92(7):57–66.

[138] Tao, W., Dongying, W., Yu, P., and Wei, F. (2015). Gas leak localization and detection method based on a multi-point ultrasonic sensor array with tdoa algorithm. *Measurement Science and Technology*, 26(9):095002.

[139] USEPA (2010). Control and mitigation of drinking water losses in distribution systems. USEPA Washington.

[140] Van Der Kleij, F. and Stephenson, M. (2002). Acoustic logging–the bristol water experience. In *Proc. IWA Specialised Conference: Leakage Management–A Practical Approach, International Water Association, Lemesos, Cyprus*.

[141] Vardy, A. and Brown, J. (2003). Transient turbulent friction in smooth pipe flows. *Journal of sound and vibration*, 259(5):1011–1036.

[142] Vardy, A. E. and Brown, J. M. (1995). Transient, turbulent, smooth pipe friction. *Journal of hydraulic research*, 33(4):435–456.

[143] Vardy, A. E. and Hwang, K.-L. (1991). A characteristics model of transient friction in pipes. *Journal of Hydraulic Research*, 29(5):669–684.

[144] Vítkovskỳ, J., Lee, P., Stephens, M., Lambert, M., Simpson, A., and Liggett, J. (2003). Leak and blockage detection in pipelines via an impulse response method.

[145] Vítkovskỳ, J., Stephens, M., Bergant, A., Simpson, A., and Lambert, M. (2006a). Numerical error in weighting function-based unsteady friction models for pipe transients. *Journal of hydraulic engineering*, 132(7):709–721.

[146] Vítkovskỳ, J. P., Bergant, A., Simpson, A. R., and Lambert, M. F. (2006b). Systematic evaluation of one-dimensional unsteady friction models in simple pipelines. *Journal of Hydraulic Engineering*, 132(7):696–708.

[147] Vítkovskỳ, J. P., Lambert, M. F., Simpson, A. R., and Liggett, J. A. (2007). Experimental observation and analysis of inverse transients for pipeline leak detection. *Journal of Water Resources Planning and Management*, 133(6):519–530.

[148] Vítkovskỳ, J. P., Lee, P. J., Zecchin, A. C., Simpson, A. R., and Lambert, M. F. (2011). Head-and flow-based formulations for frequency domain analysis of fluid transients in arbitrary pipe networks. *Journal of Hydraulic Engineering*, 137(5):556–568.

[149] Waller, R. (1969). Office acoustics—effect of background noise. *Applied Acoustics*, 2(2):121–130.

[150] Wang, X., Guo, G., Liu, S., Wu, Y., Xu, X., and Smith, K. (2020). Burst detection in district metering areas using deep learning method. *Journal of Water Resources Planning and Management*, 146(6):04020031.

[151] Wang, X.-J., Lambert, M. F., and Simpson, A. R. (2005). Detection and location of a partial blockage in a pipeline using damping of fluid transients. *Journal of water resources planning and management*, 131(3):244–249.

[152] Wang, X.-J., Lambert, M. F., Simpson, A. R., Liggett, J. A., and Vı´tkovskỳ, J. P. (2002). Leak detection in pipelines using the damping of fluid transients. *Journal of Hydraulic Engineering*, 128(7):697–711.

[153] Wang, X.-J., Lambert, M. F., Simpson, A. R., and Vítkovskỳ, J. P. (2001). Leak detection in pipelines and pipe networks: a review. In *6th Conference on Hydraulics in Civil Engineering: The State of Hydraulics; Proceedings*, page 391. Institution of Engineers, Australia.

[154] Weil, G. J., Graf, R. J., and Forister, L. M. (1994). Remote sensing pipeline rehabilitation methodologies based upon the utilization of infrared thermography. In *Urban Drainage Rehabilitation Programs and Techniques: Selected Papers on Urban Drainage Rehabilitation from 1988-1993 Water Resource Planning and Management Division Conference Sessions*, pages 173–181. ASCE.

[155] Wickramarachi, P. (2003). Effects of windowing on the spectral content of a signal. *Sound and vibration*, 37(1):10–13.

[156] Wiener, N. (1988). *The Fourier integral and certain of its applications*. CUP Archive.

[157] Wiggert, D. C. (1968). Unsteady flows in lines with distributed leakage. *Journal of the hydraulics division*, 94(1):143–162.

[158] Wylie, E. B., Streeter, V. L., and Suo, L. (1993). *Fluid transients in systems*, volume 1. Prentice Hall Englewood Cliffs, NJ.

[159] Yazdekhasti, S., Piratla, K. R., Atamturktur, S., and Khan, A. (2018). Experimental evaluation of a vibration-based leak detection technique for water pipelines. *Structure and Infrastructure Engineering*, 14(1):46–55.

[160] Yazdekhasti, S., Piratla, K. R., Atamturktur, S., and Khan, A. A. (2017). Novel vibration-based technique for detecting water pipeline leakage. *Structure and Infrastructure Engineering*, 13(6):731–742.

[161] Yoon, D.-B., Park, J.-H., and Shin, S.-H. (2012). Improvement of cross-correlation technique for leak detection of a buried pipe in a tonal noisy environment. *Nuclear engineering and technology*, 44(8):977–984.

[162] Yoon, S., Ye, W., Heidemann, J., Littlefield, B., and Shahabi, C. (2011). Swats: Wireless sensor networks for steamflood and waterflood pipeline monitoring. *IEEE network*, 25(1).

[163] Zeng, W., Gong, J., Simpson, A. R., Cazzolato, B. S., Zecchin, A. C., and Lambert, M. F. (2020). Paired-irf method for detecting leaks in pipe networks. *Journal of Water Resources Planning and Management*, 146(5):04020021.

[164] Zhang, C., Gong, J., Zecchin, A., Lambert, M., and Simpson, A. (2018a). Faster inverse transient analysis with a head-based method of characteristics and a flexible computational grid for pipeline condition assessment. *Journal of Hydraulic Engineering*, 144(4):04018007.

[165] Zhang, C., Zecchin, A. C., Lambert, M. F., Gong, J., and Simpson, A. R. (2018b). Multi-stage parameter-constraining inverse transient analysis for pipeline condition assessment. *Journal of Hydroinformatics*, 20(2):281–300.

[166] Zhang, F., Qi, Y., and Wang, H. (2017). Sliding dft for spectrum analysis of coherent wind lidar. In *International Conference in Communications, Signal Processing, and Systems*, pages 1086–1095. Springer.

[167] Zhang, J., Tan, K., Zhao, J., Wu, H., and Zhang, Y. (2008). A practical snr-guided rate adaptation. In *IEEE INFOCOM 2008-The 27th Conference on Computer Communications*, pages 2083–2091. IEEE.

[168] Zhang, W. (2011). A general framework for transmission with transceiver distortion and some applications. *IEEE Transactions on Communications*, 60(2):384–399.

[169] Ziegel, E. (1987). Numerical recipes: The art of scientific computing. *Technometrics*, 29.

[170] Zielke, W. (1968). Frequency-dependent friction in transient pipe flow. *Journal of basic engineering*, 90(1):109–115.

Appendix A

Introduction of the Appendix

The Appendix contains related data not necessary to the immediate understanding of the discussion in the thesis. The contained equations and figures are indicated in the main body of the thesis where necessary.

Appendix B

Appendix of Paper 1

B.1 Derivation of the Analytical Solution and Fourier Series Analysis

Applying the general Fourier series form period by period to Eq. (3.16) gives

$$h^*(x^*,\ t^*+(m-1)T^*) = C_0^{(m)} + \sum_{n=1}^{\infty}[C_n^{(m)}cos(n\pi t^*) + D_n^{(m)}sin(n\pi t^*)] \tag{B.1}$$

The corresponding Fourier coefficients are defined as

$$C_0^{(m)} = \frac{1}{T^*}\int_{t_0^*}^{t_0^*+T^*} h^*(x^*,\ t^*+(m-1)T^*)dt^* \tag{B.2}$$

$$C_n^{(m)} = \frac{2}{T^*}\int_{t_0^*}^{t_0^*+T^*} h^*(x^*,\ t^*+(m-1)T^*)cos(n\pi t^*)dt^* \tag{B.3}$$

$$D_n^{(m)} = \frac{2}{T^*}\int_{t_0^*}^{t_0^*+T^*} h^*(x^*,\ t^*+(m-1)T^*)sin(n\pi t^*)dt^* \tag{B.4}$$

By substituting the solution of $h^*(x^*,\ t^*+(m-1)T^*)$ into Eqs. (B.2), (B.3), and (B.4), and according to Abramowitz et al. (1) and Wang et al. (152), the Fourier coefficients are calculated as

$$C_0^{(m)} = 0 \tag{B.5}$$

$$C_n^{(m)} = -\frac{e^{-(R+R_{nB})(t_0^*+T^*)} - e^{-(R+R_{nB})t_0^*}}{(R+R_{nB})T^*} sin(n\pi x^*) A_n e^{-(R+R_{nB})(m-1)T^*} \tag{B.6}$$

$$D_n^{(m)} = -\frac{e^{-(R+R_{nB})(t_0^*+T^*)} - e^{-(R+R_{nB})t_0^*}}{(R+R_{nB})T^*} sin(n\pi x^*) B_n e^{-(R+R_{nB})(m-1)T^*} \tag{B.7}$$

Therefore, the amplitude of the nth harmonic and the first period is

$$E_n^{(1)} = -\frac{e^{-(R+R_{nB})(t_0^*+T^*)} - e^{-(R+R_{nB})t_0^*}}{(R+R_{nB})T^*} sin(n\pi x^*) \sqrt{A_n^2 + B_n^2} \tag{B.8}$$

Accordingly, the amplitude of the nth harmonic and the mth period is

$$E_n^{(m)} = E_n^{(1)} e^{-(R+R_{nB})(m-1)T^*} \quad (m = 1,\ 2,\ 3, ...) \tag{B.9}$$

Appendix C

Appendix of Paper 2

C.1 Derivation of the Analytical Solution and Fourier Transform Analysis

By fitting the typical Fourier series form to Eq. (4.1), the amplitudes of the first and the nth harmonic component in each fundamental period of the pipeline system are

$$E_n^{(1)} = -\frac{e^{-(R+R_{nB})(t_0^*+T^*)} - e^{-(R+R_{nB})t_0^*}}{(R+R_{nB})T^*} sin(n\pi x^*)\sqrt{A_n^2+B_n^2} \tag{C.1}$$

$$E_n^{(m)} = E_n^{(1)} e^{-(R+R_{nB})(m-1)T^*} \quad (m = 1,\ 2,\ 3, ...) \tag{C.2}$$

respectively, where t_0^* is the dimensionless starting time of the analysis, T^* is the dimensionless fundamental period of the pipeline system, m and n represent the number of the fundamental period of the pipeline system and the harmonic component respectively, and $E_n^{(m)}$ is the amplitude of the nth harmonic component in the mth fundamental period of the pipeline system.

According to the mathematical process in Wang et al. (152), applying the general Fourier series,

$$h^*(x^*,\ t^*+(m-1)T^*) = C_0^{(m)} + \sum_{j=1}^{\infty}[C_j^{(m)} cos(j\pi t^*) + D_j^{(m)} sin(j\pi t^*)] \tag{C.3}$$

to the analytical solution Eq. (4.1) gives

$$C_0^{(m)} = 0 \tag{C.4}$$

$$C_n^{(m)} = -\frac{e^{-(R+R_{nB})(t_0^*+T^*)} - e^{-(R+R_{nB})t_0^*}}{(R+R_{nB})T^*} sin(n\pi x^*) A_n e^{-(R+R_{nB})(m-1)T^*} \tag{C.5}$$

$$D_n^{(m)} = -\frac{e^{-(R+R_{nB})(t_0^*+T^*)} - e^{-(R+R_{nB})t_0^*}}{(R+R_{nB})T^*} sin(n\pi x^*) B_n e^{-(R+R_{nB})(m-1)T^*} \tag{C.6}$$

where $C_0^{(m)}$, $C_n^{(m)}$, and $D_n^{(m)}$ are the Fourier coefficients, and $E_n^{(m)} = \sqrt{\left(C_n^{(m)}\right)^2 + \left(D_n^{(m)}\right)^2}$. Thus, according to Euler's formula, the complex form of Eq. (4.1) is

$$\begin{aligned} h^*(x^*,\ t^*) &= \sum_{n=1}^{\infty} \frac{1}{2}(C_n^{(m)} - iD_n^{(m)}) e^{i2\pi \frac{n}{T^*} t^*} + \sum_{n=1}^{\infty} \frac{1}{2}(C_{-n}^{(m)} - iD_{-n}^{(m)}) e^{i2\pi \frac{(-n)}{T^*} t^*} \\ &= \sum_{n=1}^{\infty} \frac{1}{2}(C_n^{(m)} - iD_n^{(m)}) e^{i2\pi \frac{n}{T^*} t^*} + \sum_{n=-1}^{-\infty} \frac{1}{2}(C_n^{(m)} - iD_n^{(m)}) e^{-i2\pi \frac{n}{T^*} t^*} \\ &= \sum_{n=-\infty}^{\infty} \frac{1}{2}(C_n^{(m)} - iD_n^{(m)}) e^{i2\pi \frac{n}{T^*} t^*} \quad (n \neq 0) \end{aligned} \tag{C.7}$$

Let $\frac{1}{T^*} = f_0^*$, where f_0^* is the dimensionless fundamental frequency, thus

$$h^*(x^*,\ t^*) = \sum_{n=-\infty}^{\infty} \frac{1}{2}(C_n^{(m)} - iD_n^{(m)}) e^{i2\pi n f_0^* t^*} \tag{C.8}$$

Based on the definition of the Fourier coefficient of the complex form of the Fourier series (50; 126),

$$\frac{1}{2}(C_n^{(m)} - iD_n^{(m)}) = \frac{1}{T^*} \int_{t_0^*}^{t_0^*+T^*} h^*(x^*,\ t^*) e^{-i2\pi n f_0^* t^*} dt^* \tag{C.9}$$

it is shown that

$$h^*(x^*,\ t^*) = \sum_{n=-\infty}^{\infty} \frac{1}{T^*} \int_{t_0^*}^{t_0^*+T^*} h^*(x^*,\ t^*) e^{-i2\pi n f_0^* t^*} dt^* e^{i2\pi n f_0^* t^*} \tag{C.10}$$

Letting $t_0^* = -\frac{T^*}{2}$ gives (50; 126)

$$h^*(x^*,\ t^*) = \sum_{n=-\infty}^{\infty} \left[\int_{-\frac{T^*}{2}}^{\frac{T^*}{2}} h^*(x^*,\ t^*) e^{-i2\pi n f_0^* t^*} dt^* \right] e^{i2\pi n f_0^* t^*} f_0^* \tag{C.11}$$

Letting T^* approach ∞, f_0^* becomes df^*, nf_0^* becomes continuous variable f^*, and the summation becomes the integral (50; 126). Thus,

$$h^*(x^*,\ t^*) = \lim_{T^* \to \infty} \left\{ \sum_{n=-\infty}^{\infty} \left[\int_{-\frac{T^*}{2}}^{\frac{T^*}{2}} h^*(x^*,\ t^*) e^{-i2\pi n f_0^* t^*} dt^* \right] e^{i2\pi n f_0^* t^*} f_0^* \right\} \tag{C.12}$$

becomes

$$h^*(x^*,\ t^*) = \int_{-\infty}^{\infty} \left[\int_{-\infty}^{\infty} h^*(x^*,\ t^*) e^{-i2\pi f^* t^*} dt^* \right] e^{i2\pi f^* t^*} df^* \tag{C.13}$$

Therefore,

$$h^*(x^*,\ t^*) = \int_{-\infty}^{\infty} F(f^*) e^{i2\pi f^* t^*} df^* \tag{C.14}$$

where

$$F(f^*) = \int_{-\infty}^{\infty} h^*(x^*,\ t^*) e^{-i2\pi f^* t^*} dt^* \tag{C.15}$$

Substituting Eq. (C.8) into Eq. (C.15) and expressing the continuous variable f^* back to nf_0^* to represent all the resonance responses gives

$$F(nf_0^*) = \int_{-\infty}^{\infty} \frac{1}{2}(C_n^{(m)} - iD_n^{(m)}) dt^* \tag{C.16}$$

where n could be any integer from minus infinity to infinity. In terms of the signal in the given time range $[t_1,\ t_2]$, Eq. (C.16) becomes

$$F(nf_0^*) = \int_{t_1^*}^{t_2^*} \frac{1}{2}(C_n^{(m)} - iD_n^{(m)}) dt^* = \frac{1}{2}(C_n^{(m)} - iD_n^{(m)})(t_2^* - t_1^*) \tag{C.17}$$

Analyzing the signal every window gap with a fixed dimensionless interval

length t_a^* provides

$$F(nf_0^*) = \int_{t_0^*}^{t_0^*+t_a^*} \frac{1}{2}(C_n^{(m)} - iD_n^{(m)})dt^* = \frac{t_a^*}{2}(C_n^{(m)} - iD_n^{(m)}) \tag{C.18}$$

Therefore, according to Eqs. (C.2), (C.5),and (C.6), the absolute value of the Fourier transform of $h^*(x^*,\ t^*)$ is

$$|F(nf_0^*)| = \frac{t_a^*}{2}\sqrt{\left(C_n^{(m)}\right)^2 + \left(D_n^{(m)}\right)^2} = \frac{t_a^*}{2}E_n^{(m)} \tag{C.19}$$

Equation (C.19) makes it possible and reasonable to analyze the resonance responses of the measured head disturbance within a window, instead of each fundamental period of the pipeline system, indicating that the measured signal can be analyzed for any manually given or determined length t_a. Under this specific condition, the expression of the amplitude of the harmonic component $E_n^{(m)}$ from Eqs. (C.2) and (C.1) becomes

$$E_n^{(m)} = E_n^{(1)} e^{-(R+R_{nB})(m-1)t_a^*} \tag{C.20}$$

It can be seen that normalizing the direct results of the DFT of the signal by dividing the dimensionless length of the signal in an analyzed window length t_a^*, and then multiplying by two can provide the amplitude of the nth harmonic component in the mth analyzed time window.

C.2 Supplemental Figures

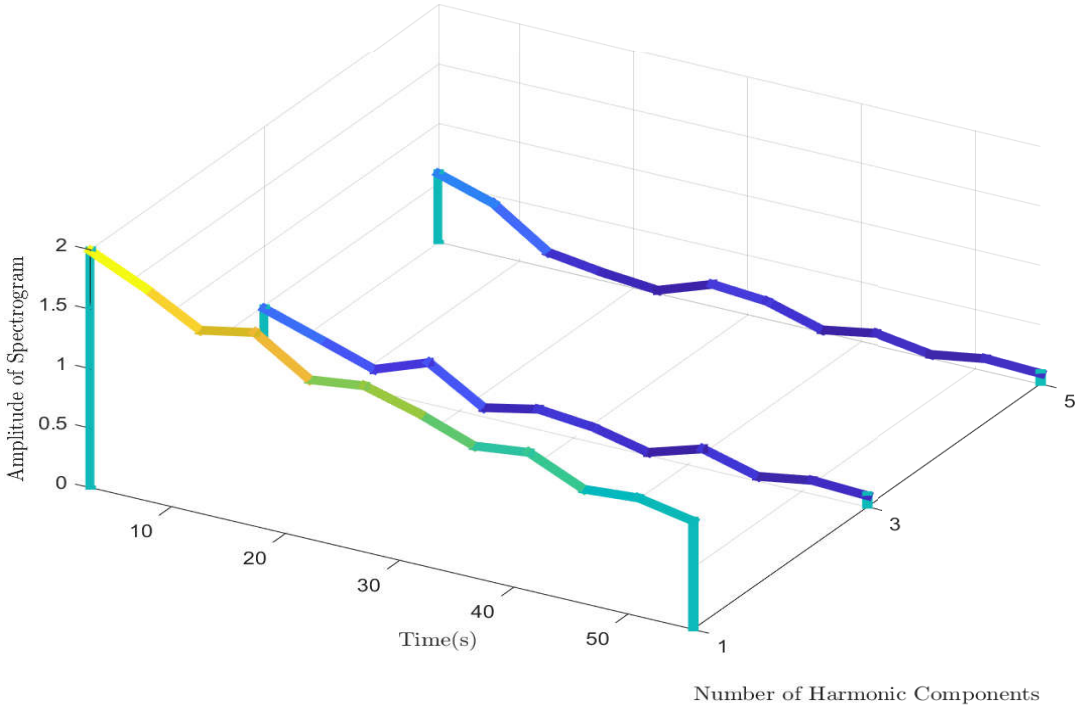

Figure C.1: Discrete harmonic spectrogram from Case 2

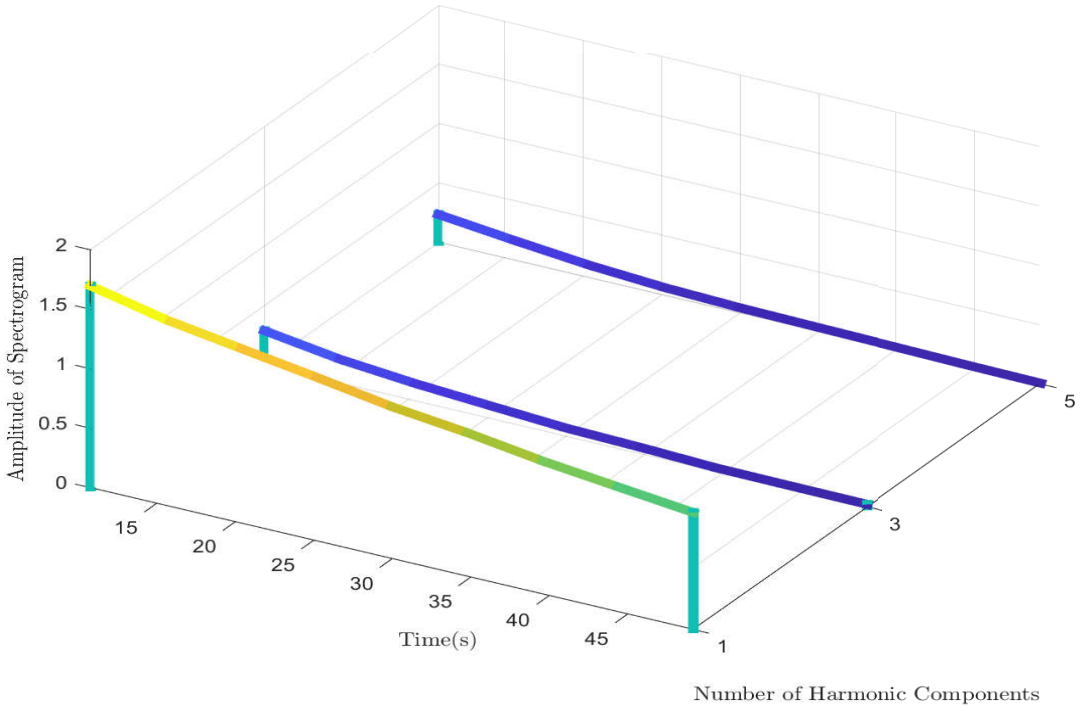

Figure C.2: Discrete harmonic spectrogram from Case 3 (1)

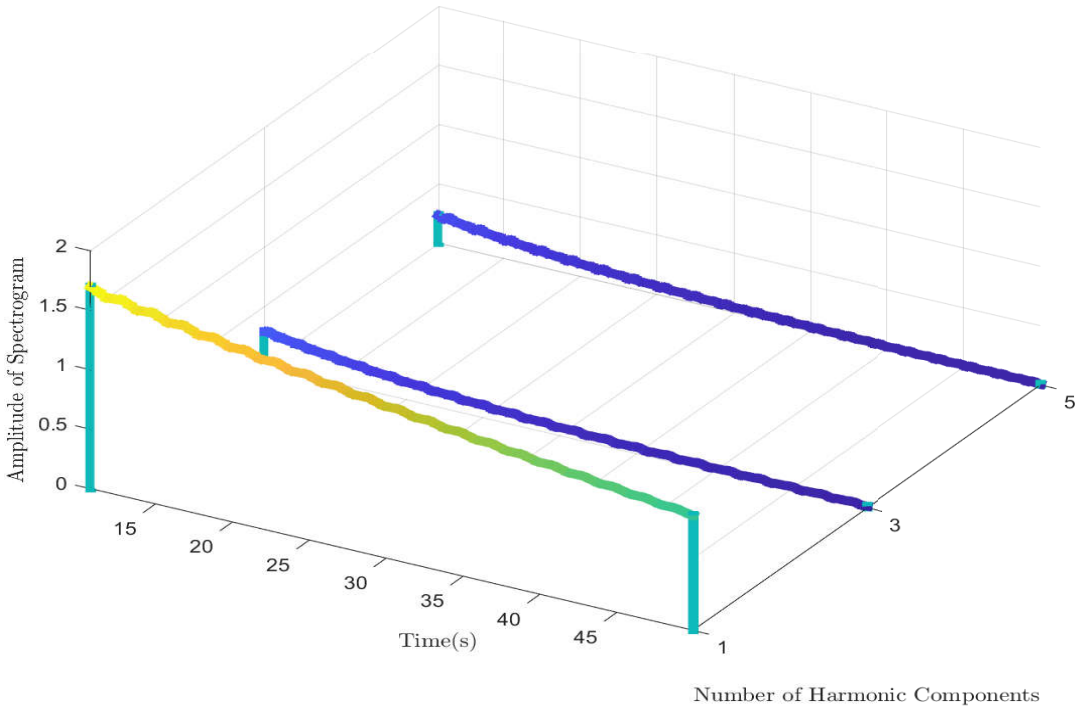

Figure C.3: Discrete harmonic spectrogram from Case 4

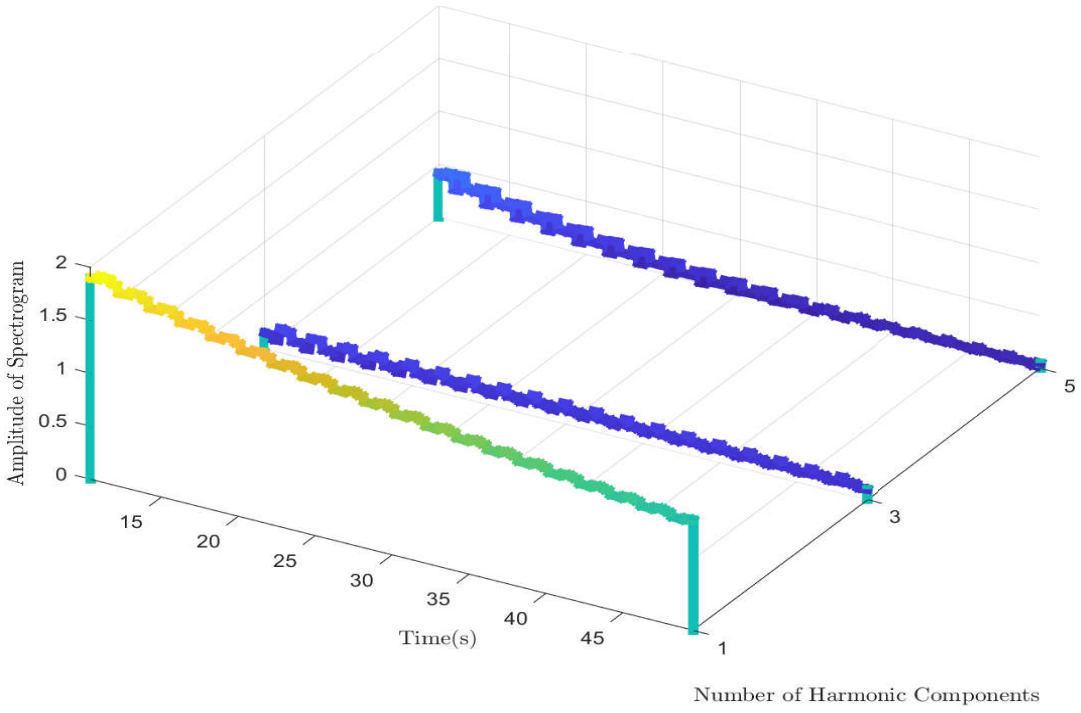

Figure C.4: Discrete harmonic spectrogram from Case 5

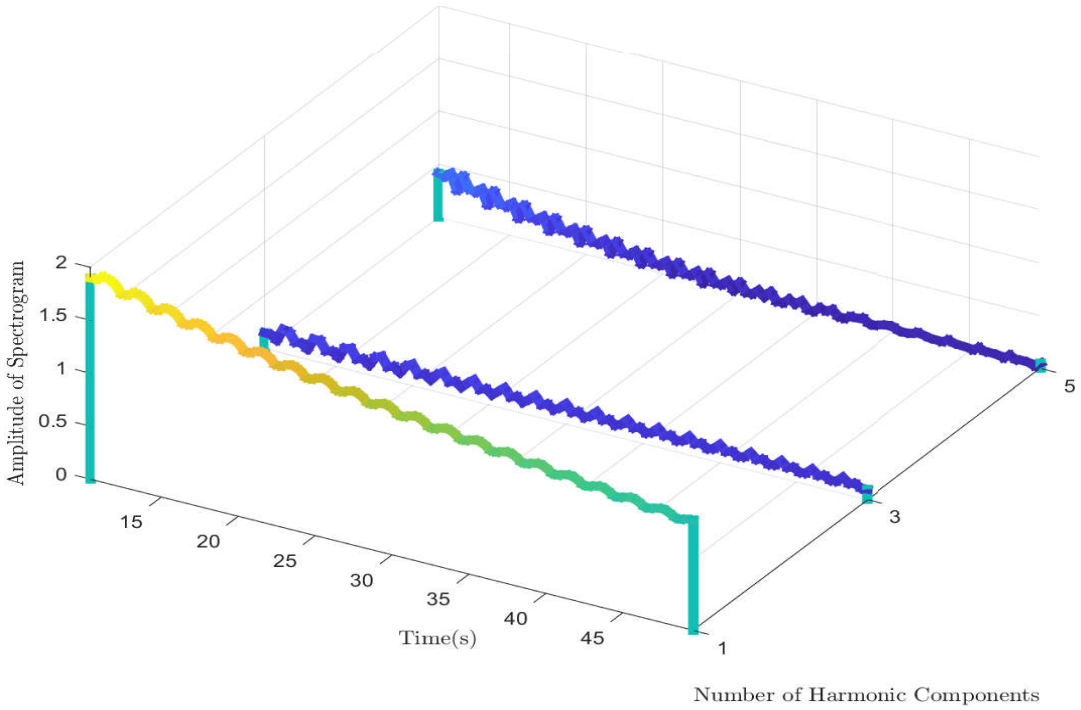

Figure C.5: Discrete harmonic spectrogram from Case 6

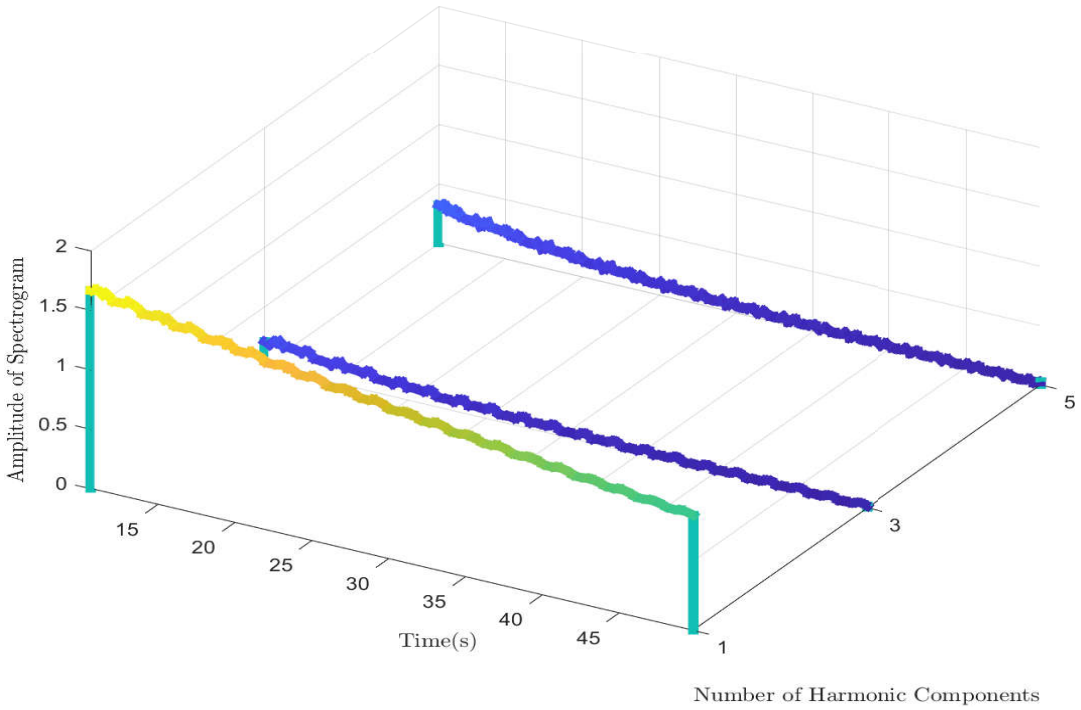

Figure C.6: Discrete harmonic spectrogram from Case 7

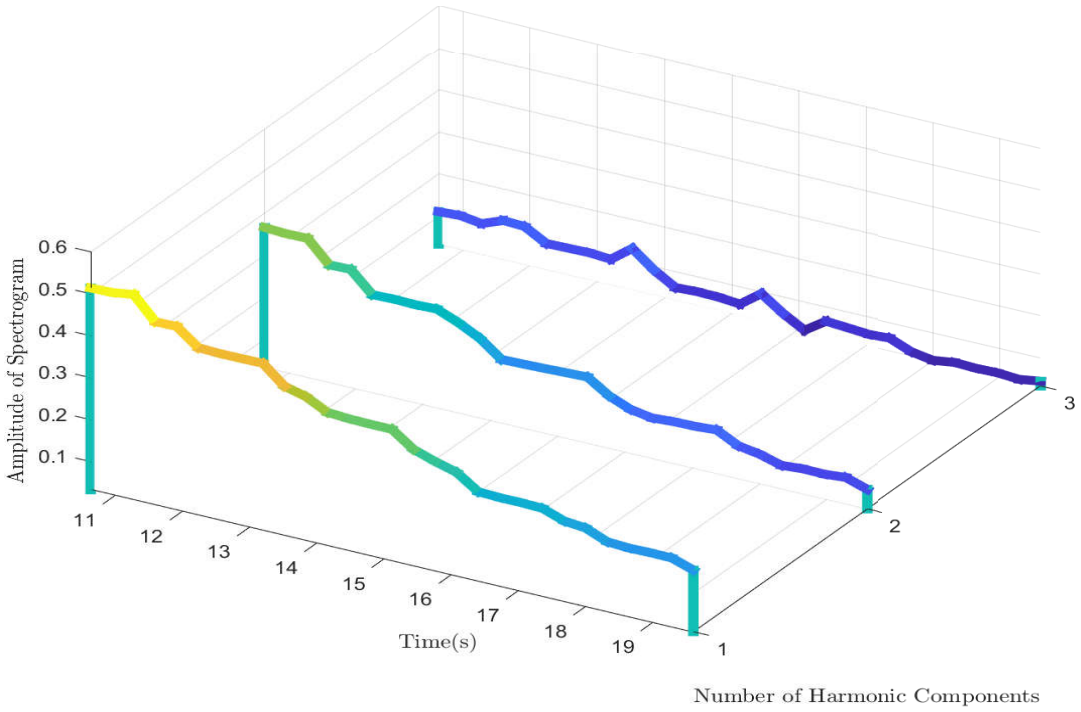

Figure C.7: Discrete harmonic spectrogram from Case 8

Appendix D

Appendix of Paper 4

D.1 Derivation of the Fourier Transform Analysis

According to the mathematical process in Wang et al. (152), applying the general Fourier series

$$h^*(x^*,\ t^*+(m-1)T^*) = C_0^{(m)} + \sum_{j=1}^{\infty}[C_j^{(m)}cos(j\pi t^*) + D_j^{(m)}sin(j\pi t^*)] \tag{D.1}$$

to the analytical solution Eq. (E.1) gives

$$C_0^{(m)} = 0 \tag{D.2}$$

$$C_n^{(m)} = -\frac{e^{-(R+R_{nL})(t_0^*+T^*)} - e^{-(R+R_{nL})t_0^*}}{(R+R_{nL})T^*} sin(n\pi x^*) A_n e^{-(R+R_{nL})(m-1)T^*} \tag{D.3}$$

$$D_n^{(m)} = -\frac{e^{-(R+R_{nL})(t_0^*+T^*)} - e^{-(R+R_{nL})t_0^*}}{(R+R_{nL})T^*} sin(n\pi x^*) B_n e^{-(R+R_{nL})(m-1)T^*} \tag{D.4}$$

where $C_0^{(m)}$, $C_n^{(m)}$, and $D_n^{(m)}$ are the Fourier coefficients, and $E_n^{(m)} = \sqrt{\left(C_n^{(m)}\right)^2 + \left(D_n^{(m)}\right)^2}$.

Thus, according to Euler's formula, the complex form of Eq. (E.1) is

$$\begin{aligned} h^*(x^*,\ t^*) &= \sum_{n=1}^{\infty}\frac{1}{2}(C_n^{(m)} - iD_n^{(m)})e^{i2\pi\frac{n}{T^*}t^*} + \sum_{n=1}^{\infty}\frac{1}{2}(C_{-n}^{(m)} - iD_{-n}^{(m)})e^{i2\pi\frac{(-n)}{T^*}t^*} \\ &= \sum_{n=1}^{\infty}\frac{1}{2}(C_n^{(m)} - iD_n^{(m)})e^{i2\pi\frac{n}{T^*}t^*} + \sum_{n=-1}^{-\infty}\frac{1}{2}(C_n^{(m)} - iD_n^{(m)})e^{-i2\pi\frac{n}{T^*}t^*} \\ &= \sum_{n=-\infty}^{\infty}\frac{1}{2}(C_n^{(m)} - iD_n^{(m)})e^{i2\pi\frac{n}{T^*}t^*} \quad (n \neq 0) \end{aligned} \tag{D.5}$$

Let $\frac{1}{T^*} = f_0^*$, thus

$$h^*(x^*,\ t^*) = \sum_{n=-\infty}^{\infty}\frac{1}{2}(C_n^{(m)} - iD_n^{(m)})e^{i2\pi n f_0^* t^*} \tag{D.6}$$

Based on the definition of the Fourier coefficient of the complex form of the Fourier series,

$$\frac{1}{2}(C_n^{(m)} - iD_n^{(m)}) = \frac{1}{T^*}\int_{t_0^*}^{t_0^*+T^*} h^*(x^*,\ t^*)e^{-i2\pi n f_0^* t^*}dt^* \tag{D.7}$$

it is shown that

$$h^*(x^*,\ t^*) = \sum_{n=-\infty}^{\infty}\frac{1}{T^*}\int_{t_0^*}^{t_0^*+T^*} h^*(x^*,\ t^*)e^{-i2\pi n f_0^* t^*}dt^* e^{i2\pi n f_0^* t^*} \tag{D.8}$$

Letting $t_0^* = -\frac{T^*}{2}$ gives

$$h^*(x^*,\ t^*) = \sum_{n=-\infty}^{\infty}\left[\int_{-\frac{T^*}{2}}^{\frac{T^*}{2}} h^*(x^*,\ t^*)e^{-i2\pi n f_0^* t^*}dt^*\right]e^{i2\pi n f_0^* t^*} f_0^* \tag{D.9}$$

Letting T^* approach ∞, f_0^* becomes df^*, nf_0^* becomes continuous variable f^*, and the summation becomes the integral. Thus,

$$h^*(x^*,\ t^*) = \lim_{T^*\to\infty}\left\{\sum_{n=-\infty}^{\infty}\left[\int_{-\frac{T^*}{2}}^{\frac{T^*}{2}} h^*(x^*,\ t^*)e^{-i2\pi n f_0^* t^*}dt^*\right]e^{i2\pi n f_0^* t^*} f_0^*\right\} \tag{D.10}$$

becomes

$$h^*(x^*,\ t^*) = \int_{-\infty}^{\infty} \left[\int_{-\infty}^{\infty} h^*(x^*,\ t^*) e^{-i2\pi f^* t^*} dt^* \right] e^{i2\pi f^* t^*} df^* \tag{D.11}$$

Therefore,

$$h^*(x^*,\ t^*) = \int_{-\infty}^{\infty} F(f^*) e^{i2\pi f^* t^*} df^* \tag{D.12}$$

where

$$F(f^*) = \int_{-\infty}^{\infty} h^*(x^*,\ t^*) e^{-i2\pi f^* t^*} dt^* \tag{D.13}$$

Substituting Eq. (D.6) into Eq. (D.13) and expressing the continuous variable f^* back to nf_0^* to represent all the resonance responses gives

$$F(nf_0^*) = \int_{-\infty}^{\infty} \frac{1}{2}(C_n^{(m)} - iD_n^{(m)}) dt^* \tag{D.14}$$

where n could be any integer from minus infinity to infinity now. In terms of the signal in the given time range $[t_0,\ t_0 + T]$, Eq. (D.14) becomes

$$F(nf_0^*) = \int_{t_0^*}^{t_0^*+T^*} \frac{1}{2}(C_n^{(m)} - iD_n^{(m)}) dt^* = \frac{T^*}{2}(C_n^{(m)} - iD_n^{(m)}) \tag{D.15}$$

Therefore, according to Eqs. (E.4), (D.3), (D.4), the absolute value of the Fourier transform of $h^*(x^*,\ t^*)$ is

$$F(nf_0^*) = \frac{T^*}{2}\sqrt{\left(C_n^{(m)}\right)^2 + \left(D_n^{(m)}\right)^2} = \frac{T^*}{2}E_n^{(m)} \tag{D.16}$$

In the Fourier Transform process, the results are generally normalized by multiplying by two and dividing by the length of data. Therefore, the resonance responses in the results of the Fourier Transform in each period are equal to $E_n^{(m)}$.

D.2 Supplemental Figures

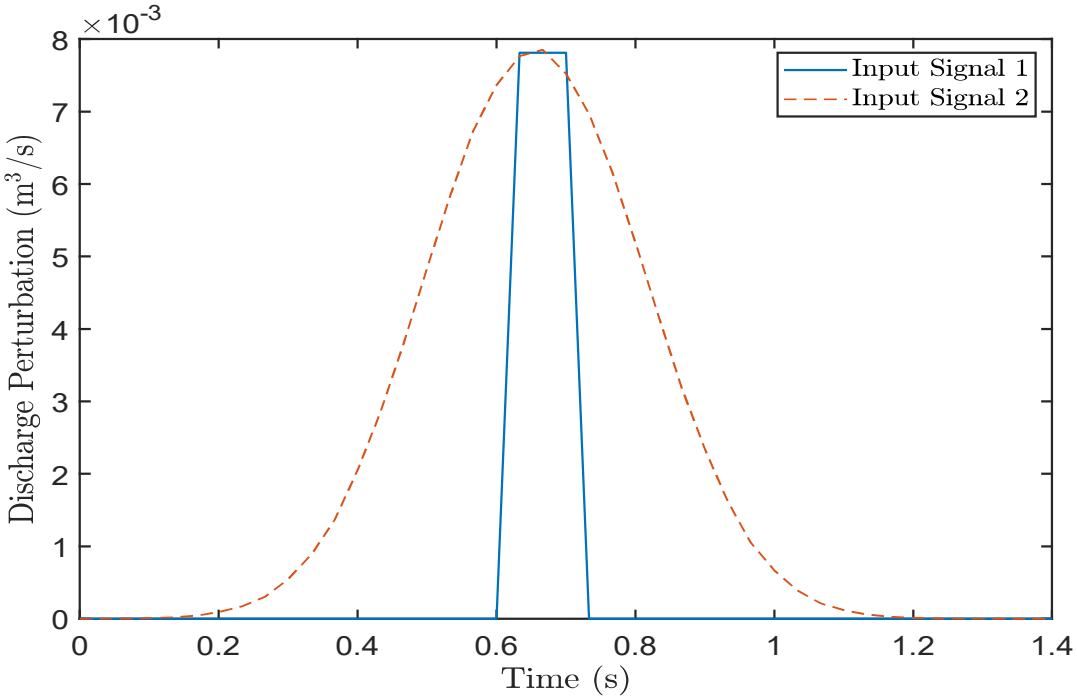

Figure D.1: Inputs signals from Cases 2 and 3

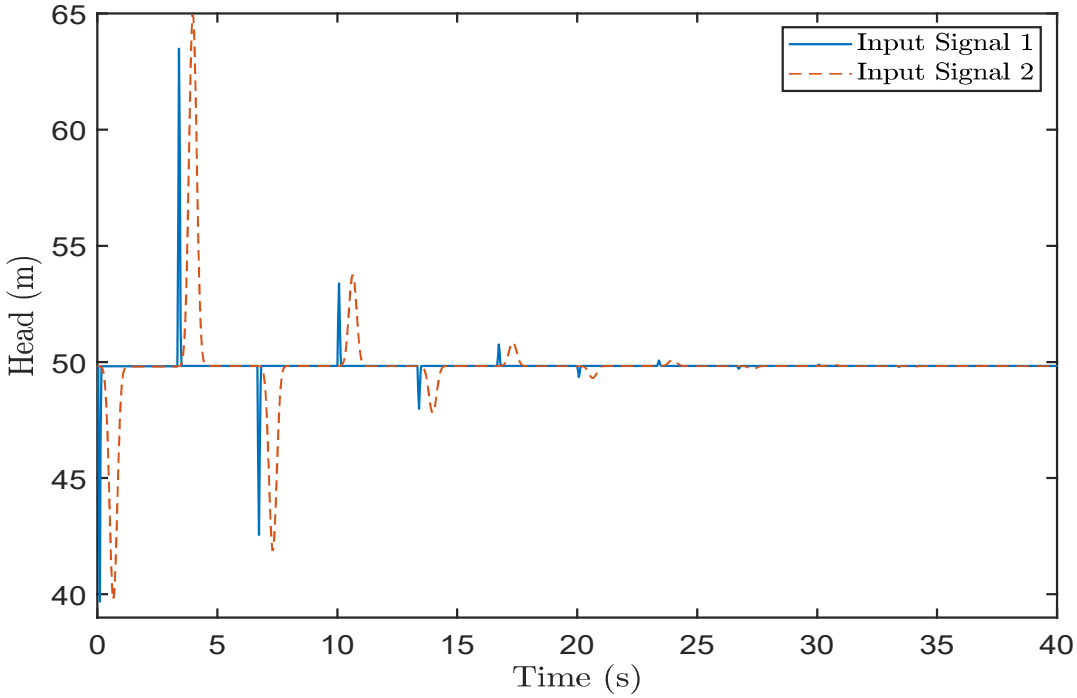

Figure D.2: Output signals from Cases 2 and 3

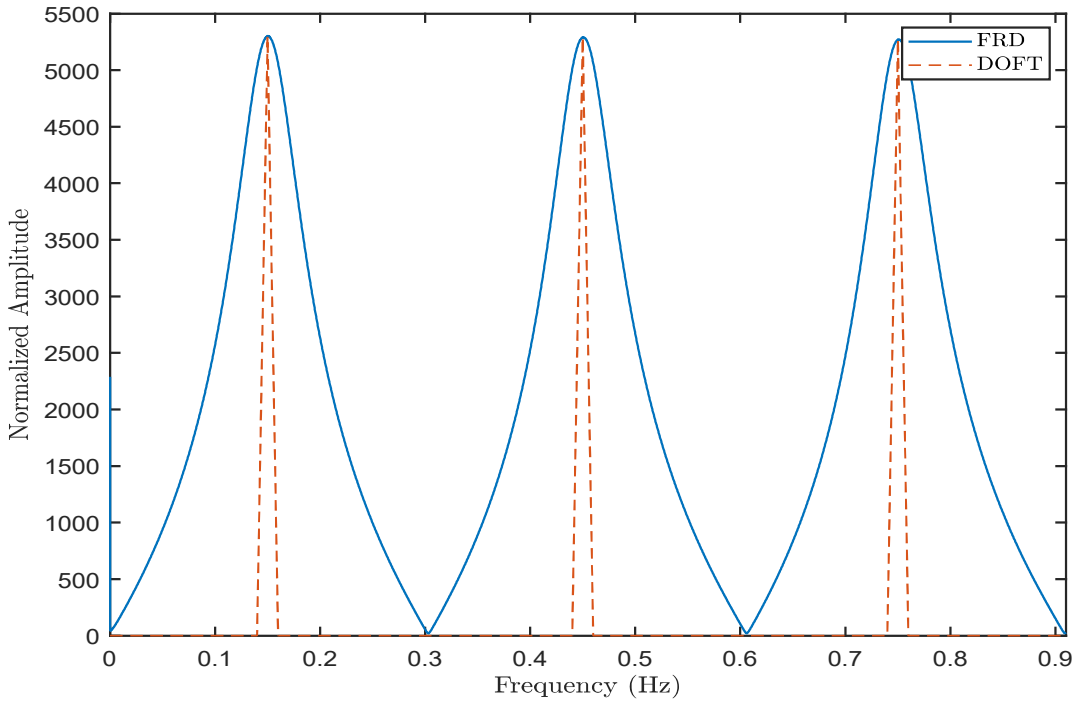

Figure D.3: DOFT and FRD results from Case 3

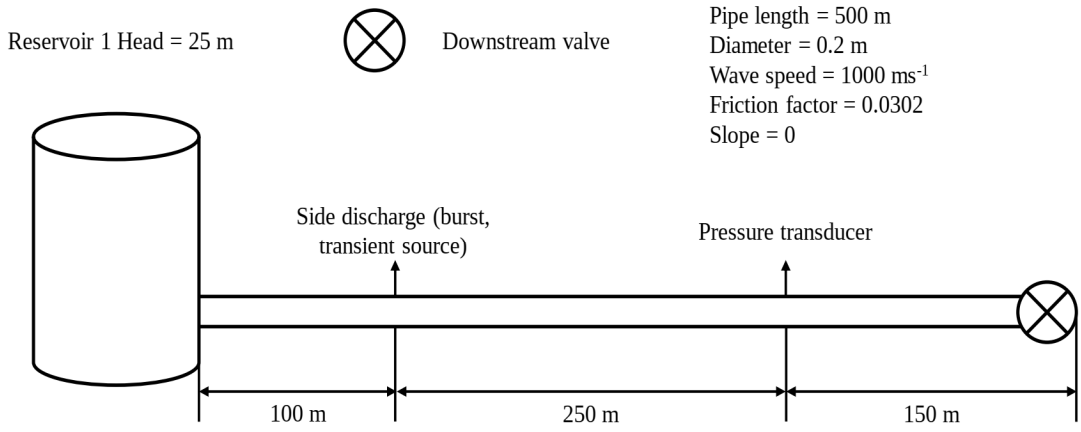

Figure D.4: Pipeline configuration from Case 5

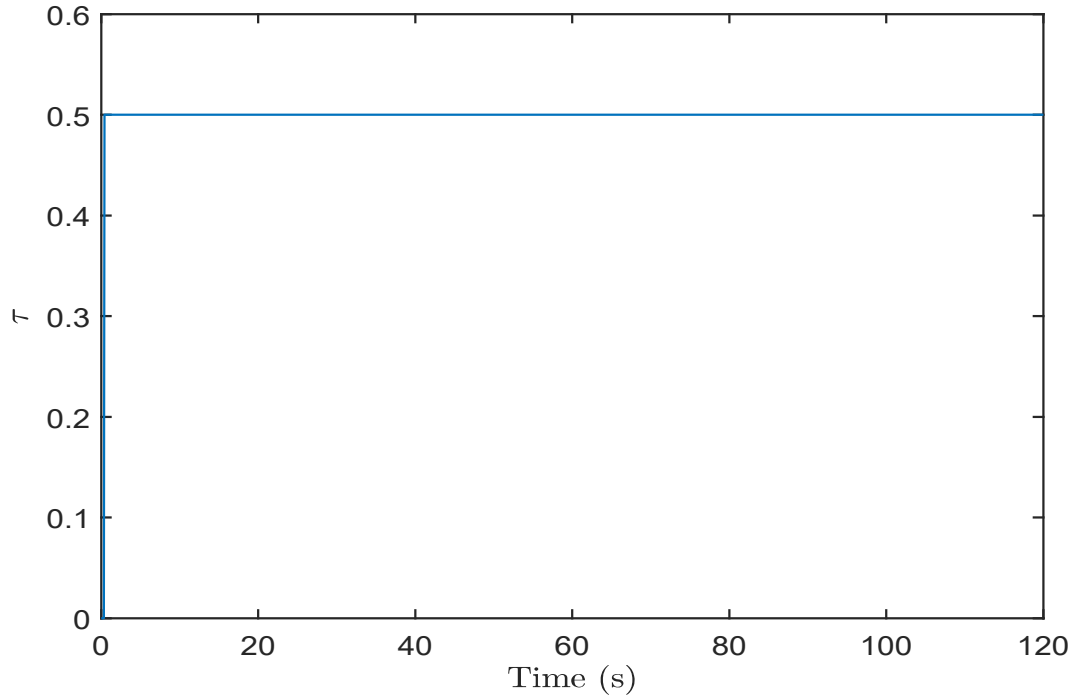

Figure D.5: Input signal from Case 5

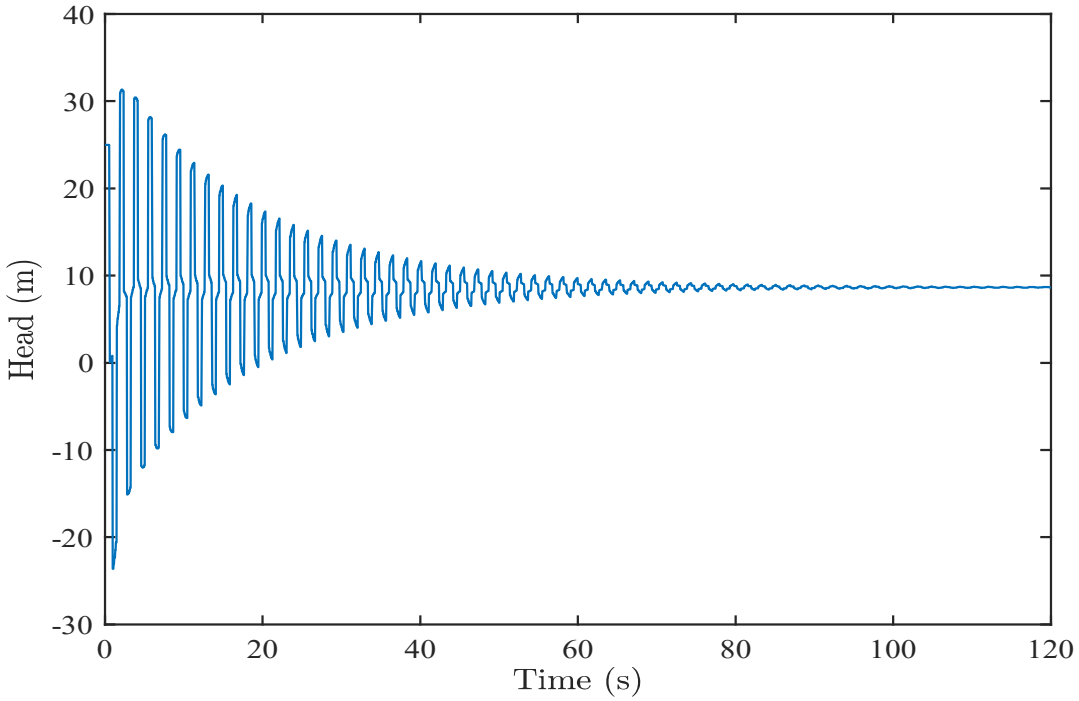

Figure D.6: Output signal from Case 5

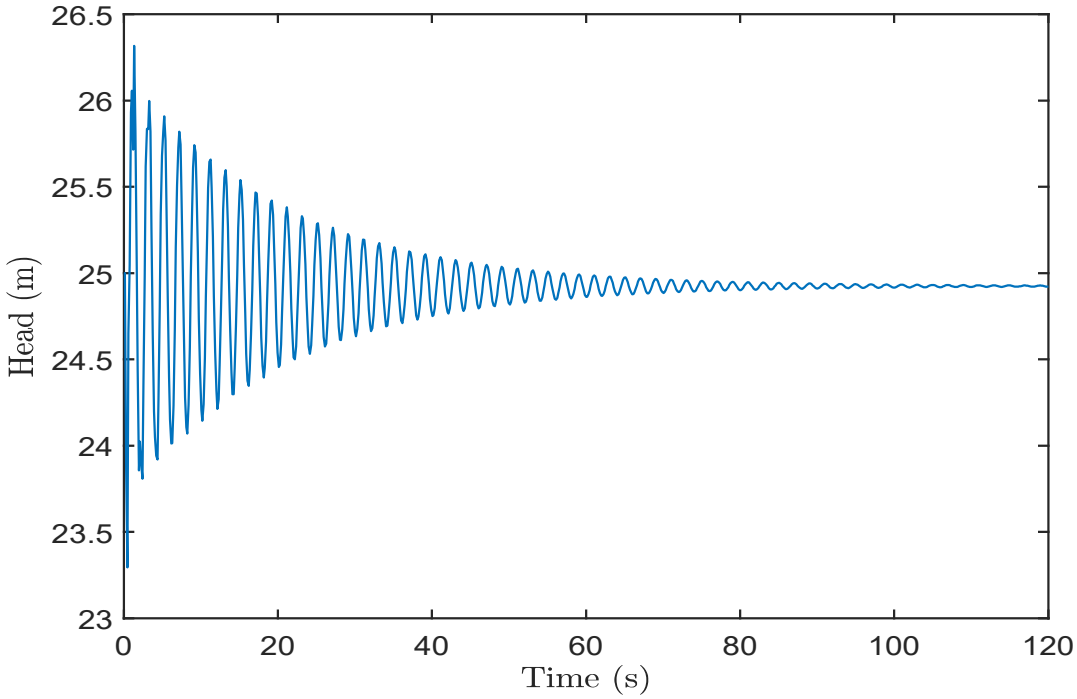

Figure D.7: Low sampled output signal from Case 6

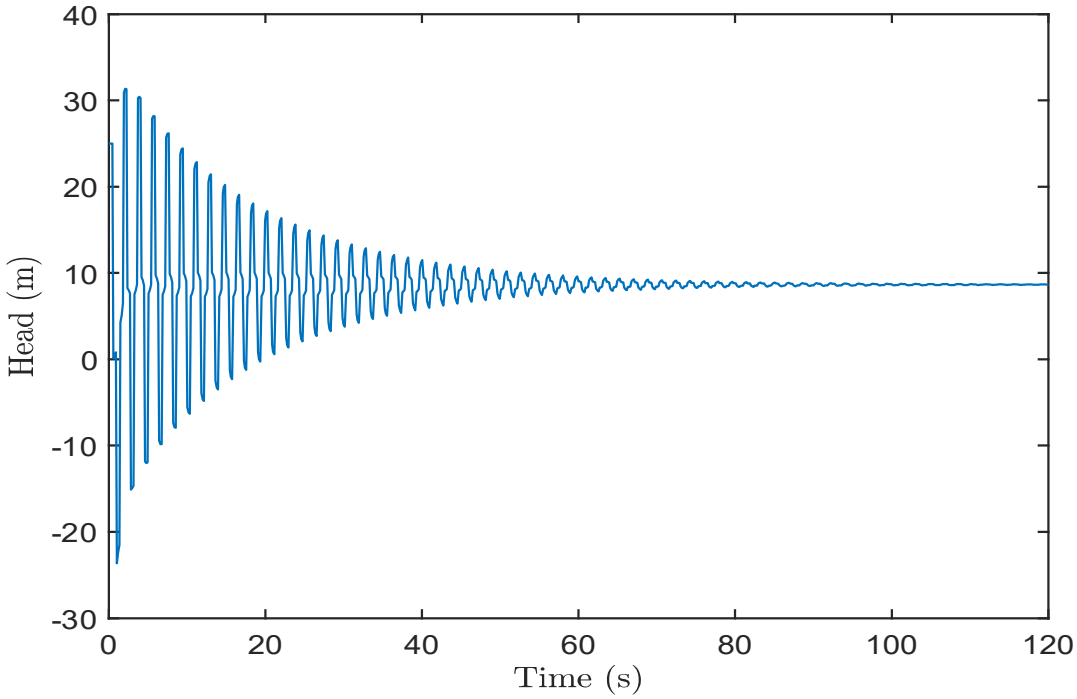

Figure D.8: Low sampled output signal from Case 7

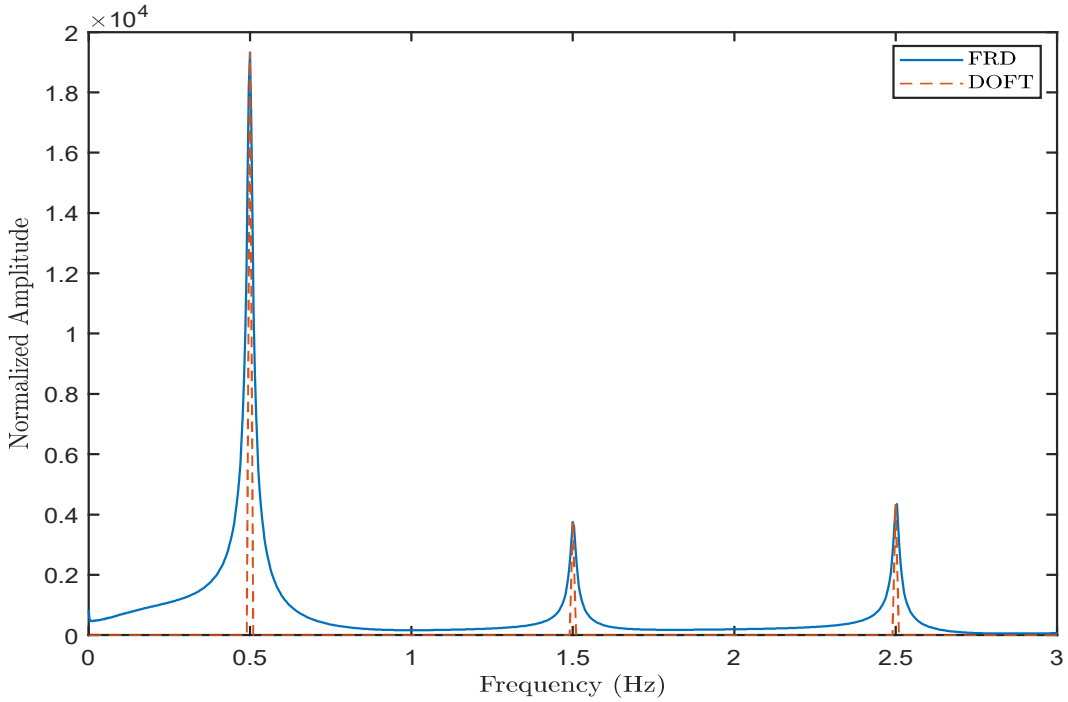

Figure D.9: DOFT and FRD results from Case 7

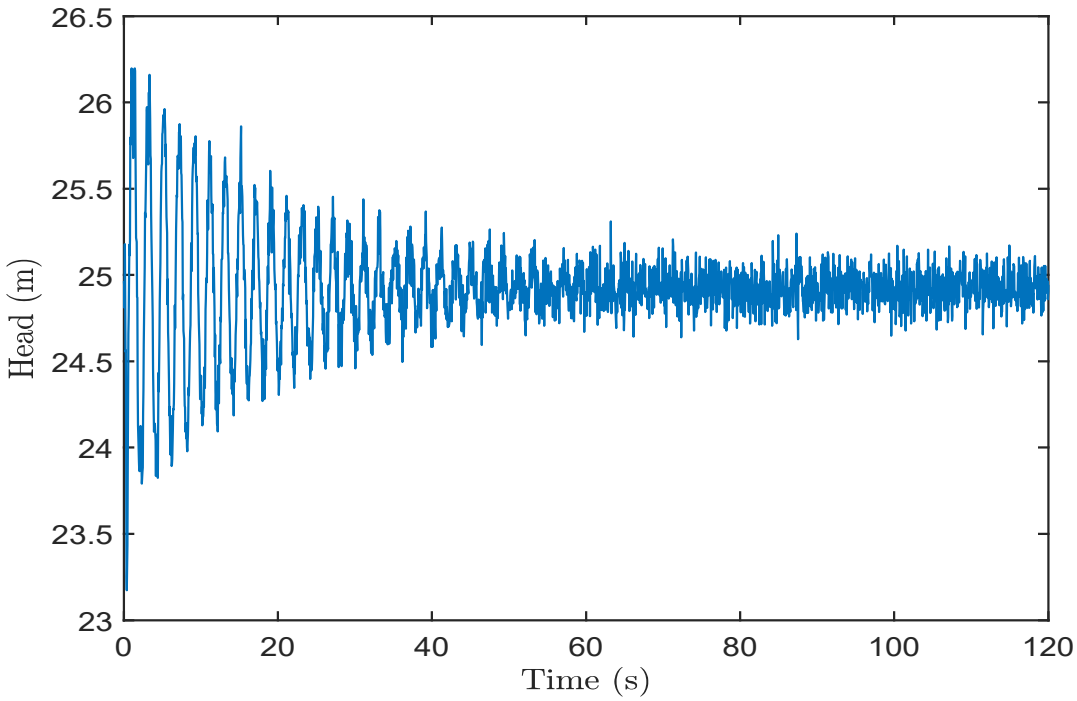

Figure D.10: Output signal from Test 2 of Case 8

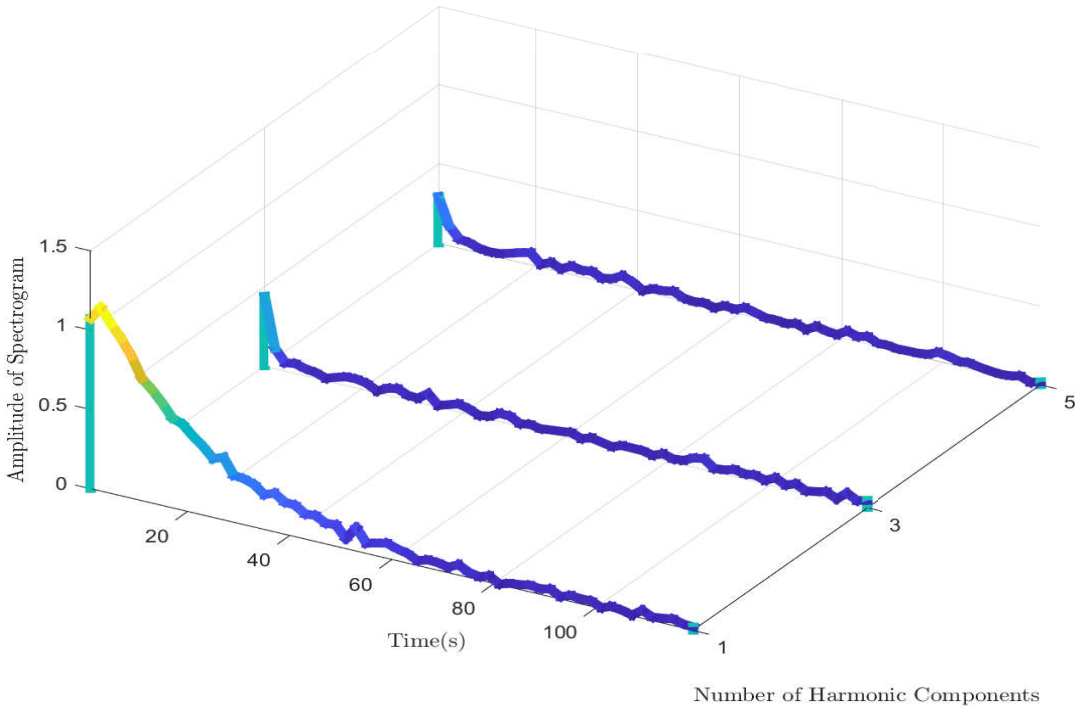

Figure D.11: Discrete harmonic spectrogram from Test 2 of Case 8

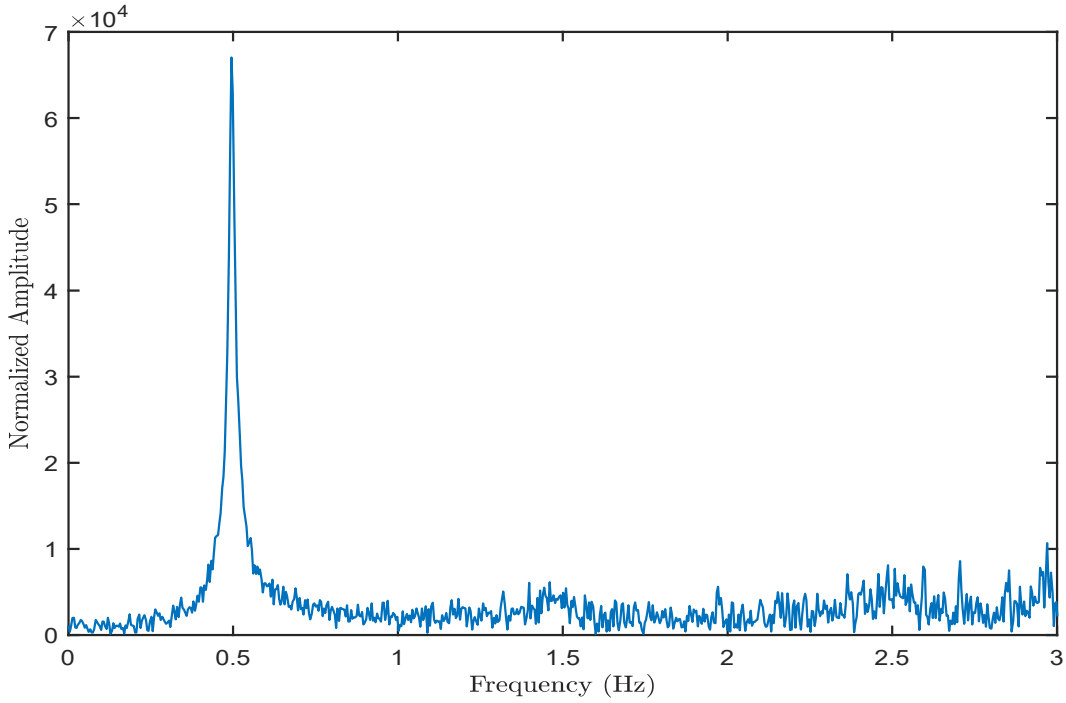

Figure D.12: FRD result from Test 2 of Case 8

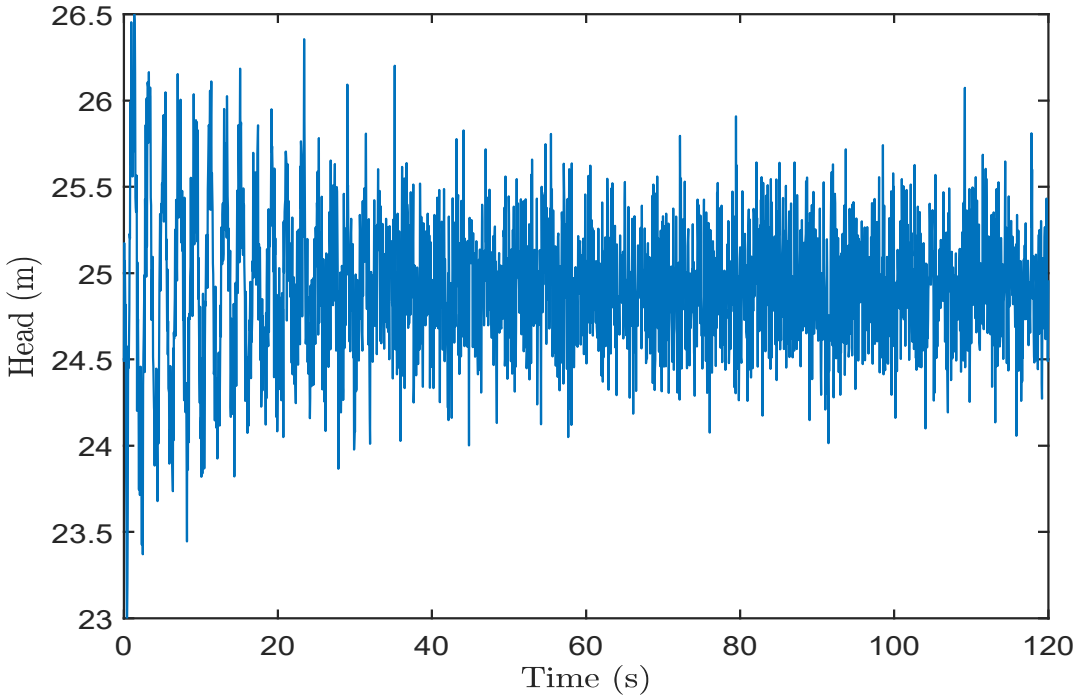

Figure D.13: Output signal from Test 3 of Case 8

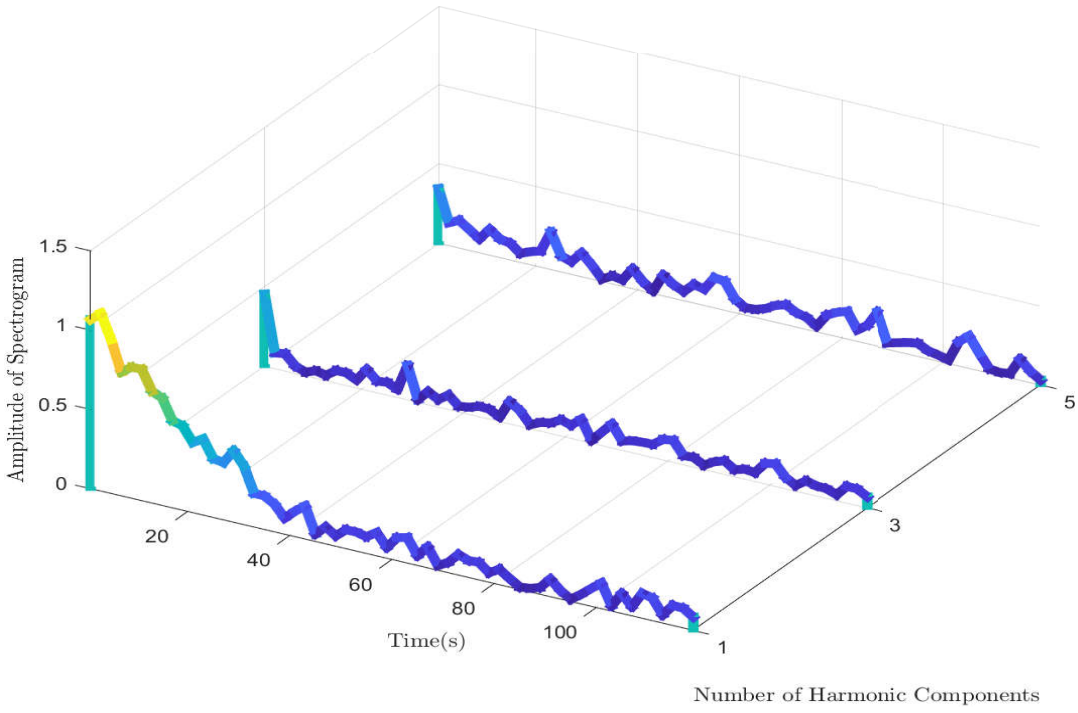

Figure D.14: Discrete harmonic spectrogram from Test 3 of Case 8

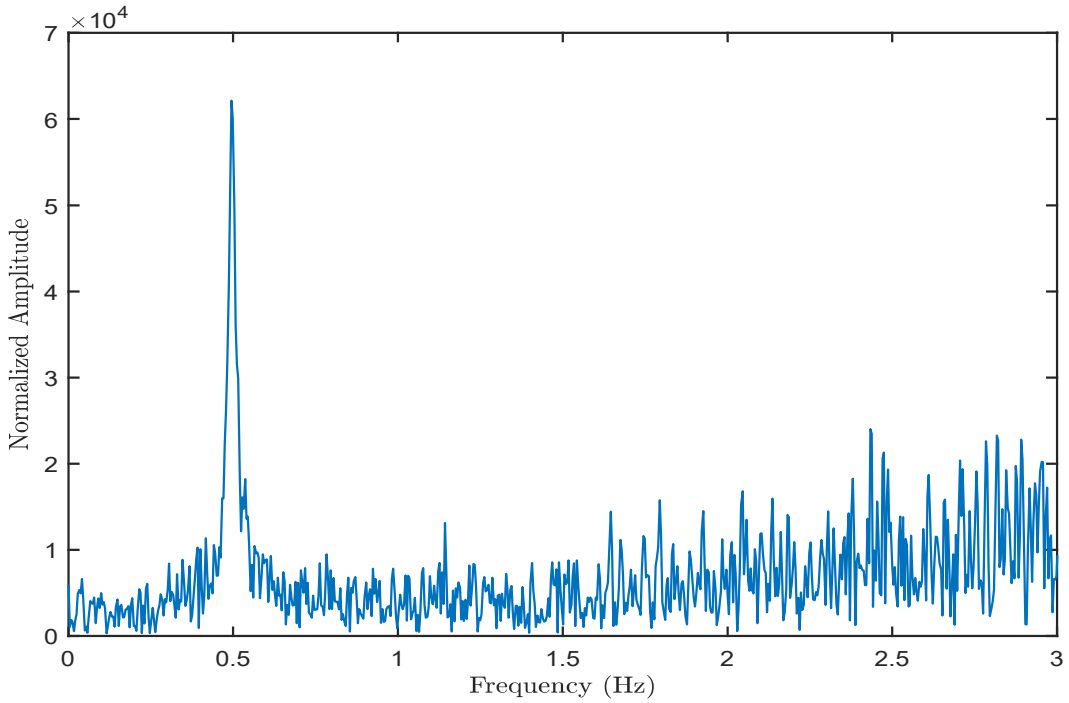

Figure D.15: FRD result from Test 3 of Case 8

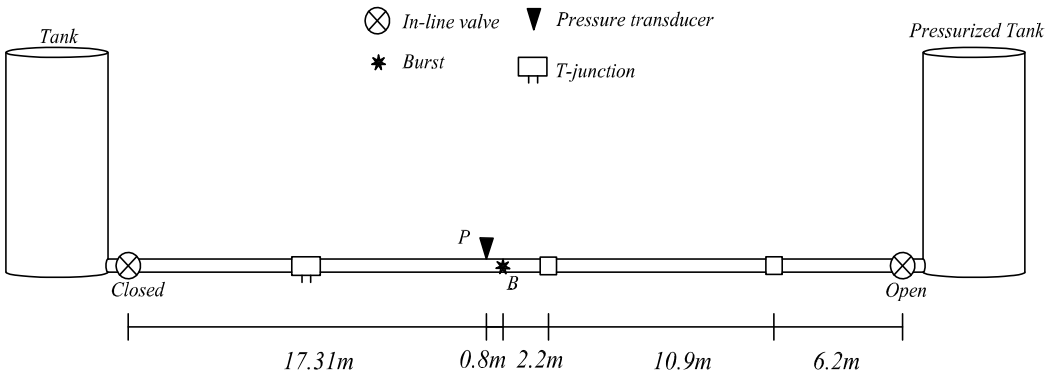

Figure D.16: Pipeline configuration from Experimental Case 2

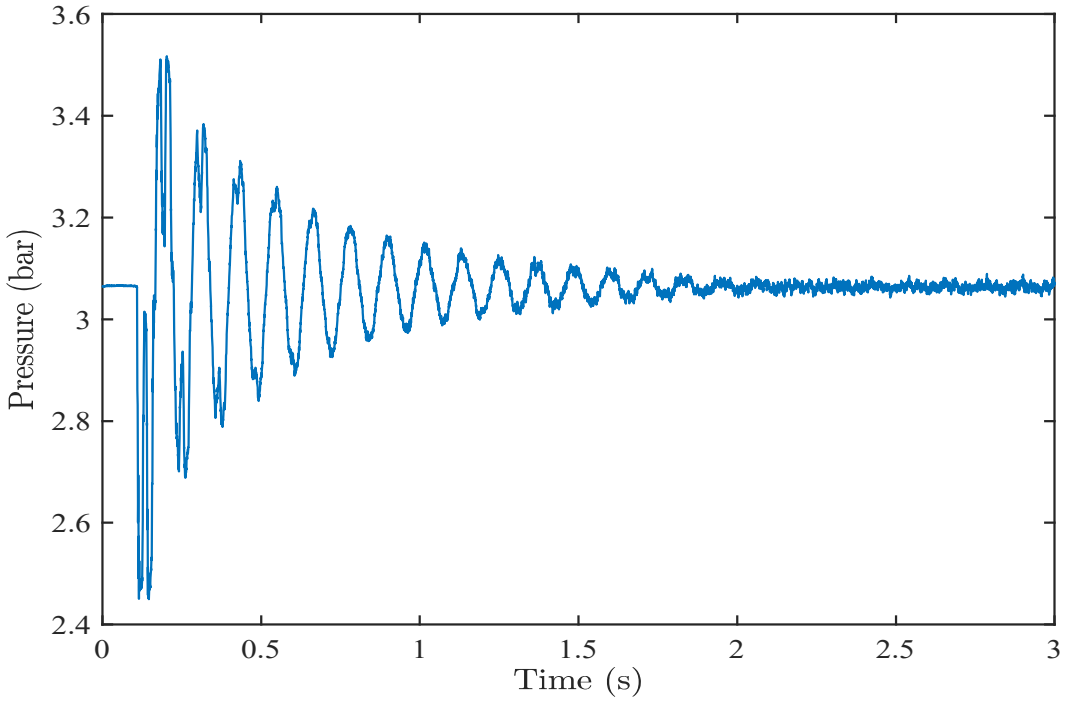

Figure D.17: Measured time trace from Experimental Case 2

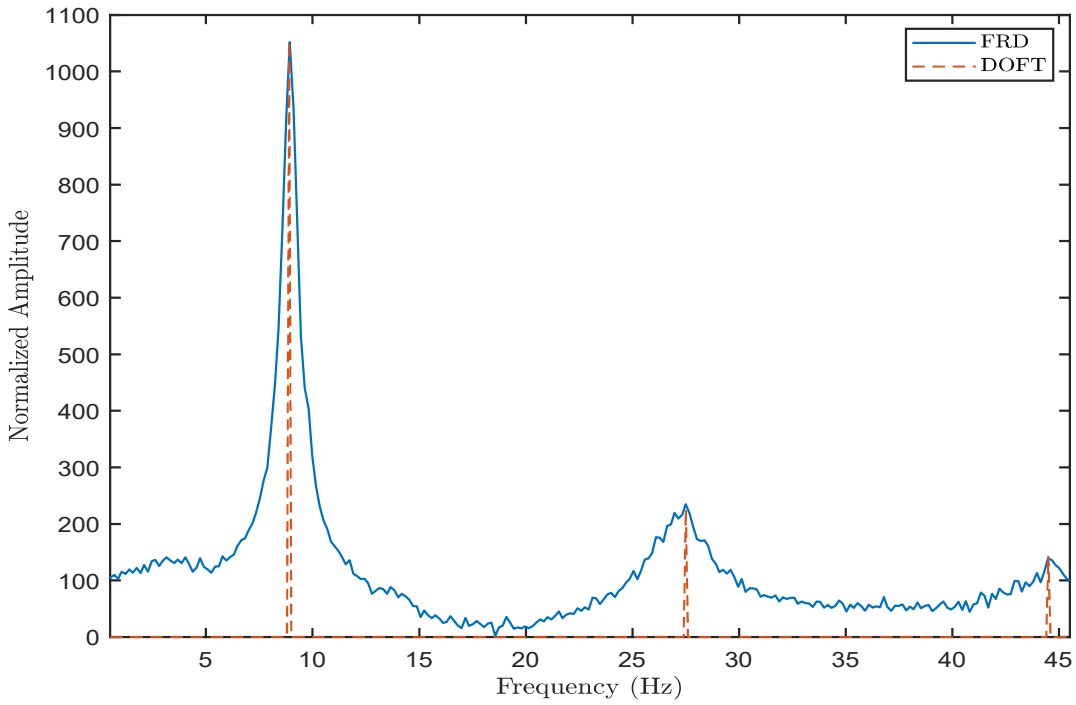

Figure D.18: DOFT and FRD results from Experimental Case 2

Appendix E

Linking and Comparison of the Damping of Fluid Transients and Frequency Response Diagram Methods for Pipe Leak and Burst Detection and Localization

(Revised Journal Paper 4)

Xiao-xuan Du, Martin F. Lambert, Lei Chen, and Eric Hu

Submitted to *Journal of Hydraulic Engineering*

Abstract

The purpose of the paper is to illustrate the relationship between methods that utilize the damping of fluid transients and the approaches based on the frequency response diagram, and to discuss the two methods for both leak and burst detection. Although both the methods are based on the Fourier transform of the signal, they have different signal processing approaches. This paper reveals the mathematical relationship between the two methods for both the leak and the burst problems. The mathematical relationship between the two methods has been verified both numerically and experimentally. Additionally, the two methods have been compared from the perspectives of input signal bandwidth, problem type, low sampling rate capability, robustness, and real-time data monitoring capability. The applicability of the two methods in these aspects has been discussed.

E.1 Introduction

Transient pressure-based pipeline leak detection methods have been explored by diverse researchers, based on meeting the inspection process requirement during the working cycle of the system (29; 63; 84; 89; 102; 113; 152; 169). Frequency domain-based methods can be applied successfully in practice with high accuracy (42; 52; 66; 72; 85; 87; 111; 148; 152).

Leak detection methods based on the damping of fluid transients (DOFT) have been researched by Wang et al. (2005; 2002) and Nixon et al. (2006). These methods utilize the damping in the transient signal caused by the leak in the pipeline. By computing the damped harmonic components in the results of Fourier transform, fast Fourier transform (FFT) or discrete Fourier transform (DFT), and utilizing the different damping of various harmonic components, the leak can be confirmed and located (151; 152). Furthermore, the validity range

of the DOFT method has been explored in terms of different materials (109). Du et al. (2020) improved the technique and applied it to the burst problem. Additionally, Du et al. (2021) further improved the technique from the perspective of real-time burst detection, localization, and cross-sectional area quantification with low data sampling and transmission rates.

The application of frequency-based methods to the area of pipeline leak detection has been explored (52; 53; 54; 55; 56; 84; 85; 86; 87). The frequency response diagram (FRD) methods in Gong et al. (2013a; 2016a; 2018a; 2018b; 2016b) and Lee et al. (2006; 2005a; 2005b) apply the theory of frequency response function (FRF) on the basis of the energy cross-spectral density of the measured (i.e., output) and input signals, which is the FFT of the cross-correlation function. The leak can be detected by computing the damped FRD, and can then be located, for example, by substituting the peak values of the first three resonance responses from the resultant FRD to the solution of the leak location (52).

The signal processing approaches of the DOFT and FRD methods are based on the theory of the Fourier transform, and have been verified both numerically and experimentally. However, the specific steps of the signal processing approaches in these methods are different. In the DOFT methods, the FFT/DFT of the output signal is utilized. The resultant amplitudes of the FFT/DFT of each harmonic component were compared window by window to determine the damping by fitting the exponential equation form (152). In the DOFT method, only the measured signal was utilized, while in the FRD method, both the input and measured signals were applied, and the resultant FRD was computed from the output signal, which is completely damped after the input signal is applied.

In the FRD methods, the FRD was generated by using the general form of FRF, which utilizes both the input and the output signals. The output signal is the measured signal from the occurrence of the transient until the steady

state is achieved. The input signal is the source of the transient. In Lee et al. (2006; 2005a; 2005b), the input signal was modified from a step function into an impulse function by adding a reversed, shifted input signal. During the process of generating FRD, the FFT of the cross-correlation and auto-correlation functions were computed for the whole time period from the transient until the steady state (52; 53; 54; 55; 56; 84; 85; 86; 87).

The following gaps exist in the reviewed methods in the literature. Firstly, no exploration has been conducted in terms of the mathematical relationship between these two Fourier transform-based techniques. Secondly, the applicability of the FRD method has not been explored in the areas of burst detection, low sampling rate, robustness, and real-time data monitoring. Thirdly, no research or corresponding discussion have been conducted between the two methods in terms of input signal bandwidth, problem type, low sampling rate capability, robustness, and real-time data monitoring capability. This paper presents the detailed mathematical modeling that reveals the exact relationship between the DOFT and FRD methods from the perspectives of both the leak and the burst problems. This relationship has been verified both numerically and experimentally. In addition, an exploration of the two methods has been undertaken in terms of the previously mentioned aspects.

In the following section, the mathematical relationship between the DOFT and FRD methods is presented, followed by ten numerical verifications. Then, two experimental verifications are presented, followed by the conclusion and discussion.

E.2 Relationship between Transient Damping and Frequency Response Function

The general solution of the dimensionless measured head disturbance, h^*, in Wang et al. (2002) for leak problem is expressed as

$$h^*(x^*,\ t^*) = \sum_{n=1}^{\infty} \left\{ e^{-(R+R_{nL})t^*} [A_n cos(n\pi t^*) + B_n sin(n\pi t^*)] sin(n\pi x^*) \right\} \quad (n = 1,\ 2,\ 3, \ldots) \tag{E.1}$$

where x^* and t^* in Eq. (E.1) are the non-dimensionalized distance along the pipe and the time respectively, using the following definitions

$$h^* = \frac{h}{H_1},\ t^* = \frac{t}{L/a},\ x^* = \frac{x}{L} \tag{E.2}$$

where h is the head disturbance caused by the leak, H_1 is the reference head, which is the head measured at the tank, t is the time, L is the length of the pipe, a is the wave speed, and x is the distance along the pipe. R is the friction damping, R_{nL} is the leak damping, and A_n and B_n are the Fourier coefficients expressed in Wang et al. (2002). By fitting the typical Fourier series form to Eq. (E.1), the amplitudes of the first and the nth harmonic component in each period are

$$E_n^{(1)} = -\frac{e^{-(R+R_{nL})(t_0^*+T^*)} - e^{-(R+R_{nL})t_0^*}}{(R+R_{nL})T^*} sin(n\pi x^*) \sqrt{A_n^2 + B_n^2} \tag{E.3}$$

$$E_n^{(m)} = E_n^{(1)} e^{-(R+R_{nL})(m-1)T^*} \quad (m = 1,\ 2,\ 3, \ldots) \tag{E.4}$$

respectively, where t_0^* is the dimensionless starting time of the analysis, T^* is the dimensionless fundamental period of the pipeline system, and m and n represent the number of the period and the harmonic component respectively.

The utilized FRF in Gong et al. (2013a; 2016a; 2018a; 2018b; 2016b) and Lee et al. (2006; 2005a; 2005b) is expressed as

$$H(\omega) = \frac{R_{in\&out}}{R_{in\&in}} \tag{E.5}$$

where $H(\omega)$ is the FRF, $R_{in\&out}$ is the Fourier transform of the cross-correlation function between input and output signals, and $R_{in\&in}$ is the auto-correlation function of the input signal. In fact, $R_{in\&out}$ is the cross spectral density of the input and output signals, and $R_{in\&in}$ is the auto spectral density of the input signal. However, Lee et al. (2006; 2005a; 2005b) modified the input signal into a finite energy form, and established the output signal as the finite energy signal, thus $R_{in\&out}$ and $R_{in\&in}$ are the cross and auto spectral densities in energy instead of power. According to the relationship between the correlation functions and convolution, and applying the general Fourier transform procedure, Eq. (E.5) becomes (15; 110; 156)

$$H(\omega) = \frac{X(\omega)Y^*(\omega)}{X(\omega)X^*(\omega)} \tag{E.6}$$

where X and Y are the Fourier transform results of the input and output signals respectively, and Y^* is the conjugate of Y.

According to the derivation procedure of the Fourier transform, when $\omega = n\omega_0$, where ω_0 is the fundamental angular frequency of the system, the resonance responses, $X^*(\omega)$ and $Y^*(\omega)$ become

$$\begin{aligned} X^*(n\omega_0) &= X(n\omega_0) \\ Y^*(n\omega_0) &= Y(n\omega_0) \end{aligned} \tag{E.7}$$

since the imaginary number is canceled (7). It can be seen that when considering the resonance responses, Y^* in Eq. (E.6) is actually dimensional Eq. (E.4) when there is only one window of the whole signal, and the length of the window is equal to the time period from the application of input signal to the complete decay of output signal. The details of the derivation of the Fourier transform of Eq (E.4) in each period are presented in the Appendix. Therefore, the FRF in the FRD method is actually the Fourier series solution in the DOFT method scaled by the Fourier transform result of the input signal, with the window length of the time period from the application of input signal to the complete decay of output signal.

According to the time shift and linearity theorems of Fourier transform, adding the time shift formulation to the Fourier transform of the signal period by period is equivalent to the Fourier transform of the whole signal in the time period from the application of input signal to the complete decay of output signal. Therefore, the resonance responses in the Fourier transform of the signal in the dimensionless frequency domain in the time period from the application of input signal to the complete decay of output signal, $Y(n\omega_0^*)$, where ω_0^* is the dimensionless fundamental angular frequency of the system, can be expressed by Eq. (E.4), and shown as

$$Y(n\omega_0^*) = \sum_{m=1}^{N} E_n^{(1)} e^{-(R+R_{nL})(m-1)T^*} e^{-in\omega_0^*(m-1)T^*} \tag{E.8}$$

or

$$Y(nf_0^*) = \sum_{m=1}^{N} E_n^{(1)} e^{-(R+R_{nL})(m-1)T^*} e^{-i2\pi n f_0^*(m-1)T^*} \tag{E.9}$$

where N is the total number of periods contained in the time period from the application of input signal to the complete decay of output signal, and f_0^* is the dimensionless fundamental frequency of the system.

Based on the previous analysis and when considering the resonance responses in the dimensionless frequency domain, the mathematical relationship between the Fourier series solution in the DOFT method and the FRF in the FRD method is shown as

$$\begin{aligned} H(n\omega_0^*) &= \frac{X(n\omega_0^*)\sum_{m=1}^{N} E_n^{(1)} e^{-(R+R_{nL})(m-1)T^*} e^{-in\omega_0^*(m-1)T^*}}{\left[X(n\omega_0^*)\right]^2} \\ &= \frac{X(n\omega_0^*)\sum_{m=1}^{N} E_n^{(1)} e^{-(R+R_{nL}+in\omega_0^*)(m-1)T^*}}{\left[X(n\omega_0^*)\right]^2} \\ &= \frac{\sum_{m=1}^{N} E_n^{(1)} e^{-(R+R_{nL}+in\omega_0^*)(m-1)T^*}}{X(n\omega_0^*)} \end{aligned} \tag{E.10}$$

or

$$H(nf_0^*) = \frac{\sum_{m=1}^{N} E_n^{(1)} e^{-(R+R_{nL}+i2\pi n f_0^*)(m-1)T^*}}{X(nf_0^*)} \tag{E.11}$$

The dimensionless fundamental frequency and the dimensionless fundamental period in the terms $e^{-in\omega_0^*(m-1)T^*}$ and $e^{-i2\pi n f_0^*(m-1)T^*}$ in Eqs. (E.9) and (E.8), respectively, can be canceled, since the signal was analyzed for every fundamental period in Wang et al. (2002), and m and n in Eqs. (E.9) and (E.8) are

integers, thus the terms $e^{-in\omega_0^*(m-1)T^*}$ and $e^{-i2\pi nf_0^*(m-1)T^*}$ are equal to unity in Eqs. (E.9) and (E.8). Therefore, Eqs. (E.10) and (E.11) are simplified as

$$H(n\omega_0^*) = \frac{\sum_{m=1}^{N} E_n^{(1)} e^{-(R+R_{nL})(m-1)T^*}}{X(n\omega_0^*)} \tag{E.12}$$

or

$$H(nf_0^*) = \frac{\sum_{m=1}^{N} E_n^{(1)} e^{-(R+R_{nL})(m-1)T^*}}{X(nf_0^*)} \tag{E.13}$$

Therefore, the mathematical relationship between the DOFT and FRD methods for the leak problem is revealed by Eqs. (E.12) and (E.13). According to the research into burst detection using the DOFT theory presented in Du et al. (2020), Eqs. (E.12) and (E.13) can be simplified into the following forms for the burst conditions

$$H(n\omega_0^*) = \frac{\sum_{m=1}^{N} E_n^{(1)} e^{-(R+R_{nB})(m-1)T^*}}{X(n\omega_0^*)} \tag{E.14}$$

or

$$H(nf_0^*) = \frac{\sum_{m=1}^{N} E_n^{(1)} e^{-(R+R_{nB})(m-1)T^*}}{X(nf_0^*)} \tag{E.15}$$

where $E_n^{(1)}$ has the same form as Eq. (E.3) but with R_{nB} instead of R_{nL}, and

R_{nB} is the burst damping which is defined in Du et al. (2020), and shown as

$$R_{nB} = K_B sin^2(n\pi x_B^*) \tag{E.16}$$

in which K_B is a self-defined burst parameter that contains the cross-sectional area of the burst, which is presented in Du et al. (2020), and x_B^* is the dimensionless burst location along the pipeline. According to the summation of the geometric sequence, Eqs. (E.14) and (E.15) can be simplified as

$$H(n\omega_0^*) = \frac{E_n^{(1)}(1 - e^{-(R+R_{nB})mT^*})}{X(n\omega_0^*)(1 - e^{-(R+R_{nB})T^*})} \tag{E.17}$$

or

$$H(nf_0^*) = \frac{E_n^{(1)}(1 - e^{-(R+R_{nB})mT^*})}{X(nf_0^*)(1 - e^{-(R+R_{nB})T^*})} \tag{E.18}$$

According to the leak localization solution for a reservoir-pipe-valve (RPV) system in Gong et al. (2013a), and substituting Eqs. (E.14) and (E.15), the burst localization solution can be expressed as

$$x_B^* = \frac{1}{\pi} arccos(\frac{\pm\sqrt{1+P_B}}{2}) \tag{E.19}$$

where P_B is a self-defined parameter, and shown as

$$P_B = \left\{ \left[\frac{E_5^{(1)}(1-e^{-(R+R_{5B})mT^*})}{X(5f_0^*)(1-e^{-(R+R_{5B})T^*})} - \frac{E_1^{(1)}(1-e^{-(R+R_{1B})mT^*})}{X(f_0^*)(1-e^{-(R+R_{1B})T^*})} \right] \frac{E_3^{(1)}(1-e^{-(R+R_{3B})mT^*})}{X(3f_0^*)(1-e^{-(R+R_{3B})T^*})} \right\} \Bigg/ \left\{ \left[\frac{E_3^{(1)}(1-e^{-(R+R_{3B})mT^*})}{X(3f_0^*)(1-e^{-(R+R_{3B})T^*})} - \frac{E_1^{(1)}(1-e^{-(R+R_{1B})mT^*})}{X(f_0^*)(1-e^{-(R+R_{1B})T^*})} \right] \frac{E_5^{(1)}(1-e^{-(R+R_{5B})mT^*})}{X(5f_0^*)(1-e^{-(R+R_{5B})T^*})} \right\} \tag{E.20}$$

Thus, the mathematical relationship between the DOFT and FRD methods for the burst problem is revealed by Eqs. (E.14) to (E.20). Ten numerical verifications have been conducted and presented in the next section. They are designed to verify the mathematical relationship, and compare and discuss the methods of the DOFT and FRD from the perspectives of input signal bandwidth, problem type, low sampling rate capability, robustness, and real-time analysis capability.

E.3 Numerical Verification

Ten numerical scenarios have been conducted, which are referred to as Cases 1 to 10, respectively. Case 1 is to verify the mathematical relationship between the DOFT and FRD methods. Cases 2 and 3 are designed to verify the relationship between two methods with different input signal bandwidths. Cases 4 and 5 are implemented to verify the relationship for both leak and burst problem. Cases 6 and 7 are conducted to compare and discuss the two methods in terms of the low sampling rate capability. Case 8, which contains three tests, is designed for robustness comparison between the two methods. Cases 9 and 10 are conducted to compare the two methods regarding the real-time data monitoring capability. Since only the first three resonance responses (i.e., the 1st, 3rd, 5th harmonics for the RPV system) of the measured signal were explored and

discussed in the previous research, only the results of the first three resonance response responses are included in this section (35; 52; 152).

E.3.1 Verification for the Mathematical Relationship

In order to verify the mathematical relationship between the FRD and DOFT of the signal shown in Eq. (E.13), Cases 1 to 3 have been conducted, of which Case 1 is for numerical verification of the mathematical relationship, and Cases 2 and 3 are for mathematical relationship verification with different input bandwidths. In Case 1, the applied data is from Lee (2005), in which the transient is generated by a manually-controlled valve. The pipeline system for Case 1 is shown in Figure E.1 along with all the necessary parameters, where C_v is the maximum cross-sectional area of the inline valve, which is located at the downstream boundary of the system. The parameter orifice opening coefficient, τ, is applied to describe the actual cross-sectional area, as defined in Lee (2005). This is expressed as $C_d A_V/(C_d A_p)_{REF}$ for the inline and side discharge valves, where C_v is the orifice coefficient of the valves, A_V and A_p are the cross-sectional areas of the valves and the pipe respectively, and REF indicates the reference quantity.

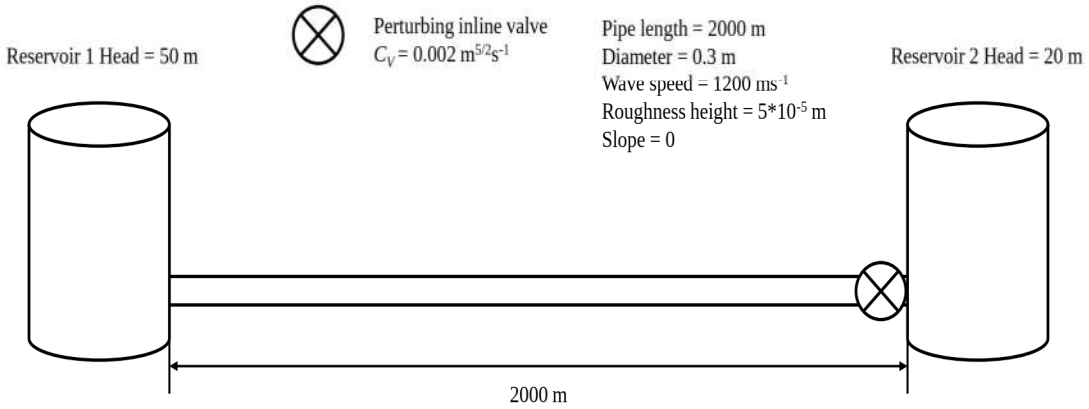

Figure E.1: Pipeline configuration from Cases 1-3

In Case 1, $\Delta\tau$, the change of the cross-sectional area of the applied inline

valve between the status of fully closed and aimed opening, is set to be 0.012. The system is under the condition of no-leak, and the transient is generated by the downstream inline valve. During the process of Case 1, the inline valve was initially fully closed. Then it was opened for a very short time, and fully closed again. In Case 1, the input is the valve perturbation τ, and the output is the head time trace measured at the downstream boundary. The input and the output signals are shown in Figures E.2 and E.3.

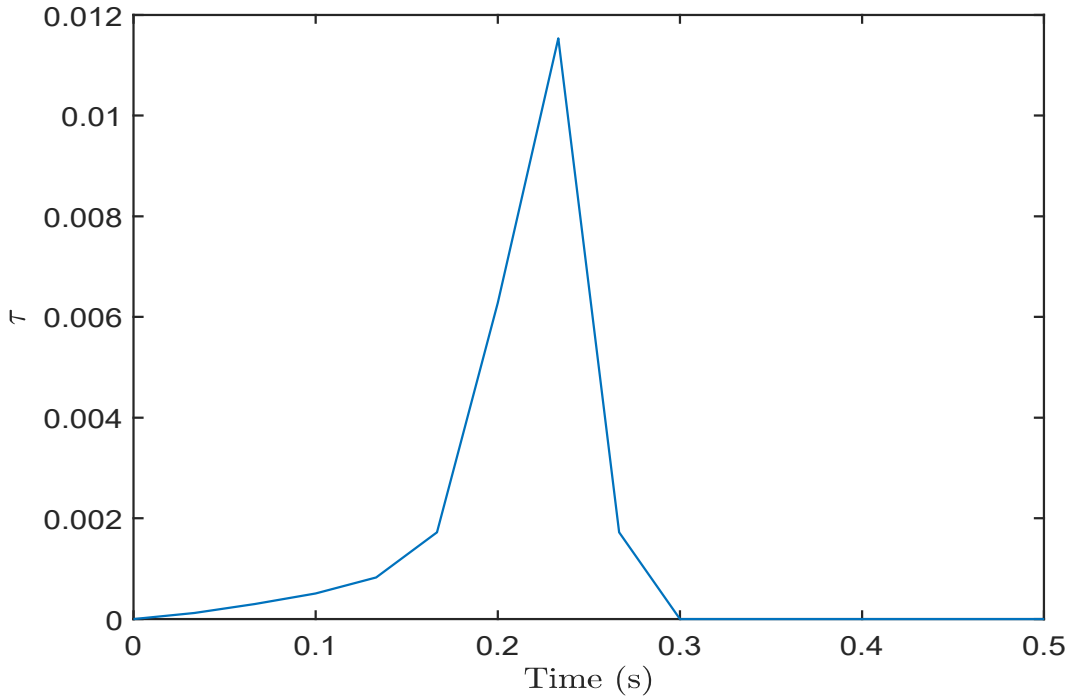

Figure E.2: Input signal from Case 1

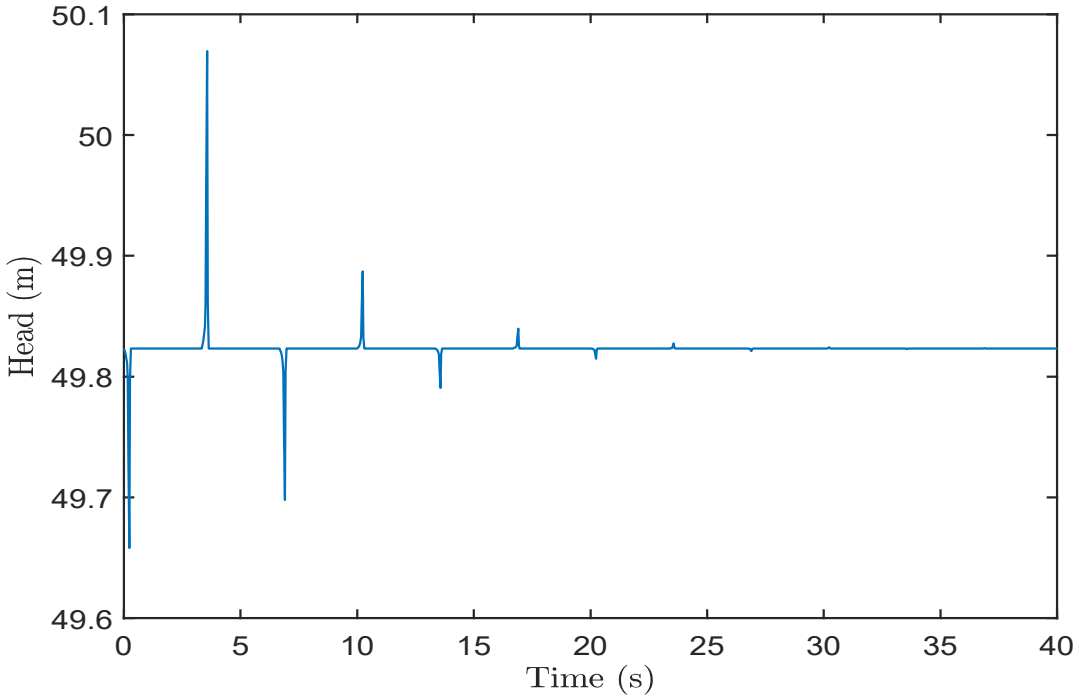

Figure E.3: Output signal from Case 1

Applying the signal processing algorithm in Wang et al. (2002), Lee et al. (2006), and Du et al. (2020) provides the results shown in Figure E.4, in which *FRD* is the result of FRF presented as Eq. (E.5), and *DOFT* represents the right side in Eq. (E.13), which is generated by letting the solution in Wang et al. (2002) divided by the frequency responses of the input signal. It is worth noting that the frequency responses of the output signal have been normalized by the frequency responses of the input signal, based on Eqs. (E.5) and (E.13). Based on the results shown in Figure E.4, it can be shown that the amplitude of the presented quantities is closely matched for the first three resonance response peaks.

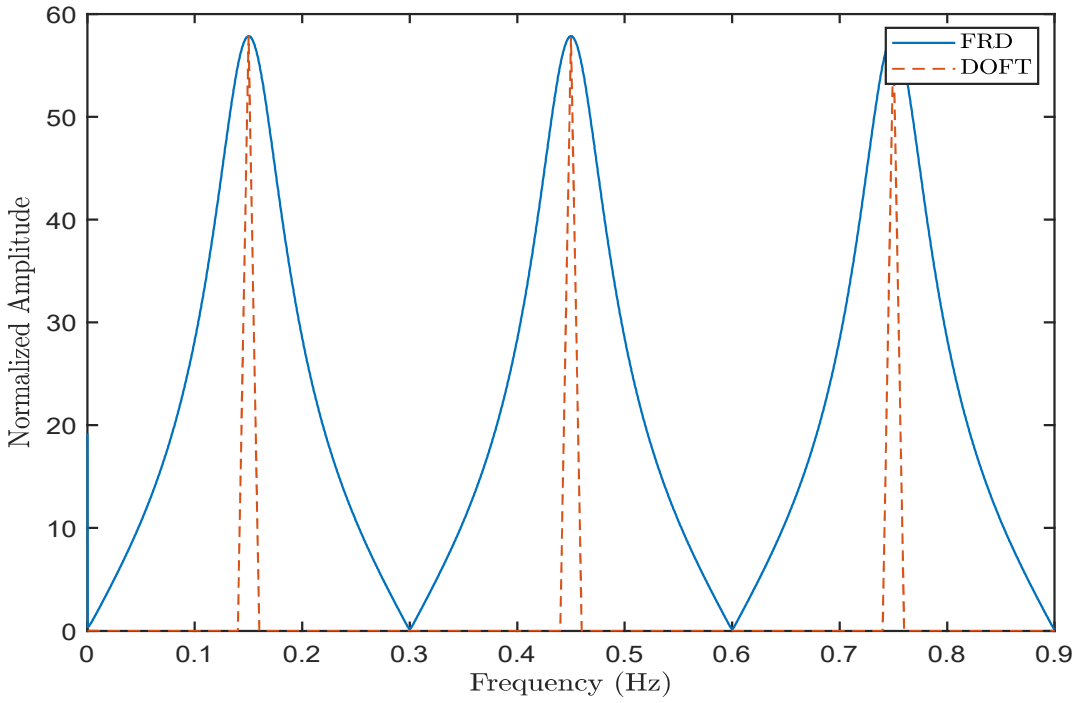

Figure E.4: DOFT and FRD results from Case 1

E.3.2 Verification for Different Input Signal Bandwidths

Cases 2 and 3 have been implemented to verify the mathematical correlation under the conditions of different input signal bandwidths. The pipeline system for Cases 2 and 3 is the same as the configuration in Cases 1, except that the downstream inline valve is replaced by a side discharge valve. During Cases 2 and 3, the same operation of the inline valve as in Cases 1 was applied to the side discharge valve to generate the transient. The side discharge valve was operated with different opening and closing speeds to generate different input signal bandwidths, and the input signals of these two cases are shown in Figure D.1, in which $InputSignal1$ and $InputSignal2$ represent the input signal of Cases 2 and 3 respectively. The corresponding output signals of these two cases are shown in Figure D.2, in which $OutputSignal1$ and $OutputSignal2$ represent the output signals of Cases 2 and 3 respectively. In the two cases, the applied data are from Lee (2005). The corresponding results are shown in Figures E.5 and D.3. It is worth noting that the magnitude of the input signal is $C_d A_V$

instead of τ.

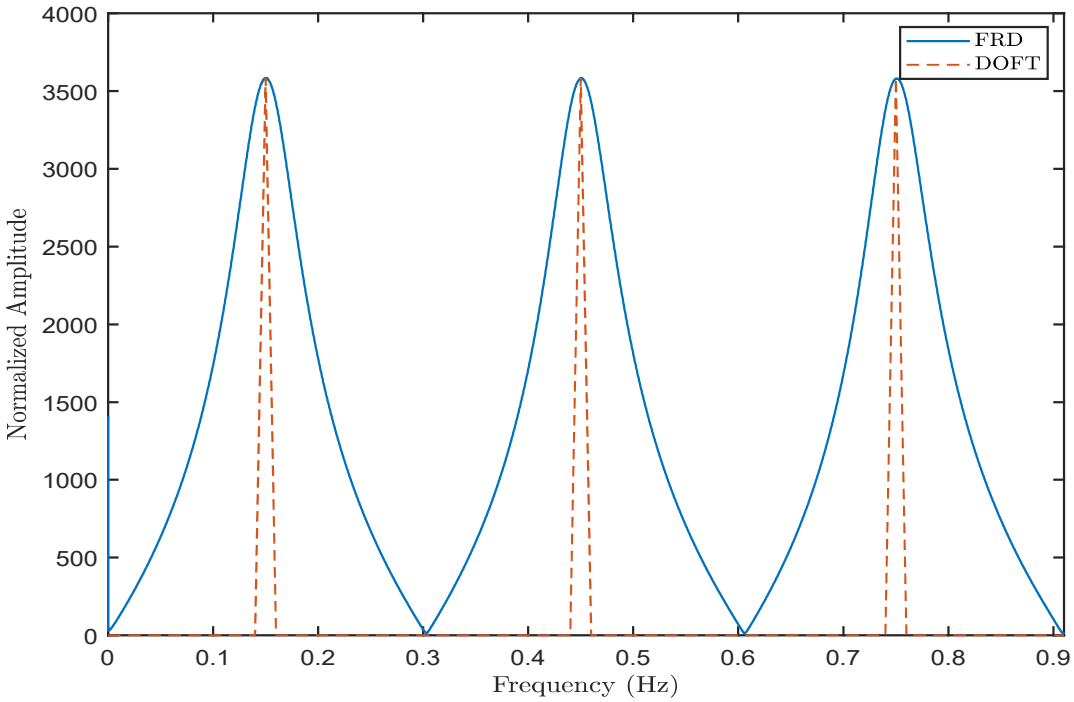

Figure E.5: DOFT and FRD results from Case 2

Based on the results shown in Figures E.5 and D.3, the mathematical correlation between the DOFT and FRD techniques is verified through different input signal bandwidths.

E.3.3 Verification and Comparison for Leak and Burst Problems

To verify the explored mathematical relationship in the paper, and to compare the DOFT and FRD methods in terms of the problem type, Cases 4 and 5 have been conducted. Case 4 is the leak case and Case 5 is the burst case.

The pipeline system for Case 4 is the RPV system, and is shown in Figure E.6, along with all the necessary parameters. The leak is simulated by a side discharge valve, which is located at 100 m from the upstream boundary, which has the relative cross-sectional area as $C_d A_L/A_p = 0.02$, where A_L is the cross-

sectional area of the leak. During the process of Case 4, the transient is introduced by opening and then closing the downstream valve rapidly, with relative cross sectional area of $C_d A_V / A_p = 0.001$. In addition, parameter τ is re-defined as the relative cross-sectional area of the downstream valve in Case 4. The operation process of the downstream valve is linear, and the corresponding input signal is shown in Figure E.7. The measured time trace is shown in Figure E.8, with the sampling rate of 100 Hz. The corresponding fundamental period is 2 s, which is determined using the ringdown code (5; 51). Replicating the same analysis process as in previous cases, the resultant frequency responses of the first three resonance frequencies using the DOFT and FRD techniques are shown in Figure E.9. The adequate match verifies the correlation between the two methods. It should be noticed that the resonance responses are significantly damped due to the damping caused by the leak, when compared with the previous cases. By observing the damped amplitude of different harmonics in the frequency domain, the leak can be detected. The estimated leak location is at 99.45 m and 119.8 m utilizing the DOFT and FRD techniques respectively (35; 52; 152). The corresponding localization errors are 0.11% and 3.96% respectively (152).

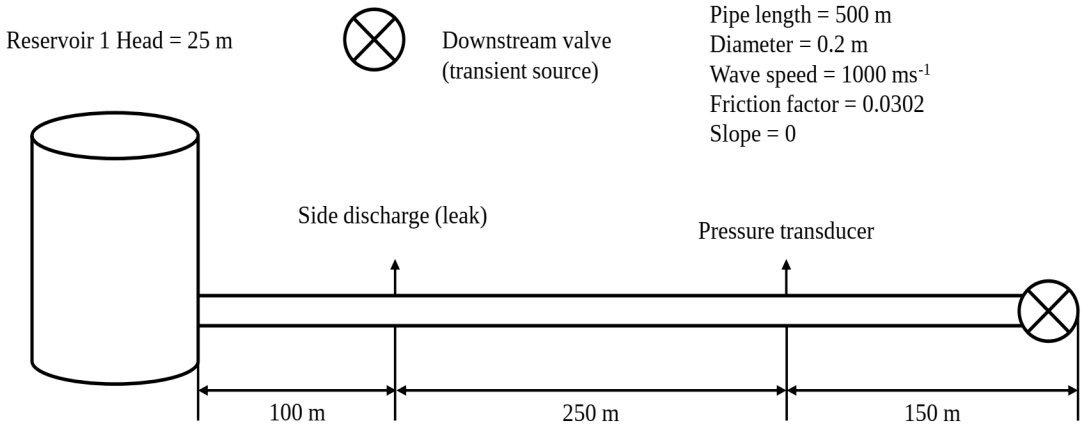

Figure E.6: Pipeline configuration from Case 4

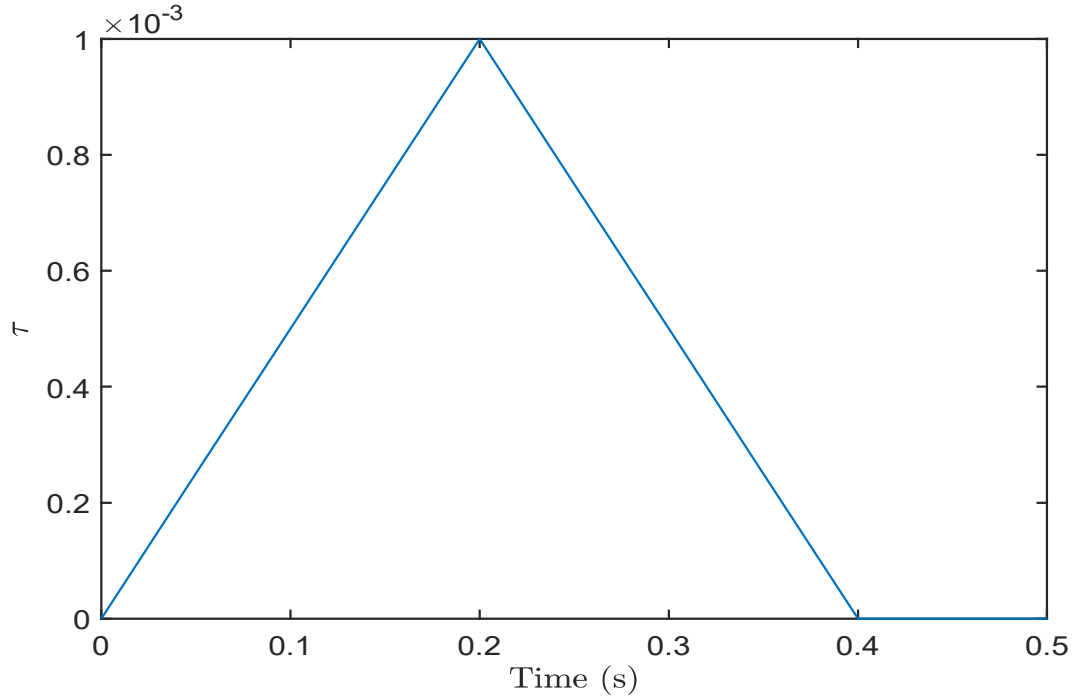

Figure E.7: Input signal from Case 4

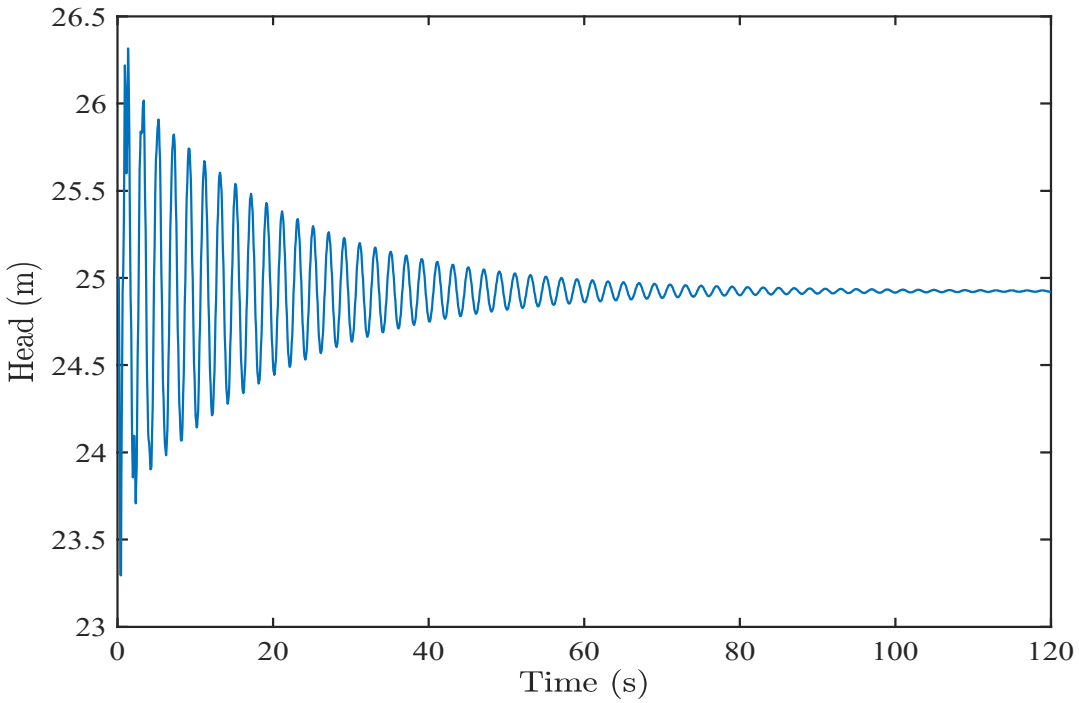

Figure E.8: Output signal from Case 4

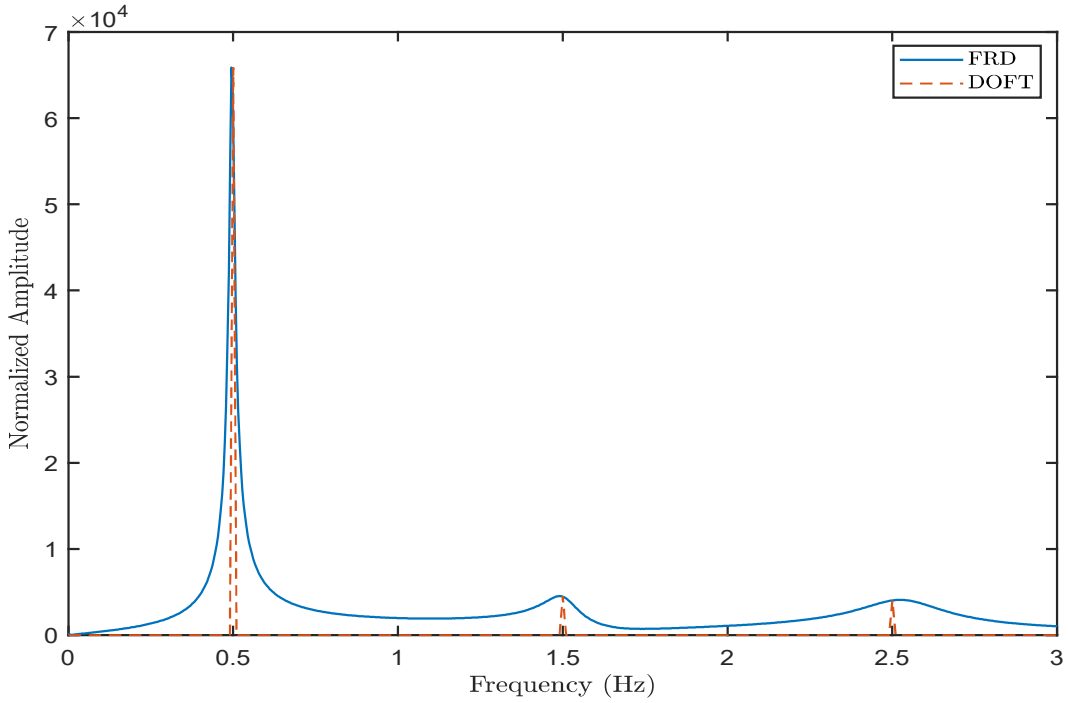

Figure E.9: DOFT and FRD results from Case 4

The applied pipeline system in Case 5 is an RPV system, which is shown in Figure D.4, in which the burst is simulated by a side discharge at 100 m from the upstream boundary, with the relative cross-sectional area of $C_d A_B/A_p = 0.5$, where A_B is the cross-sectional area of the burst, while all other parameters remain the same as in Case 4. During the process of Case 5, the initial flow rate is set to be $Q_0 = 0.001$ m^3/s by letting the downstream valve be partially opened, and the burst is set to be generated rapidly at around 0.4 s, which is the transient source. Additionally, parameter τ is re-defined as the relative cross-sectional area of the burst in Case 5. The corresponding input and output signals are shown in Figures D.5 and D.6. Since the input signal for a burst case is actually an infinite step function, the signal correction algorithm in Lee (2005) has been utilized to convert the input signal from an infinite step function to a finite impulse function, and the output signal from the infinite step function-based signal to the finite impulse function-based signal. The modified input and output signals are presented in Figures E.10 and E.11. The corresponding resultant frequency responses of the signal are shown in Figure

E.12. The results indicate that a mathematical correlation exists in the burst cases. The damped amplitude can be applied to confirm the occurrence of the burst. Utilizing the localization technique in Du et al. (2020) and Gong et al. (2013a) provides the estimated burst location at 108.2 m and 117.4 m, respectively, where the localization error is 1.64% and 3.48%, respectively.

Although the mathematical relationship between the DOFT and FRD techniques has been verified, and the faults localization has been fulfilled by utilizing both the methods, it is impossible to utilize FRD method for burst problems in practice. This is because the application of the FRD technique requires the frequency response of the input signal, but the input signal in the burst problem is generated from the burst itself, which is the unknown element that needs to be detected and estimated.

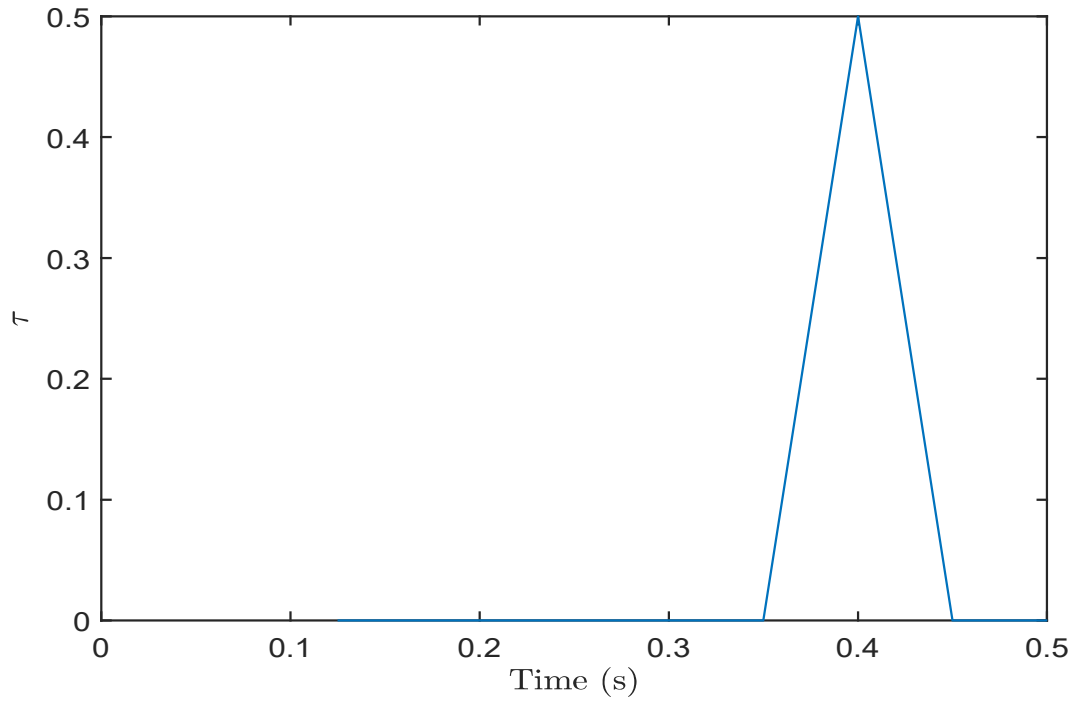

Figure E.10: Modified input signal from Case 5

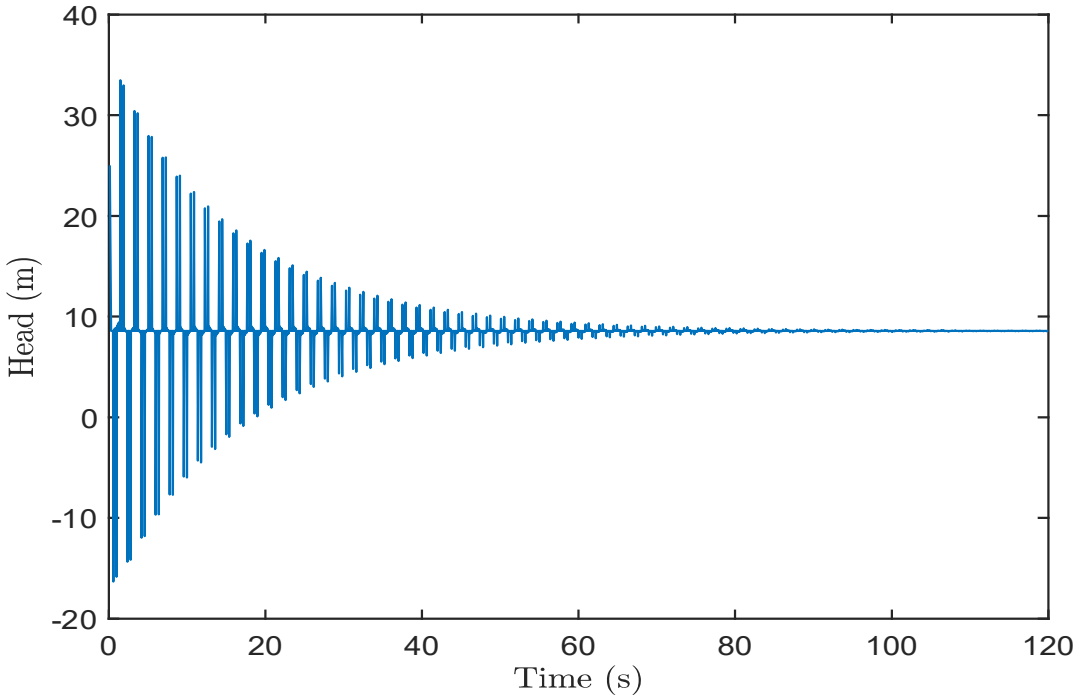

Figure E.11: Modified output signal from Case 5

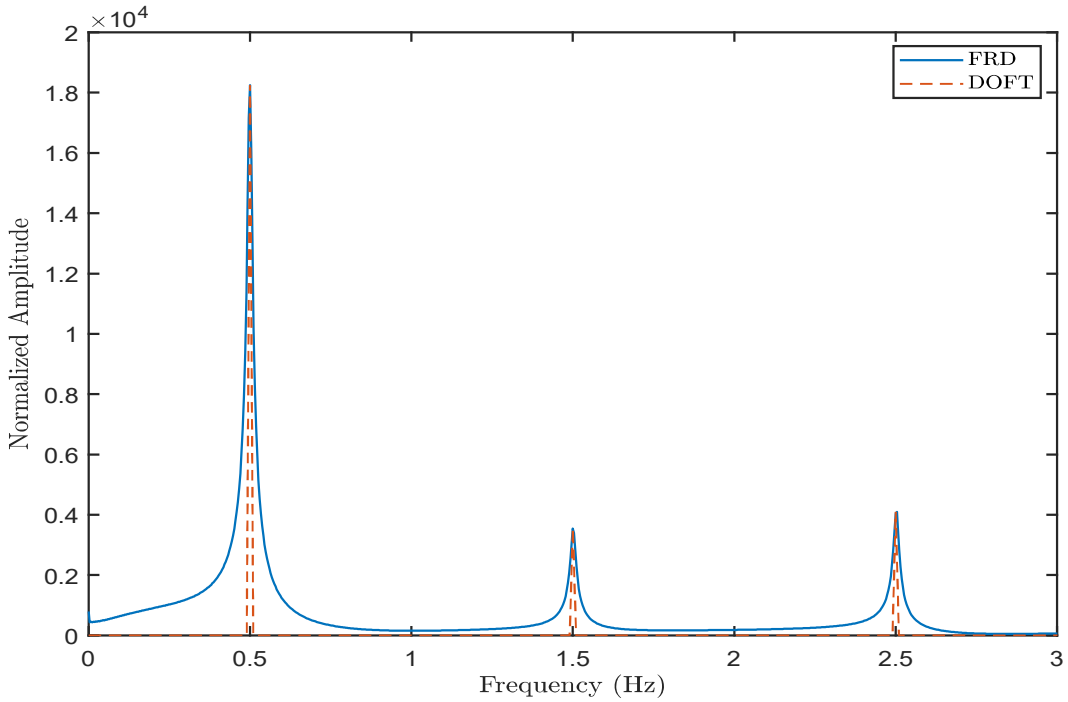

Figure E.12: DOFT and FRD results from Case 5

E.3.4 Verification and Comparison for Low Sampling Rate Capability

In order to verify and compare the DOFT and FRD techniques from the perspective of low sampling rate capability, Cases 6 and 7 have been implemented. The applied pipeline system and the relevant parameters are the same as in Cases 4 and 5, respectively, except that the sampling rate has been decreased from 100 Hz to 5 Hz, which is the Nyquist frequency of the 5th harmonic of the signal, since only the first three resonance responses are required for both the application of the DOFT and the FRD methods. The re-sampled output signals for Cases 6 and 7 are shown in Figures D.7 and D.8. Replicating the same analysis process in the previous cases provides the frequency responses of the first three resonance responses of the signals from Cases 6 and 7 using the DOFT and FRD methods, as shown in Figures E.13 and D.9. The leak and burst localization results remain the same.

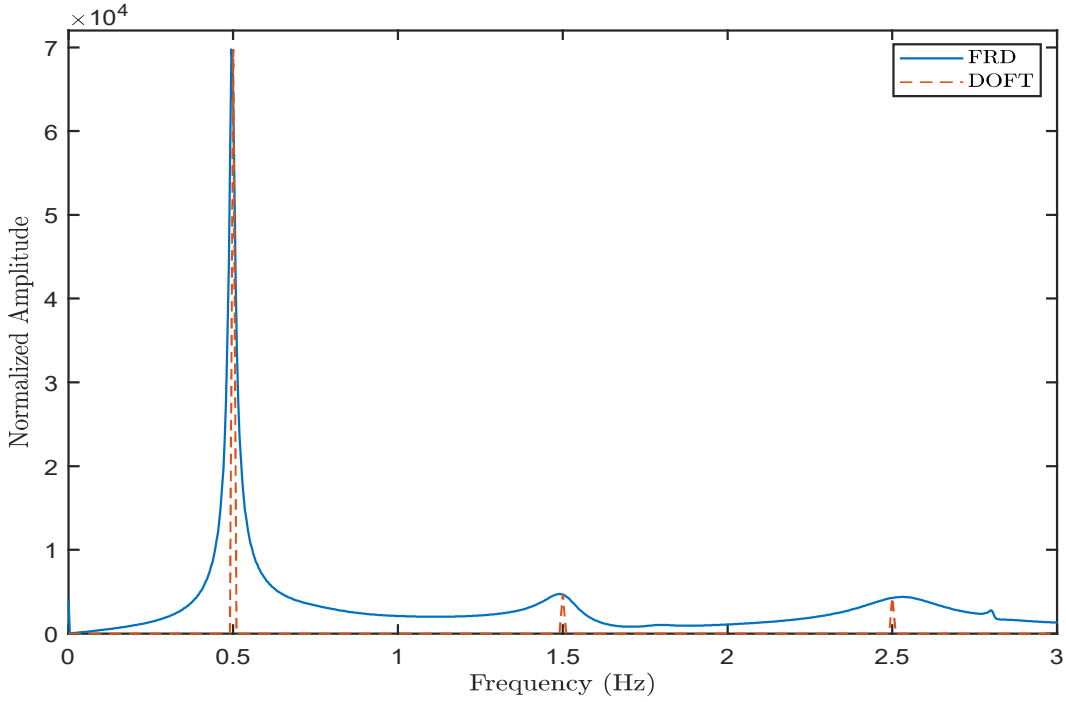

Figure E.13: DOFT and FRD results from Case 6

Based on the results shown in Figures E.13 and D.9, the mathematical rela-

tionship between the two methods has been verified. Additionally, the results illustrate that both the methods are capable of utilizing a low sampling rate (i.e., the Nyquist frequency of the 3rd resonance response).

E.3.5 Verification and Comparison for Robustness

The verification of the correlation and the comparison between the two methods in terms of the robustness has been completed by implementing Case 8. In Case 8, the applied pipeline system and the corresponding input and output signals are the same as in Case 4, which are shown in Figures E.6, E.7, and E.8, which are for the leak problem. Case 8 contains three tests, which correspond to three different signal-noise-ratios (SNR). The applied SNRs for Tests 1, 2, and 3 are 30 dB, 20 dB, and 10 dB, respectively, since the general SNR of a measured signal is around 10 dB to 30 dB (74; 167; 168). The time trace for Test 1 is shown in Figure E.14. By utilizing the technique in Du et al. (2021), which extends the work by Wang et al. (2002), the discrete harmonic spectrogram (DHS) of the signal from Test 1 is presented in Figure E.15, which contains the information of the leak damping that can be used for leak estimation. Replicating the same analysis processing the FRD method in the previous cases provides the FRD result shown in Figure E.16. Similarly, the time trace, DHS and FRD results from Test 2, with the SNR of 20 dB, are presented in Figures D.10, D.11 and D.12. Additionally, the time trace, DHS and FRD results from Test 3, with SNR of 10 dB, are shown in Figures D.13, D.14 and D.15. From the results shown in Figures D.12 and D.15, it can be noticed that the resolutions of the second and third resonance responses of the signal decrease significantly when the SNR decreases, which leads to difficulties in the leak estimation. For example, in Tests 2 and 3, the second and third resonance responses of the signal generated by utilizing the FRD method can barely be distinguished from the noise, based on Figures D.12 and D.15. The peak values of the first three resonance responses in Figures E.16, D.12, and D.15 are

summarized in Table E.1, by reading the values at particular frequencies of the first, third, and fifth harmonics. It should be noted that the peak values of the first three resonance responses from the FRD result in Case 4 have also been added to Table E.1, in order to provide the reference values under the condition of no-noise for comparison. The errors shown in Table E.1 are the relative errors that are generated by comparing the values from Case 8 with the values from Case 4. From Table E.1, it can be noticed that although the values of the first harmonic are similar in the tests, since the main energy is contained in the first resonance response, the values of the third and fifth harmonics are quite different from each other due to the negative effect from the noise.

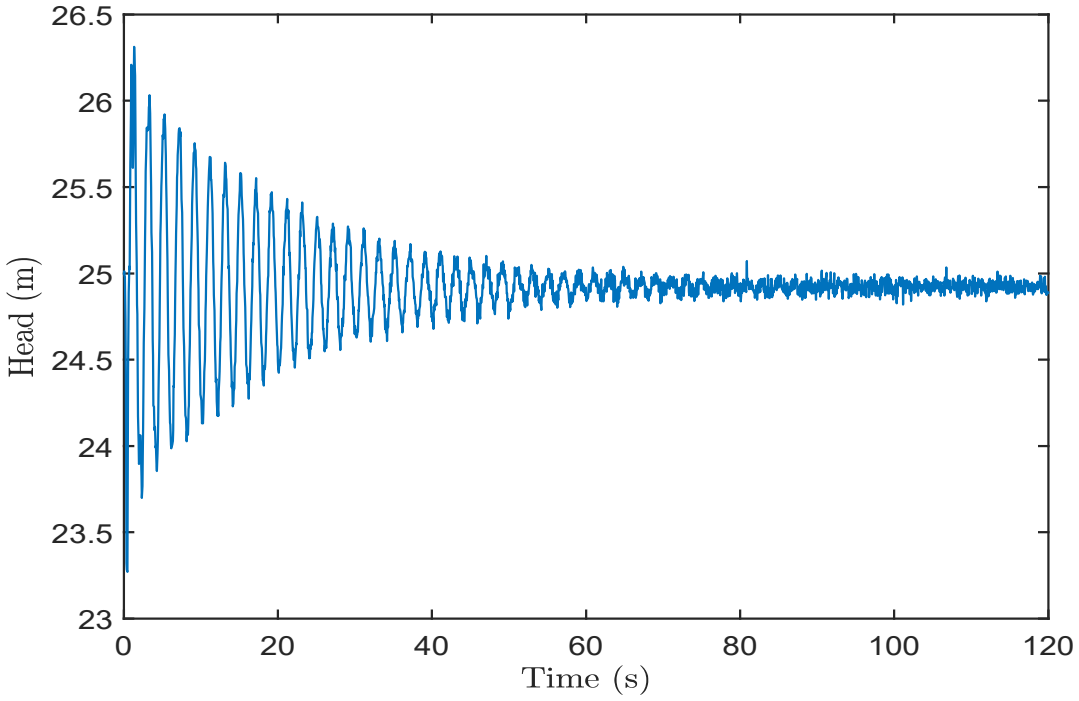

Figure E.14: Output signal from Test 1 of Case 8

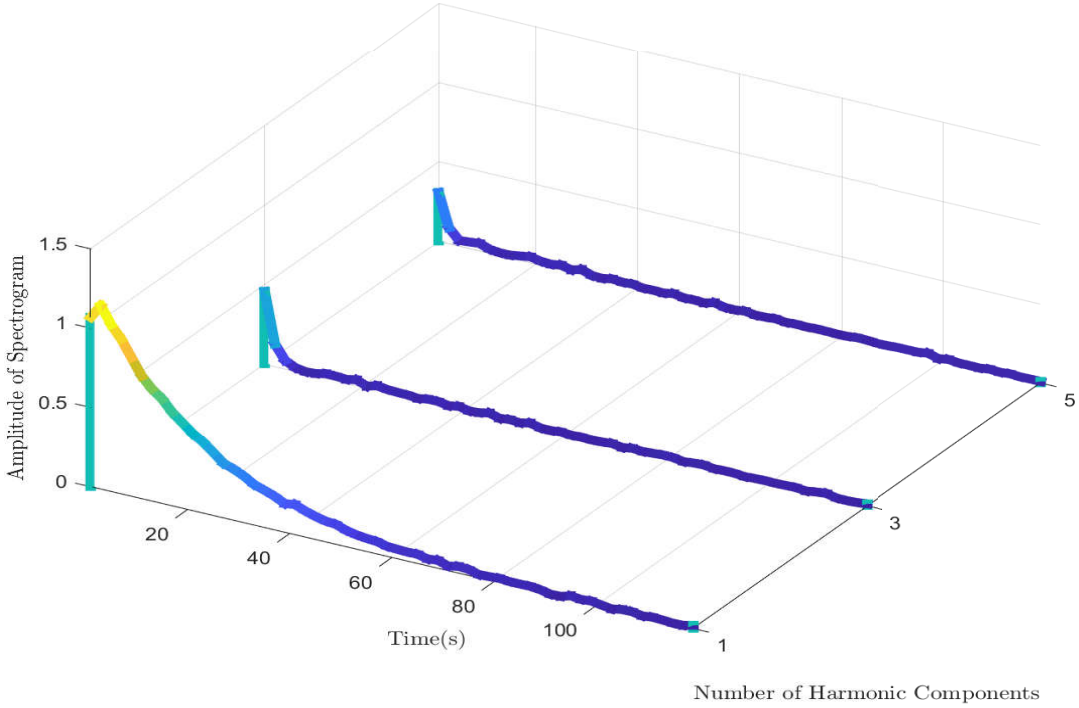

Figure E.15: Discrete harmonic spectrogram from Test 1 of Case 8

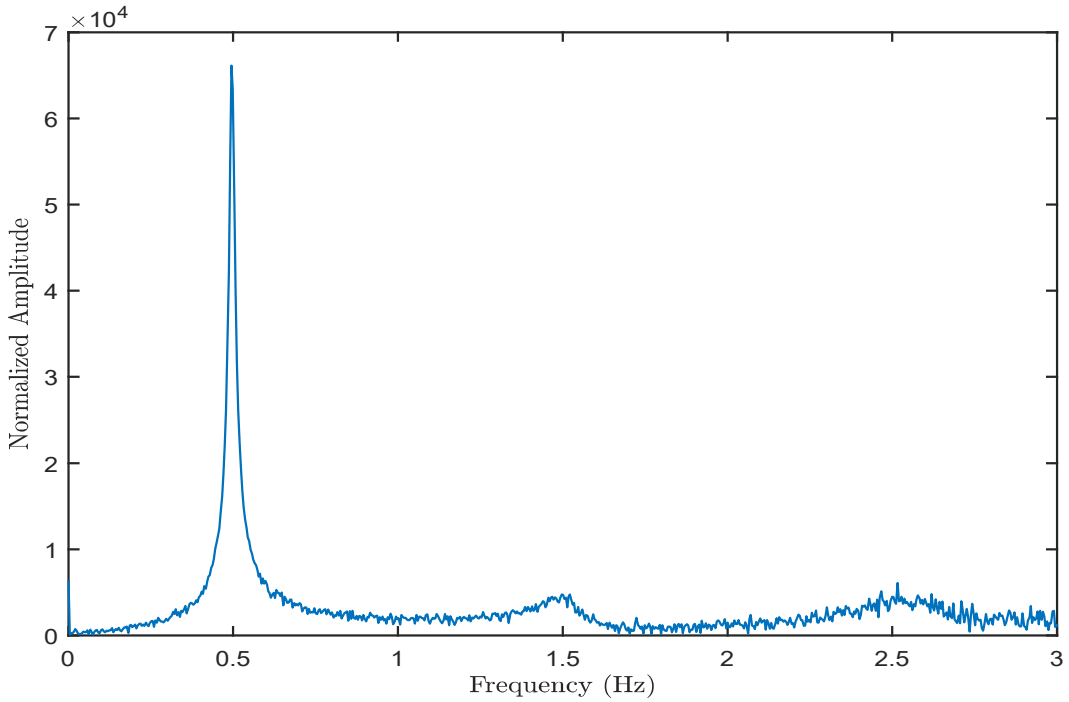

Figure E.16: FRD result from Test 1 of Case 8

The total damping can be observed from Figures E.15, D.11, and D.14, although there are some fluctuations in the resultant DHSs. The values of total damping for the first three resonance responses shown in Figures E.15, D.11, and D.14 are summarized in Table E.2. Similar to Table E.1, the reference values of the damping of the first three resonance responses and the corresponding relative errors for each test in Case 8 have been summarized in Table E.2. Although there is noise, the values of the total damping in Table E.2 are close to each other.

Although the FRD results have been negatively affected by the noise, the leak localization can still be implemented using FRD by reading the values of the FRD results at the frequencies of the first three resonance harmonics, based on the technique in Gong et al. (2013a). Similarly, the leak localization can be conducted using the DOFT techniques in Wang et al. (2002) and Du et al. (2020). The leak localization results of utilizing both the two methods are summarized in Table E.3. Based on the results presented in Table E.3, the accuracy of the leak localization results using the DOFT method is higher than the accuracy using the FRD method. This is because the application of the DOFT method focuses on the attenuation of the frequency responses of the signal at particular frequencies versus time. The damping can still be observed with the noise, since the frequency response of the noise is also damped due the leak on the pipeline. However, the application of the FRD method only focuses the peak values of the first three resonance harmonics at the end of the measurement, and thus the negative effects from noise cannot be eased. Additionally, the DOFT method utilizes more information about the signal with more analysis steps than the FRD method, since the DOFT method analyzes the signal window by window, but the FRD method analyzes the signal at the end of the measurement. Consequently, the DOFT method is more robust for the analysis of noisy signals than the FRD method, based on the results presented in Tables E.1, E.2, and E.3.

Table E.1: Comparison of peak values of the first three resonance responses in the FRD results from Case 8

Test	SNR	1st harmonic		3rd harmonic		5th harmonic	
Number	(dB)	Value	Error (%)	Value	Error (%)	Value	Error (%)
Reference	no noise	65689.1		4498.41		3929.18	
1	30	66137	0.68	4759.38	5.8	4495.44	14.41
2	20	67041.7	2.06	3127.83	30.47	4150.53	5.63
3	10	62139.1	5.4	3170.02	29.53	8200.01	108.7

Table E.2: Comparison of values of total damping of the first three resonance responses in the DOFT results from Case 8

Test	SNR	1st harmonic		3rd harmonic		5th harmonic	
Number	(dB)	Value	Error (%)	Value	Error (%)	Value	Error (%)
Reference	no noise	0.0254		0.0957		0.246	
1	30	0.0254	0	0.0944	1.36	0.24	2.44
2	20	0.0261	2.76	0.089	7	0.2186	11.14
3	10	0.0263	3.54	0.1102	15.15	0.2201	10.53

Table E.3: Leak localization results from Case 8

Test	SNR	Leak location	DOFT result	DOFT error	FRD result	FRD error
Number	(dB)	(m)	(m)	(%)	(m)	(%)
1	30	100	101.35	0.27	122.5	4.5
2	20	100	108.6	1.72	135.3	7.06
3	10	100	112.3	2.46	151.2	10.24

E.3.6 Comparison and Discussion for Real-time Data Monitoring Capability

According to the work in Du et al. (2021), utilizing the Fourier transform-based techniques for real-time data monitoring can be implemented by analyzing the signal window by window with the window gap to be the real-time data acquisition speed, which is the reciprocal of the sampling rate. Accordingly, the analyzed window can be moved slightly to adapt to the real-time data acquisition speed, and thus every new data point that is acquired can then be processed one time step at a time. However, utilizing the FRD method in a window instead of the whole range of data is impossible for application to real-time data monitoring. Firstly, the required signal length for leak localization solution in Gong et al. (2013a) limits its applicability to real-time data monitoring, since the required signal length is from the occurrence of the transient to steady state. Accordingly, the leak cannot be localized when analyzing the signal in a window rather than using the whole range of data via the FRD method, since there is no corresponding solution to the leak location. Secondly, the required input signal limits the potential of the real-time data monitoring capability of the FRD method, based on Eq. (E.5). This is because only when the input signal is non-zero can the result of using the FRD method be generated. Accordingly, for example, if the input signal is the impulse signal, and the lower limit of the selected window is after the impulse, the input signal in the selected window will be all zero values, and thus the FRD result cannot be generated. A numerical scenario, Case 9, has been performed to verify the second point of view of the previously-mentioned analyses, since it is unnecessary to implement a verification scenario for the first one under the condition that there is no solution to the leak location to be applied.

In Case 9, the applied input signal is the same as in Case 4, which is the leak case, as shown in Figure E.7. The selected window length is the fundamental

period of the signal, which is 2 s. The lower limit of the window is 0.7 s, and the upper limit of the window is 2.7 s. The corresponding FFT result of the input signal in the selected window is shown in Figure E.17. As shown in Figure E.17, the FFT result of the input signal in the selected window is inapplicable to the FRD method, since it only contains zero values. Accordingly, the FRD method cannot be utilized. Therefore, analyzing the signal window by window using the FRD method is restricted by the input signal. Based on the fact that there is no solution to the leak location when utilizing the FRD method in a window instead of the whole range of data, and the limitation from the input signal, it is impossible to utilize the FRD method for real-time data monitoring, because real-time data monitoring requires the signal to be analyzed window by window for every sampling time step (36).

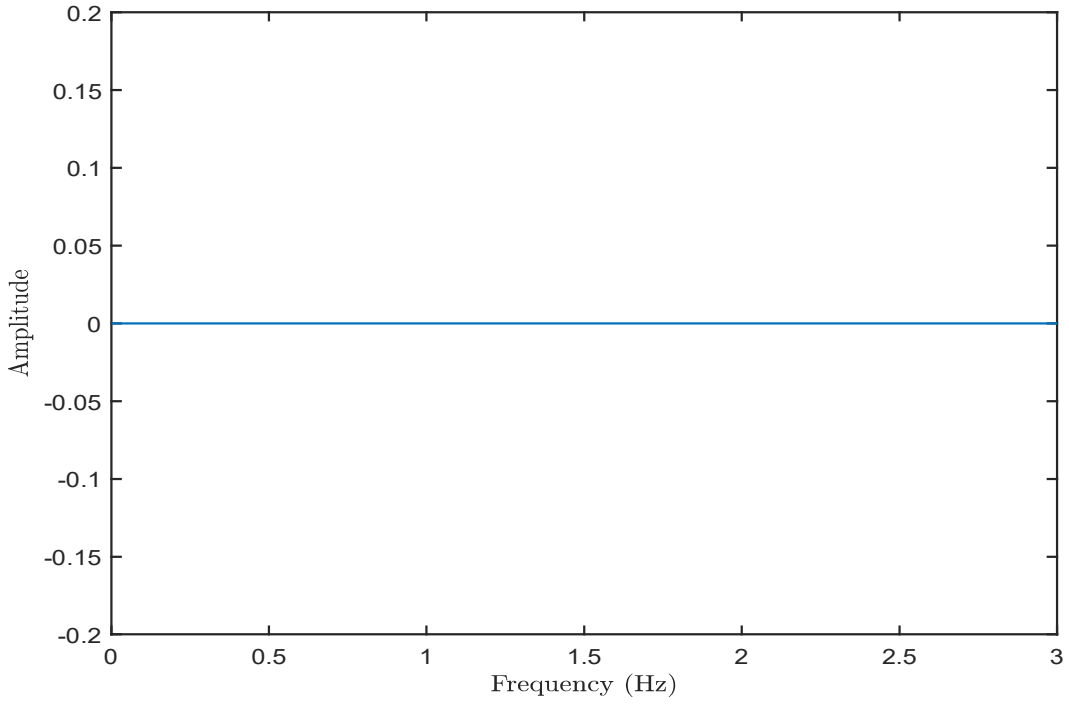

Figure E.17: FFT result of the input signal from Case 9

Conversely, the DOFT method can be applied to real-time data monitoring based on the previous research, as long as the window gap between the current and the next windows equals the reciprocal of the sampling rate (36). A numerical scenario, Case 10, has been implemented to verify the DOFT method for real-

time data monitoring of the leak problem. In Case 10, the window length is set to be the fundamental period of the signal, 4 s, and the window gap is set to be the reciprocal of the sampling rate, which is 0.05 s. The applied input and output signals are the same as in Case 4, as shown in Figures E.7 and E.8. Utilizing the technique in Du et al. (2021) provides the resultant DHS as presented in Figure E.18, and the leak localization result of 99.45 m, with the localization error of 0.11%. It is worth noting that the resultant DHS shown in Figure E.18 is only analyzed in the time period from 0 s to 20 s, since the application of DOFT does not require the signal to be analyzed in the time period from the application of input signal to the complete decay of output signal, which is 120 s in this case. Based on the results from Cases 9 and 10, the DOFT method can be applied to real-time data monitoring, while the FRD method has no capability to be applied to the area of real-time.

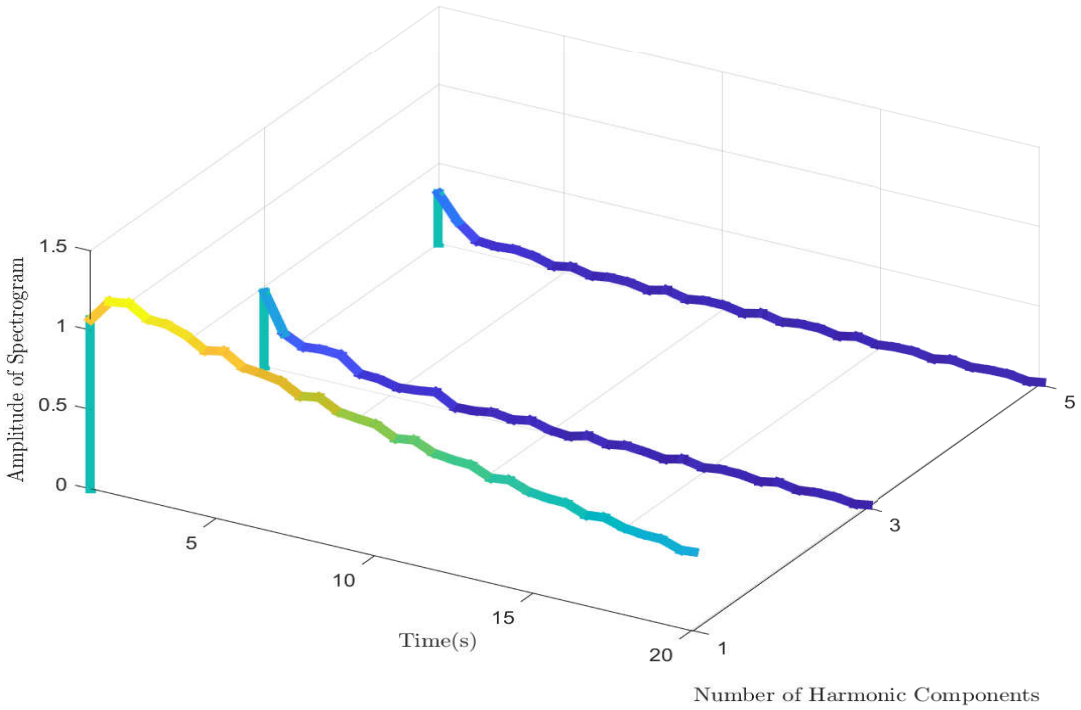

Figure E.18: Discrete harmonic spectrogram from Case 10

E.4 Experimental Verification for the Mathematical Relationship

Two experimental scenarios have been conducted to verify the mathematical relationship between the DOFT and FRD methods in this paper, which are referred to as Experimental Cases 1 and 2. Both cases were conducted in the Robin Hydraulics Laboratory at the University of Adelaide. In Experimental Case 1, the applied data is from Lee (2005), and the corresponding experimental pipeline system is shown in Figure E.19. As shown in Figure E.19, the downstream valve is fully closed, and the transient is generated by closing the side discharge located at 0.16 m from the downstream boundary, which is initially fully opened. The output signal is measured at the same location as the transient source. The corresponding measured signal is shown in Figure E.20. Replicating the same procedures in Case 1 provides the resultant DOFT and FRD results shown in Figure E.21. It can be seen that the results using the two methods are matched adequately.

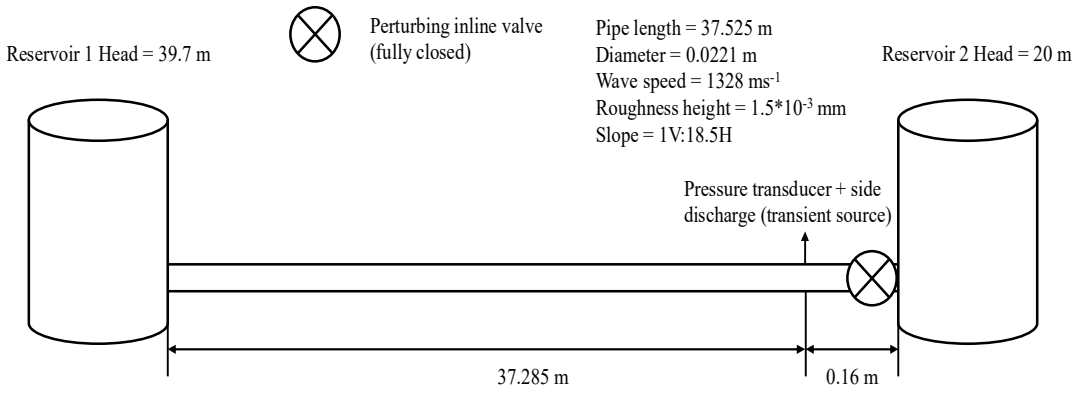

Figure E.19: Pipeline configuration from Experimental Case 1

Experimental Case 2 was conducted under the condition of a burst. The corresponding experimental pipeline system is shown in Figure D.16. The pressure transducer is located at point P, and the burst is located at point B. More details of the experimental pipeline system can be found in Vitkovsky (2007), Wang et al. (2002), and Du et al. (2020). The downstream valve of the pipe

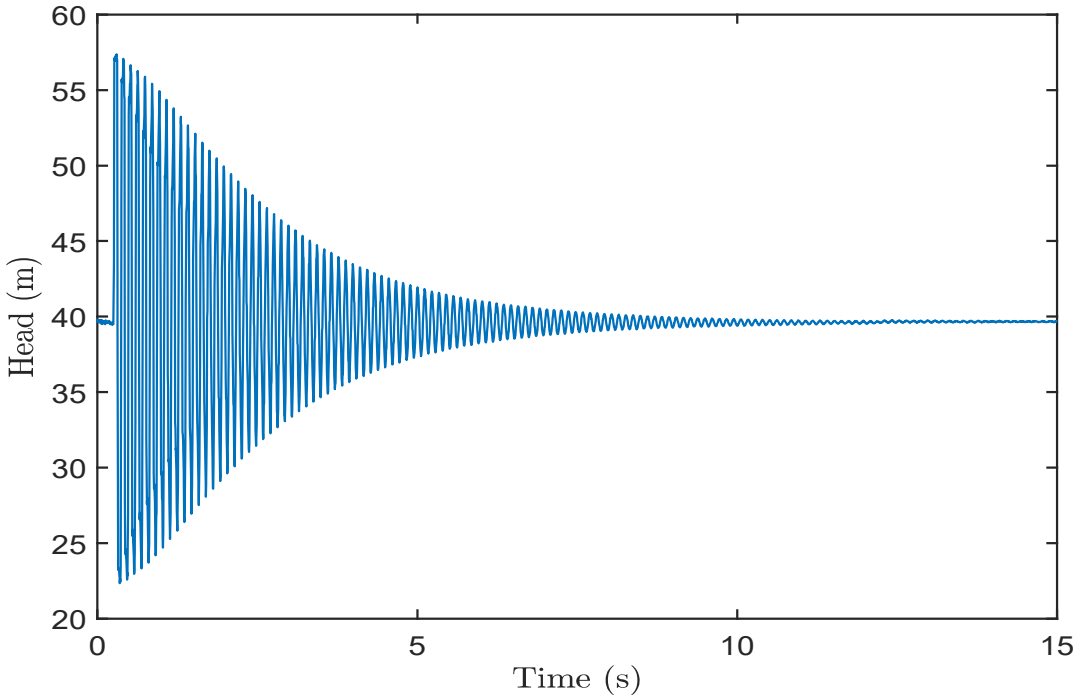

Figure E.20: Measured time trace from Experimental Case 1

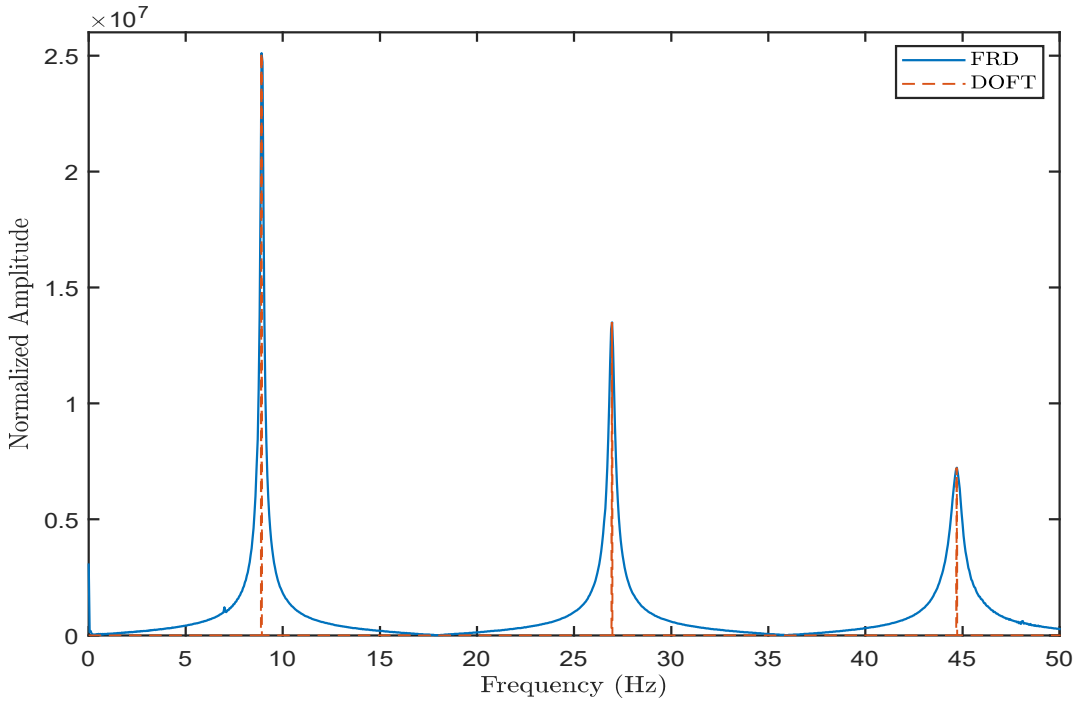

Figure E.21: DOFT and FRD results from Experimental Case 1

is set to be fully closed to isolate the west tank from the pipe system. The burst is located at 19.3 m from the upstream boundary, and is simulated by a solenoid side discharge valve. The initial flow rate of the test is $Q_0 = 0$ m^3/s, the wave speed is $a = 1320$ m/s, and the head at the upstream tank is 3.065 bar, which is the east tank. The measured time trace is shown in Figure D.17, and the resultant first three resonance responses using the DOFT and FRD methods are shown in Figure D.18. The frequency responses in Figure D.18 are matched with acceptable errors, which verifies the mathematical relationship between the DOFT and FRD methods in the paper. By utilizing the burst localization procedure in Du et al. (2020), the estimated burst location is 18.98 m, where the localization error is 0.84%.

E.5 Discussion on Pipeline System Parameters

In addition to the aspects that are discussed in the previous sections, other parameters of the pipeline system may have effects on the derived relationship in this paper. The wave speed of the pipeline can affect the reference time that is utilized in Eq. (E.2). Additionally, it can affect the overall magnitude of the leak and the burst damping, according the equations of K_L and K_B presented in Wang et al. (2002) and Du et al. (2020), respectively, which are shown as

$$K_L = \frac{C_d A_L}{A_p} \frac{2ab}{(2gH_{L0})^{1-b}} \tag{E.21}$$

and

$$K_B = \frac{C_d A_B}{A_p} \frac{2ab}{(2gH_{B0})^{1-b}} \tag{E.22}$$

where g is the gravity acceleration, H_{L0} and H_{B0} are the steady head at the leak and the burst locations, respectively, and b is the parameter of leak/burst discharge-head relationship, which is set to be a constant. According to Eqs. (E.21) and (E.22), the overall magnitudes of the leak and the burst damping are proportional to wave speed, and thus, the wave speed can affect the overall magnitude of Eqs. (E.13) and Eqs. (E.18). However, according to the derivation process in this paper, the relationship between the two methods remains unchanged from the mathematical perspective. Additionally, since the leak and the burst damping remain unchanged after their occurrence for the same pipeline, the relationship remains the same from the application perspective. Because the defect affects the overall attenuation extent of the measured signal, and thus, affects the utilized output signals of the applications of the two methods equally. Different wave speeds are utilized in numerical and experimental verifications as shown in the corresponding pipeline configuration figures, and the corresponding results verify the studied relationship between the two methods in this paper.

According to Eqs. (E.21) and (E.22), different cross-sectional areas of the applied side-discharges (i.e., to simulate leak and burst) can affect the overall magnitudes of the leak and the burst damping, since their magnitudes are proportional to the size of the leak and the burst. However, the researched relationship between the two methods remains the same from the perspectives of math and application due to the same reasons as for wave speed analysis. Different side-discharges have been utilized in Cases 4 and 5, and the corresponding analysis results verify the relationship. It is worth noting that a side-discharge has been applied to the leak problem to generate the transient event, the cross-sectional area of the applied side-discharge for transient generation can affect the magnitude of the sudden pressure rise when closing the side-discharge valve, and thus, affect the unsteady friction (78; 143).

Similarly, the pipe inner diameter has the same effect on the proposed relationship in this paper, according to Eqs. (E.21) and (E.22), since the change

of pipe inner diameter changes the inner cross-sectional area of the pipe. However, the proposed relationship remains the same due to the same reasons as for analyses of wave speed and side-discharges. Different pipe inner diameters have been applied to the conducted numerical and experimental verifications, according to their corresponding pipeline configuration figures, and the results verify the proposed relationship.

The steady and unsteady friction can affect the overall attenuation extent of the measured signal. However, for the same pipeline, the steady and unsteady friction remain unchanged after the occurrence of the transient, according to unsteady friction research in the literature (78). Therefore, the steady and unsteady friction affects the utilized output signals of the applications of the two methods equally. Steady friction has been utilized in numerical verifications, and both steady and unsteady friction have been involved in experimental verifications, and the corresponding analysis results verify the researched relationship in this paper under the condition of both the inclusion of steady and unsteady friction.

E.6 Conclusion and Discussion

The previously researched leak detection techniques based on the DOFT and FRD methods are both Fourier transform-based techniques. However, they utilize different signal processing algorithms. The mathematical derivation presented in this paper revealed the mathematical relationship between these two techniques from the perspectives of both leak and burst detection. The mathematical solutions of these two techniques are connected by utilizing the Fourier transform theorems and the basic nature of the resonance responses of the signal in frequency domain.

The mathematical relationship between the DOFT and FRD methods has been verified both numerically and experimentally by applying the leak and burst scenarios. Although the DOFT and the FRD techniques utilize different algorithms, the numerical and experimental results both provide an adequate match between them. The discussions between the two methods from the perspectives of input signal bandwidth, problem type, low sampling rate capability, robustness, and real-time data monitoring capability have been implemented. Although both the techniques match each other with different input signal bandwidths, and are capable of utilizing low sampling rate (i.e., the Nyquist frequency of the 3rd resonance response), the differences between the two methods in other discussed areas exist. It has been shown that the DOFT method can be utilized for both the leak and burst problems. However, the FRD method cannot be applied to the burst problem, since its application requires the Fourier transform of the input signal, which is the unknown element in the burst problem. The DOFT method is more robust than the FRD method with three conducted tests using different SNRs, since the noise is also damped in addition to the signal itself due to the leak, and the DOFT method is able to be utilized to analyze the damping of the signal. The DOFT method can be applied to real-time data monitoring, while this capability of the FRD method is limited by the difficulty in determining the input signal and the lack of the solution to leak location in a time period that is shorter than the time period from occurrence of the transient event to the steady state.